THESIS OF

SORBONNE UNIVERSITY
AND OF THE UNIVERSITY OF LATVIA

Subject: Physics

Doctoral school in France: “Physique en Île-de-France”

performed in

PHENIX - Physicochimie des Électrolytes et Nanosystèmes interfaciaux

and

MMML - Magnētisku mīkstu materiālu laboratorija

defended by

Andris Pāvils STIKUTS

to obtain the title:

DOCTOR OF THE SORBONNE UNIVERSITY AND THE UNIVERSITY OF LATVIA

Title of the dissertation:

Magnetic fluid droplets in rotating fields: theory, experiments and simulations

defended on 14/10/2022

in front of a jury composed of:

Mr.	Georges BOSSIS	Reviewer
Mr.	Thomas FISCHER	Reviewer
Mr.	Ali ABOU-HASSAN	Examiner
Mr.	Agris GAILĪTIS	Examiner
Mr.	Andrejs CĒBERS	Advisor
Mrs.	Régine PERZYNSKI	Advisor

THÈSE DE DOCTORAT

DE SORBONNE UNIVERSITÉ
ET DE L'UNIVERSITÉ DE LETTONIE

Spécialité : Physique

École doctorale : "Physique en Île-de-France"

réalisée à

PHENIX - Physicochimie des Électrolytes et Nanosystèmes interfaciaux

et

MMML - Magnētisku mīkstu materiālu laboratorija

présentée par

Andris Pāvils STIKUTS

pour obetinr le grade de :

DOCTEUR DE SORBONNE UNIVERSITÉ ET DE L'UNIVERSITÉ DE LETTONIE

Sujet de la thèse :

Gouttes de fluide magnétique en champ tournant : théorie, expériences et simulations

soutenue le 14/10/2022

devant le jury composé de :

M.	Georges BOSSIS	Rapporteur
M.	Thomas FISCHER	Rapporteur
M.	Ali ABOU-HASSAN	Examinateur
M.	Agris GAILĪTIS	Examinateur
M.	Andrejs CĒBERS	Directeur de thèse
M^{me}	Régine PERZYNSKI	Directrice de thèse

SORBONNAS UNIVERSITĀTES

UN LATVIJAS UNIVERSITĀTES

DISERTĀCIJA

Nozare, apakšnozare: fizika, šķidrumu un gāzu mehānika

Doktorantūras skola Francijā: “Physique en Île-de-France”

izstrādāta

PHENIX - Physicochimie des Électrolytes et Nanosystèmes interfaciaux

un

MMML - Magnētisku mīkstu materiālu laboratorija

aizstāv

Andris Pāvils STIKUTS

lai iegūtu grādu:

SORBONNAS UNIVERSITĀTES UN LATVIJAS UNIVERSITĀTES

DOKTORS

Disertācijas nosaukums:

Magnētiskā šķidruma pilieni rotējošā laukā: teorija, eksperimenti un simulācijas

aizstāvēta 14/10/2022

šādas žūrijas priekšā:

Georges BOSSIS	Recenzents
Thomas FISCHER	Recenzents
Ali ABOU-HASSAN	Eksperts
Agris GAILĪTIS	Eksperts
Andrejs CĒBERS	Darba vadītājs
Régine PERZYNSKI	Darba vadītāja

Acknowledgements

To begin, I am immensely grateful to the advisors for the thesis Andrejs Cēbers and Régine Perzynski. Thank you for accepting me under your tutelage and for sharing your insight in times when the problems seemed most confusing! I am thankful also for helping me navigate the procedures and technicalities in the cotutelle studies between two countries and universities.

I appreciate all the love and support I have received from my friends and family, to whom I could reach out in times of need. I am glad I had the wonderful company of my colleagues in Riga and in Paris , who made the days more colorful and pleasant.

I want to express my sincere gratitude to two colleagues in particular: Thank you, Aigars, for the help with writing the simulation software and keeping the spirits high! And thank you, Guntars, for your insight with the experiments and help with traversing administrative technicalities!

I am thankful to Georges Bossis and Thomas Fischer, who agreed to read and review the dissertation, and to Agris Gailītis and Ali Abou-Hassan, who agreed to participate in the jury as examiners.

Finally, I am grateful for the financial support I have received during my studies:

- scholarship for the stays in Paris from the embassy of France in Latvia,
- scholarship for first three years of the studies from SIA "Mikrotīkls" through LU Fonds,
- scholarship for the final year of the studies from the project "Strengthening of the capacity of doctoral studies at the University of Latvia within the framework of the new doctoral model", identification No. 8.2.2.0/20/I/006.

Contents

1 Preamble

1.1 System of units in magnetism

Since the establishment of the International System of Units (SI) in the 11th General Conference of Weights and Measures in 1960, it has become the most widely used system of measurements in scientific and engineering applications [1]. Despite the widespread adoption of SI, many physicists working in magnetism have retained the use of the Gaussian or Centimeter-Gram-Second (CGS) system. Ultimately the use of a particular system of measurement is arbitrary and it is relatively easy to convert the variables from one to the other.

In addition to having different units, constants in electromagnetism differ between the two systems thus changing the form of some equations. The way to convert electromagnetic quantities between the two systems is nicely summarized in the final pages of [2]. The equations need to be changed to include the constants used in the corresponding system. For magnetism, the change of variables in equations is gathered in the table 1, and the change of units is gathered in the table 2.

The vacuum magnetic permeability μ_0 used to be set exactly to $4\pi \cdot 10^{-7} H/m$ in SI and 1 in CGS, and the conversion between the two systems was done by simple multiples of 4π and powers of 10. This, however, is no longer the case since May 20, 2019 [3]. The value of vacuum magnetic permeability is now dependant on the measurement of the fine structure constant

$$\mu_0 = \frac{2h\alpha}{ce^2}, \tag{1.1}$$

where h is the Planck constant (exact), α is the fine structure constant (measured), c is the speed of light (exact), and e is the absolute value of the electron charge (exact). The current measured value of μ_0 is [4]

$$\mu_0 = 1.25663706212(19) \cdot 10^{-6} H/m \approx 4\pi \cdot 10^{-7} H/m. \tag{1.2}$$

For all practical purposes, the conversion between the two systems remains the same as before 2019, however, philosophically there is a difference - a measurement error is propagated when changing from SI to CGS. Furthermore, less confusion will be experienced and more interdisciplinary cooperation encouraged if we all move to a single measurement system, which nowadays is the SI. For these reasons, the SI will be used in this work.

Quantity	CGS	SI
Magnetic field intensity	$\boldsymbol{H}/\sqrt{4\pi\mu_0}$	$\boldsymbol{H}$
Magnetic field induction	$\boldsymbol{B}\sqrt{\mu_0/4\pi}$	$\boldsymbol{B}$
Magnetization	$\boldsymbol{M}\sqrt{4\pi/\mu_0}$	$\boldsymbol{M}$
Magnetic permeability	$\mu_0\mu$	μ
Magnetic susceptibility	$4\pi\chi$	χ

Table 1: Conversion table between CGS and SI variables in formulas [2]. To convert from SI to CGS, the symbol in the cell of SI column should be replaced with the corresponding cell in CGS column. For example, $Bm \overset{SI}{=} 4\pi\mu_0\frac{R_0H^2}{\gamma} \rightarrow Bm \overset{CGS}{=} 4\pi\mu_0\frac{R_0(H/\sqrt{4\pi\mu_0})^2}{\gamma} = \frac{R_0H^2}{\gamma}$.

Quantity	Symbol	SI	CGS
Magnetic field intensity	H	$1\ A\ m^{-1}$	$4\pi \cdot 10^{-3}\ Oe$
Magnetic field induction	B	$1\ T$	$10^4\ G$
Magnetization	M	$1\ A\ m^{-1}$	$10^{-3}\ G$

Table 2: Conversion table between CGS and SI units [2]. The columns list the same amount of a physical quantity expressed in either SI or CGS system.

2 Introduction

2.1 Magnetic fluids

Magnetic fluids also called ferrofluids first developed in the 1960s in the USA [5] are intriguing materials that are both liquid and strongly influenced by magnetic fields [6, 7]. Ferrofluids are made of solid magnetic (for example, certain iron oxide) nanoparticles suspended in a carrier liquid. The small size of the nanoparticles (diameter $d \approx 10\ nm$) ensures both that the particles contain a single magnetic domain, and that due to thermal fluctuations they remain in the bulk fluid. This results in a liquid that experiences a force in a magnetic field gradient as a whole, and that remains liquid, as opposed to magnetic particles being pulled out of the fluid. A related class of materials are the magnetorheological fluids, where the size of the magnetic particles dispersed in a fluid is larger - on the order of micrometers. Magnetorheological fluids rapidly change the properties of their fluidity depending on the applied magnetic field, which makes them interesting in many industrial applications [8, 9], however, they will not be examined in this dissertation.

The ability to precisely manipulate liquid matter with external magnetic field has resulted in fundamental scientific research of magnetism in matter, the development of novel chemical procedures for the syntheses of magnetic fluids [10], multiple commercial and non-commercial applications [11, 12], and even art [13]. Through the years significant progress has been made in the field of physics dealing with magnetic liquids named

ferrohydrodynamics by one of its pioneers R. E. Rosensweig [14]. For a more in-depth overview of the field, see one of several textbooks that have been written on it [10, 15, 16].

2.1.1 Structure and stability

The magnetic nanoparticles in ferrofluids experience external forces that can cause their sedimentation from the suspension - namely, gravity and magnetic forces. For the ferrofluid to be stable, the energy due to the thermal motion should be larger than the energy due to the external forces.

First, let us compare the gravitational to thermal energies

$$\frac{\Delta\rho V_{NP} g L}{k_B T} \leq 1, \tag{2.1}$$

where $\Delta\rho \approx 4000\ kg/m^3$ is the difference of densities between the nanoparticles and the carrier fluid, V_{NP} is the magnetic particle volume, $g = 9.8\ m/s^2$ is the free-fall acceleration, $L = 5\ cm$ is a typical container height, $k_B = 1.38 \cdot 10^{-23}\ J/K$ is the Boltzmann constant and $T = 293\ K$ is the room temperature. Assuming a spherical nanoparticle, this results in the diameter of the particle such that it remains suspended in a gravitational field $d \leq 34\ nm$.

Second, a magnetic field gradient can produce a force that causes the sedimentation of suspended particles, therefore, let us compare magnetic to thermal energies (the form of the magnetic energy is from page 34 of [15])

$$\frac{\mu_0 m_{NP} H}{k_B T} \leq 1, \tag{2.2}$$

where $m_{NP} = M_{NP} V_{NP}$ is the magnetic moment of the nanoparticle, $M_{NP} \approx 3 \cdot 10^5\ A/m$ is the saturation magnetization of the nanoparticle [17] (since they are single domain particles), $\mu_0 H = 0.1\ T$ is the magnetic field strength of a common permanent magnet. This results in the diameter of the particle such that it remains suspended in a magnetic field gradient $d \leq 6.4\ nm$.

This simple analysis explains why the particles suspended in a magnetic fluid need to be only several nanometers in diameter. The method how historically such small particles were created was by milling larger magnetic particles [5], however, nowadays chemical precipitation is commonly used [18]. Importantly, the nanoparticles experience

attractive forces that can cause them to agglomerate into structures that are larger than the necessary size for the stability of the suspension. These forces include magnetic dipole-dipole interactions and more importantly van der Waals forces. To remedy this, it is necessary to create short-range repulsive forces between the nanoparticles. It is commonly done either by coating the nanoparticles with long molecules [15] that produce steric repulsion or coating them with a charge layer [18]. The choice of the carrier fluid is broad ranging from various hydrocarbon solvents to water [10, 15] and more recently ionic liquids - salts that are liquid at room temperatures [19].

The magnetic nanoparticles are held in suspension by a balance of several interactions. This balance can be tipped by changing the surrounding conditions, and a reversible gas-liquid type phase transition can occur [16]. This transition occurs when the applied magnetic field is increased or the temperature is decreased [20, 21]. For the case of charge stabilized nanoparticles, the phase separation can be induced by the increase of ionic strength [22]. In this phase transition the ferrofluid forms two liquid phases with different concentration of nanoparticles in them. Since the phase transition onset is sensitive to the size of the nanoparticles, a method akin to fractional distillation can be used to obtain monodisperse ferrofluids [23]. In the phase separation the concentrated phase appears as many micron-sized droplets (see section 4.1), which are highly magnetic and have a low surface tension allowing for the observation of strong magnetic effects already at small field values [24].

The simplest model for the equilibrium magnetization of a ferrofluid is Langevin's theory, where it is assumed that the inter-particle interactions are negligible and they interact only with the external field [15]. The energy of the nanoparticles in the external field $-\mu_0 \boldsymbol{m}_{NP} \cdot \boldsymbol{H}$ is distributed according to the Boltzmann distribution, which leads to the average magnetization of the ferrofluid

$$\frac{M}{M_s} = \coth(\xi) - \frac{1}{\xi}, \tag{2.3}$$

where M_s is the saturation magnetization of the ferrofluid (when all the nanoparticles have their magnetic moments aligned with the external field $\boldsymbol{H}$), and $\xi = \mu_0 m_{NP} H/(k_B T)$. Even though it contains suspended nanoparticles with a permanent magnetic moment, the ferrofluid itself does not possess a remnant magnetization when the external field is turned off. Due to thermal agitation the once aligned nanoparticles soon become oriented in uniformly random directions. Therefore magnetic fluids exhibit superparamagnetic

behavior. It might be noted that the inter-particle interactions are negligible when the volume fraction of the nanoparticles $\phi_{NP} \ll 1$, but as described in section 4.1, the actual nanoparticle volume fraction in the magnetic droplets is around 30%. In this more clustered scenario the interactions between the nanoparticles are strong and they can, for example, form chains [25].

2.1.2 Some effects of magnetic fluids

In the field of fluid mechanics many beautiful and fascinating patterns and instabilities arise, which have captivated the attention of researchers for centuries [26, 27]. The addition of the magnetic field only increase the variety and intricacy of the patterns that develop. Here we mention only a few of them.

Perhaps the most famous effect magnetic fluids is the normal field instability. When a strong enough magnetic field is applied in the direction normal to the surface of the ferrofluid, the flat surface becomes unstable and fluid spikes arranged in a hexagonal formation grow out of it [28]. An analysis based on the energy minimization method has shown that there are three stable configuration of the ferrofluid surface depending on the magnetic field strength - a flat surface, a hexagonal arrangement of spikes, and a square arrangement of spikes [29]. Furthermore, it was shown that transition from one stable configuration to the next is governed by a hysteresis i.e. the instability occurs above a critical magnetic field value, and it is not immediately reversed by decreasing the magnetic field. The hysteresis loop has been observed experimentally [30].

If a magnetic field normal to the ferrofluid interface seeks to destabilize it, the opposite effect happens if the field is tangential to it - the onset of surface instabilities that would develop without the application of the field are delayed [15, 31]. For example, the Kelvin–Helmholtz instability, which develops between two liquids that are moving with different velocities, has been observed to be calmed by the application of a tangential magnetic field [32, 33].

Another stunning instability occurs in magnetic fluids confined to a thin layer [34], for example, in a Hele-Shaw cell or if the magnetic fluid is contained in a thin liquid film [35]. If a drop of ferrofluid is placed between plates and a magnetic field is applied perpendicular to the plates, the circular drop becomes unstable and elongates; increasing the field the elongated shape develops thickened tips that also split in two. By this continued bifurcation a maze-like structure develops [36]. A similar phenomenon to this

labyrinthine instability is the magnetic micro-convection [37]. If a ferrofluid is adjacent to a miscible non-magnetic fluid, the application of a magnetic field first causes fingers to grow between the fluids, which then disappear due to the diffusion of magnetic nanoparticles in the non-magnetic liquid. The magnetic micro-convection is proposed as a viable mechanism to facilitate the mixing of fluids in microfluidics channels [38, 39].

Typically the hydrodynamic stress acting on a fluid is symmetric, which is a consequence from the assumption that there is no body torque acting on the fluid. This assumption is no longer valid for magnetic fluids in time-varying magnetic fields or in external flows with non-zero rotation since there are nanoparticles that rotate to align with the field with a finite angular velocity. This causes the magnetization $\boldsymbol{M}$ and the external magnetic field $\boldsymbol{H}$ to not be aligned resulting in a peculiar anti-symmetric stress component in the fluid. The misalignment between the external field and the magnetization of the ferrofluid can be modeled with a phenomenological magnetization relaxation equation [40]

$$\frac{d\boldsymbol{M}}{dt} - \boldsymbol{\omega}_0 \times \boldsymbol{M} = -\frac{1}{\tau}(\boldsymbol{M} - \boldsymbol{M}_0), \tag{2.4}$$

where $\boldsymbol{\omega}_0$ is the local rotation velocity of the fluid, τ is a characteristic time in which the magnetization returns to zero when the field is turned off, and $\boldsymbol{M}_0$ is equilibrium magnetization if the fluid would not be rotating. A famous consequence of the finite magnetization relaxation time is the apparent increase of viscosity in magnetic fluids when the field is turned on [41].

2.2 Magnetic droplets

The ability to manipulate droplets from the outside with magnetic fields has found many applications. For example, in the field of microfluidics the magnetic field can be used to sort, transport and form the droplets [42]. The magnetic droplets can be used as microrobots to transport cargo and traverse obstacles [43, 44]. Bio-compatible magnetic droplets can be used as a measurement tool for the mechanic properties of tissues [45, 46]. In all of these cases it is vital to be able to accurately calculate the dynamics of the droplets in applied magnetic fields to better be able to control them.

Before the advent of magnetic fluids, the behavior of droplets under electric fields was studied [47, 48]. This lead to the development of the field of *electrohydrodynamics* [49]. Due to the similarities in equations between electrostatics and magnetostatics, a lot of the results can be carried over from one field to the other. One notable difference is the

presence of the electric charge, which has resulted in some effects in electric problems that do not occur in magnetic ones. Some examples include droplets in electric fields, which develop conical tips, where the accumulated charge is shed as a stream of tiny droplets [48]; or the Quincke rotation (or electrorotation) of droplets in constant electric fields due to a charge build up on their surface [50, 51].

A magnetic fluid droplet placed in a static homogeneous magnetic field experiences an additional pressure jump across its surface equal to $\mu_0 M_n^2/2$, where M_n is the component of the droplet's magnetization normal to the surface. Since for a spherical droplet the magnetization is in the direction of the external field, the droplet elongates until surface tension counteracts the magnetic force [52, 53]. Interestingly, also nonmagnetic bubbles in a magnetic fluid elongate in the direction of the field [53, 54]. As the droplet elongates its shape is well described as an ellipsoid up to the aspect ratio $a/b \leq 7$ [55], after which it becomes more sharp at the tips than an ellipsoid and may even develop conical tips [56]. Streaming of tiny droplets from ferrofluid drops in magnetic field has not been observed. More recent numerical simulations place the aspect ration when a droplet ceases to be ellipsoidal at $a/b \leq 4$ [57]. After the development of phase separated ferrofluid droplets [24], which have a large magnetic permeability μ and a small surface tension, more extreme deformations were observable in small magnetic fields. Of note is the appearance of a hysteresis in the droplet elongation for large values of $\mu \geq 21\mu_0$. Above a critical magnetic field value the droplet strongly elongates; if the field is then reduced, the droplet remains elongated, until another critical field value is reached below which the droplet strongly contracts.

Along with the experimental observation of magnetic droplets in static field a number of theoretical descriptions have been proposed. Assuming a prolate spheroidal shape and linear magnetization of the droplet, the equilibrium elongation can be calculated in various ways: by energy minimization [24], by the virial method [58, 59] or by the enforcement of the dynamic boundary condition on the equator and the poles of the droplet [48, 60]. Recently after comparison with numerical simulations, a semi-analytical equation was proposed that is valid for large aspect ratios $a/b \leq 12$, when the droplets are no longer spheroidal [61]. The development of the theoretical equilibrium curves allows for the indirect measurement of physical properties such as the magnetic permeability and surface tension of microscopic magnetic droplets - something that is hard to do directly [24, 62]. The assumption of the spheroidal shape allows also to describe the dynamics of ferrofluid droplets [63, 58, 59]. Small deformation theories show that the droplets

exponentially approach an equilibrium elongation in an external magnetic field [64, 65].

In a time-dependant magnetic field, the behavior of magnetic droplets is rich and varied. In a slow rotating field the droplets elongate and rotate in the direction of the field like compass needles. The viscous friction can cause the tips of the droplets to be bent [66], and even break the droplets in half [67]. In larger groupings of needle-like droplets the resulting size of the droplets was determined from a competition between the droplet break-up and coalescence [67]. For fast rotating fields, the influence of the magnetic field can be averaged over the rotation period. In this regime, in small magnetic field the droplets initially are oblate spheroids in the plane of the rotating field. Above a critical magnetic field value, the droplets experience a spontaneous symmetry breaking and they elongate tangential to the plane of the rotating field. Increasing the field further, this elongated shape becomes unstable and the droplet again takes up an oblate, very flattened shape, and a crown of fingers appears on its perimeter, which is reminiscent of the normal field instability [68, 69]. This oblate-prolate-oblate shape instability has been theoretically analyzed under the assumption that the droplet is ellipsoidal [68, 70]. Also in this instability, a hysteresis can be observed above a critical value of magnetic permeability μ. A droplet in a fast precessing field undergoes similar shape instabilities [69]. For intermediate field rotation frequencies, the motion of the droplets can become unsteady - they can form swirling "S", "8" and "O" shapes that do not remain stationary [71]. As a slender droplet moves from the steady motion in a low frequency field to the motion in an intermediate frequency field, a shock-wave of the tangent vector angle propagates from its tips to the center [72]. The behavior of the droplets depending on the rotating field strength and frequency was experimentally classified [71]. In a time-dependant field, the rotation of the magnetic nanoparticles can become important and give rise to flows inside the droplet [73], which is why even the shapes in the fast-rotating field are slowly rotating in the field rotation direction [68]. In this dissertation we explore the dynamics of droplets in the intermediate frequency range, where the simple averaging of the magnetic interaction over the rotation period is not valid.

In parallel to the experimental and theoretical description of droplets in external fields, the development of various numerical methods has advanced [74]. Such numerical tools are vital in the description of the droplets where the theoretical assumptions, such as the ellipsoidal shape of the droplet are no longer valid. The sharp tips of the droplets in a constant field have been successfully reproduced by axi-symmetric simulations [57, 60, 75]. The dynamics of of droplets in a constant field have also been calculated [57]. In a

rotating field, the problem ceases to be axi-symmetric, which complicates its numerical calculation. Two dimensional fluid models were used to calculate the equilibrium shapes and dynamics of magnetic droplets in rotating fields [76]. More recently, the equilibrium shapes in infinitely fast-rotating magnetic field were calculated in three dimensions, where the algorithm was significantly simplified by the assumption of equal viscosities of the magnetic droplet and the surrounding fluid [62]. The time dependant dynamics of a magnetic droplet in time-varying magnetic field has so far not been explored numerically in three dimensions, which is something that is tackled in this dissertation. A promising approach for the numerical scheme are the boundary element methods (BEM) [77, 78], which have been used to calculate the dynamics of highly-deformed viscous non-magnetic droplets in an external flow [79, 80, 81]. BEM have already been shown to be able to calculate the electrorotation and small deformation of a droplet in an electric field [51].

An interesting phenomenon that has gained significant attention recently is the active or driven (i.e. systems out of the thermodynamic equilibrium) self-assembly of colloidal particles [82]. A common driving mechanism is an external time-varying magnetic field that pumps energy into solid magnetic particles [83, 84, 85, 86, 87]. In addition to being fascinating in themselves, the magnetically driven colloids can serve as model systems for the more complicated and intricate situation of biological out-of-equilibrium self assembly [88, 89]. It has been reported that dynamic self-assembly can be done with ferrofluid droplets atop a non-wetting surface in an oscillating magnetic field [90]. Magnetic droplets on a liquid-air interface can be assembled in a precessing field, where depending on the field angle, the attraction and thus spacing between the droplets can be modified [91]. In a rotating field, due to a large surface tension several ferrofluid droplets can come close together and not coalesce, but instead orbit each other in a non-steady manner [92]. This non-steady orbiting has been replicated for a pair of droplets in two-dimensional simulations [93]. By coincidence in this work we observed, how in a rotating field phase separated microscopic magnetic droplets form two-dimensional nearly rigid ensembles that rotate in the direction of the magnetic field.

2.3 Objective and structure of the work

In summary the motion of magnetic droplets in a static homogeneous field is quite thoroughly researched experimentally, theoretically and with simulations. However, the theoretical or numerical description of magnetic droplet dynamics in a rotating field is

lacking, despite the experimental observation of a range of intricate non-stationary droplet behavior depending on the field strength and frequency [71]. This motivates the objective of this work: **Investigate the time-dependent dynamics of magnetic droplets in a rotating magnetic field.** The objective is achieved by doing the following tasks:

1. Using magnetic fluid model, develop an analytic description of individual droplet dynamics in simple cases, such as weak fields and small deformations, taking into account different viscosities inside and outside the droplet.

2. Using magnetic fluid model, develop simulation software to calculate the dynamics of droplets in situations where the analytic descriptions no longer work.

3. Using the simulation software, characterize the motion of magnetic droplets in rotating fields.

4. Perform experimental measurements on microscopic magnetic droplets obtained by phase separation and evaluate how well the magnetic fluid model describes their dynamics.

5. Experimentally observe the collective dynamics of ensembles of droplets.

6. Develop models that describe the collective dynamics of ensembles of droplets.

This dissertation is split into several sections. Section 3 states the magnetic fluid model that is used in the theoretical description of the droplet. Section 4 describes the experimental setup and the characteristics of the sample. Section 5 shows the analytic solution of the model in the limit of small deformations and weak field. It also shows a comparison with the experiment using the magnetic droplets obtained by phase separation. Section 6 describes the simulation based on boundary element methods, which was used to calculate the dynamics of magnetic droplets with substantial deformations. Section 7 deals with the experimental observation of droplet ensembles in a rotating field and their modeling using simple approximations. Finally, 8 is a concluding section that summarizes the main results of this work and ends with some general conclusions.

3 Mathematical formulation of the problem

3.1 Motivation

The phase separated magnetic droplets are a unique material, whose properties are not sufficiently understood. Inside the droplets, the concentration of magnetic nanoparticles is very large (their volume fraction is around $\phi_{drop} \approx 30\%$ [23]). It might mean that clusters of the nanoparticles could be forming inside the droplets, which could influence their magnetic and rheological properties. Furthermore, the droplets are in a thermodynamic equilibrium with regards to the magnetic nanoparticles leaving and entering the droplet's volume. This nanoparticle motion is happening through the surface area, which can change its size by a couple orders of magnitude in the experiments. The particular droplets used in this work are characterized more in section 4. In summary, the system is complicated, however, we seek to find a relatively simple model that captures the observed behavior of the droplets in a rotating field. We will examine the model of a simple magnetic fluid [15], which has worked in the past to calculate equilibrium shapes of the droplets in an infinitely fast-rotating magnetic field [62].

We consider a magnetic fluid droplet suspended in an infinite nonmagnetic carrier fluid (figure 3.1). The magnetic droplet (interior domain, whose properties will be denoted with the superscript (i)) has the magnetic permeability μ and viscosity $\eta^{(i)}$. The surrounding fluid (exterior domain, whose properties will be denoted with the superscript (e)) has the magnetic permeability equal to the vacuum magnetic permeability μ_0 and viscosity $\eta^{(e)}$. A surface tension characterized by the surface tension coefficient γ exists between the two domains.

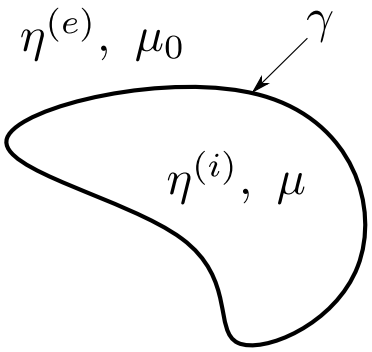

Figure 3.1: A sketch of the magnetic droplet with the viscosity $\eta^{(i)}$ and magnetic permeability μ suspended in an infinite fluid with viscosity $\eta^{(e)}$ and magnetic permeability μ_0. Surface tension acts on the droplet with the surface tension coefficient γ.

3.2 Formulation of the magnetostatic problem

An external magnetic field $\boldsymbol{H}_\infty$ is applied. Magnetic field produces a body force $f_i = \frac{\partial T_{ik}}{\partial x_k}$ in the fluid described by the Maxwell stress tensor [16]

$$\mathsf{T} = -\frac{1}{2}\mu_0 H^2 \mathsf{I} + \boldsymbol{H}\boldsymbol{B}, \tag{3.1}$$

where I is the identity tensor, $\boldsymbol{H}$ and $\boldsymbol{B} = \mu_0(\boldsymbol{H} + \boldsymbol{M})$ are magnetic field intensity and induction, respectively. $\boldsymbol{M}$ is the magnetization. It might be noted that other equivalent formulations of the Maxwell stress tensor exist [15]. In theoretical treatment of the problem, it will be assumed that the magnetization is linear

$$\boldsymbol{M} = \chi \boldsymbol{H}, \quad \boldsymbol{B} = \mu_0(1+\chi)\boldsymbol{H} = \mu \boldsymbol{H}, \tag{3.2}$$

where χ and μ are the magnetic susceptibility and permeability, respectively.

To calculate the magnetic stress, we first need to solve for the magnetic field inside and outside the droplet. To do this we use the equations of magnetostatics, [94]:

$$\boldsymbol{\nabla} \times \boldsymbol{H} = \boldsymbol{0}, \tag{3.3}$$

$$\boldsymbol{\nabla} \cdot \boldsymbol{B} = 0, \tag{3.4}$$

which are valid when $R_0/t_0 \ll c$ and Maxwell's equations for the electric and magnetic field decouple (see derivation in appendix A.1). R_0 and t_0 are characteristic length and time scales of the problem, respectively, and c is the speed of light. This is equivalent to the requirement that $R_0 \ll \lambda_{EM}$, where λ_{EM} is the wavelength of the electromagnetic radiation emitted due to the changing magnetic field.

Equation (3.3) is satisfied, if the magnetic field is a gradient of a potential

$$\boldsymbol{H} = \boldsymbol{\nabla}\psi. \tag{3.5}$$

Combined with (3.4), we see that the magnetic potential ψ is the solution to the Laplace equation both inside and outside the droplet

$$\Delta\psi = 0 \tag{3.6}$$

From the Maxwell's equations it is evident that on the boundary of different media the normal $\boldsymbol{B}$ field is continuous and the tangential $\boldsymbol{H}$ field is continuous [94]. This leads to the following boundary conditions on the droplet surface:

$$\mu_0 \boldsymbol{n} \cdot \boldsymbol{\nabla} \psi^{(e)} - \mu \boldsymbol{n} \cdot \boldsymbol{\nabla} \psi^{(i)} = 0 \tag{3.7}$$

$$\psi^{(e)} - \psi^{(i)} = 0, \tag{3.8}$$

where $\boldsymbol{n}$ is the outward normal on the droplet. Lastly, we require that ψ be bounded, and far away from the droplet the perturbation of the magnetic field by the droplet vanishes

$$\boldsymbol{\nabla} \psi|_{r \to \infty} = \boldsymbol{H}_\infty, \tag{3.9}$$

or equivalently

$$\psi|_{r \to \infty} = \psi_\infty = \boldsymbol{H}_\infty \cdot \boldsymbol{x}, \tag{3.10}$$

where $\boldsymbol{x}$ is the radius vector.

3.3 Formulation of the hydrodynamic problem

The motion of fluids inside and outside of the droplet is governed by the equations of incompressibility and conservation of momentum [95]:

$$\boldsymbol{\nabla} \cdot \boldsymbol{v} = 0, \tag{3.11}$$

$$\rho \frac{D\boldsymbol{v}}{Dt} = -\boldsymbol{\nabla} \tilde{p} + \eta \Delta \boldsymbol{v} + \boldsymbol{f}, \tag{3.12}$$

where $\boldsymbol{v}$ is the velocity, ρ is the density, $\tilde{p}$ is the pressure and η is the dynamic viscosity of the fluid. $\boldsymbol{f}$ is the force per unit volume acting on the bulk fluid. $\frac{D}{Dt} = \frac{\partial}{\partial t} + \boldsymbol{v} \cdot \boldsymbol{\nabla}$ is the material derivative. Another useful quantity is the hydrodynamic stress tensor

$$\tilde{\sigma}_{ij} = -\tilde{p} \delta_{ij} + \eta \left(\frac{\partial v_i}{\partial x_j} + \frac{\partial v_j}{\partial x_i} \right), \tag{3.13}$$

where δ_{ij} is the Kronecker delta and T denotes the transpose. The equations of motion with it are written as

$$\rho \frac{Dv_i}{Dt} = \frac{\partial \tilde{\sigma}_{ij}}{\partial x_j} + f_i. \tag{3.14}$$

When the fluid is magnetic, we can connect the force per unit volume with the Maxwell

stress tensor $f_i = \frac{\partial T_{ik}}{\partial x_k}$. We can simplify the force due to Maxwell stress tensor by writing it as a gradient of magnetic pressure (derivation is in appendix A.2)

$$\boldsymbol{f} = -\boldsymbol{\nabla} p_M, \tag{3.15}$$

$$p_M = -\frac{1}{2}\mu_0 \left(\frac{\mu}{\mu_0} - 1\right) H^2. \tag{3.16}$$

If the Reynolds number of the flow in and around the droplet is sufficiently small $Re \ll 1$, equation (3.12) can be linearized thus significantly simplifying the problem. Reynolds number is the dimensionless ratio between inertial over viscous forces. It can be expressed as [95]

$$Re = \frac{\rho u R_0}{\eta}, \tag{3.17}$$

where u and R_0 are a characteristic velocity scale and a characteristic length scale in the problem.

Experimentally we see that undeformed magnetic microdroplets are typically around $R_0 \approx 10\ \mu m$ in radius, which is the characteristic length scale. Their viscosity is around 100 times larger than their surrounding medium, which can be taken to be approximately the viscosity of water $\eta^{(i)}/100 \approx \eta^{(e)} \approx 1\ mPa{\cdot}s$ [68, 96]. But their density is only a couple of times larger than the density of the surrounding medium $\rho^{(i)}/2.5 \approx \rho^{(e)} \approx 1000\ kg/m^3$ [71]. From the ratio ρ/η, it is evident that the Reynolds number should be larger outside than inside the droplet. Therefore, let us look at the worst case - the flow outside the droplet. We can estimate the characteristic velocity scale as $u = R_0/\tau$, where τ is a characteristic time scale. The choice of τ is not immediately obvious, because the motion of the droplet can qualitatively vary depending on the applied magnetic field strength and rotation frequency. For the case where the dominant motion of the droplet is due to the surface deformation, a characteristic time scale of

$$\tau_{def} = \frac{R_0(16\eta^{(e)} + 19\eta^{(i)})(3\eta^{(e)} + 2\eta^{(i)})}{40\gamma(\eta^{(e)} + \eta^{(i)})} \tag{3.18}$$

should be used [64], where $\gamma \approx 10^{-6}\ N/m$ is the surface tension of the droplet [96]. Outside the droplet this leads to $Re = 10^{-4}$. On the other hand, for the case when the motion is dominated by the rotation of the droplet as a compass needle in a rotating

magnetic field, the characteristic time scale should be

$$\tau_{rot} = \frac{1}{2\pi f}, \tag{3.19}$$

where f is the rotation frequency of the magnetic field. With reasonable magnetic field strength for very large frequencies $f > 100\ Hz$, the droplets no longer rotate as compass needles but flatten out and their motion is dominated by surface deformations. Therefore, to estimate this time scale, we take $f = 50\ Hz$, which leads to $Re = 3 \cdot 10^{-2}$, still a small value.

Because of the small Reynolds number we can neglect the inertia of the fluids and equation (3.12) simplifies to the Stokes equation [95]

$$-\boldsymbol{\nabla}\tilde{p} + \eta\Delta\boldsymbol{v} - \boldsymbol{\nabla}p_M = \mathbf{0}. \tag{3.20}$$

Let us examine the boundary conditions for the problem. When the free surface between the two incompressible fluids deforms, it is because one fluid moves away and another takes its place. There can be no flow through the interface. Therefore, the normal velocity of one fluid at the interface is equal to the normal velocity of the other fluid, in other words - it is continuous:

$$\boldsymbol{v}^{(i)} \cdot \boldsymbol{n} - \boldsymbol{v}^{(e)} \cdot \boldsymbol{n} = 0. \tag{3.21}$$

Furthermore, slipping in the tangential direction is possible only if the viscosity of one of the fluids is zero (for example a bubble of air inside water). Otherwise, there would be a finite jump in $\boldsymbol{v}$ over an infinitely small distance resulting in infinitely large $\eta\Delta\boldsymbol{v}$ term in the equation (3.12). Therefore, we require that the tangential velocity on the two fluid interface is also continuous:

$$\mathbf{P}_{||} \cdot \boldsymbol{v}^{(i)} - \mathbf{P}_{||} \cdot \boldsymbol{v}^{(e)} = \mathbf{0}, \tag{3.22}$$

where $\mathbf{P}_{||} = \mathbf{I} - \boldsymbol{nn}$ is the operator for projecting a vector on the droplet surface. Combining the equations (3.21) and (3.22), we get that the velocity on the droplet interface is continuous

$$\boldsymbol{v}^{(i)} - \boldsymbol{v}^{(e)} = \mathbf{0}. \tag{3.23}$$

Lastly, the sum total of all the forces acting on the boundary should be zero:

$$\boldsymbol{n} \cdot (\tilde{\boldsymbol{\sigma}}^{(e)} - \tilde{\boldsymbol{\sigma}}^{(i)}) \cdot \boldsymbol{n} + \boldsymbol{n} \cdot (\mathbf{T}^{(e)} - \mathbf{T}^{(i)}) \cdot \boldsymbol{n} - \gamma(k_1 + k_2) = 0; \tag{3.24}$$

$$\mathbf{P}_{||} \cdot (\tilde{\boldsymbol{\sigma}}^{(e)} - \tilde{\boldsymbol{\sigma}}^{(i)}) \cdot \boldsymbol{n} + \mathbf{P}_{||} \cdot (\mathbf{T}^{(e)} - \mathbf{T}^{(i)}) \cdot \boldsymbol{n} = \mathbf{0}, \tag{3.25}$$

where $\mathbf{T}$ is the Maxwell stress tensor, γ is the surface tension coefficient and k_1, k_2 are the principal curvatures of the droplet's surface. The force difference on the boundary due to the Maxwell stress tensor is $\mathbf{P}_{||} \cdot (\mathbf{T}^{(e)} - \mathbf{T}^{(i)}) \cdot \boldsymbol{n} = \mathbf{0}$ in the tangential direction, and $\boldsymbol{n} \cdot (\mathbf{T}^{(e)} - \mathbf{T}^{(i)}) \cdot \boldsymbol{n} = \frac{\mu_0}{2} {M_n^{(i)}}^2$ in the normal direction, where M_n is the magnetization in the normal direction (derivation is in appendix A.3).

Far away from the droplet we may impose a background flow with velocity $\boldsymbol{v_\infty}$, pressure p_∞ and therefore a hydrodynamic stress $\boldsymbol{\sigma_\infty}$. Far away the perturbations arising from the droplet vanish and we have

$$\boldsymbol{v}|_{r\to\infty} = \boldsymbol{v_\infty}, \quad \tilde{p}|_{r\to\infty} = p_\infty, \quad \tilde{\boldsymbol{\sigma}}|_{r\to\infty} = \boldsymbol{\sigma_\infty}. \tag{3.26}$$

3.3.1 Formulation of the problem for the effective pressure

It is possible to combine the hydrodynamic pressure with the magnetic pressure (written in eq. (3.16)) into an effective pressure

$$p = \tilde{p} + p_M, \tag{3.27}$$

which allows us to write

$$-\boldsymbol{\nabla} p + \eta \Delta \boldsymbol{v} = \mathbf{0}. \tag{3.28}$$

The boundary conditions on the droplet's surface need to be modified to take into account the effective pressure and the effective hydrodynamic stress tensor $\sigma_{ij} = -p\delta_{ij} + \eta\left(\frac{\partial v_i}{\partial x_j} + \frac{\partial v_j}{\partial x_i}\right)$. The boundary condition for velocity continuity remains unchanged:

$$\boldsymbol{v}^{(e)} - \boldsymbol{v}^{(i)} = \mathbf{0}. \tag{3.29}$$

The expression for the forces on the surface in the normal direction is changed to

$$\boldsymbol{n} \cdot (\boldsymbol{\sigma}^{(e)} - \boldsymbol{\sigma}^{(i)}) \cdot \boldsymbol{n} + f_M - \gamma(k_1 + k_2) = 0, \tag{3.30}$$

where

$$f_M = \frac{1}{2}\mu_0 \left(\frac{\mu}{\mu_0} - 1\right) \left(\frac{\mu}{\mu_0} {H_n^{(i)}}^2 + {H_t^{(i)}}^2\right) \tag{3.31}$$

is the effective magnetic surface force, H_n and H_t are the normal and tangential magnetic field intensity values (derivation is in appendix A.4). The boundary condition for tangential forces is unchanged

$$\mathbf{P}_{||} \cdot (\boldsymbol{\sigma}^{(e)} - \boldsymbol{\sigma}^{(i)}) \cdot \boldsymbol{n} = \mathbf{0}. \tag{3.32}$$

The conditions far away from the droplet also remain unchanged

$$\boldsymbol{v}|_{r\to\infty} = \boldsymbol{v_\infty}, \quad p|_{r\to\infty} = p_\infty, \quad \boldsymbol{\sigma}|_{r\to\infty} = \boldsymbol{\sigma_\infty}. \tag{3.33}$$

3.4 Dimensionless variables

Three dimensionless parameters arise naturally in the problem

- $\lambda = \frac{\eta^{(i)}}{\eta^{(e)}}$, the viscosity ratio,
- $\mu_r = \frac{\mu}{\mu_0}$, the relative magnetic permeability,
- $Bm = 4\pi\mu_0 \frac{R_0 H_\infty^2}{\gamma}$, the magnetic Bond number. It is proportional to a characteristic magnetic force over a characteristic force due to surface tension.

Note that different authors have used different expressions for the magnetic Bond number. And care should be taken when comparing their different results. For example, the constant multiple is different such as $Bm = \mu_0 \frac{R_0 H_\infty^2}{\gamma}$ in [67] and $Bm = \mu_0 \frac{R_0 H_\infty^2}{2\gamma}$ in [60]. Few authors call this dimensionless ratio the magnetic capillary number Ca_m [97]. Sometimes the quantity that is called the magnetic Bond number includes magnetization instead of magnetic field intensity $Bm = \frac{\mu_0}{4\pi} \frac{R_\infty M^2}{\gamma}$ [16]. The choice of the magnetic Bond number in this work corresponds to [62].

4 Experimental setup

4.1 Sample

In this work we used a water based ferrofluid containing maghemite (γ-Fe_2O_3) nanoparticles coated with a citrate layer. The citrate ions on the surface of the nanoparticles are negatively charged and thus prevent their agglomeration. The concentration of free citrate in the carrier fluid is $[\text{cit}]_{\text{free}} = 0.06 mol/L$. The nanoparticle size is log-normally distributed

$$p(d) = \frac{1}{\sigma d\sqrt{2\pi}} e^{-\frac{(\ln \frac{d}{d_0})^2}{2\sigma^2}}, \tag{4.1}$$

where the median diameter of the nanoparticles is $d_0 \approx 7nm$ and their polydispersity is $\sigma \approx 0.3$. The nanoparticles are small enough to contain only a single magnetic domain [17]. Their magnetic moment is

$$m_{NP} = M_{NP}\frac{\pi d^3}{6}, \tag{4.2}$$

where $M_{NP} \approx 3 \cdot 10^5 A/m$ is the saturation magnetization of the nanoparticles [17]. The volume fraction of the nanoparticles in the ferrofluid is $\phi_{FF} \approx 4.6\%$. Therefore we can calculate its saturation magnetization (when all the magnetic nanoparticles are aligned) as

$$M_{FF} = \phi_{FF} M_{NP} \approx 1.4 \cdot 10^4 A/m \tag{4.3}$$

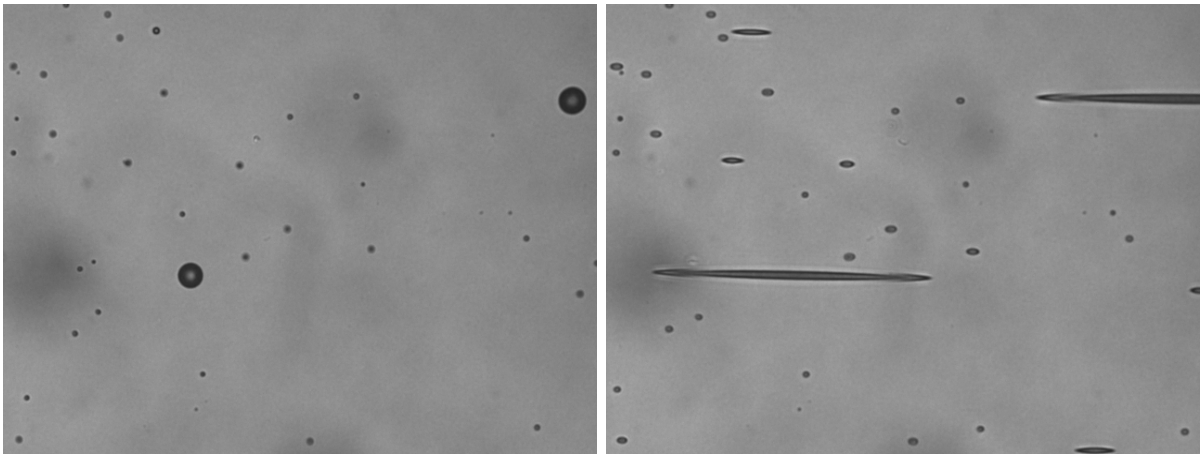

Figure 4.1: Destabilized ferrofluid. The concentrated phase forms magnetic droplets seen as darker disks of various diameters surrounded by a dilute phase (left). The droplets elongate in the direction of the applied field (right). The field of view is $132\mu m \times 100\mu m$.

When the ferrofluid is stable, it can be described as a gas of magnetic nanoparticles [16]. The ferrofluid can be destabilized creating a gas-liquid type phase transition. In this

phase transition, the ferrofluid separates into two phases with different concentrations of magnetic nanoparticles (figure 4.1). The destabilizing can be achieved by increasing the magnetic field, decreasing the temperature or increasing the ionic strength of the ferrofluid (by dissolving salt, for example) [20, 21, 22, 23, 98].

The concentrated phase forms droplets with a typical diameter of several micrometers, which is akin to the condensation of vapor. The magnetic nanoparticle volume fraction in it is hard to measure directly, but it is around $\phi_{drop} \approx 30\%$, and it is relatively weakly affected by the amount of added salt [23]. This leads to the approximate saturation magnetization for the fluid in the droplets

$$M_{drop} = \phi_{drop} M_{NP} \approx 9 \cdot 10^4 A/m. \tag{4.4}$$

The dilute phase typically contains a much lower volume fraction of magnetic nanoparticles $\phi_{dilute} \approx 0 \ldots 4\%$, which is relatively strongly affected by the amount of added salt [23].

4.2 Experimental device

The experiments were done using an optical bright-field microscope that is augmented by a custom-build coil setup for generating magnetic fields (figure 4.2). We apply a $\pi/2$ phase shifted sinusoidal signals on the coils and thus generate a homogeneous rotating magnetic field. It is possible to create also a vertical magnetic field component, however it was not used in this work. We placed the phase-separated ferrofluid sample in a thin glass cell (height $h_{cell} \approx 100 \ldots 200 \mu m$), and placed the cell in the sample holder. We recorded the droplets using a camera attached to the microscope and saved the images in an 8-bit gray-scale format. Two similar experimental devices were used - one in Paris and one in Riga.

The coil system in Paris is water cooled, which permits the maximum current in the coils of $I_{max} = 3.5A$, which corresponds to $H_\infty = 4.7 \cdot 10^3 A/m$. In Paris the glass cells were produced by Hellma Analytics and were $h_{cell} = 100 \mu m$ in thickness. The camera used in Paris is AVT Guppy F-046B, which produces a gray-scale $640px \times 480px$ image.

The coils in Riga are cooled with Huber Ministat 230 device, where water + glycol mixture is used as a coolant. We managed to easily reach currents of $I = 5A$ ($H_\infty = 7.0 \cdot 10^3 A/m$) without overheating the coils. The glass cells were made using two glass slides, which were separated by a double-sided adhesive tape. The separation between

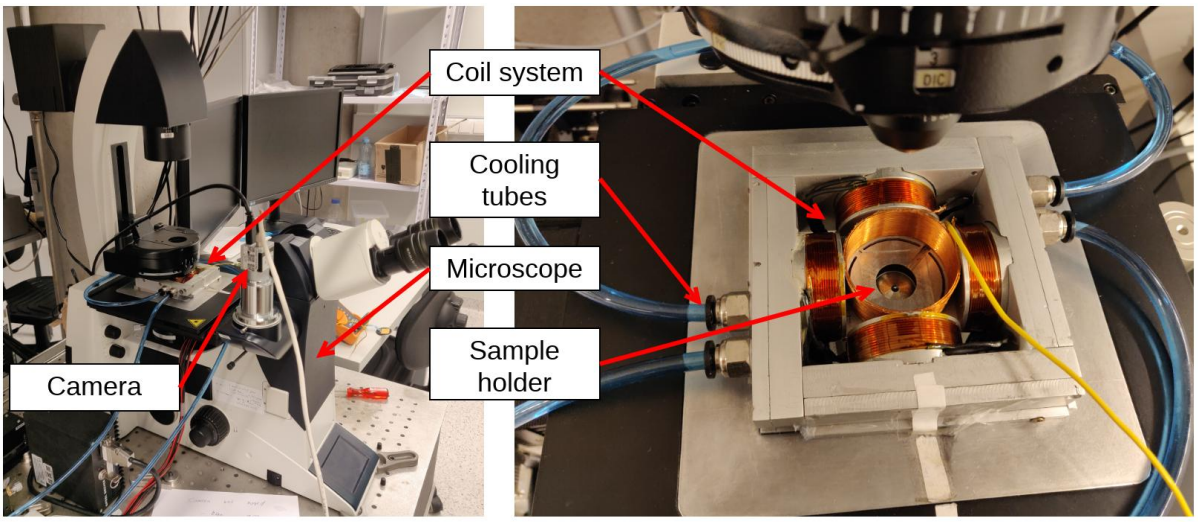

Figure 4.2: Microscope setup in Riga for observing magnetic droplets under the action of magnetic fields. The setup in Paris is similar and is described in the thesis of G. Kitenbergs [69].

them was measured to be $h_{cell} \approx 200\mu m$. The camera used in Riga is Basler acA1920-155um, which produces a gray-scale $1920px \times 1200px$ image.

4.3 Image processing

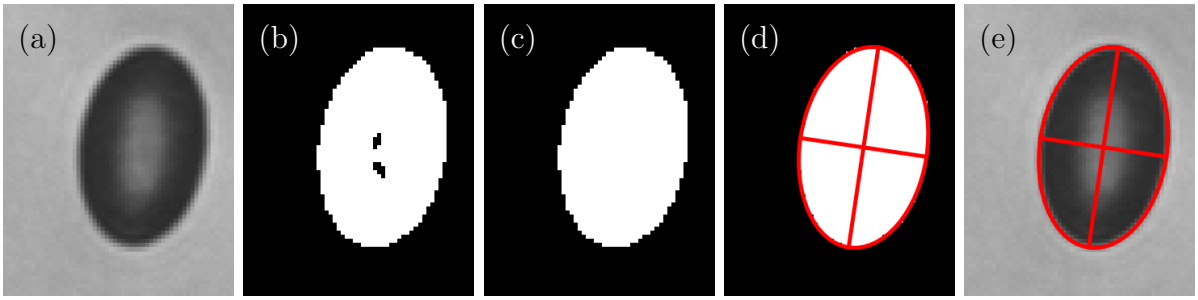

Figure 4.3: Procedure for determining the droplet's shape. (a) shows the original image, (b) shows image thresholded by Otsu's method, (c) shows the hole filling, (d) shows the ellipse fit, (e) shows the fitted ellipse atop the original image.

To describe the droplet with an ellipse the following procedure is used (figure 4.3):

1. The image of the droplet is segmented into dark and light regions using Otsu's method for thresholding as implemented in the Python library Scikit-Image.

2. The holes within the droplet are filled.

3. The ellipse that best describes the droplet is found using the method of image moments as implemented in the Python library's Scikit-Image function `measure regionprops`. In particular, the ellipse is such that its second central moments

M_{02}, M_{11}, M_{20} defined by

$$M_{ij} = \sum_x \sum_y (x - \bar{x})^i (y - \bar{y})^j I(x, y) \tag{4.5}$$

are the same as the that of the image segment. x, y are the coordinates of pixels and $I(x, y)$ is 1 if the pixel x, y is part of the segment, and 0 otherwise. $\bar{x}$ and $\bar{y}$ are the centroid coordinates of the segment.

4.4 Determination of droplet parameters

The magnetic droplets obtained by phase separation are microscopic in size and direct measurements to obtain their physical properties such as magnetic permeability, surface tension and viscosity are hard to do. Luckily there are indirect methods based on the measurement of the droplet's elongation in an external field and relaxation to a sphere after the field is turned off - something that can be easily done with the previously mentioned experimental setup.

4.4.1 Equilibrium elongation: energy minimization

One approach to determine the equilibrium elongation of the droplet is the minimization of its magnetic and surface tension energy [24]. The energy of a paramagnetic body placed in an external magnetic field $\boldsymbol{H}_\infty$ is [94]

$$E_m = -\frac{\mu_0}{2} \int_V \boldsymbol{M}^{(i)} \cdot \boldsymbol{H}_\infty dV, \tag{4.6}$$

where linear magnetization is assumed, the medium surrounding the body has $\mu = \mu_0$, and the integral is taken over the volume of the paramagnetic body. Then the total energy functional that is minimal for the equilibrium shape of the droplet is [24, 62]

$$E_{tot} = -\frac{\mu_0}{2} \int_V \boldsymbol{M}^{(i)} \cdot \boldsymbol{H}_\infty dV + \gamma S, \tag{4.7}$$

where γ is the surface tension coefficient and S is the droplet's surface area.

Assuming a prolate spheroidal shape (with semi-axes $a \geq b = c$), we can analytically minimize E_{tot} with respect to the aspect ratio a/b. The magnetic field inside a spheroidal

droplet elongated in the direction of the homogeneous $\boldsymbol{H}_\infty$ is given by [94]

$$\boldsymbol{H}^{(i)} = \boldsymbol{H}_{\boldsymbol{\infty}} - N_d \boldsymbol{M}^{(i)} = \frac{\boldsymbol{H}_\infty}{1 + \chi N}, \tag{4.8}$$

where $\chi = \mu/\mu_0 - 1$ is the droplet's susceptibility. N_d is the shape dependent demagnetization factor [99]

$$N_d = \frac{1 - e^2}{2e^3} \left(-2e + \ln \frac{1+e}{1-e} \right), \tag{4.9}$$

where $e = \sqrt{1 - b^2/a^2}$ is the eccentricity of the droplet. The volume and area of a prolate spheroid are [100]

$$V = \frac{4\pi}{3} a b^2, \quad S = 2\pi b^2 (1 + \frac{a}{be} \arcsin e). \tag{4.10}$$

Minimizing (4.7) with respect to the aspect ratio a/b yields the equilibrium aspect ratio for a given magnetic field intensity [24]

$$\frac{Bm}{8\pi} = \frac{\mu_0 H_\infty^2 R_0}{2\gamma} = \left(\frac{1}{\frac{\mu}{\mu_0} - 1} + N_d \right)^2 \frac{\left(3 - 2e^2 - \frac{(3-4e^2)\arcsin e}{e(1-e^2)^{1/2}} \right)}{(1-e^2)^{2/3} \left(-\frac{6}{e^2} + \frac{3-e^2}{e^3} \ln \frac{1+e}{1-e} \right)}. \tag{4.11}$$

It might be noted that the same theoretical curve is achieved by the virial method [58].

4.4.2 Equilibrium elongation: selective enforcement of force balance

Another way to calculate the equilibrium elongation of a droplet was shown by Afkhami et al. [60], who used a method previously used by G. I. Taylor do describe the deformation of a water droplet in an electric field [48]. In equilibrium the effective normal force boundary condition (3.30) on the droplet's surface reads

$$p^{(i)} + \frac{1}{2}\mu_0 \left(\frac{\mu}{\mu_0} - 1 \right) \left(\frac{\mu}{\mu_0} {H_n^{(i)}}^2 + {H_t^{(i)}}^2 \right) - \gamma(k_1 + k_2) = 0, \tag{4.12}$$

where $p^{(i)} = const$ since in equilibrium $\boldsymbol{\nabla} p^{(i)} = \boldsymbol{0}$. Similarly $p^{(e)}$ was set to 0 and does not appear in the formula.

Assuming a prolate spheroidal droplet, the equation (4.12) cannot be satisfied everywhere on the surface since there are only two free parameters $p^{(i)}$ and the aspect ratio a/b. The mean curvatures $k_1 + k_2$ are set by the ellipsoid and so is the magnetic field $\boldsymbol{H}^{(i)}$ according to (4.8). We can however approximately satisfy the equation by enforcing the force balance on the equator and on the poles of the droplet. This leads to the equilibrium

aspect ratio for a given magnetic field intensity [60]

$$\frac{Bm}{8\pi} = \frac{\mu_0 H_\infty^2 R_0}{2\gamma} = \left(\frac{1}{\frac{\mu}{\mu_0} - 1} + N_d\right)^2 \left(\frac{a}{b}\right)^{\frac{1}{3}} \left(2\frac{a}{b} - \left(\frac{a}{b}\right)^{-2} - 1\right). \tag{4.13}$$

Recently a numerical study was done, where the author tried to improve upon the equation (4.13) to take into account that the droplet shape deviates from an ellipsoid [61]. The semi-analytic equation for the equilibrium aspect ratio for a given magnetic field intensity was determined to be (b/a instead of a/b in the formula is not a typo)

$$\frac{Bm}{8\pi} = \frac{\mu_0 H_\infty^2 R_0}{2\gamma} = \left(\frac{1}{\frac{\mu}{\mu_0} - 1} + N_d + 0.0043\right)^2 \left(\frac{b}{a}\right)^{0.3} \left(1 + \left(\frac{b}{a}\right)^{-2} - 2\frac{b}{a}\right). \tag{4.14}$$

It might be noted, that the equation (4.14) was tested for deformations $a/b \leq 12$, and values of magnetic permeability $\mu/\mu_0 \leq 11$. However, simulations showed that the unmodified equation (4.13) is accurate only for $a/b \leq 4$ [61].

4.4.3 Equilibrium elongation: comparison of theoretical equations

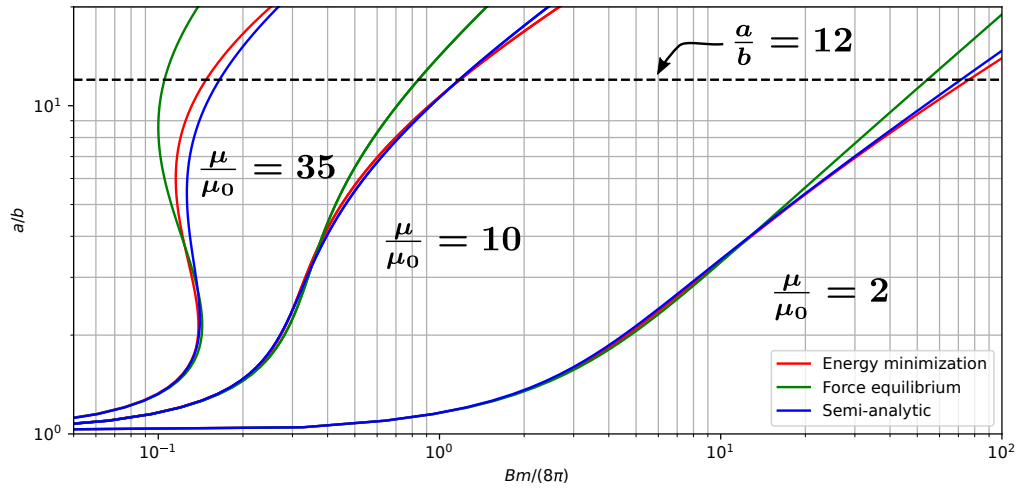

Figure 4.4: The equilibrium droplet aspect ratio depending on the external magnetic field as described with $Bm/(8\pi)$. The graph shows the comparison between the equation (4.11) in red, (4.13) in green, and (4.14) blue. The μ values used in the equations are depicted next to the curves. The dashed line is $a/b = 12$.

Plotting the three theoretical curves for the equilibrium aspect ratio of the droplet (figure 4.4), we can compare the quality of these models. A benchmark for the quality is the semi-analytic curve (4.14), which was tested against simulations for $a/b \leq 12$ and $\mu/\mu_0 \leq 11$.

For small deformations all three curves coincide. We see that the curve attained by the selective force balance (4.13) deviates from the semi-analytic curve already at $a/b \approx 4$. However the energy minimization curve (4.11) well describes the aspect ratio in the whole region where the semi-analytic curve was tested [61]. It is surprising since the droplet ceases to be ellipsoidal, and the magnetization inside the droplet becomes nonuniform for larger deformations. For example, for $\mu/\mu_0 = 3$ and $a/b = 9.97$ the magnetization at the droplet's tips is $6\% \dots 7\%$ larger than the magnetization on the equator [61].

In our case it turns out, that the droplet's magnetic permeability is around $\mu/\mu_0 \gtrsim 30$, which is outside the applicability range of the semi-analytic curve. Since the energy minimization curve (4.11) worked well where the semi-analytic curve was tested, and it does not have the ad-hoc constants present in the semi-analytic curve (4.14), we chose to employ it to fit the experimental data.

It might be noted that above a critical magnetic permeability of the droplet ($\mu/\mu_0 \approx 21$ for the energy minimization curve (4.11)), the equilibrium aspect ratio depending on Bm becomes multi-valued. This results in a hysteresis in the droplet aspect ratio as the magnetic field changes. Increasing the field above a critical value of Bm the droplet strongly elongates. Afterwards the droplet does not return to its previous shape when the field is decreased back, but rather it follows the "upper branch" of the curve. Then after decreasing the field another critical value of Bm is reached and the droplet strongly contracts.

4.4.4 Equilibrium elongation: comparison with experiment

We chose a magnetic droplet and incrementally elongated it in external field. We recorded images of the droplet and the current in the coils from which we calculated the magnetic field. From the images we also determined the spherical droplet's radius.

During the experiment, which lasted nearly 17 minutes, the droplet was changing its volume. Possibly this was because the microscope lamp was heating the sample. It is known that decreasing the temperature facilitates the appearance of the concentrated phase (magnetic droplets) in the ferrofluid [20, 21]. At the start the droplet's radius was $R_0^{start} = 4.0\ \mu m$ and at the end it had decreased to $R_0^{end} = 3.4 \mu m$. We therefore used an average value $R_0 = (3.7 \pm 0.3)\ \mu m$ when comparing the experiment to theory.

The equilibrium aspect ratio a/b of the droplet depending on the magnetic field is shown in figure 4.5. The error bars are mostly due to the changing R_0. We fit the

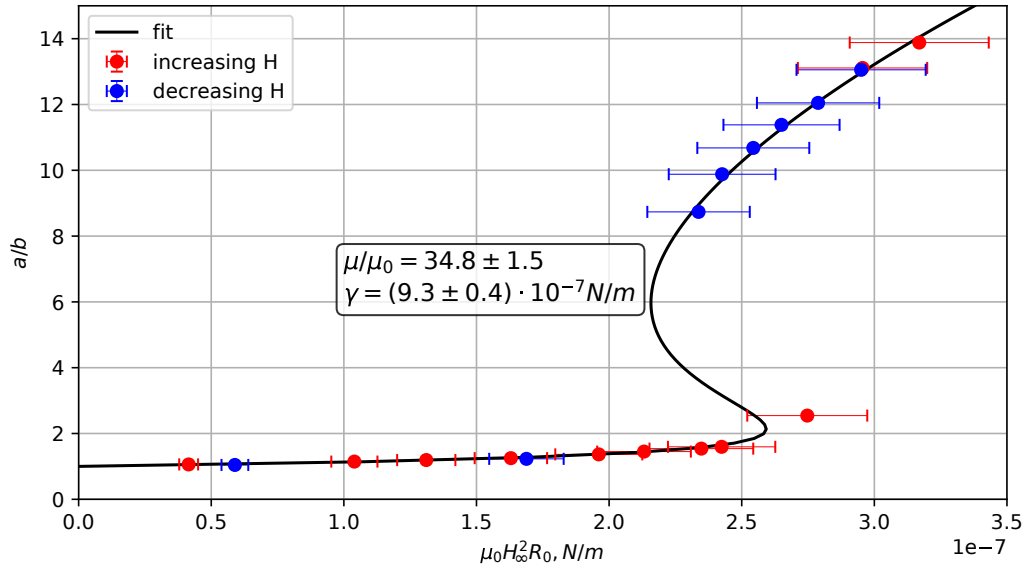

Figure 4.5: The equilibrium droplet aspect ratio depending on the external magnetic field. The points indicate experimental measurements and the black line is the fitted theoretical curve (4.11). The fit parameters are indicated in the text box on top of the graph.

theoretical curve attained by energy minimization (4.11) using non-linear least squares as implemented in SciPy `curve_fit`. We get that the droplet permeability is $\mu/\mu_0 = 34.8 \pm 1.5$ and its surface tension is $\gamma = (9.4 \pm 0.4) \cdot 10^{-7}\ N/m$. The errors are determined as the square roots of the diagonal elements in the covariance matrix returned by `curve_fit` function.

4.4.5 Relaxation to a sphere: comparison with experiment

Once we know the droplet's surface tension, we can assess its viscosity by performing a relaxation experiment. The same droplet was elongated and then let to relax to a sphere after turning off the magnetic field. According to the small deformation theory (discussed in section 5), the droplet's elongation $\epsilon_1 = (a - b)/b$ should exponentially decay to zero with the characteristic time τ, which is expressed in equation (5.71).

The measured decay of ϵ_1 is plotted in figure 4.6. Interestingly, ϵ_1 follows an exponential decay law beyond the applicability limits of the small deformation theory. Fitting a decaying exponent gives the characteristic time of $\tau = (6.03 \pm 0.06)\ s$. To determine the droplet's viscosity $\eta^{(i)}$, we use the previously determined surface tension coefficient $\gamma = (9.4 \pm 0.4) \cdot 10^{-7}\ N/m$. The experiment was done before the incremental elongation of the droplet in the external field, and during the relaxation the radius of the droplet was relatively unchanging $R_0 = (4.08 \pm 0.02)\ \mu m$. Finally assuming that the surrounding

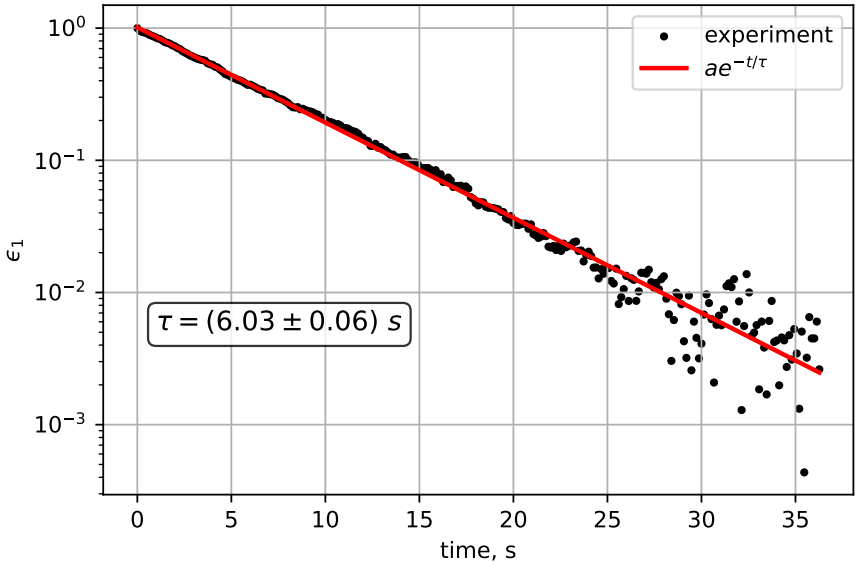

Figure 4.6: Experimental relaxation to a sphere of an initially elongated droplet. The red line is the best fit exponential decay. The fitted τ is shown in the text box.

fluid has the viscosity of water $\eta^{(e)} = 10^{-3}\ Pa \cdot s$, we can calculate the viscosity of the magnetic droplet from (5.71). It is $\eta^{(i)} = (1.46 \pm 0.05)\ Pa \cdot s$. This means that for our experimental system the viscosity ratio is $\lambda = \eta^{(i)}/\eta^{(e)} \approx 1460$.

5 Small deformation dynamics

5.1 Introduction

Analytic solutions for magnetic droplet dynamics are feasible only in the simplest cases. One such case is the limit where the droplet is close to spherical. The small deformation dynamics of droplets in a homogeneous stationary field (electric or magnetic) have been studied analytically, where it was shown that a droplet exponentially approaches an ellipsoidal equilibrium shape [65]. The dynamics of nonmagnetic viscous drops in external flows has also been extensively theoretically explored in the limit of small deformations [101]. A common approach to calculate the motion of ellipsoidal droplets in external flows are phenomenological models for the time evolution of a tensor that describes the shape of the droplet [102].

In this section we will extend the current results by deriving the dynamics of weakly deformed drop in a rotating field. First, we use a phenomenological equation that describes the evolution of the anisotropy tensor of an ellipsoidal droplet. Second, we asymptotically solve the hydrodynamic problem using perturbation theory to validate the phenomenological approach and to determine the constants in the phenomenological model. Third, we use the boundary element method to numerically validate the small deformation solution and find the limits where it is valid. Finally, we compare the results with experimental observation.

5.2 Description of a slightly deformed droplet

In the limit where the magnetic forces are much weaker than the capillary forces ($Bm \ll 1$) the droplet can be described as an ellipsoid with the semiaxes a, b, c and with the unit vectors $\boldsymbol{n}^1, \boldsymbol{n}^2, \boldsymbol{n}^3$ pointing in the direction of each semiaxis.

Alternatively when $a \geq b \geq c$ two non-negative deformation parameters can be used to describe the droplet's shape, the elongation

$$\epsilon_1 = \frac{a-b}{b} \tag{5.1}$$

and the flatness

$$\epsilon_2 = \frac{b-c}{b}, \tag{5.2}$$

which together with the incompressibility condition $abc = R_0^3$ can be used to retrieve the

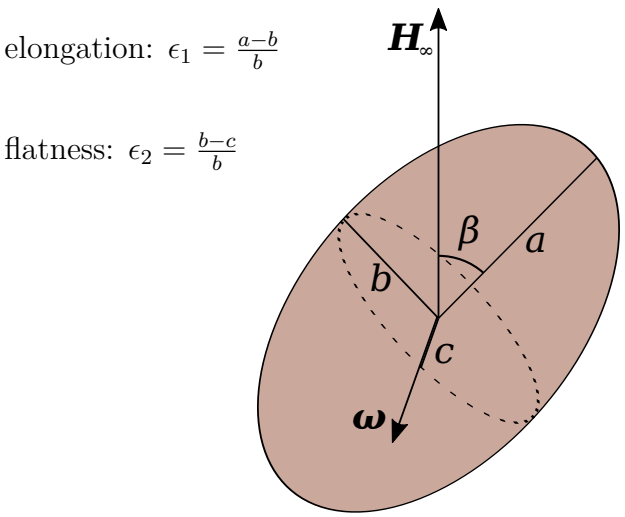

Figure 5.1: The parameters describing the droplet's shape in a rotating magnetic field. β is negative when the droplet's largest axis is trailing the rotating magnetic field $\boldsymbol{H}_\infty$. The field rotates in the $\boldsymbol{\omega}$ direction.

semiaxes. In the case when the droplet is a spheroid, the so called Taylor deformation parameter is commonly used [101, 103, 104], which can be defined as $D = (a_\parallel - a_\perp)/(a_\parallel + a_\perp)$, where $a_\parallel$ is the droplet's length along its symmetry axis and $a_\perp$ is its length perpendicular to the symmetry axis. When the droplet is a prolate spheroid, the Taylor deformation parameter is related to the deformation parameters used in this work by

$$D = \frac{\epsilon_1}{\epsilon_1 + 2} = \frac{\epsilon_1}{2} + O(\epsilon_1^2), \tag{5.3}$$

and when the droplet is an oblate spheroid by

$$D = \frac{\epsilon_2}{\epsilon_2 - 2} = -\frac{\epsilon_2}{2} + O(\epsilon_2^2). \tag{5.4}$$

When the motion is in the plane of the rotating magnetic field, the shortest axis c aligns with the magnetic field rotation direction and the droplet's orientation is determined by a single angle β that its longest axis makes with the magnetic field (Figure 5.1). β is chosen to be positive when the droplet's largest axis is leading the field and negative when it is trailing the field. In general we would need two more angles to describe the out-of-plane motion.

5.3 Anisotropy tensor approach

A common approach to calculate droplet dynamics in imposed flows are phenomenological models describing the time evolution of the anisotropy tensor, that characterizes

the ellipsoidal droplet's shape. There are a few ways in which the tensor quantity is defined. For example, the tensor is defined (up to a factor and summand) as $\mathbf{q} = \int_S \boldsymbol{n}\boldsymbol{n} dS$ in models, which are built on Doi-Ohta theory [105, 106]. $\boldsymbol{n}$ is the normal vector and the integral is over the droplet's surface. Another definition of the tensor is used in the Maffetone-Minale model (and others based on it) [107] - they use a tensor $\mathbf{S}$ that has eigenvalues equal to a^2, b^2, c^2. Different models used to describe the evolution of the droplet's shape are shown in a review article [102]. The anisotropy tensor approach has proved itself to be useful in describing the experiments of droplet dynamics in external flows [108]. Since the models for the time evolution of the anisotropy tensor are phenomenological, they can be extended to describe more complicated cases, such as interaction with walls, non-Newtonian fluids, and as we will show - the influence of the magnetic field. However, the phenomenological models need to be verified by an experiment, simulation or *ab-initio* models.

The ellipsoidal droplet shape is expressed by a quadratic form

$$\boldsymbol{x} \cdot \mathbf{A} \cdot \boldsymbol{x} = 1, \tag{5.5}$$

where $\boldsymbol{x}$ is the radius vector, $\mathbf{A}$ is a real symmetric tensor with eigenvalues $1/c^2$, $1/b^2$, $1/a^2$ and eigenvectors aligned with the ellipsoid's semiaxes. Here we define the anisotropy tensor to be

$$\boldsymbol{\zeta} = R_0^2 \mathbf{A} - \mathbf{I}, \tag{5.6}$$

where $\mathbf{I}$ is the identity tensor. Note that $\mathbf{A}$ was scaled with the undeformed droplet's radius and $\boldsymbol{\zeta}$ is dimensionless. The eigenvalues of $\boldsymbol{\zeta}$ are $\lambda_1 = R_0^2/c^2 - 1$, $\lambda_2 = R_0^2/b^2 - 1$, $\lambda_3 = R_0^2/a^2 - 1$ and unit eigenvectors $\boldsymbol{n}^1, \boldsymbol{n}^2, \boldsymbol{n}^3$ are aligned with the ellipsoid axes. We may write the anisotropy tensor using them

$$\zeta_{ij} = \sum_{k=1}^{3} \lambda_k n_i^k n_j^k. \tag{5.7}$$

5.3.1 General dynamics

A phenomenological equation for the anisotropy tensor of a magnetic droplet in a homogeneous stationary magnetic field (analogous to the equation (2.4)) reads [64]

$$\frac{d\zeta_{ij}}{dt} - e_{ipr}\Omega_p \zeta_{rj} - e_{jpr}\Omega_p \zeta_{ir} = -\frac{1}{\tau}(\zeta_{ij} - \zeta_{ij}^0), \tag{5.8}$$

where e_{ipr} is the Levi-Civita symbol, $\boldsymbol{\Omega}$ is the angular velocity of the surrounding fluid and $\boldsymbol{\zeta}^0$, τ are phenomenological constants - the equilibrium anisotropy tensor and the characteristic relaxation time to this equilibrium, respectively. A brief explanation of (5.8) is as follows [109]. The left-hand side is the Jaumann derivative, which describes how the components of the tensor evolve due to the rotation. The right-hand side shows that the droplet exponentially takes up the equilibrium shape characterized by the tensor $\boldsymbol{\zeta}^0$. The model could be improved to include the effects of shear flow, and therefore describe the rheology of dilute suspension of magnetic droplets (see the Maffettone-Minale model, that uses a tensor $\mathbf{S}$ similar to the inverse of the one used in this work $\mathbf{S} = R_0^2(\boldsymbol{\zeta} + \mathbf{I})^{-1}$ [107]).

Inserting the $\boldsymbol{\zeta}$ expression from (5.7) into (5.8) and taking the dot product on both sides with the eigenvector $\boldsymbol{n}^m$, we get an equation for the time evolution of the eigenvalues

$$\frac{d\lambda_m}{dt} = -\frac{1}{\tau}\left(\lambda_m - \boldsymbol{n}^m \cdot \boldsymbol{\zeta}^0 \cdot \boldsymbol{n}^m\right). \tag{5.9}$$

To close the system, we now need the equations for the eigenvector time evolution. Since the eigenvectors are unit length and always orthogonal to each other, they only rotate with the angular velocity $\boldsymbol{P}$

$$\frac{d\boldsymbol{n}^m}{dt} = \boldsymbol{P} \times \boldsymbol{n}^m. \tag{5.10}$$

To find $\boldsymbol{P}$, we first insert (5.7) into (5.8) and take the dot product with $\boldsymbol{n}^m$ from the left hand side and with $\boldsymbol{n}^l$ from the right hand side and get

$$\frac{d\boldsymbol{n}^m}{dt} \cdot \boldsymbol{n}^l - (\boldsymbol{\Omega} \times \boldsymbol{n}^m) \cdot \boldsymbol{n}^l = -\frac{\boldsymbol{n}^m \cdot \boldsymbol{\zeta}^0 \cdot \boldsymbol{n}^l}{\tau(\lambda_m - \lambda_l)}, \tag{5.11}$$

where we insert (5.10) and after the rearrangement of the triple product we get

$$(\boldsymbol{P} - \boldsymbol{\Omega}) \cdot (\boldsymbol{n}^m \times \boldsymbol{n}^l) = -\frac{\boldsymbol{n}^m \cdot \boldsymbol{\zeta}^0 \cdot \boldsymbol{n}^l}{\tau(\lambda_m - \lambda_l)}. \tag{5.12}$$

If the eigenvectors are such that they form the basis for a right handed coordinate system

$$\begin{cases} \boldsymbol{n}^1 = \boldsymbol{n}^2 \times \boldsymbol{n}^3 \\ \boldsymbol{n}^2 = \boldsymbol{n}^3 \times \boldsymbol{n}^1 \\ \boldsymbol{n}^3 = \boldsymbol{n}^1 \times \boldsymbol{n}^2 \end{cases}, \tag{5.13}$$

then since $\boldsymbol{P}-\boldsymbol{\Omega}=\sum_{k=1}^{3}((\boldsymbol{P}-\boldsymbol{\Omega})\cdot\boldsymbol{n}^k)\boldsymbol{n}^k$ we get an equation for the angular velocity

$$\boldsymbol{P}=\boldsymbol{\Omega}-\frac{1}{\tau}\left(\frac{\boldsymbol{n}^1\cdot\boldsymbol{\zeta}^0\cdot\boldsymbol{n}^2}{(\lambda_1-\lambda_2)}\boldsymbol{n}^3+\frac{\boldsymbol{n}^2\cdot\boldsymbol{\zeta}^0\cdot\boldsymbol{n}^3}{(\lambda_2-\lambda_3)}\boldsymbol{n}^1+\frac{\boldsymbol{n}^3\cdot\boldsymbol{\zeta}^0\cdot\boldsymbol{n}^1}{(\lambda_3-\lambda_1)}\boldsymbol{n}^2\right). \tag{5.14}$$

The equations (5.9), (5.10) and (5.14) can be used to calculate the shape evolution for a magnetic droplet in a rotating flow and in a stationary magnetic field that would produce the deformation corresponding to $\boldsymbol{\zeta}^0$ in a non-rotating flow. Alternatively we can change the reference frame to calculate the shape evolution for a droplet in a rotating (or precessing) magnetic field as will be shown in the next part.

5.3.2 In-plane dynamics

When the magnetic field is rotating with the angular velocity $\boldsymbol{\omega}=\omega\boldsymbol{e}_x$, we can change the reference frame such that the field is pointing in the z axis direction and there is an additional fluid flow rotating with the angular velocity $\boldsymbol{\Omega}=-\omega\boldsymbol{e}_x$. No additional stresses are formed in this non-inertial reference frame since we are working in the Stokes flow limit. In this reference frame we can use (5.8).

When $\omega=0$, the droplet elongates in the z direction and takes up a prolate shape characterized by its elongation

$$\delta=[\epsilon_1]_{\omega=0}. \tag{5.15}$$

The conservation of volume puts a constraint on the eigenvalues of the anisotropy tensor $\prod_{i=1}^{3}(1+\lambda_i)=1$, which in the limit of small deformations simplifies to

$$\lambda_1+\lambda_2+\lambda_3=0. \tag{5.16}$$

Using (5.15) and the constraint (5.16), we can write the equilibrium anisotropy tensor

$$\boldsymbol{\zeta}^0=\begin{pmatrix}\frac{2\delta}{3} & 0 & 0\\ 0 & \frac{2\delta}{3} & 0\\ 0 & 0 & -\frac{4\delta}{3}\end{pmatrix}. \tag{5.17}$$

With this and setting $\boldsymbol{\Omega}=-\omega\boldsymbol{e}_x$, the equation (5.8) results in three independent sets

of equations

$$\begin{cases} \dfrac{d\zeta_{22}}{dt} = -\dfrac{1}{\tau}\left(\zeta_{22} - \dfrac{2\delta}{3}\right) + 2\omega\zeta_{23} \\ \dfrac{d\zeta_{23}}{dt} = -\dfrac{1}{\tau}\zeta_{23} - \omega\zeta_{22} + \omega\zeta_{33} \\ \dfrac{d\zeta_{33}}{dt} = -\dfrac{1}{\tau}\left(\zeta_{33} + \dfrac{4\delta}{3}\right) - 2\omega\zeta_{23} \end{cases}. \tag{5.18}$$

$$\begin{cases} \dfrac{d\zeta_{12}}{dt} = -\dfrac{1}{\tau}\zeta_{12} + \omega\zeta_{13} \\ \dfrac{d\zeta_{13}}{dt} = -\dfrac{1}{\tau}\zeta_{13} - \omega\zeta_{12} \end{cases}, \tag{5.19}$$

$$\frac{d\zeta_{11}}{dt} = -\frac{1}{\tau}\left(\zeta_{11} - \frac{2\delta}{3}\right), \tag{5.20}$$

The system (5.18) describes the in-plane motion of the droplet's shape - when one of the droplet's axis is aligned with the field rotation direction. The system (5.19) describes the out-of-plane motion and will not be further analyzed in the work. This motion decays exponentially and the in-plane motion is stable. Finally, (5.20) is required to satisfy the volume conservation. Its solution is redundant since the trace of the anisotropy tensor is always zero as can be seen from (5.16).

The eigenvectors of the anisotropy tensor follow the ellipsoid semiaxes and for the in-plane motion are

$$\begin{cases} \boldsymbol{n}^1 = \boldsymbol{e}_x \\ \boldsymbol{n}^2 = \boldsymbol{e}_y\cos(\beta) + \boldsymbol{e}_z\sin(\beta) \\ \boldsymbol{n}^3 = -\boldsymbol{e}_y\sin(\beta) + \boldsymbol{e}_z\cos(\beta) \end{cases}. \tag{5.21}$$

Plugging them into (5.7), we get

$$\begin{cases} \zeta_{22} = \lambda_2\cos^2(\beta) + \lambda_3\sin^2(\beta) \\ \zeta_{23} = (\lambda_2 - \lambda_3)\cos(\beta)\sin(\beta) \\ \zeta_{33} = \lambda_2\sin^2(\beta) + \lambda_3\cos^2(\beta) \end{cases}, \tag{5.22}$$

which we substitute in (5.18) to get the time derivatives of the eigenvalues of the anisotropy tensor and the angle β

$$\begin{cases} \dfrac{d\lambda_2}{dt} = -\dfrac{1}{\tau}\left(\lambda_2 + \dfrac{\delta}{3} - \delta\cos(2\beta)\right) \\ \dfrac{d\lambda_3}{dt} = -\dfrac{1}{\tau}\left(\lambda_3 + \dfrac{\delta}{3} + \delta\cos(2\beta)\right) \\ \dfrac{d\beta}{dt} = -\omega + \dfrac{\delta\sin(2\beta)}{\tau(\lambda_3 - \lambda_2)} \end{cases}. \tag{5.23}$$

In the limit of small deformations, the elongation and flatness parameters, are related to the eigenvalues of the anisotropy tensor by

$$\begin{cases} \epsilon_1 = \dfrac{1}{2}(\lambda_2 - \lambda_3) \\ \epsilon_2 = \dfrac{1}{2}(\lambda_1 - \lambda_2) = \dfrac{1}{2}(-2\lambda_2 - \lambda_3) \end{cases}, \tag{5.24}$$

which we insert into (5.23) to get how the droplet's elongation and flatness together with the angle β change with time

$$\begin{cases} \dfrac{d\epsilon_1}{dt} = -\dfrac{1}{\tau}\left(\epsilon_1 - \delta\cos(2\beta)\right) \\ \dfrac{d\epsilon_2}{dt} = -\dfrac{1}{\tau}\left(\epsilon_2 - \delta\sin^2(\beta)\right) \\ \dfrac{d\beta}{dt} = -\omega - \dfrac{\delta\cos(\beta)\sin(\beta)}{\tau\epsilon_1} \end{cases}. \tag{5.25}$$

The final system of equations (5.25) contains two phenomenological constants - the characteristic small deformation decay time τ and the elongation δ of the droplet in stationary magnetic field. These constants can be determined either experimentally or from an *ab initio* model such as the hydrodynamic solution described in section 5.4.

5.4 Hydrodynamic approach

We solve the hydrodynamic and magnetostatic problems formulated in sections 3.2 and 3.3 in the limit of small deformations and weak magnetic field using perturbation theory [109]. Such an approach has been fruitful in describing the dynamics of nearly spherical viscous droplets in external flows [110], droplets covered in surfactant in external flows [111], droplets in electric fields [104, 112] and their emulsions [103].

We introduce a small parameter ε that is proportional to the small deviation from a spherical drop. In spherical coordinates

$$\begin{cases} x = r\cos(\phi)\sin(\theta) \\ y = r\sin(\phi)\sin(\theta) \\ z = r\cos(\phi) \end{cases}, \tag{5.26}$$

we can write the shape of a droplet with a small deviation as $r = R_0\left(1 + \varepsilon f(\theta, \phi)\right)$, where $f(\theta, \phi)$ describes the shape and ε the magnitude of the deviation. For an ellipsoidal droplet we will show that the parameter ε is proportional to the elongation and flatness

of the droplet $\epsilon_1 = O(\varepsilon)$, $\epsilon_2 = O(\varepsilon)$.

We write the physical parameters describing the problem in power series of ε

$$\begin{aligned} \boldsymbol{v} &= \boldsymbol{v}_0 + \varepsilon \boldsymbol{v}_1 + O(\varepsilon^2), \\ \tilde{p} &= \tilde{p}_0 + \varepsilon \tilde{p}_1 + O(\varepsilon^2), \\ f_M &= f_{M0} + \varepsilon f_{M1} + O(\varepsilon^2). \end{aligned} \tag{5.27}$$

Parameters with index 0 correspond to the undeformed (spherical) droplet and show the effects of the magnetic forcing. Parameters with index 1 correspond to the effect of surface deformation and show, for example, the flow due to surface tension. In the approximate solution, we assume that the magnetic Bond number Bm is also small, therefore we omit all terms that scale as $O(\varepsilon^2)$ and $O(\varepsilon Bm)$.

We solve the problem for a stationary magnetic field pointing in the z direction and then to get the solution for a field that rotates we add a constant flow rotating in the opposite direction (i.e. we use a reference frame in which the magnetic field is pointing in the z direction).

5.4.1 Spherical droplet, magnetostatic problem

First we need to calculate the magnetic field inside the droplet. Finding the magnetic (or equivalently electric) field in a paramagnetic (dielectric) sphere is a classic textbook problem that can be solved in several ways [2, 15, 94, 113, 114]. Nonetheless, we present a solution to introduce the method that will be used in the more complex case - the hydrodynamic problem.

We use the fact that the Laplace equation for the magnetic potential ψ (3.6) is automatically satisfied by a linear combination of spherical harmonics multiplied by appropriate powers of r [2]

$$\psi(r,\theta,\phi) = \sum_{l=0}^{\infty} \sum_{m=-l}^{l} \left(d_l^m \left(\frac{r}{R_0} \right)^l + d_{-l-1}^m \left(\frac{r}{R_0} \right)^{-l-1} \right) Y_l^m(\theta,\phi), \tag{5.28}$$

where d_l^m are coefficients determined by the boundary conditions. The spherical harmonics are defined as [2]

$$Y_l^m(\theta,\phi) = \sqrt{\frac{2l+1}{4\pi} \frac{(l-m)!}{(l+m)!}} P_l^m(\cos\theta) e^{im\phi}, \tag{5.29}$$

where P_l^m is the associated Legendre polynomial[1]. For $0 \leq m \leq l$ it is given by [2]

$$P_l^m(x) = \frac{(-1)^m}{2^l l!}(1-x^2)^{\frac{m}{2}} \frac{d^{l+m}}{dx^{l+m}}(x^2-1)^l, \tag{5.30}$$

and for $-l \leq m < 0$ it is given by [2]

$$P_l^{-m}(x) = (-1)^m \frac{(l-m)!}{(l+m)!} P_l^m(x). \tag{5.31}$$

It is worth noting a couple of useful properties of the spherical harmonics. They are orthonormal with respect to integration over the full solid angle [2]

$$\int_0^{2\pi} d\phi \int_0^{\pi} Y_n^m(\theta,\phi)\bar{Y}_{l'}^{m'}(\theta,\phi)\sin\theta d\theta = \delta_{ll'}\delta_{mm'}, \tag{5.32}$$

where the $\bar{Y}$ is the complex conjugate of Y, and δ_{ij} is the Kronecker delta. The spherical harmonics form a complete set of basis functions [113], meaning that any reasonably well behaved function $f(\theta,\phi)$ can be expressed as a linear combination in this basis

$$f(\theta,\phi) = \sum_{l=0}^{\infty}\sum_{m=-l}^{l} A_l^m Y_l^m(\theta,\phi). \tag{5.33}$$

Combining (5.32) and (5.33), we get that the coefficients of expansion in spherical harmonics can be determined by integration

$$A_l^m = \int_0^{2\pi} d\phi \int_0^{\pi} f(\theta,\phi)\bar{Y}_l^m(\theta,\phi)\sin\theta d\theta. \tag{5.34}$$

For the magnetic field solution to be physical, we keep only part of (5.28) outside the droplet

$$\psi(r,\theta,\phi)^{(e)} = D_1^m \left(\frac{r}{R_0}\right) Y_1^m(\theta,\phi) + \sum_{l=0}^{\infty}\sum_{m=-l}^{l} D_{-l-1}^m \left(\frac{r}{R_0}\right)^{-l-1} Y_l^m(\theta,\phi), \tag{5.35}$$

and inside the droplet

$$\psi(r,\theta,\phi)^{(i)} = \sum_{l=1}^{\infty}\left(\frac{r}{R_0}\right)^l \sum_{m=-l}^{l} d_l^m Y_l^m(\theta,\phi), \tag{5.36}$$

[1]Some authors [113] place the Condon-Shortley phase $(-1)^m$ in front of Spherical harmonic definition (5.29) instead of in front of the associated Legendre polynomial definition (5.30). The convention used in this work corresponds also to Wolfram Mathematica functions `SphericalHarmonicY` and `LegendreP`.

where we changed the coefficients to capital D for the potential outside the droplet for further clarity. We also omitted the term proportional to r^0, because it results in zero magnetic field. From the symmetry in the problem, it is evident that there should be no dependence on the angle ϕ. Therefore, D^0_{-l-1} and d^0_l are the only non-zero coefficients.

Next we need to find satisfy the boundary conditions. From (3.10) we see that

$$\psi^{(e)}|_{r\to\infty} = D^0_1 \left(\frac{r}{R_0}\right) Y^0_1 = H_\infty r\cos\theta, \tag{5.37}$$

which gives $D^0_1 = R_0\sqrt{\frac{4\pi}{3}}H_\infty$. From (3.8), at $r = R_0$ we have

$$\sum_{l=1}^{\infty} d^0_l Y^0_l = R_0\sqrt{\frac{4\pi}{3}}H_\infty Y^0_1 + \sum_{l=0}^{\infty} D^0_{-l-1} Y^0_l, \tag{5.38}$$

and from (3.7), since $\boldsymbol{n} = \boldsymbol{e}_r$ and $\boldsymbol{e}_r \cdot \boldsymbol{\nabla} = \frac{\partial}{\partial r}$, at $r = R_0$ we have

$$\mu_r \sum_{l=1}^{\infty} l d^0_l Y^0_l = R_0\sqrt{\frac{4\pi}{3}}H_\infty Y^0_1 + \sum_{l=0}^{\infty} (-l-1)\, D^0_{-l-1} Y^0_l. \tag{5.39}$$

We use the fact that the sum in (5.38) and (5.39) is over orthogonal functions and we multiply both sides by $\bar{Y}^0_{l'}(\theta,\phi)$ and integrate over the full solid angle, and using (5.32), we get a system of equations for the coefficients

$$\begin{cases} d^0_{l'} & = R_0\sqrt{\frac{4\pi}{3}}H_\infty \delta_{1l'} + D^0_{-l'-1} \\ \mu_r l' d^0_{l'} & = R_0\sqrt{\frac{4\pi}{3}}H_\infty \delta_{1l'} + (-l'-1)\, D^0_{-l'-1} \end{cases}. \tag{5.40}$$

The solution to the system is 0 for all $l' \neq 1$, and $d^0_1 = \frac{2R_0H_\infty\sqrt{3\pi}}{\mu_r+2}$, $D^0_{-2} = -\frac{2R_0H_\infty\sqrt{\pi/3}(\mu_r-1)}{\mu_r+2}$ when $l' = 1$.

Finally, once we know the coefficients d and D, we can substitute them in (5.36) and (5.35), and write the magnetic potential inside the spherical droplet

$$\psi^{(i)} = \frac{3R_0H_\infty}{\mu_r+2}\frac{r}{R_0}\cos\theta \tag{5.41}$$

and outside it

$$\psi^{(e)} = R_0H_\infty\left(\frac{r}{R_0} - \frac{\mu_r-1}{\mu_r+2}\left(\frac{R_0}{r}\right)^2\right)\cos\theta. \tag{5.42}$$

We get the magnetic field inside and outside the droplet by taking the gradient of the

corresponding potential $\boldsymbol{H} = \boldsymbol{\nabla}\psi$. To determine the effective magnetic surface force (3.31), only the inside field is necessary, which is

$$\boldsymbol{H}^{(i)} = \frac{3H_\infty}{\mu_r + 2}\left[\boldsymbol{e}_r \cos\theta - \boldsymbol{e}_\theta \sin\theta\right] = \frac{3H_\infty}{\mu_r + 2}\boldsymbol{e}_z. \tag{5.43}$$

We can easily read that $H_n^{(i)} = \frac{3H_\infty}{\mu_r+2}\cos\theta$ and $\boldsymbol{H}_t^{(i)} = -\frac{3H_\infty}{\mu_r+2}\boldsymbol{e}_\theta \sin\theta$, hence the effective magnetic surface force (3.31) for a spherical droplet in a uniform field is

$$f_M = \frac{\gamma}{R_0}\left(\frac{9Bm}{8\pi}\frac{\mu_r - 1}{(\mu_r+2)^2}\left(\mu_r \cos^2\theta + \sin^2\theta\right)\right). \tag{5.44}$$

5.4.2 Spherical droplet, hydrodynamic problem

Once we know the forces acting on the droplet - the effective magnetic surface force f_M and the surface tension $-\gamma(k_1 + k_2) = -2\gamma/R_0$, we can calculate the flow that arises. The solution to the Stokes equations (3.28) also can be expressed in terms of spherical harmonics. This is the so called Lamb's solution [115, 116], which for the flow outside and inside the droplet reads

$$\begin{aligned}\boldsymbol{v}^{(e)} =& \sum_{l=1}^{\infty}\frac{1}{\eta^{(e)}}\left[-\frac{(l-2)r^2\boldsymbol{\nabla}p_{-l-1}^{(e)}}{2l(2l-1)} + \frac{(l+1)\boldsymbol{r}p_{-l-1}^{(e)}}{l(2l-1)}\right] \\ &+ \sum_{l=0}^{\infty}\left[\boldsymbol{\nabla}\phi_{-l-1}^{(e)} + \boldsymbol{\nabla}\times\left(\boldsymbol{r}\chi_{-l-1}^{(e)}\right)\right],\end{aligned} \tag{5.45}$$

$$\begin{aligned}\boldsymbol{v}^{(i)} =& \sum_{l=0}^{\infty}\frac{1}{\eta^{(i)}}\left[\frac{(l+3)r^2\boldsymbol{\nabla}p_l^{(i)}}{2(l+1)(2l+3)} - \frac{l\boldsymbol{r}p_l^{(i)}}{(l+1)(2l+3)}\right] \\ &+ \sum_{l=0}^{\infty}\left[\boldsymbol{\nabla}\phi_l^{(i)} + \boldsymbol{\nabla}\times\left(\boldsymbol{r}\chi_l^{(i)}\right)\right],\end{aligned} \tag{5.46}$$

where where $p_l^{(i)}$, $p_{-l-1}^{(e)}$, $\phi_l^{(i)}$, $\phi_{-l-1}^{(e)}$, $\chi_l^{(i)}$ and $\chi_{-l-1}^{(e)}$ are solid spherical harmonics (spherical harmonics multiplied by an appropriate power of r)

$$p_l^{(i)} = \left(\frac{r}{R_0}\right)^n \sum_{m=-l}^{l} a_l^m Y_l^m, \quad p_{-l-1}^{(e)} = \left(\frac{r}{R_0}\right)^{-l-1}\sum_{m=-l}^{l} A_l^m Y_l^m,$$

$$\phi_l^{(i)} = \left(\frac{r}{R_0}\right)^n \sum_{m=-l}^{l} b_l^m Y_l^m, \quad \phi_{-l-1}^{(e)} = \left(\frac{r}{R_0}\right)^{-l-1}\sum_{m=-l}^{l} B_l^m Y_l^m,$$

$$\chi_l^{(i)} = \left(\frac{r}{R_0}\right)^l \sum_{m=-l}^{l} c_l^m Y_l^m, \quad \chi_{-l-1}^{(e)} = \left(\frac{r}{R_0}\right)^{-l-1}\sum_{m=-l}^{l} C_l^m Y_l^m.$$

Each term in the first sum in both (5.45) and (5.46) describes the flow arising due to pressure $p^{(e)}_{-l-1}$ and $p^{(i)}_l$, respectively. The second sum describes the flow that can arise with zero pressure. The total effective pressure (hydrodynamic plus magnetic pressure) is then found as

$$p^{(e)} = \sum_{l=1}^{\infty} p^{(e)}_{-l-1}, \quad p^{(i)} = \sum_{l=0}^{\infty} p^{(i)}_l. \tag{5.47}$$

The coefficients a, A, b, B, c, C can be determined from the boundary conditions. The normal force acting on the spherical droplet boundary that is due to magnetic forcing and surface tension reads

$$f_M - \gamma(k_1 + k_2) = \frac{\gamma}{R_0}\left[\frac{9Bm}{8\pi}\frac{\mu_r - 1}{(\mu_r + 2)^2}\left(\mu_r \cos^2\theta + \sin^2\theta\right) - 2\right]. \tag{5.48}$$

Expanding it in spherical harmonics (5.33), we get

$$f_M - \gamma(k_1 + k_2) = \frac{\gamma}{R_0}\sqrt{\pi}\left(\frac{3Bm(\mu - 1)}{4\pi(\mu + 2)} - 4\right)Y_0^0 + \frac{\gamma}{R_0}\frac{3Bm(\mu - 1)^2}{2\sqrt{5\pi}(\mu + 2)^2}Y_2^0. \tag{5.49}$$

To satisfy the boundary condition (3.30), $f_M - \gamma(k_1 + k_2)$ should be opposed by a hydrodynamic stress with the same surface harmonics. Similarly to [112] examining different summands of (5.45) and (5.46), we see that only $l = 0$ and $l = 2$ are needed. Furthermore, since the problem is symmetric in ϕ, only $m = 0$ is needed, and the term $\boldsymbol{\nabla} \times (\boldsymbol{r}\chi)$ in (5.45), (5.46) is not needed. The only remaining non-zero coefficients in Lamb's solution are $a_0^0,\ B_0^0,\ a_2^0,\ b_2^0,\ A_2^0,\ B_2^0$.

Now that there are a finite number of unknown coefficients, the calculations are algebraically cumbersome, but straightforward and were done in Wolfram Mathematica. The now finite sums of (5.45), (5.46) were substituted in the boundary conditions (3.29), (3.30), (3.32). The equations were evaluated at the droplet boundary $r = R_0$, and expanded in spherical harmonics (5.34). To satisfy the boundary conditions for all θ and ϕ, the coefficients in this expansion should be zero, which gives us 6 equations for the 6 unknowns.

We get that the velocities are

$$\begin{aligned}\boldsymbol{v}_0^{(i)} =& \frac{\gamma}{\eta^{(e)}} M_2 \left[\left(\frac{L_4}{L_2 L_3}\left(\frac{r}{R_0}\right) - \frac{3}{L_3}\left(\frac{r}{R_0}\right)^3\right)(1 + 3\cos(2\theta))\,\boldsymbol{e}_r \right. \\ &\left. + \left(-\frac{3L_4}{L_2 L_3}\left(\frac{r}{R_0}\right) + \frac{15}{L_3}\left(\frac{r}{R_0}\right)^3\right)\sin(2\theta)\boldsymbol{e}_\theta\right],\end{aligned} \tag{5.50}$$

$$\begin{aligned}\boldsymbol{v}_0^{(e)} =&\frac{\gamma}{\eta^{(e)}} M_2 \left[\left(\frac{1}{L_2} / \left(\frac{r}{R_0} \right)^2 - \frac{3L_1}{L_2 L_3} / \left(\frac{r}{R_0} \right)^4 \right) (1 + 3\cos(2\theta))\, \boldsymbol{e}_r \right. \\ &\left. + \left(-\frac{6L_1}{L_2 L_3} / \left(\frac{r}{R_0} \right)^4 \right) \sin(2\theta) \boldsymbol{e}_\theta \right],\end{aligned} \tag{5.51}$$

And the pressures are

$$p_0^{(i)} = \frac{\gamma}{R_0} \left(2 - M_1 - \frac{21\lambda M_2}{L_3} (1 + 3\cos(2\theta)) \left(\frac{r}{R_0} \right)^2 \right), \tag{5.52}$$

$$p_0^{(e)} = \frac{\gamma}{R_0} \frac{2M_2}{L_2} (1 + 3\cos(2\theta)) / \left(\frac{r}{R_0} \right)^3, \tag{5.53}$$

where the following notation was used

$$\begin{aligned} &M_1 = \frac{3Bm}{8\pi} \frac{\mu_r - 1}{\mu_r + 2}, \quad M_2 = \frac{3Bm}{16\pi} \frac{(\mu_r - 1)^2}{(\mu_r + 2)^2}, \\ &L_1 = (2 + 3\lambda), \quad L_2 = (3 + 2\lambda), \\ &L_3 = (16 + 19\lambda), \quad L_4 = (19 + 16\lambda). \end{aligned} \tag{5.54}$$

The velocity streamlines are depicted in figure 5.2. We see that as expected the droplet elongates in the direction of the applied field. Evaluated on the surface $r = R_0$, the velocity is

$$\begin{aligned}[\boldsymbol{v}_0]_{r=R_0} = \frac{\gamma}{\eta^{(e)}} \frac{M_2}{L_2 L_3} [&10(1 + \lambda)(1 + 3\cos(2\theta)) \boldsymbol{e_r} \\ &- 6L_1 \sin(2\theta) \boldsymbol{e_\theta}].\end{aligned} \tag{5.55}$$

5.4.3 Deformed droplet, hydrodynamic problem

To get the next order terms in (5.27), assume that the droplet is an ellipsoid, whose longest axis is rotated by an angle β from the z direction. Up to the leading order in ϵ_1 and ϵ_2 such an ellipsoid is described by

$$\frac{\epsilon_1 - \epsilon_2}{3} + (1 + 2\epsilon_2) \frac{x^2}{R_0^2} + \frac{(y\cos(\beta) + z\sin(\beta))^2}{R_0^2} + (1 - 2\epsilon_1) \frac{(z\cos(\beta) - y\sin(\beta))^2}{R_0^2} = 1. \tag{5.56}$$

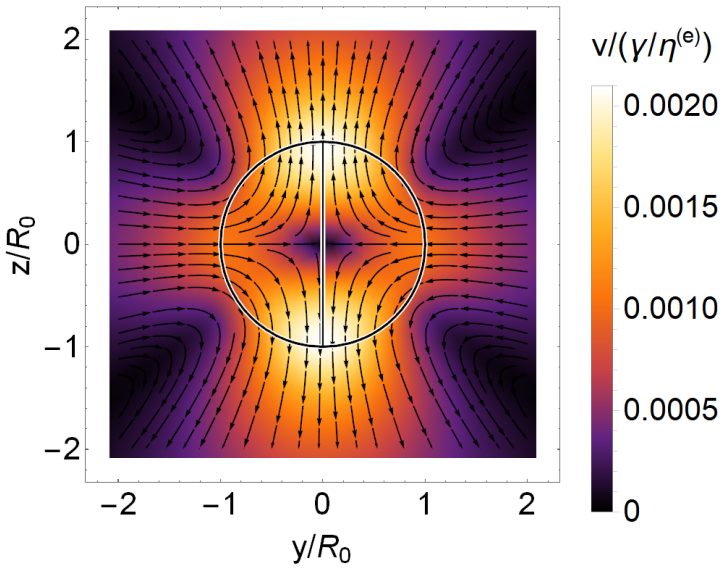

Figure 5.2: Velocity streamplot of a spherical magnetic droplet (its boundary is depicted by the circle) with $\mu_r = 10$, $Bm = 5$, $\lambda = 100$ in a homogeneous magnetic field along the z direction. Color indicates the magnitude of the velocity in units of $\gamma/\eta^{(e)}$. The cross section is taken at $x = 0$.

Changing into spherical coordinates it becomes

$$\begin{aligned} r &= R_0\left(1+\varepsilon f(\theta,\phi)\right) \\ &= R_0\left(1+\alpha_2^2 Y_2^{-2}+\alpha_2^1 Y_2^{-1}+\alpha_2^0 Y_2^0+\alpha_2^1 Y_2^1+\alpha_2^2 Y_2^2\right), \end{aligned} \tag{5.57}$$

where $\varepsilon f(\theta,\phi)$ was expanded into spherical harmonics. The coefficients in front of them are all $O(\varepsilon)$ and are

$$\begin{aligned} \alpha_2^0 &= \sqrt{\frac{\pi}{45}}\Big(\epsilon_1\big(1+3\cos(2\beta)\big)+2\epsilon_2\Big), \\ \alpha_2^1 &= -2i\sqrt{\frac{2\pi}{15}}\epsilon_1\cos(\beta)\sin(\beta), \\ \alpha_2^2 &= -\sqrt{\frac{\pi}{30}}\Big(\epsilon_1\big(1-\cos(2\beta)\big)+2\epsilon_2\Big). \end{aligned} \tag{5.58}$$

For an ellipsoid the coefficients are the same in front of the spherical harmonics with opposite m numbers (Y_l^m and Y_l^{-m}).

We can express the droplet as a level surface $\xi = r - R_0\left(1+\varepsilon f(\theta,\phi)\right) = 0$. Then the normal vector and the curvature can be found by

$$\boldsymbol{n} = \left[\frac{\boldsymbol{\nabla}\xi}{|\boldsymbol{\nabla}\xi|}\right]_{r=R_0(1+\varepsilon f)} \tag{5.59}$$

and

$$k_1 + k_2 = \left[\boldsymbol{\nabla}\cdot\boldsymbol{n}\right]_{r=R_0(1+\varepsilon f)}. \tag{5.60}$$

We write both $\boldsymbol{n}$ and $k_1 + k_2$ in Taylor series for small ε and Bm and omit all terms higher than the first power. The magnetic surface force f_M already is $O(Bm)$ and remains unchanged from the spherical case up to the first order in ε and Bm.

Next order corrections $\varepsilon \boldsymbol{v}_1^{(e)}$, $\varepsilon p_1^{(e)}$ and $\varepsilon \boldsymbol{v}_1^{(i)}$, $\varepsilon p_1^{(i)}$ also obey the Stokes equations, therefore they may be written in the form of Lamb's solution. Coefficients in the Lamb's solution are now found by enforcing the boundary conditions on the full fields $\boldsymbol{v}_0^{(e)} + \varepsilon \boldsymbol{v}_1^{(e)}$, $p_0^{(e)} + \varepsilon p_1^{(e)}$ and $\boldsymbol{v}_0^{(i)} + \varepsilon \boldsymbol{v}_1^{(i)}$, $p_0^{(i)} + \varepsilon p_1^{(i)}$ up to first order in ε and Bm.

Just as in the spherical case, we examine what summands of the Lamb's solution that need to be attained to satisfy the normal force boundary condition (3.30). We see that only the terms with $l = 2$ are needed, the rest are zero. However now since there is no longer a symmetry around ϕ, all $m = -l, ..., l$ are needed. Nonetheless, there are now only a finite number of unknown coefficients that can be found by plugging the full velocity and pressure fields in the boundary conditions (3.29), (3.30),(3.32). The boundary conditions are evaluated on the deformed surface $r = R_0(1+\varepsilon f)$. They are expanded in Taylor series up to first order of ε and Bm. And again we expand them in spherical harmonics and require that all the coefficients be zero to satisfy the boundary conditions for all θ, ϕ.

Solving these equations in Wolfram Mathematica, we get the first order correction fields

$$\begin{aligned}\varepsilon \boldsymbol{v}_1^{(i)} =& \frac{\gamma}{\eta^{(e)}} \left(-\frac{L_4}{L_2 L_3} \left(\frac{r}{R_0} \right) + \frac{3}{L_3} \left(\frac{r}{R_0} \right)^3 \right) E_1 \boldsymbol{e}_r \\ &+ \frac{\gamma}{\eta^{(e)}} \left(\frac{L_4}{L_2 L_3} \left(\frac{r}{R_0} \right) - \frac{5}{L_3} \left(\frac{r}{R_0} \right)^3 \right) E_2 \boldsymbol{e}_\theta \\ &+ \frac{\gamma}{\eta^{(e)}} \left(\frac{L_4}{L_2 L_3} \left(\frac{r}{R_0} \right) - \frac{5}{L_3} \left(\frac{r}{R_0} \right)^3 \right) E_3 \boldsymbol{e}_\phi,\end{aligned} \tag{5.61}$$

$$\begin{aligned}\varepsilon \boldsymbol{v}_1^{(e)} =& \frac{\gamma}{\eta^{(e)}} \left(-\frac{1}{L_2} \Big/ \left(\frac{r}{R_0} \right)^2 + \frac{3L_1}{L_2 L_3} \Big/ \left(\frac{r}{R_0} \right)^4 \right) E_1 \boldsymbol{e}_r \\ &+ \frac{\gamma}{\eta^{(e)}} \frac{2L_1}{L_2 L_3} E_2 \boldsymbol{e}_\theta \Big/ \left(\frac{r}{R_0} \right)^4 \\ &+ \frac{\gamma}{\eta^{(e)}} \frac{2L_1}{L_2 L_3} E_3 \boldsymbol{e}_\phi \Big/ \left(\frac{r}{R_0} \right)^4,\end{aligned} \tag{5.62}$$

$$\varepsilon p_1^{(i)} = \frac{\gamma}{R_0} \frac{21 \lambda E_1}{L_3} \left(\frac{r}{R_0} \right)^2, \tag{5.63}$$

$$\varepsilon p_1^{(e)} = -\frac{\gamma}{R_0}\frac{2E_1}{L_2}\Big/\left(\frac{r}{R_0}\right)^3, \tag{5.64}$$

where we introduced

$$\begin{aligned} E_1 = &-2\epsilon_1 \sin(2\beta)\sin(2\theta)\sin(\phi) \\ &+ \sin^2(\theta)\cos(2\phi)(\epsilon_1\cos(2\beta) - \epsilon_1 - 2\epsilon_2) \\ &+ \frac{1}{6}(3\cos(2\theta)+1)(3\epsilon_1\cos(2\beta) + \epsilon_1 + 2\epsilon_2), \end{aligned} \tag{5.65}$$

$$\begin{aligned} E_2 = &-\frac{1}{2}\epsilon_1\cos(2\beta)\sin(2\theta)(\cos(2\phi) - 3) \\ &+ 2\epsilon_1\sin(2\beta)\cos(2\theta)\sin(\phi) \\ &+ \sin(2\theta)(\epsilon_1 + 2\epsilon_2)\cos^2(\phi), \end{aligned} \tag{5.66}$$

$$\begin{aligned} E_3 = 2\cos(\phi)[&\epsilon_1\sin(2\beta)\cos(\theta) \\ &+ \sin(\theta)\sin(\phi)(\epsilon_1\cos(2\beta) - \epsilon_1 - 2\epsilon_2)]. \end{aligned} \tag{5.67}$$

The now obtained fields $\boldsymbol{v}_0^{(e)} + \varepsilon\boldsymbol{v}_1^{(e)}$, $p_0^{(e)} + \varepsilon p_1^{(e)}$ and $\boldsymbol{v}_0^{(i)} + \varepsilon\boldsymbol{v}_1^{(i)}$, $p_0^{(i)} + \varepsilon p_1^{(i)}$ are for the case when the magnetic field is pointing in the z direction. To get the solution for a rotating field with the angular velocity $\boldsymbol{\omega} = \omega\boldsymbol{e}_x$, we add a constant rotational velocity field $\boldsymbol{v}_{rot} = -\omega\boldsymbol{e}_x \times \boldsymbol{r}$ to both inside and outside flows. This is equivalent to being in a rotating reference frame, whose z axis follows the magnetic field.

To find the way the droplet evolves over time, we need only the velocity on its boundary $\boldsymbol{v}^{(b)} = [\boldsymbol{v}]_{r=R_0(1+\varepsilon f)}$ (we have added the rotational flow). If the droplet's shape is described by $r = \rho(\theta,\phi,t) = R_0\,(1 + \varepsilon f(\theta,\phi,t))$, then the kinematic boundary condition dictates that

$$\frac{\partial\rho}{\partial t} = v_r^{(b)} - \frac{1}{r}\left(v_\theta^{(b)}\frac{\partial\rho}{\partial\theta} + \frac{v_\phi^{(b)}}{\sin(\theta)}\frac{\partial\rho}{\partial\phi}\right), \tag{5.68}$$

which we evaluate up to the first order in ε and Bm. Expanding the droplet's shape in spherical harmonics $r = \rho(\theta,\phi,t) = R_0\sum_{l=0}^{\infty}\sum_{m=-l}^{l}\alpha_l^m(t)Y_l^m(\theta,\phi)$, and plugging it into the kinematic boundary condition (5.68), we get the time derivatives of the expansion

coefficients:

$$\begin{cases} \dfrac{d\alpha_2^2}{dt} = i\omega\alpha_2^1 - \dfrac{\alpha_2^2}{\tau} \\ \dfrac{d\alpha_2^1}{dt} = \dfrac{i\omega}{2}\left(\sqrt{6}\alpha_2^0 + 2\alpha_2^2\right) - \dfrac{\alpha_2^1}{\tau} \\ \dfrac{d\alpha_2^0}{dt} = i\sqrt{6}\omega\alpha_2^1 + \dfrac{4\sqrt{5\pi}\delta}{15\tau} - \dfrac{\alpha_2^0}{\tau} \end{cases} . \tag{5.69}$$

Coefficients with opposite signs in m have the same time derivatives $d\alpha_l^m/dt = d\alpha_l^{-m}/dt$. And all time derivatives with $l \neq 2$ are zero. This means that a droplet with an initially ellipsoidal shape remains ellipsoidal. We have introduced the constants

$$\delta = \frac{9Bm}{32\pi}\frac{(\mu_r - 1)^2}{(\mu_r + 2)^2}, \tag{5.70}$$

and

$$\tau = \frac{R_0\eta^{(e)}}{\gamma}\frac{(3 + 2\lambda)(16 + 19\lambda)}{40(1 + \lambda)}. \tag{5.71}$$

As we will show shortly, they are the same constants as the ones used in the phenomenological approach (5.25), but from this hydrodynamic solution we get their explicit expressions. The elongation in non-rotating magnetic field (5.70) corresponds to the small deformation limit of the expressions obtained in works analyzing the equilibrium shape of ellipsoidal magnetic droplets in stationary field [24, 60, 58]. And the characteristic decay time of small perturbations from equilibrium (5.71) corresponds with the one obtained in other works concerning small deformations of droplets [64, 101].

If we plug the equations (5.58) into (5.69), and collect the time derivatives of the deformation parameters ϵ_1 and ϵ_2, and the angle β, we get the same system of equations as was obtained with the phenomenological approach (5.25). This validates the phenomenological approach and determines the phenomenological constants τ and δ. The phenomenological equation describing the evolution of the anisotropy tensor (5.8) is exact up to the first order in ε and Bm

5.5 Analysis and comparison with numeric simulations and experiment

5.5.1 Fixed points and their stability

The fixed points for the system (5.25) are

$$\begin{cases} \epsilon_1^* = \dfrac{\delta}{\sqrt{1+4\tau^2\omega^2}} \\ \epsilon_2^* = \dfrac{\delta}{2}\left(1 - \dfrac{1}{\sqrt{1+4\tau^2\omega^2}}\right), \\ \beta^* = -\dfrac{1}{2}\arctan(2\tau\omega) + n\pi \end{cases} \tag{5.72}$$

where n is an integer. For stationary field $\boldsymbol{H}_\infty$ ($\tau\omega = 0$), the droplet aligns with the magnetic field $\beta^* = n\pi$ and takes up a prolate shape $\epsilon_2^* = 0$. For fast rotating field $\tau\omega \to \infty$, the droplet lags the field by $\beta^* \to -\pi/4 + n\pi$ and is nearly oblate $\epsilon_1^* \to 0$ with a flatness approaching $\epsilon_2^* \to \delta/2$.

To investigate the stability of the fixed points, we linearize the equations (5.25) around them. For small perturbations $\Delta\epsilon_1$, $\Delta\epsilon_2$, $\Delta\beta$ from the fixed point, we have

$$\frac{d}{dt}\begin{pmatrix} \Delta\epsilon_1 \\ \Delta\epsilon_2 \\ \Delta\beta \end{pmatrix} = \begin{pmatrix} -\frac{1}{\tau} & 0 & \frac{4\delta\omega}{\sqrt{1+4\tau^2\omega^2}} \\ 0 & -\frac{1}{\tau} & -\frac{2\delta\omega}{\sqrt{1+4\tau^2\omega^2}} \\ -\frac{\omega\sqrt{1+4\tau^2\omega^2}}{\delta} & 0 & -\frac{1}{\tau} \end{pmatrix} \begin{pmatrix} \Delta\epsilon_1 \\ \Delta\epsilon_2 \\ \Delta\beta \end{pmatrix}. \tag{5.73}$$

This matrix has the eigenvalues $-1/\tau$, $-1/\tau - 2i\omega$, $-1/\tau + 2i\omega$, which indicates that the fixed points are stable focuses. The perturbations decay to the equilibrium while experiencing an oscillation with a frequency of 2ω - twice the frequency of the rotating magnetic field.

5.5.2 Qualitative behavior of the droplet

We can rescale the deformation parameters by the deformation at stationary field ($\tilde{\epsilon}_1 = \epsilon_1/\delta$, $\tilde{\epsilon}_2 = \epsilon_2/\delta$), and we can rescale time by the characteristic small perturbation decay time $\tilde{t} = t/\tau$. In this rescaled form the equations governing the droplet's shape in

a rotating field (5.25) read

$$\begin{cases} \dfrac{d\tilde{\epsilon}_1}{d\tilde{t}} = -\tilde{\epsilon}_1 + \cos(2\beta) \\ \dfrac{d\tilde{\epsilon}_2}{d\tilde{t}} = -\tilde{\epsilon}_2 + \sin^2(\beta) \\ \dfrac{d\beta}{d\tilde{t}} = -\tau\omega - \dfrac{\cos(\beta)\sin(\beta)}{\tilde{\epsilon}_1} \end{cases} . \tag{5.74}$$

We now see that up to a scaling, the droplet's behavior in the limit of small deformations is governed by a single parameter $\tau\omega$. The parameter $\tau\omega$ is proportional to the capillary number, which is the ratio of viscous forces to surface tension forces [117].

We can use the fact that ϵ_1 and β form a closed system to visualize the evolution of them on a phase portrait (figure 5.3). The phase portrait is similar to one of a damped pendulum. If initially the droplet is elongated enough, it overshoots the equilibrium angle β several times before it settles down. However, unlike a damped pendulum, this system is completely dissipative and there is no inertia. But just like in the case of a damped pendulum, there is a competition of two time scales - the characteristic small perturbation decay time τ and the oscillation period $T = \pi/\omega$ (which is two times smaller than the magnetic field rotation period).

The significance of the $\tau\omega$ parameter is illustrated in figure 5.4, where an initially spherical droplet is placed in a magnetic field rotating with different frequencies. If $\tau\omega$ is small, the droplet reaches its equilibrium shape monotonically. And if the frequency of the magnetic field is large enough ($\tau\omega$ is large), the droplet reaches the equilibrium undergoing several oscillations along the way.

5.5.3 Velocity field around the droplet and the torque of the droplet

Another benefit to solving the full hydrodynamic problem is that we can visualize the velocity field around a droplet for different magnetic field rotation frequencies (figure 5.5). Visually it seems that the velocity is not rotating, and indeed by integrating the external stress tensor on the surface of the droplet, we get that up to the first order in ε and Bm, the torque produced by the droplet on the external fluid is zero.

$$\boldsymbol{\mathcal{T}} = -\int \boldsymbol{r} \times (\boldsymbol{\sigma}^{(\mathbf{e})} \cdot \boldsymbol{n}) dS = \mathbf{0} + O(\varepsilon^2, \varepsilon Bm, Bm^2). \tag{5.75}$$

The droplet appears to rotate behind the magnetic field, but this effect comes from the deformation of its surface produced by a non rotating velocity field.

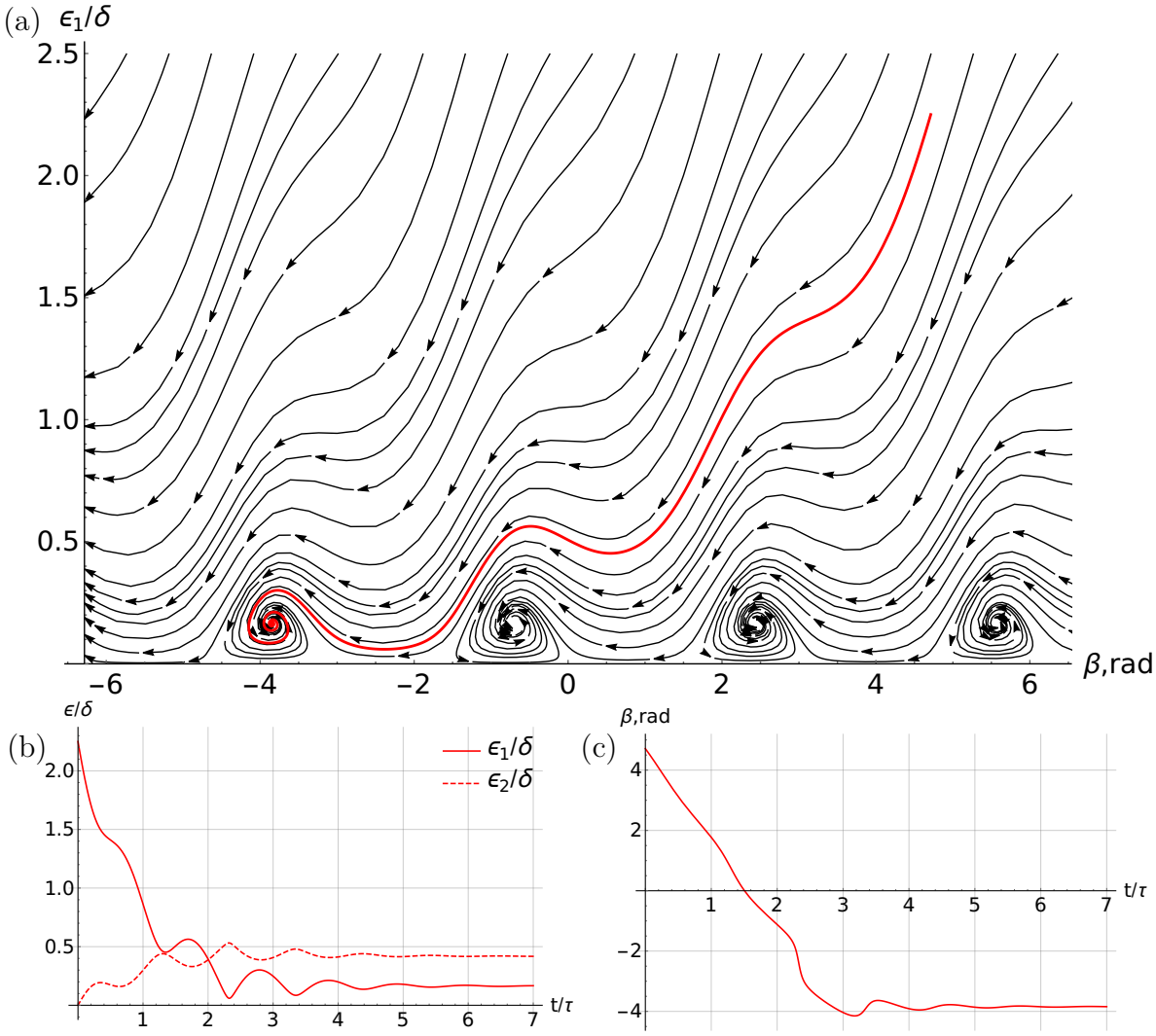

Figure 5.3: (a) depicts the phase portrait of the scaled droplet elongation ϵ_1/δ and the angle β between the droplet's largest axis and the magnetic field. (b) and (c) depict the change over time of the droplet's parameters ϵ_1/δ, ϵ_2/δ and β which correspond to the red trajectory in the phase portrait (a). The field rotates with the frequency $\omega = 3/\tau$.

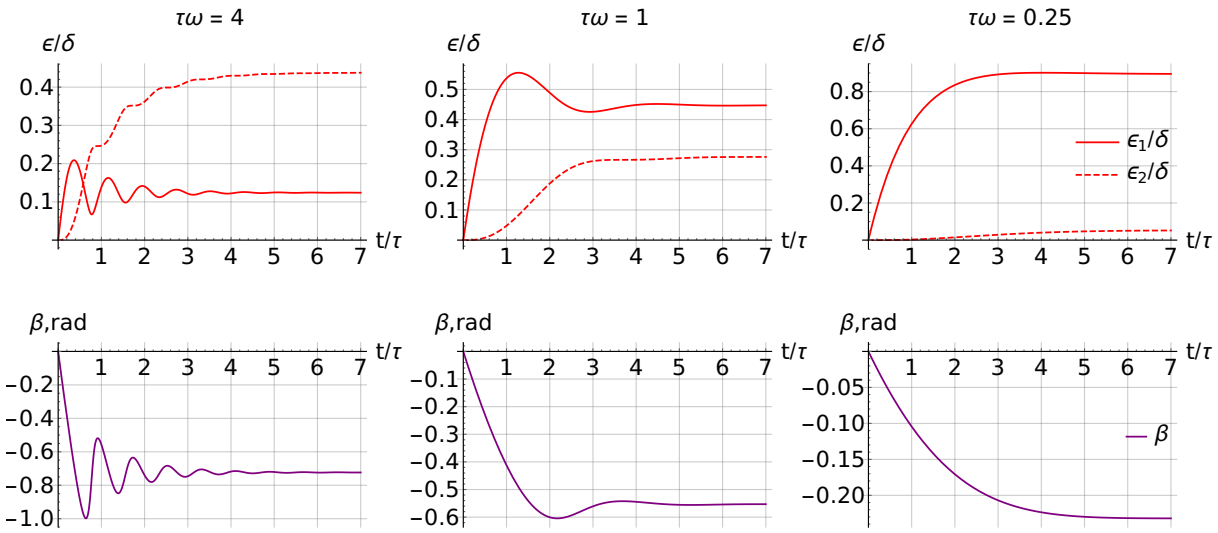

Figure 5.4: Settling to an equilibrium of a droplet that is initially spherical. Each column corresponds to a different magnetic field rotation frequency $\tau\omega$ denoted above it. Top row depicts the droplet's elongation ϵ_1 and flatness ϵ_2, while the bottom row depicts the angle β between the field and the droplet's longest axis.

A similar effect was found in [118], where the authors examined a sesile water (dielectric) droplets acted upon by a rotating electric field. The droplet motion mimicked a rotation, however the velocity field was found to be non-rotating.

The torque the magnetic field imparts on the droplet and thus the torque the droplet exerts on the surrounding fluid is $\mu_0(4\pi R_0^3/3)\boldsymbol{M} \times \boldsymbol{H}_\infty$, where $\boldsymbol{M}$ is the droplet's magnetization. It is proportional to Bm (which comes from the vector magnitude product $|\boldsymbol{M}||\boldsymbol{H}_\infty|$) multiplied by the deformation of of the droplet ϵ_1, ϵ_2 (which comes from the misalignment between $\boldsymbol{M}$ and $\boldsymbol{H}_\infty$; for a spherical drop $\boldsymbol{M}$ and $\boldsymbol{H}_\infty$ are parallel). Therefore, next order small deformation theory would be needed to describe the torque.

5.5.4 Comparison with BEM simulations and the limits of the small deformation theory

To validate the analytic results, we use numerical BEM simulations. We simulate the time evolution of an initially spherical droplet and let it reach an equilibrium shape, which we then compare against (5.72). Simulation is run with the following dimensionless parameters: $Bm = 0.1$, $\lambda = 100$, $\mu_r = 10$, and the dimensionless frequency of the rotating field $\omega/(\gamma/(R_0\eta^{(e)}))$ varied. Such parameters mean that $\delta = 0.005$ and $\tau = 96.3/(R_0\eta^{(e)}/\gamma)$. A 3D ellipsoid is fitted to the mesh points of the simulation. From it we determine the semiaxes' lengths and their orientations, which we use to find the deformation parameters ϵ_1, ϵ_2 and the angle β. Their equilibrium values are depicted

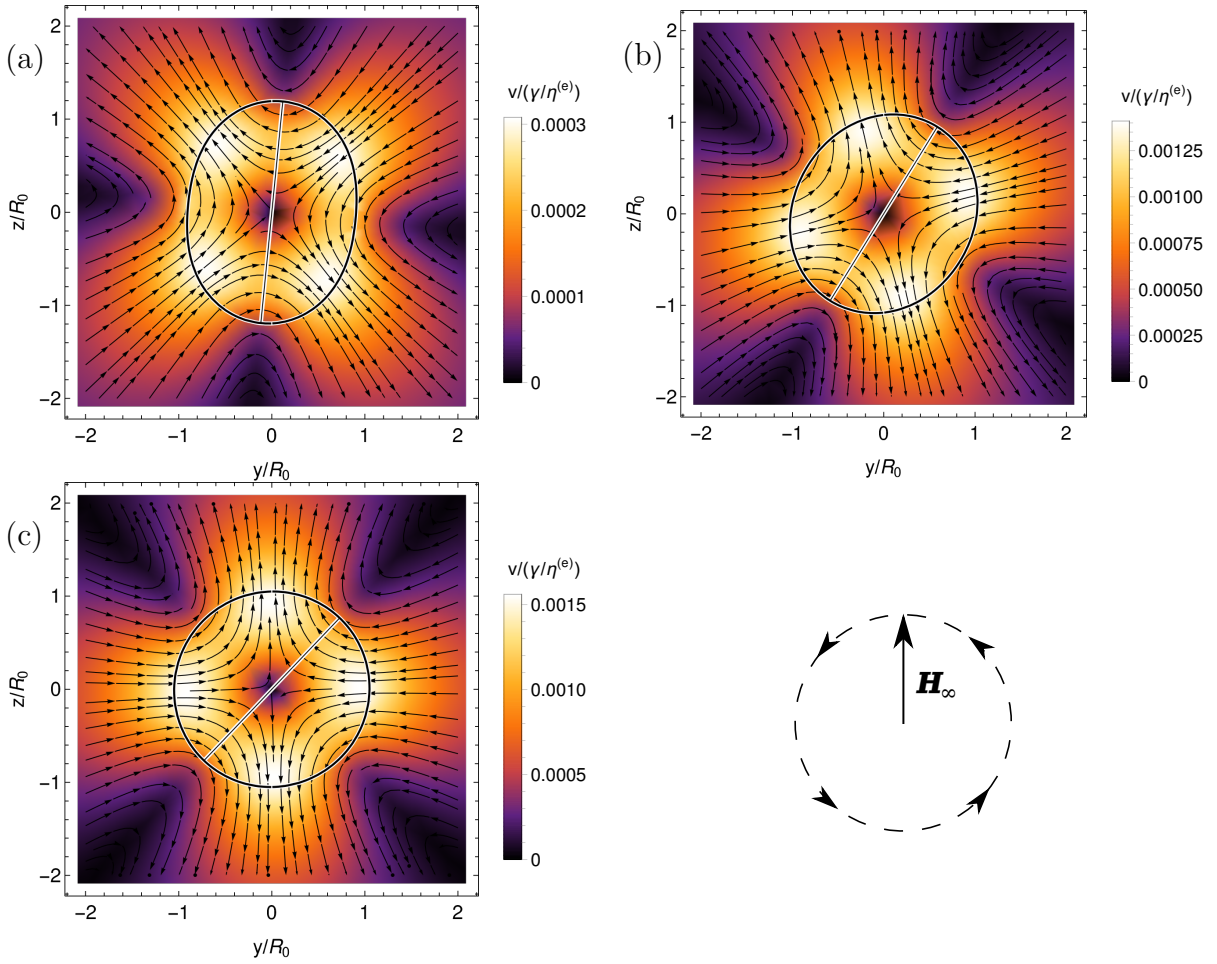

Figure 5.5: Illustration of the velocity field around droplets that have reached their equilibrium shape in a rotating magnetic field of different frequencies, which are (a) $\tau\omega = 0.1$, (b) $\tau\omega = 1$ and (c) $\tau\omega = 10$. The elongation in stationary field $\boldsymbol{H}_\infty$ would be $\delta = 0.3$. The cross-section at $x = 0$ is shown. Droplet shapes and their longest axis are outlined, and the velocity magnitude scaled by $\gamma/\eta^{(e)}$ is shown in color. The plot is made in the laboratory reference frame, where the magnetic field is rotating in the counter-clockwise direction and is momentarily pointing along the z axis. The velocity field is such that the droplet deforms in such a way that its longest axis follows the field.

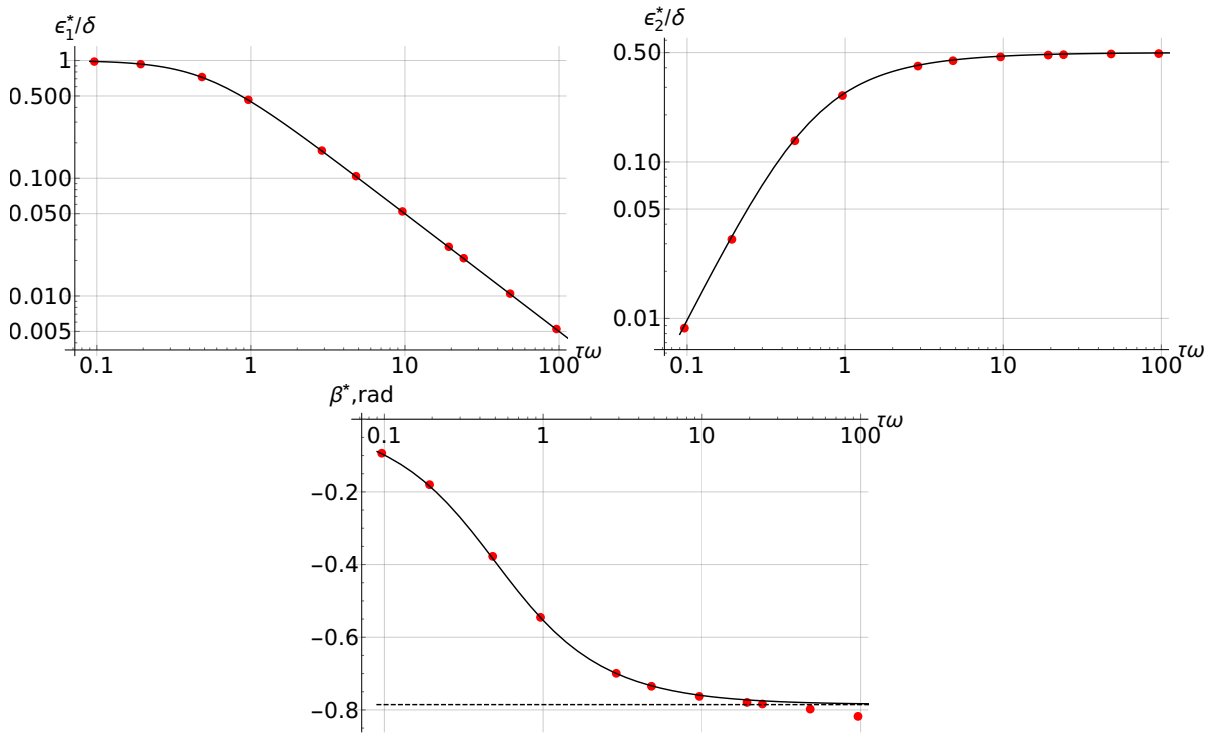

Figure 5.6: Equilibrium elongation ϵ_1, flatness ϵ_2 and the lagging angle β as a function of the rotating magnetic field frequency. In stationary field, the droplet elongates to $\delta = 0.005$. The lines are the analytic equilibrium values (5.72) and the red points are from the BEM simulations. The dashed line in the β^* graph is $-\frac{\pi}{4}$.

in figure 5.6. Excellent agreement can be seen between the theoretical and numerical equilibrium values of the deformation parameters. And for the angle β agreement is excellent when the field rotates slower, but some deviation from the theoretical curve can be seen for larger rotation frequencies. This might possibly be attributed to the fact that when $\tau\omega$ is large, the droplet becomes nearly oblate and the angle β as measured between the largest axis of the droplet and the magnetic field becomes ill defined.

BEM simulations can also be used to find the limits, where the small deformation theory is applicable. To do that we run the simulation with the following parameters: $\omega = 0.05/(\gamma/(R_0\eta^{(e)}))$, $\lambda = 100$, $\mu_r = 10$ and Bm was varied. For these parameters $\tau = 96.3/(R_0\eta^{(e)}/\gamma)$ and δ varied. The results can be seen in figure 5.7. We see that to have less than 10% error, the small deformation theory should be used for weak enough magnetic fields such that $\delta \lesssim 0.3$.

For the chosen magnetic droplet and rotating field parameters, the droplet's behavior qualitatively agrees with the small deformation theory up to $Bm \lesssim 12$ or $\delta \lesssim 0.6$. The droplet is quasi oblate ($\epsilon_2 > \epsilon_1$) and both deformation parameters increase as Bm increases. However, when the field strength reaches a critical value $Bm \approx 13$ or $\delta \approx 0.65$, the droplet strongly elongates reaching $\epsilon_1 \approx 2.7$ and become nearly axisymmetric $\epsilon_2 \approx 0.03$

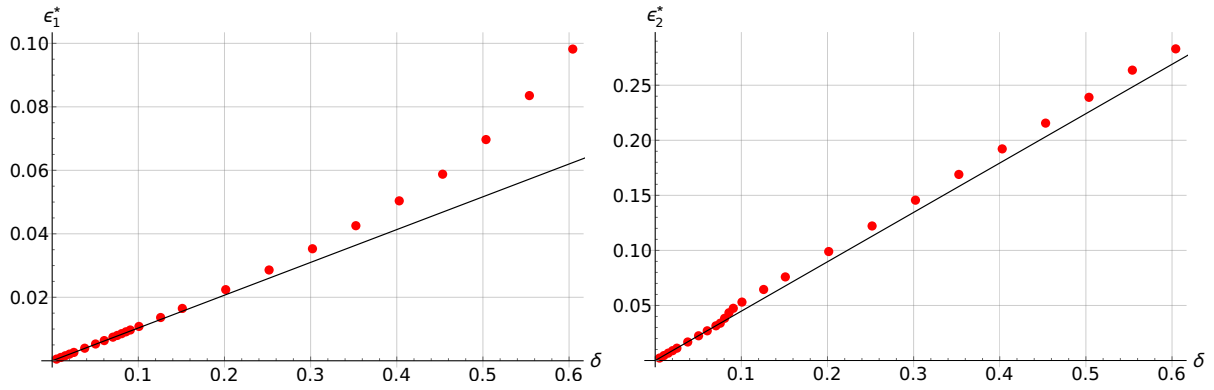

Figure 5.7: Equilibrium elongation ϵ_1 and flatness ϵ_2 as a function of the rotating magnetic field strength as measured by the droplet's elongation in stationary field δ. The frequency of the field is such that $\tau\omega = 4.8$. The lines are the analytic equilibrium values (5.72) and the red points are from the BEM simulations.

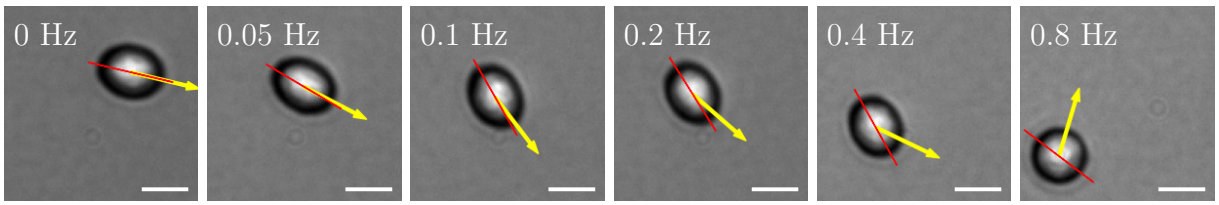

Figure 5.8: Experimental stationary shapes of magnetic droplets in a rotating magnetic field with different frequencies. The red line denotes the droplet's longest axis and the yellow arrow is the magnetic field direction. The field $\mu_0 H_\infty = 510\ \mu T$ is rotating counterclockwise in the plane of the image. The white scale is 10 μm long. The droplet's shape in the rightmost image is nearly circular from this viewing angle, therefore it was not possible to accurately determine the direction of its largest axis.

before the simulation breaks down due to the inability to adequately describe the large curvature of the droplet. This bifurcation is not described by the small deformation theory up to first order in Bm and ε.

5.5.5 Comparison with experiments

We first observe a droplet obtained by phase separation (droplet 1 in table 3). Magnetic field of magnitude $\mu_0 H_\infty = 510\ \mu T$ was applied with different rotation frequencies $f = \omega/(2\pi)$. Such magnetic field when stationary resulted in the elongation of the droplet $\delta = 0.25 \pm 0.01$. (The error here might be underestimated, since, as will be shown later, there is a constant parasitic background field disturbing the measurements.) The droplet's shape is tracked as the magnetic field rotates (figure 5.8).

From the two deformation parameters only ϵ_1 can be detected directly, which together with the angle β between the magnetic field and the droplet's largest axis is shown in figure 5.9. The data for ϵ_1 is very noisy, however β is more stable and can be analyzed for all frequencies except 0.8 Hz. Visually it is evident that the exponential transition to an

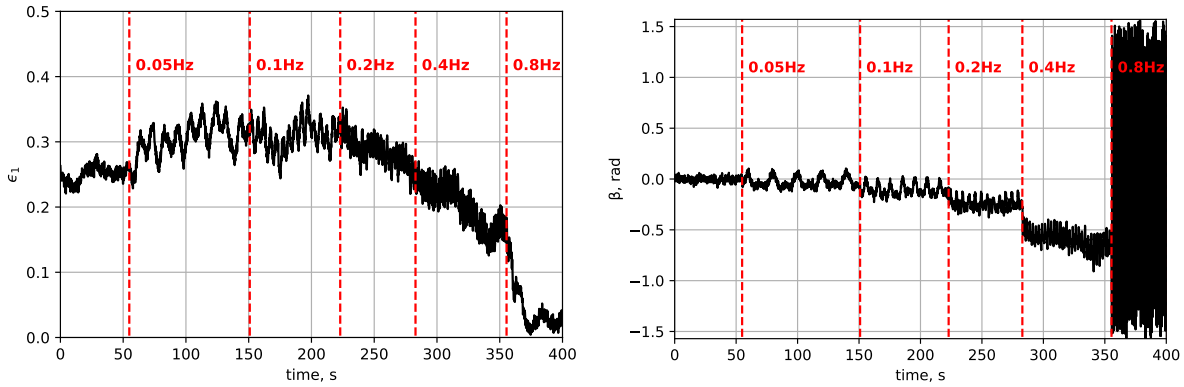

Figure 5.9: The elongation ϵ_1 and the angle β droplet makes with the magnetic field as a function of time. For the first seconds the magnetic field $\mu_0 H_\infty = 510\ \mu T$ is stationary and then it's frequency is increased. The effect of the constant background field can be seen as periodic spikes in both ϵ_1 and β. When the rotation frequency is $0.8Hz$, β can no longer be determined since the droplet is nearly circular in the microscope.

equilibrium happens fast and nearly all of the time when the field of a particular frequency is applied, the droplet has already achieved its equilibrium angle β^*. The oscillations in β are due to the background parasitic magnetic field, which for smaller rotation frequencies even results in the droplet seemingly leading the magnetic field during some parts of the rotation. To get the experimental equilibrium value β^*, we average all the β values during the time a field of a particular frequency is applied. To estimate the error, we calculate the standard deviation of it. Knowing β^* and the field rotation frequency, we can calculate the characteristic small deformation decay time τ from (5.72). The error in τ is estimated by varying the angle β^* within one standard deviation. The calculated τ values are constant within the margin of error and are $\tau_{rot} = (0.11 \pm 0.03)s$ (figure 5.10 (a)), where the average value was calculated using inverse squared errors as weights.

According to the small deformation theory, there is another way to determine τ. When a droplet relaxes to the equilibrium shape in stationary field, its elongation ϵ_1 reaches exponentially to the equilibrium value with a characteristic time of τ. Setting $\omega = 0$ and $\beta = 0$ from (5.25) we have

$$(\epsilon_1 - \epsilon_1^*) \propto e^{-t/\tau}, \tag{5.76}$$

where ϵ_1^* is the droplet's final elongation. We elongate the same droplet (droplet 1 in table 3) and let it relax in zero applied field to find that this decay time is $\tau_{rel} = (7.7 \pm 0.2)s$ (figure 5.10 (b)). The droplet does not reach zero elongation when the field is turned off. It settles to $\epsilon_1^* = 0.052 \pm 0.001$, which indicates that there is parasitic background field in the experimental setup. Estimating from the measurements on a different droplet (section 4.4.4) that the surface tension is $\gamma = 9.3 \cdot 10^{-7} N/m$ and the relative magnetic

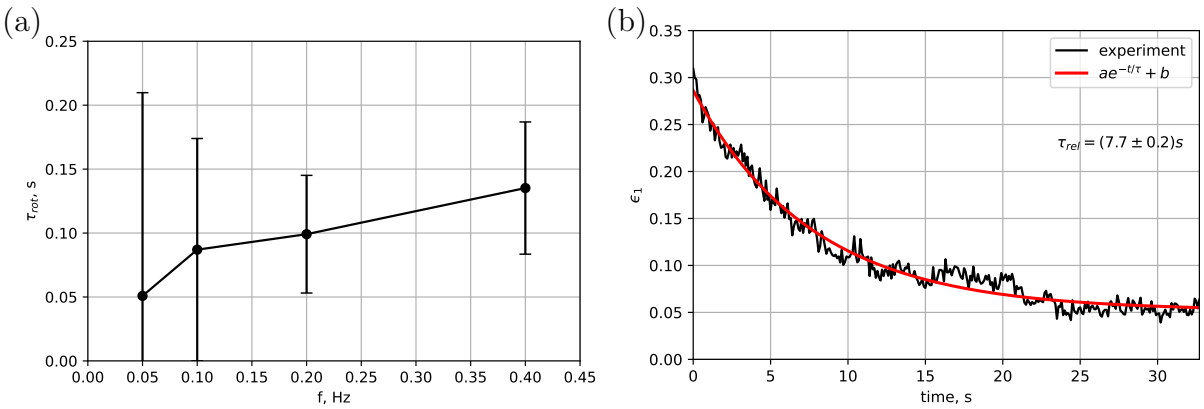

Figure 5.10: (a) the values of the small deformation decay time τ_{rot} as calculated from the equilibrium angles β^* in a rotating magnetic field for different rotation frequencies. (b) The relaxation of ϵ_1 when the magnetic field is turned off. The data points are fitted with a decaying exponential function to determine the small deformation decay time τ_{rel}. According to the small deformation theory, τ_{rot} should be equal to τ_{rel}.

permeability is $\mu_r = 34.8$, and having $R_0 = 7\ \mu m$, from (5.70) we get that the background field has a component in the plane of the image of approximately 96 μT. This parasitic field has a noticeable influence on the experimental results, since its roughly 19% of the rotating magnetic field strength.

According to the small deformation theory τ_{rot} should be equal to τ_{rel}, however experimentally there is a discrepancy of nearly two orders of magnitude. To see whether the magnetic field magnitude influences τ, another experiment was done, this time on a different droplet (droplet 2 in table 3) with radius $R_0 = 1.5\ \mu m$, which remained unchanged during the whole experiment. The droplet was elongated by applying stationary magnetic field $\mu_0 H_\infty = 466\ \mu T$, and the droplet exponentially approached the elongated shape ($\epsilon_1^* = 0.075 \pm 0.001$) with the characteristic time $\tau = (6.65 \pm 0.02)s$. Then the field was turned off and the droplet relaxed to a nearly spherical shape ($\epsilon_1^* = 0.0083 \pm 0.0002$) with the characteristic time $\tau = (4.02 \pm 0.02)s$. While the influence of magnetic field on the characteristic time τ cannot be ruled out, the difference in the last experiment was nowhere close to the difference between τ_{rot} and τ_{rel}. Furthermore, in the last experiment, the existence of the magnetic field resulted in a slightly increased τ - the opposite was true for the rotating field.

There are not many experimental works that quantitatively examine the motion of a single magnetic droplet in a weak rotating field. One such experiment was done in [92], where a mineral oil ferrofluid droplet (droplet 3 in table 3) with $\mu_r = 4.5$ was suspended in a glycerol-water mixture of the same density. The paper reports the viscosity of the ferrofluid of $\eta^{(i)} = 3\ mPa \cdot s$ and the external viscosity $\eta^{(e)} = 120.6\ mPa \cdot s$, which means

that $\lambda = 0.025$. The surface tension is reported to be around $\gamma = 2.5\ mN/m$, the external field used was $\mu_0 H_\infty = 4.7\ mT$ and it was rotating with $f = 1\ Hz$. Examining the last frame of the figure 5 in [92], it was determined that the undeformed droplet's radius was around $R_0 = 0.55mm$, and the equilibrium elongation in this rotating field was $\epsilon_1^* = 0.55$. From these parameters, the magnetic Bond number in the experiment was estimated to be $Bm = 48.5$, which according to the equation (5.70) means $\delta = 1.2$. From the theoretical equation (5.71) we get $\tau_{rel} = 16.4\ s$. However, using the expression for the equilibrium elongation ϵ_1^* in a rotating field (5.72), we get that $\tau_{rot} = 0.16\ s$, which again is two orders of magnitude smaller than expected. Even though the small deformation theory is not precise in the case when $\delta > 0.3$, such a big discrepancy is unexpected.

	$\tau_{rel},\ s$	$\tau_{rot},\ s$
Droplet 1	7.7 ± 0.2	0.11 ± 0.03
Droplet 2 field on	6.65 ± 0.02	
Droplet 2 field off	4.02 ± 0.02	
Droplet 3	16.4 (theoretical)	0.16

Table 3: The characteristic small deformation decay time τ_{rel} as measured with the relaxation experiment using the formula (5.76), and τ_{rot} as measured from the droplet's equilibrium shape in a rotating field using the formulas (5.72).

5.6 Summary and discussion

We have solved the problem of a magnetic fluid droplet in a rotating field analytically in the limit of small deformations and weak field. In particular, the solution is found up to first order in ε and Bm. Comparison with numerical simulations show that the small deformation condition is valid when $\delta < 0.3$, where δ is the parameter expressed in the equation (5.70). In this limit, the shape of the droplet is governed by a system or three nonlinear differential equations (5.25). The qualitative behavior of the droplet is determined by a single dimensionless parameter $\tau\omega$ - the product of the characteristic small perturbation decay time and the angular frequency of the rotating field. $\tau\omega$ determines whether the droplet will undergo oscillations in shape as it settles to an equilibrium, and whether in equilibrium the droplet will be more flattened or more elongated.

Some interesting peculiarities in the solution can be seen. The system is completely dissipate, however, despite that in a rotating field there can be oscillations in the droplet's shape. A phase portrait of the droplet's shape parameters (figure 5.3) is similar to that

of a damped pendulum. This is the result of the interplay of two characteristic time scales: the small perturbation decay time τ and the half-period of the rotating magnetic field π/ω. In equilibrium, the droplets pseudo-rotate following the magnetic field. This apparent rotation produces zero torque on the surrounding fluid, and the motion is the result of surface deformations.

According to the small deformation theory, the value of the small deformation decay time τ should be the same in a rotating field and in a stationary or zero field. Experimentally the value τ_{rel} describing the exponential approach to the equilibrium shape is a couple of orders of magnitude larger than the τ_{rot} obtained from the equilibrium shape of the droplet in a rotating field. This indicates that the magnetic fluid model described in chapters 3.2 and 3.3, while able to qualitatively replicate the experiment, has a significant quantitative disagreement when a rotating field is applied. This disagreement seems to be there both for phase separated magnetic fluid droplets and ones obtained by introducing ferrofluid in an immiscible carrier fluid. Examining (5.71), it appears that in the rotating field the droplet seems to have effectively larger surface tension or smaller viscosity compared to a stationary or zero field. We can hypothesize some internal organization of the nanoparticles in the concentrated magnetic fluid droplet, which would not respond at the same time scale to a rotation and to a relaxation.

6 Boundary element calculations

6.1 Introduction

By formulating the problem in boundary integral form, we arrive at equations that only need to be evaluated on the droplet's surface. Numerically solving boundary integrals is the basis of the boundary element methods (BEM) [77, 78].

Some advantages of BEM is that the only domain that needs to be discretized is the droplet's surface. And in doing so, the problem is solved for infinite domain, since, as it will be shown, the velocity or the magnetic potential can be found anywhere by an integral on the surface. BEM is also well suited for free surface problems since the mesh can be moved with the calculated velocity, however some mesh upkeep is necessary. The complexity of the algorithm scales as $O(N^2)$, where N is the number of surface elements.

There also are some limitations to BEM. Most notably - the integral kernels contain singularities that need special care to be accurately numerically integrated. The discretized integrals form linear systems with dense matrices, which complicates their solution. BEM can only be used to solve linear differential equations that have known Green's functions. Fortunately in our case these limitations can be overcome.

BEM has already been proven useful in calculating the equilibrium shapes of magnetic fluid droplets in infinitely fast rotating fields, where the characteristic surface deformation time τ is much larger than the field rotation period [62]. In that work the authors assumed that the viscosity of the droplet is equal to that of the surrounding medium i.e. $\lambda = 1$, which significantly simplifies the equations. This does not impact the equilibrium shape, however, it does not allow for the calculation of the non-equilibrium dynamics of the droplets when $\lambda \neq 1$, which is often the case experimentally. BEM has been used to successfully calculate the dynamics of highly-deformed viscous non-magnetic droplets with $\lambda \neq 1$ in an external flow [79, 80, 81]. Here we expand the algorithm in [62] to be able to calculate the dynamics of the droplets when $\lambda \neq 1$. The code of the BEM simulation for calculating magnetic droplet dynamics is available in GitHub [119].

6.2 Integral representation of the magnetostatic problem

A Green's function Γ of the Laplace equation (3.6) satisfies the Laplace equation together with a point forcing term [77, 78]

$$\Delta\Gamma + \delta(\boldsymbol{x} - \boldsymbol{y}) = 0, \tag{6.1}$$

where δ is the 3D Dirac delta function, and the forcing is being done in point $\boldsymbol{y}$. For infinite domain, the Green function for the Laplace equation is [77, 78]

$$\Gamma(\boldsymbol{x}, \boldsymbol{y}) = \frac{1}{4\pi|\boldsymbol{X}|}, \tag{6.2}$$

where $\boldsymbol{X} = \boldsymbol{x} - \boldsymbol{y}$.

It is easy to see that any two twice differentiable functions ψ_1 and ψ_2 satisfy Green's second identity [78, 113]

$$\boldsymbol{\nabla} \cdot (\psi_1 \boldsymbol{\nabla}\psi_2 - \psi_2 \boldsymbol{\nabla}\psi_1) = \psi_1 \Delta\psi_2 - \psi_2 \Delta\psi_1. \tag{6.3}$$

If we set $\psi_2 = \psi$, where ψ is the magnetic potential that satisfies (3.6), and $\psi_1 = \Gamma$, we get

$$\boldsymbol{\nabla} \cdot (\Gamma \boldsymbol{\nabla}\psi - \psi \boldsymbol{\nabla}\Gamma) = \psi\Delta\Gamma = \psi\delta(\boldsymbol{x} - \boldsymbol{y}). \tag{6.4}$$

Integrating (6.4) over the droplet's volume $V^{(i)}$ and using the properties of the Dirac delta function and the divergence theorem ($\int_V \boldsymbol{\nabla} \cdot \boldsymbol{f} dV = \int_S \boldsymbol{f} \cdot \boldsymbol{n} dS$) we have [62, 78]

$$\int_S \Gamma(\boldsymbol{x}, \boldsymbol{y}) \boldsymbol{\nabla}_x \psi^{(i)}(\boldsymbol{x}) \cdot \boldsymbol{n}_{\boldsymbol{x}} dS_x - \int_S \psi^{(i)}(\boldsymbol{x}) \boldsymbol{\nabla}_x \Gamma(\boldsymbol{x}, \boldsymbol{y}) \cdot \boldsymbol{n}_{\boldsymbol{x}} dS_x = \begin{cases} \psi^{(i)}(\boldsymbol{y}), \text{ if } \boldsymbol{y} \in V^{(i)} \\ \dfrac{\psi^{(i)}(\boldsymbol{y})}{2}, \text{ if } \boldsymbol{y} \in S \\ 0, \text{ if } \boldsymbol{y} \in V^{(e)} \end{cases}, \tag{6.5}$$

where $\boldsymbol{n}_{\boldsymbol{x}} = \boldsymbol{n}(\boldsymbol{x})$ is the outward normal vector of the droplet, and index x in $\boldsymbol{\nabla}_x$ and dS_x denotes that the differentiation or integration is carried out with respect to $\boldsymbol{x}$. Special care should be taken in the case when $\boldsymbol{y} \in S$, which is further detailed in the appendix A.5. ψ is now $\psi^{(i)}$, since we integrated inside the droplet, $V^{(e)}$ is the volume outside the droplet and S is the droplet's surface.

Similarly, we integrate (6.4) over $V^{(e)}$ and using the divergence theorem rewrite it as a sum of integrals over the surface S of the droplet and a surface S_∞ far away from

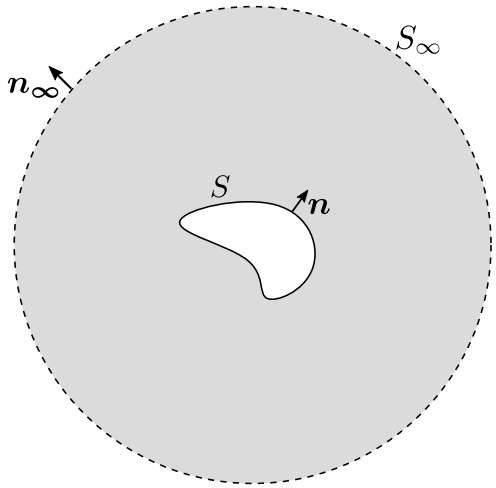

Figure 6.1: Sketch of the integration volume $V^{(e)}$ between the droplet S and a surface far away from the droplet S_∞.

the droplet (figure 6.1), where the perturbations in $\psi^{(e)}$ due to the droplet vanish (i.e. $\psi^{(e)} = \psi_\infty$ on S_∞)

$$\begin{aligned} &\int_{S_\infty} \Gamma(\boldsymbol{x},\boldsymbol{y})\boldsymbol{\nabla}_x\psi_\infty(\boldsymbol{x})\cdot\boldsymbol{n_{\infty x}}dS_x - \int_{S_\infty}\psi_\infty(\boldsymbol{x})\boldsymbol{\nabla}_x\Gamma(\boldsymbol{x},\boldsymbol{y})\cdot\boldsymbol{n_{\infty x}}dS_x + \\ &+\int_S \Gamma(\boldsymbol{x},\boldsymbol{y})\boldsymbol{\nabla}_x\psi^{(e)}(\boldsymbol{x})\cdot(-\boldsymbol{n_x})dS_x - \int_S \psi^{(e)}(\boldsymbol{x})\boldsymbol{\nabla}_x\Gamma(\boldsymbol{x},\boldsymbol{y})\cdot(-\boldsymbol{n_x})dS_x = \\ &= \begin{cases} 0, \text{ if } \boldsymbol{y}\in V^{(i)} \\ \dfrac{\psi^{(e)}(\boldsymbol{y})}{2}, \text{ if } \boldsymbol{y}\in S \\ \psi^{(e)}(\boldsymbol{y}), \text{ if } \boldsymbol{y}\in V^{(e)} \end{cases}, \end{aligned} \tag{6.6}$$

where again $\boldsymbol{n}_x$ is the outward normal vector of the droplet, $\psi = \psi^{(e)}$ since the integral was over $V^{(e)}$, and $\boldsymbol{n}_\infty$ is the outward normal from the integration volume on S_∞. The case when $\boldsymbol{y} \in S$ can be evaluated the similarly to equation (6.5). The integrals over S_∞ equal $\psi_\infty(\boldsymbol{y})$ as can be seen from (6.4) and the divergence theorem. This results in the equation for the external magnetic potential

$$\begin{aligned} &\psi_\infty(\boldsymbol{y}) - \int_S \Gamma(\boldsymbol{x},\boldsymbol{y})\boldsymbol{\nabla}_x\psi^{(e)}(\boldsymbol{x})\cdot\boldsymbol{n_x}dS_x + \int_S \psi^{(e)}(\boldsymbol{x})\boldsymbol{\nabla}_x\Gamma(\boldsymbol{x},\boldsymbol{y})\cdot\boldsymbol{n_x}dS_x = \\ &= \begin{cases} 0, \text{ if } \boldsymbol{y}\in V^{(i)} \\ \dfrac{\psi^{(e)}(\boldsymbol{y})}{2}, \text{ if } \boldsymbol{y}\in S \\ \psi^{(e)}(\boldsymbol{y}), \text{ if } \boldsymbol{y}\in V^{(e)} \end{cases}. \end{aligned} \tag{6.7}$$

If we know the distribution of ψ and $\boldsymbol{n}\cdot\boldsymbol{\nabla}\psi$ (either internal or external, since we can

get the other one from the boundary conditions (3.7), (3.8)) on the droplet's surface, we can use the equations (6.5) and (6.7) to calculate the magnetic potential in any point in the space inside and outside the droplet, respectively.

6.2.1 Boundary integral equation for the magnetic potential

Now we look at the case when $\boldsymbol{y} \in S$. Multiplying (6.5) by μ_r, adding (6.7) to it and taking into account the boundary conditions (3.7), (3.8), after rearrangement we can write a boundary integral equation for the magnetic potential ψ on the droplet's surface [62]

$$\psi(\boldsymbol{y}) = \frac{2\psi_\infty(\boldsymbol{y})}{\mu_r + 1} - 2\frac{\mu_r - 1}{\mu_r + 1}\int_S \psi(\boldsymbol{x})\boldsymbol{\nabla}_x\Gamma(\boldsymbol{x}, \boldsymbol{y}) \cdot \boldsymbol{n}_{\boldsymbol{x}} dS_x. \tag{6.8}$$

On the surface $\psi^{(e)} = \psi^{(i)}$, hence the suffixes are omitted.

The integrand in (6.8) scales as $O(|\boldsymbol{X}|^{-1})$ as $\boldsymbol{x} \to \boldsymbol{y}$, which can be seen by expanding $\boldsymbol{\nabla}_x\Gamma(\boldsymbol{x}, \boldsymbol{y}) \cdot \boldsymbol{n}_{\boldsymbol{x}}$ in Taylor series for small $\boldsymbol{X}$ in a local coordinate system centered on $\boldsymbol{y}$ (figure 6.2). $\psi(x)$ is assumed to scale as $O(1)$ as $\boldsymbol{x} \to \boldsymbol{y}$. It is worth remembering that $\boldsymbol{X} \cdot \boldsymbol{n}_{\boldsymbol{x}} = O(|\boldsymbol{X}|^2)$ as $\boldsymbol{x} \to \boldsymbol{y}$. Integrating over an area, the $O(|\boldsymbol{X}|^{-1})$ singularity is considered weak since the integral is convergent [120], as can be seen by integrating the singular region in local coordinates centered on the singular point: a term proportional to $|\boldsymbol{X}|$ arises from the differential area, which cancels out the singularity.

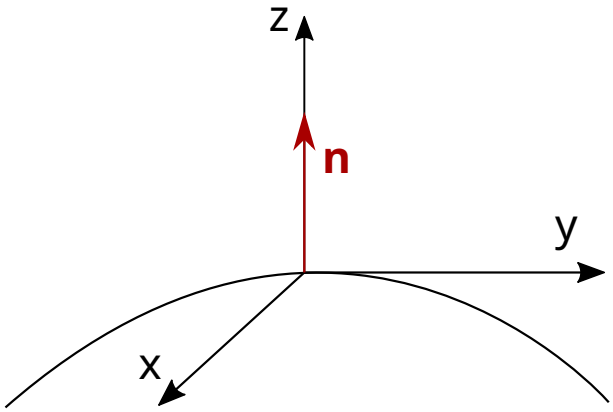

Figure 6.2: Local coordinates of a given point on the droplet surface have the z axis pointing in the direction of the normal of the droplet and the origin laying on top of the surface. Close to the origin, the droplet's shape is a paraboloid $z = f(x, y) = Ax^2 + Bxy + Cy^2$. The radius vector becomes $\boldsymbol{x}(x, y) = x\boldsymbol{e}_x + y\boldsymbol{e}_y + f(x, y)\boldsymbol{e}_z$, and the normal vector and curvature can be found from differentiation of $f(x, y)$.

Nonetheless, it's possible to get rid of the singular behavior of the integral (6.8) all together to facilitate its numeric evaluation. We can use a technique called *singularity*

subtraction [62, 77, 121]. We use the identity

$$\int_S \boldsymbol{\nabla}_x \Gamma(\boldsymbol{x}, \boldsymbol{y}) \cdot \boldsymbol{n}_{\boldsymbol{x}} dS_x = -\frac{1}{2}, \tag{6.9}$$

whose derivation is in the appendix A.6. We multiply (6.9) by $2\psi(\boldsymbol{y})(\mu_r - 1)/(\mu_r + 1)$ and add it to the right-hand side of (6.8) and subtract $(-1/2)2\psi(\boldsymbol{y})(\mu_r - 1)/(\mu_r + 1)$ to maintain the equality.

After some algebraic manipulation we arrive at the regularized boundary integral equation for the magnetic potential

$$\psi(\boldsymbol{y}) = \psi_\infty(\boldsymbol{y}) - (\mu_r - 1) \int_S [\psi(\boldsymbol{x}) - \psi(\boldsymbol{y})] \boldsymbol{\nabla}_x \Gamma(\boldsymbol{x}, \boldsymbol{y}) \cdot \boldsymbol{n}_{\boldsymbol{x}} dS_x. \tag{6.10}$$

The integrand here scales as $O(1)$ as $\boldsymbol{x} \to \boldsymbol{y}$. It can be seen by noting that for smooth magnetic potential $\psi(\boldsymbol{x}) - \psi(\boldsymbol{y}) \approx [\nabla\psi]_{\boldsymbol{x}=\boldsymbol{y}} \cdot \boldsymbol{X}$, which scales as $O(|\boldsymbol{X}|)$ as $\boldsymbol{x} \to \boldsymbol{y}$.

6.2.2 Eigensolutions to the homogeneous boundary integral equation for the magnetic potential

The integral equation (6.8) can be written in the form

$$\psi(\boldsymbol{y}) = \frac{2\psi_\infty(\boldsymbol{y})}{\mu_r + 1} + 2\mathcal{M} \int_S \psi(\boldsymbol{x}) \boldsymbol{\nabla}_x \Gamma(\boldsymbol{x}, \boldsymbol{y}) \cdot \boldsymbol{n}_{\boldsymbol{x}} dS_x, \tag{6.11}$$

where $\mathcal{M} = -(\mu_r - 1)/(\mu_r + 1)$. It can be shown that when $\mathcal{M} = -1$, there exists a non-trivial solution for the homogeneous problem

$$\psi(\boldsymbol{y}) = 2\mathcal{M} \int_S \psi(\boldsymbol{x}) \boldsymbol{\nabla}_x \Gamma(\boldsymbol{x}, \boldsymbol{y}) \cdot \boldsymbol{n}_{\boldsymbol{x}} dS_x. \tag{6.12}$$

To see that, we multiply (6.9) by $-2C$, where C is a constant, to find

$$C = -2 \int_S C \boldsymbol{\nabla}_x \Gamma(\boldsymbol{x}, \boldsymbol{y}) \cdot \boldsymbol{n}_{\boldsymbol{x}} dS_x. \tag{6.13}$$

$\psi(\boldsymbol{y}) = C$ is a solution to (6.12) when $\mathcal{M} = -1$.

This makes the boundary integral equation (6.8) is ill-posed, when $\mathcal{M} = -1$, since an arbitrary constant can be added to the solution. In practice this means that when $\mu_r \gg 1$, a numerical error is introduced that changes the true solution to $\psi(\boldsymbol{y})$ by some small constant. If the boundary integral equation is solved iteratively by successive substitutions

$\psi^{(n+1)} = 2\psi_\infty/(\mu_r - 1) + \int_S \psi^{(n)} \boldsymbol{\nabla}\Gamma \cdot \boldsymbol{n} dS$, it might not converge when $\mu_r \gg 1$ [77].

In our approach we do not solve the integral equation iteratively, and afterwards only the derivatives of $\psi(\boldsymbol{y})$ are used. Therefore, there is no need to remove the unwanted eigensolution to the homogeneous boundary integral equation. However, that will not be the case for the boundary integral equation of velocity, which we will examine in section 6.3.2.

6.2.3 Calculation of the magnetic field

To calculate the effective magnetic surface force (3.31), both the magnitude of normal $H_n^{(i)}$ and tangential $H_t^{(i)}$ magnetic field on the surface is necessary. Since in the numerical simulations the mesh is on the surface of the droplet, $H_t^{(i)}$ can be accurately calculated by numerical differentiation

$$\boldsymbol{H_t^{(i)}} = \mathbf{P}_\parallel \cdot \boldsymbol{\nabla}\psi, \tag{6.14}$$

where $\mathbf{P}_\parallel = \mathbf{I} - \boldsymbol{nn}$ is the operator for projecting a vector on the droplet surface.

To find $H_n^{(i)}$ once ψ is known, one can use (6.5) to get a boundary integral equation for the normal component of the magnetic field

$$\int_S H_n^{(i)}(\boldsymbol{x})\Gamma(\boldsymbol{x},\boldsymbol{y})dS_x = \frac{\psi(\boldsymbol{y})}{2} + \int_S \psi(\boldsymbol{x})\boldsymbol{\nabla}_x\Gamma(\boldsymbol{x},\boldsymbol{y}) \cdot \boldsymbol{n_x} dS_x, \tag{6.15}$$

however, it is a Fredholm integral equation of the first kind and their solutions are prone to errors [62, 77]. An intuition of why that is the case can be gleaned by the observation that if $H_n^{(i)}$ is a solution to (6.15), then so is $H_n^{(i)} + b$, provided that $\int_S b(\boldsymbol{x})\Gamma(\boldsymbol{x},\boldsymbol{y})dS_x = 0$. b could be a rapidly oscillating function, but whose integral is zero. Such a limitation is not experienced by (6.8), which is a Fredholm integral equation of the second kind for ψ [77]: ψ is both under the integral and directly added to the equation.

Therefore, different approach is used for finding $H_n^{(i)}$. Since there is a discontinuity in the magnetic field across the droplet boundary, it can be represented by an equivalent fictive surface current density $\boldsymbol{K}$ such that $\boldsymbol{B^{(e)}} - \boldsymbol{B^{(i)}} = \mu_0 \boldsymbol{K} \times \boldsymbol{n}$ [94]. Taking a cross product with $\boldsymbol{n}$ and noting that $\boldsymbol{K}$ is orthogonal to $\boldsymbol{n}$, we get on the surface

$$\boldsymbol{K} = \frac{1}{\mu_0}\boldsymbol{n} \times \left(\boldsymbol{B^{(e)}} - \boldsymbol{B^{(i)}}\right) = -\frac{\mu_r - 1}{\mu_0}\boldsymbol{n} \times \boldsymbol{B^{(e)}}, \tag{6.16}$$

where for the last equality we use the continuity of the tangential component of the $\boldsymbol{H}$ field: $\boldsymbol{n} \times \left(\boldsymbol{H^{(e)}} - \boldsymbol{H^{(i)}}\right) = \mathbf{0}$. This fictive surface current produces the perturbation in

the external magnetic field described by the Biot-Savart law [62, 94]

$$\boldsymbol{B}^{(e)}(\boldsymbol{y}) = \boldsymbol{B}_{\boldsymbol{\infty}}(\boldsymbol{y}) - \frac{\mu_0}{4\pi}\int_S \boldsymbol{K}(\boldsymbol{x}) \times \frac{\boldsymbol{X}}{|\boldsymbol{X}|^3} dS_x. \tag{6.17}$$

Plugging (6.16) into (6.17) and noting that $\boldsymbol{n} \times \boldsymbol{B}^{(e)} = \boldsymbol{n} \times \boldsymbol{B}_{\boldsymbol{t}}^{(e)}$, we get an equation for the magnetic field outside the droplet that only requires the knowledge of the tangential component of the field

$$\boldsymbol{B}^{(e)}(\boldsymbol{y}) = \boldsymbol{B}_{\boldsymbol{\infty}}(\boldsymbol{y}) - (\mu_r - 1)\int_S \left(\boldsymbol{n}_{\boldsymbol{x}} \times \boldsymbol{B}_{\boldsymbol{t}}^{(e)}(\boldsymbol{x})\right) \times \boldsymbol{\nabla}_x \Gamma(\boldsymbol{x}, \boldsymbol{y}) dS_x. \tag{6.18}$$

Letting $\boldsymbol{y}$ approach the droplet surface the expression becomes (derivation is in appendix A.7)

$$\boldsymbol{B}^{(e)}(\boldsymbol{y}) = \boldsymbol{B}_{\boldsymbol{\infty}}(\boldsymbol{y}) - (\mu_r - 1)\mathcal{P}\int_S \left(\boldsymbol{n}_{\boldsymbol{x}} \times \boldsymbol{B}_{\boldsymbol{t}}^{(e)}(\boldsymbol{x})\right) \times \boldsymbol{\nabla}_x \Gamma(\boldsymbol{x}, \boldsymbol{y}) dS_x - \frac{\mu_r - 1}{2}\boldsymbol{B}_{\boldsymbol{t}}^{(e)}(\boldsymbol{y}), \tag{6.19}$$

where $\mathcal{P}$ denotes the Cauchy principal value of the integral, which is needed to evaluate it, since the integrand is strongly singular: it scales as $O(|\boldsymbol{X}|^{-2})$ as $\boldsymbol{x} \to \boldsymbol{y}$, and the integral is therefore divergent. Multiplying by $\boldsymbol{n}_{\boldsymbol{y}}$ and switching to $\boldsymbol{H}^{(i)}$ we arrive at an expression to calculate $H_n^{(i)}$ knowing $\boldsymbol{H}_{\boldsymbol{t}}^{(i)}$

$$H_n^{(i)}(\boldsymbol{y}) = \frac{\boldsymbol{H}_{\boldsymbol{\infty}}(\boldsymbol{y}) \cdot \boldsymbol{n}_{\boldsymbol{y}}}{\mu_r} - \frac{\mu_r - 1}{\mu_r}\boldsymbol{n}_{\boldsymbol{y}} \cdot \mathcal{P}\int_S \left(\boldsymbol{n}_{\boldsymbol{x}} \times \boldsymbol{H}_{\boldsymbol{t}}^{(i)}(\boldsymbol{x})\right) \times \boldsymbol{\nabla}_x \Gamma(\boldsymbol{x}, \boldsymbol{y}) dS_x. \tag{6.20}$$

Calculating the Cauchy principal value is hard to do numerically, therefore to regularize (6.20), we first rewrite it using the Jacobi identity for the vector triple product $(\boldsymbol{n}_{\boldsymbol{x}} \times \boldsymbol{H}_{\boldsymbol{t}}) \times \boldsymbol{\nabla}\Gamma = \boldsymbol{n}_{\boldsymbol{x}} \times (\boldsymbol{H}_{\boldsymbol{t}} \times \boldsymbol{\nabla}\Gamma) - \boldsymbol{H}_{\boldsymbol{t}} \times (\boldsymbol{n}_{\boldsymbol{x}} \times \boldsymbol{\nabla}\Gamma)$, and we expand the first term on the right hand side as $\boldsymbol{n}_{\boldsymbol{x}} \times (\boldsymbol{H}_{\boldsymbol{t}} \times \boldsymbol{\nabla}\Gamma) = \boldsymbol{H}_{\boldsymbol{t}}(\boldsymbol{n}_{\boldsymbol{x}} \cdot \boldsymbol{\nabla}\Gamma) - \boldsymbol{\nabla}\Gamma(\boldsymbol{n}_{\boldsymbol{x}} \cdot \boldsymbol{H}_{\boldsymbol{t}})$. But we note that $\boldsymbol{n}_{\boldsymbol{x}} \cdot \boldsymbol{H}_{\boldsymbol{t}} = 0$. This leaves us with

$$\begin{aligned} H_n^{(i)}(\boldsymbol{y}) = &\frac{\boldsymbol{H}_{\boldsymbol{\infty}}(\boldsymbol{y}) \cdot \boldsymbol{n}_{\boldsymbol{y}}}{\mu_r} - \frac{\mu_r - 1}{\mu_r}\boldsymbol{n}_{\boldsymbol{y}} \cdot \mathcal{P}\int_S \Big[\\ &\boldsymbol{H}_{\boldsymbol{t}}^{(i)}(\boldsymbol{x})\left(\boldsymbol{n}_{\boldsymbol{x}} \cdot \boldsymbol{\nabla}_x \Gamma(\boldsymbol{x}, \boldsymbol{y})\right) - \boldsymbol{H}_{\boldsymbol{t}}^{(i)}(\boldsymbol{x}) \times \left(\boldsymbol{n}_{\boldsymbol{x}} \times \boldsymbol{\nabla}_x \Gamma(\boldsymbol{x}, \boldsymbol{y})\right)\Big] dS_x, \end{aligned} \tag{6.21}$$

where now singularity subtraction can be performed using the identities (6.9) and

$$\mathcal{P}\int_S \boldsymbol{n}_{\boldsymbol{x}} \times \boldsymbol{\nabla}_x \Gamma(\boldsymbol{x}, \boldsymbol{y}) dS_x = \boldsymbol{0}, \tag{6.22}$$

whose derivation is in the appendix A.8. After singularity subtraction, noting that $\boldsymbol{H_t^{(i)}}(\boldsymbol{y}) \cdot \boldsymbol{n_y} = 0$, we arrive at the regularized expression to calculate $H_n^{(i)}$

$$H_n^{(i)}(\boldsymbol{y}) = \frac{\boldsymbol{H_\infty}(\boldsymbol{y}) \cdot \boldsymbol{n_y}}{\mu_r} - \frac{\mu_r - 1}{\mu_r} \int_S \boldsymbol{n_y} \cdot \Bigg[\Big[\boldsymbol{H_t^{(i)}}(\boldsymbol{x}) - \boldsymbol{H_t^{(i)}}(\boldsymbol{y})\Big] (\boldsymbol{n_x} \cdot \boldsymbol{\nabla}_x \Gamma(\boldsymbol{x}, \boldsymbol{y})) - \Big[\boldsymbol{H_t^{(i)}}(\boldsymbol{x}) - \boldsymbol{H_t^{(i)}}(\boldsymbol{y})\Big] \times (\boldsymbol{n_x} \times \boldsymbol{\nabla}_x \Gamma(\boldsymbol{x}, \boldsymbol{y})) \Bigg] dS_x, \tag{6.23}$$

whose integrand now scales as $O(|\boldsymbol{X}|^{-1})$ when $\boldsymbol{x} \to \boldsymbol{y}$, and the integral converges.

6.2.4 Effective magnetic surface force of finitely and infinitely fast rotating magnetic field

When the external magnetic field $\boldsymbol{H}_\infty$ rotation frequency is finite, at each time step t the resulting field $\boldsymbol{H}(\boldsymbol{H}_\infty)$ is calculated for the background field pointing in the appropriate direction according to the formula

$$\boldsymbol{H}_\infty = H_\infty \cos(\omega t)\boldsymbol{e}_x + H_\infty \sin(\omega t)\boldsymbol{e}_y. \tag{6.24}$$

Afterwards, the effective magnetic surface force is found according to the formula (3.31) modified to use the pressure scale γ/R_0

$$f_M = \frac{\gamma}{R_0} \frac{Bm}{8\pi} (\mu_r - 1) \left(\mu_r \left(\frac{H_n^{(i)}(\boldsymbol{y})}{H_\infty} \right)^2 + \left(\frac{H_t^{(i)}(\boldsymbol{y})}{H_\infty} \right)^2 \right). \tag{6.25}$$

When the rotation period of the magnetic field is much shorter than the characteristic droplet shape perturbation time $2\pi/\omega \ll \tau$, the effective magnetic surface force can be averaged over the rotation period [62]. Due to the linearity of the magnetostatic problem, the resulting field follows the superposition principle

$$\boldsymbol{H}(\alpha \boldsymbol{a} + \beta \boldsymbol{b}) = \alpha \boldsymbol{H}(\boldsymbol{a}) + \beta \boldsymbol{H}(\boldsymbol{b}). \tag{6.26}$$

We set $\alpha = H_\infty \cos(\omega t)$, $\boldsymbol{a} = \boldsymbol{e}_x$, $\beta = H_\infty \sin(\omega t)$, $\boldsymbol{b} = \boldsymbol{e}_y$ to get

$$\boldsymbol{H}(\boldsymbol{H}_\infty) = H_\infty \cos(\omega t)\boldsymbol{H}(\boldsymbol{e}_x) + H_\infty \sin(\omega t)\boldsymbol{H}(\boldsymbol{e}_y). \tag{6.27}$$

Then the effective magnetic force becomes

$$f_M = \frac{\gamma}{R_0}\frac{Bm}{8\pi}(\mu_r - 1)\Big(\mu_r\left[\cos(\omega t)H_n(\boldsymbol{e}_x) + \sin(\omega t)H_n(\boldsymbol{e}_y)\right]^2 + \left[\cos(\omega t)H_t(\boldsymbol{e}_x) + \sin(\omega t)H_t(\boldsymbol{e}_y)\right]^2\Big). \tag{6.28}$$

Averaging over the rotation period $T = 2\pi/\omega$, we get the effective magnetic surface force for infinitely fast rotating field

$$\langle f_M\rangle = \frac{1}{T}\int_0^T f_M dt = \frac{\gamma}{R_0}\frac{Bm}{16\pi}(\mu_r - 1)\Big(\mu_r\left[H_n^2(\boldsymbol{e}_x) + H_n^2(\boldsymbol{e}_y)\right] + \left[H_t^2(\boldsymbol{e}_x) + H_t^2(\boldsymbol{e}_y)\right]\Big). \tag{6.29}$$

In summary, to calculate $\langle f_M\rangle$, we calculate the resulting field for two background fields $\boldsymbol{e}_x$ and $\boldsymbol{e}_y$ and then use the formula (6.29).

6.3 Integral representation of the hydrodynamic problem

Let us consider the Stokes equations with a point force acting on the fluid

$$-\boldsymbol{\nabla}p + \eta\Delta\boldsymbol{v} + \boldsymbol{b}\delta(\boldsymbol{x} - \boldsymbol{y}) = \boldsymbol{0}, \quad \boldsymbol{\nabla}\cdot\boldsymbol{v} = 0, \tag{6.30}$$

where $\boldsymbol{b}$ is an arbitrary constant vector describing the magnitude and direction of the force. Alternatively, using $\boldsymbol{\nabla}\cdot\boldsymbol{v} = 0$ and the definition of hydrodynamic stress $\sigma_{ij} = -\delta_{ij}p + \eta(\partial_j v_i + \partial_i v_j)$, we can write

$$\frac{\partial\sigma_{ij}}{\partial x_j} + b_i\delta(\boldsymbol{x} - \boldsymbol{y}) = 0 \tag{6.31}$$

The solution to (6.30) and (6.31) can be expressed through Green's function tensors G, $\boldsymbol{P}$ and T [77, 122]

$$v_i = \frac{1}{8\pi\eta}G_{ij}b_j, \quad p = \frac{1}{8\pi}P_j b_j, \quad \sigma_{ik} = \frac{1}{8\pi}T_{ijk}b_j \tag{6.32}$$

where the factors before the expressions are a matter of convention. The tensor T used in the expression for the hydrodynamic stress tensor is [77, 122]

$$T_{ijk} = -\delta_{ik}P_j + \frac{\partial G_{ij}}{\partial x_k} + \frac{\partial G_{kj}}{\partial x_i}. \tag{6.33}$$

In infinite domain the Green's function tensors are [77, 78, 122]

$$G_{ij}(\boldsymbol{x},\boldsymbol{y}) = \frac{\delta_{ij}}{|\boldsymbol{X}|} + \frac{X_i X_j}{|\boldsymbol{X}|^3}, \quad P_j(\boldsymbol{x},\boldsymbol{y}) = 2\frac{X_j}{|\boldsymbol{X}|^3}, \quad T_{ijk}(\boldsymbol{x},\boldsymbol{y}) = -6\frac{X_i X_j X_k}{|\boldsymbol{X}|^5}, \tag{6.34}$$

where it is reminded that $\boldsymbol{X} = \boldsymbol{x} - \boldsymbol{y}$. For infinite domain $\mathbf{G}$ is sometimes called the Stokeslet.

Two solutions $(\boldsymbol{v}, \boldsymbol{\sigma})$ and $(\boldsymbol{v}', \boldsymbol{\sigma}')$ for the Stokes flow satisfy the generalized Lorentz reciprocal identity [116] (derivation is in the appendix A.9)

$$\frac{\partial}{\partial x_k}(v_i'\sigma_{ik} - v_i\sigma_{ik}') = v_i'\frac{\partial \sigma_{ik}}{\partial x_k} - v_i\frac{\partial \sigma_{ik}'}{\partial x_k}. \tag{6.35}$$

Identifying $(\boldsymbol{v}', \boldsymbol{\sigma}')$ with the solution resulting from a point force acting on the fluid, and $(\boldsymbol{v}, \boldsymbol{\sigma})$ with the solution to the unforced Stokes equations, we get

$$\frac{\partial}{\partial x_k}\left(\frac{1}{8\pi\eta}G_{ij}b_j\sigma_{ik} - v_i\frac{1}{8\pi}T_{ijk}b_j\right) = v_i b_i \delta(\boldsymbol{x}-\boldsymbol{y}), \tag{6.36}$$

where we used (6.31) for the right-hand side. Since $\boldsymbol{b}$ is arbitrary, we have

$$\frac{1}{8\pi}\frac{\partial}{\partial x_j}\left(\frac{1}{\eta}G_{ik}\sigma_{ij} - v_i T_{ikj}\right) = v_k\delta(\boldsymbol{x}-\boldsymbol{y}). \tag{6.37}$$

Integrating (6.37) over the droplet's volume $V^{(i)}$ and using the properties of the Dirac delta function and the divergence theorem ($\int_V \boldsymbol{\nabla}\cdot\boldsymbol{f}dV = \int_S \boldsymbol{f}\cdot\boldsymbol{n}dS$) we have

$$\frac{1}{8\pi\eta^{(i)}}\int_S G_{ik}(\boldsymbol{x},\boldsymbol{y})\sigma_{ij}^{(i)}(\boldsymbol{x})n_{xj}dS_x - \frac{1}{8\pi}\int_S v_i^{(i)}(\boldsymbol{x})T_{ikj}(\boldsymbol{x},\boldsymbol{y})n_{xj}dS_x = \begin{cases} v_k^{(i)}(\boldsymbol{y}), \text{ if } \boldsymbol{y}\in V^{(i)} \\ \dfrac{v_k^{(i)}(\boldsymbol{y})}{2}, \text{ if } \boldsymbol{y}\in S \\ 0, \text{ if } \boldsymbol{y}\in V^{(e)} \end{cases}, \tag{6.38}$$

where the index x indicates that the normal vector is evaluated at point $\boldsymbol{x}$. The case when $\boldsymbol{y}\in S$ is looked at in the appendix A.10. Similarly we integrate (6.37) over $V^{(e)}$. Using the divergence theorem we rewrite the integral as a sum of integrals over the surface S of the droplet and a surface S_∞ far away from the droplet (figure 6.1). On the far away surface the perturbations in $\boldsymbol{v^{(e)}}$ and $\boldsymbol{\sigma^{(e)}}$ due to the droplet vanish (i.e. $\boldsymbol{v^{(e)}} = \boldsymbol{v_\infty}$ and

$\boldsymbol{\sigma^{(e)}} = \boldsymbol{\sigma_\infty}$ on S_∞). We get

$$\begin{aligned}
&\frac{1}{8\pi\eta^{(e)}}\int_{S_\infty} G_{ik}(\boldsymbol{x},\boldsymbol{y})\sigma_{\infty ij}(\boldsymbol{x})n_{\infty xj}dS_x - \frac{1}{8\pi}\int_{S_\infty} v_{\infty i}(\boldsymbol{x})T_{ikj}(\boldsymbol{x},\boldsymbol{y})n_{\infty xj}dS_x + \\
&+\frac{1}{8\pi\eta^{(e)}}\int_S G_{ik}(\boldsymbol{x},\boldsymbol{y})\sigma^{(e)}_{ij}(\boldsymbol{x})(-n_{xj})dS_x - \frac{1}{8\pi}\int_S v^{(e)}_i(\boldsymbol{x})T_{ikj}(\boldsymbol{x},\boldsymbol{y})(-n_{xj})dS_x = \\
&= \begin{cases} 0, \text{ if } \boldsymbol{y} \in V^{(i)} \\ \dfrac{v^{(e)}_k(\boldsymbol{y})}{2}, \text{ if } \boldsymbol{y} \in S \\ v^{(e)}_k(\boldsymbol{y}), \text{ if } \boldsymbol{y} \in V^{(e)} \end{cases} .
\end{aligned} \tag{6.39}$$

Since $\boldsymbol{n}$ is the outward normal of the droplet, and it is pointing inside the integration volume, a minus sign is in front of it. The case when $\boldsymbol{y} \in S$ was evaluated similarly as in (6.38). The integrals over S_∞ equal $v_{\infty k}(\boldsymbol{y})$ as can be seen from (6.37) and the divergence theorem. This results in the equation for the external velocity field

$$\begin{aligned}
&v_{\infty k}(\boldsymbol{y}) - \frac{1}{8\pi\eta^{(e)}}\int_S G_{ik}(\boldsymbol{x},\boldsymbol{y})\sigma^{(e)}_{ij}(\boldsymbol{x})n_{xj}dS_x + \frac{1}{8\pi}\int_S v^{(e)}_i(\boldsymbol{x})T_{ikj}(\boldsymbol{x},\boldsymbol{y})n_{xj}dS_x = \\
&= \begin{cases} 0, \text{ if } \boldsymbol{y} \in V^{(i)} \\ \dfrac{v^{(e)}_k(\boldsymbol{y})}{2}, \text{ if } \boldsymbol{y} \in S \\ v^{(e)}_k(\boldsymbol{y}), \text{ if } \boldsymbol{y} \in V^{(e)} \end{cases} .
\end{aligned} \tag{6.40}$$

If we know the distribution of $\boldsymbol{v}$ and $\boldsymbol{\sigma}$ on the droplet's surface, we can calculate the velocity anywhere in the surrounding fluid or inside the droplet by the use of equations (6.38) and (6.40).

6.3.1 Boundary integral equation for the velocity

We observe the case when $\boldsymbol{y} \in S$. Multiplying (6.38) by $\eta^{(i)}$ and (6.40) by $\eta^{(e)}$ and adding them, after some algebraic manipulation we arrive at the boundary integral equation for the surface velocity of the droplet

$$\begin{aligned}
v_k(\boldsymbol{y}) = &\frac{2}{1+\lambda}v_{\infty k}(\boldsymbol{y}) \\
&+ \frac{1}{1+\lambda}\frac{1}{4\pi\eta^{(e)}}\int_S f_M(\boldsymbol{x})G_{ik}(\boldsymbol{x},\boldsymbol{y})n_{xi}dS_x \\
&- \frac{1}{1+\lambda}\frac{\gamma}{4\pi\eta^{(e)}}\int_S \left(k_1(\boldsymbol{x})+k_2(\boldsymbol{x})\right)G_{ik}(\boldsymbol{x},\boldsymbol{y})n_{xi}dS_x \\
&+ \frac{1-\lambda}{1+\lambda}\frac{1}{4\pi}\int_S v_i(\boldsymbol{x})T_{ikj}(\boldsymbol{x},\boldsymbol{y})n_{xj}dS_x,
\end{aligned} \tag{6.41}$$

where we remind that λ is the ratio of internal to external viscosity. We used the dynamic boundary conditions (3.30) and (3.32) to rewrite the stress difference across the boundary in terms of the effective magnetic force and the capillary force

$$(\boldsymbol{\sigma}^{(e)} - \boldsymbol{\sigma}^{(i)}) \cdot \boldsymbol{n} + f_M \boldsymbol{n} - \gamma(k_1 + k_2)\boldsymbol{n} = \boldsymbol{0}. \tag{6.42}$$

All the integrands in (6.41) scale as $O(|\boldsymbol{X}|^{-1})$ as $\boldsymbol{x} \to \boldsymbol{y}$, therefore the integrals converge.

6.3.2 Eigensolutions to the homogeneous boundary integral equation for the velocity

The integral equation (6.41) can be rewritten as

$$v_k(\boldsymbol{y}) = F_k(\boldsymbol{y}) + \kappa \frac{1}{4\pi} \int_S v_i(\boldsymbol{x}) T_{ikj}(\boldsymbol{x}, \boldsymbol{y}) n_{xj} dS_x, \tag{6.43}$$

where all the terms not containing the velocity are inside the forcing function $\boldsymbol{F}$ and $\kappa = (1-\lambda)/(1+\lambda)$. It is known [77, 116, 122, 123] that for $\kappa = 1$ and $\kappa = -1$ there exist non-trivial solutions for the homogeneous problem

$$v_k(\boldsymbol{y}) = \kappa \frac{1}{4\pi} \int_S v_i(\boldsymbol{x}) T_{ikj}(\boldsymbol{x}, \boldsymbol{y}) n_{xj} dS_x. \tag{6.44}$$

This makes the boundary integral equation ill-posed when $\kappa = \pm 1$, since an arbitrary multiple of the solution to (6.44) can be added to the solution of (6.43). In practice this introduces errors in numerical solutions when $\lambda \ll 1$ and $\lambda \gg 1$ and solving for $\boldsymbol{v}$ by iterative substitutions $v_k^{(n+1)} = F_k + \kappa/(4\pi) \int_S v_i^{(n)} T_{ikj} n_j dS_x$ might not converge [77]. This is significant for our case since experimentally λ for magnetic droplets can be as large as 1400 (section 4.4.5, [62]) and as small as 0.025 [92].

To arrive at the eigensolution corresponding for $\kappa = -1$, let us examine the integral representation of the velocity inside the droplet (6.38), when $\boldsymbol{y} \in S$

$$v_k^{(i)}(\boldsymbol{y}) = \frac{1}{4\pi\eta^{(i)}} \int_S G_{ik}(\boldsymbol{x}, \boldsymbol{y}) \sigma_{ij}^{(i)}(\boldsymbol{x}) n_{xj} dS_x - \frac{1}{4\pi} \int_S v_i^{(i)}(\boldsymbol{x}) T_{ikj}(\boldsymbol{x}, \boldsymbol{y}) n_{xj} dS_x. \tag{6.45}$$

Clearly (6.44) would be satisfied by such a flow $v_k^{(i)}$, whose corresponding hydrodynamic stress tensor satisfies $\int_S G_{ik} \sigma_{ij}^{(i)} n_j dS_x = 0$. One such flow is the solid body motion

$$\boldsymbol{v} = \boldsymbol{V} + \boldsymbol{\Omega} \times \boldsymbol{x}, \tag{6.46}$$

where $\boldsymbol{V}$ and $\boldsymbol{\Omega}$ are arbitrary constant vectors. For solid body motion, the stress tensor is $\sigma_{ij} = -p\delta_{ij}$, where p is just a constant pressure. Using the identity (proof is in appendix A.11)

$$\int_S G_{ik}(\boldsymbol{x}, \boldsymbol{y}) n_{xi} dS_x = 0, \tag{6.47}$$

we see that indeed for solid body motion $\int_S G_{ik}\sigma^{(i)}_{ij} n_j dS_x = 0$ and it is an eigensolution for $\kappa = -1$ or $\lambda \to \infty$.

Next, to get the eigensolution for $\kappa = 1$, we examine the integral representation of the velocity outside the droplet (6.40), when $\boldsymbol{y} \in S$. We set $\boldsymbol{v}_\infty = \boldsymbol{0}$

$$v^{(e)}_k(\boldsymbol{y}) = -\frac{1}{4\pi\eta^{(e)}} \int_S G_{ik}(\boldsymbol{x}, \boldsymbol{y}) \sigma^{(e)}_{ij}(\boldsymbol{x}) n_{xj} dS_x + \frac{1}{4\pi} \int_S v^{(e)}_i(\boldsymbol{x}) T_{ikj}(\boldsymbol{x}, \boldsymbol{y}) n_{xj} dS_x. \tag{6.48}$$

The solid body motion is not an eigensolution for this case, since we require that the velocity decays to zero far away from the surface. A flow that is an eigensolution is the expansion or contraction of the surface, i.e. a flow in the direction of the surface normal

$$\boldsymbol{v} = C\boldsymbol{n}, \tag{6.49}$$

where C is a constant. Let us now illustrate that it indeed is the case. The flow rate through the droplet's surface is

$$Q = \int_S \boldsymbol{v} \cdot \boldsymbol{n} dS = CS, \tag{6.50}$$

Viewing from far away, the flow due to the droplet can be represented as a flow arising from a point source [124],

$$\boldsymbol{v_\infty} = \frac{Q}{4\pi} \frac{\boldsymbol{x}}{x^3}, \quad p_\infty = 0, \quad \boldsymbol{\sigma_\infty} = 2\eta^{(e)} \left(\frac{\mathbf{I}}{x^3} - 3\frac{\boldsymbol{x}\boldsymbol{x}}{x^5} \right), \tag{6.51}$$

where $\boldsymbol{x}$ here is the radius vector originating from the droplet. As $x \to \infty$, the velocity indeed vanishes, but now we see the asymptotic behavior. In absence of force sources, the force transmitted through any closed surface is the same and we have

$$\int_S \sigma^{(e)}_{ij}(\boldsymbol{x}) n_{xj} dS_x = \int_{S_\infty} \sigma_{\infty ij}(\boldsymbol{x}) n_{xj} dS_x = 0, \tag{6.52}$$

since $S_\infty \propto x^2$, but $\boldsymbol{\sigma_\infty} \propto x^{-3}$. But for such a flow ($\boldsymbol{v} = C\boldsymbol{n}$), on the surface S we have $(\partial_j v_i + \partial_i v_j) n_j = 0$. This can be seen since $(\partial_i n_j) n_j = \partial_i (n_j n_j)/2 = 0$, and since the normal

vector is a gradient of a level surface[2] $\boldsymbol{n} = \boldsymbol{\nabla} f$, then $(\partial_j n_i) n_j = (\partial^2_{ij} f) n_j = (\partial_i n_j) n_j = 0$. But that means (6.52) becomes

$$\int_S p^{(e)}(\boldsymbol{x}) n_{xi} dS_x = 0 \implies p^{(e)}|_{x \in S} = const. \tag{6.53}$$

And therefore $\int_S G_{ik}(\boldsymbol{x}, \boldsymbol{y}) \sigma^{(e)}_{ij}(\boldsymbol{x}) n_{xj} dS_x = const \int_S G_{ik}(\boldsymbol{x}, \boldsymbol{y}) n_{xi} dS_x = 0$, which means that flow proportional to the surface normal vector is a solution to the homogeneous problem (6.44) to for $\kappa = 1$ or $\lambda = 0$.

6.3.3 Wielandt's deflation

It is possible to formulate an equivalent problem to (6.41) that has the unwanted eigenvalues and eigensolutions removed. This is done by a technique called Wielandt's deflation [77, 116, 123]. Similarly how it is done in [77], we will illustrate the idea of Wielandt's deflation by drawing parallels with linear algebra.

A corresponding problem to the integral equation (6.41) is

$$x_i = \kappa A_{ij} x_j + b_i, \tag{6.54}$$

where $\boldsymbol{x}$ is the vector to be solved for, $\mathbf{A}$ is a given matrix, $\boldsymbol{b}$ is a given vector and κ is a given number. Let matrix $\mathbf{A}$ have an eigenvalue λ and the corresponding eigenvector $\boldsymbol{z}$, i.e. $A_{ij} z_j = \lambda z_i$. Then if $\kappa \approx 1/\lambda$, the solution to the equation (6.54) can be approximately augmented by a multiple of $\boldsymbol{z}$, which leads to poor convergence.

Let us consider a "deflated" matrix $B_{ij} = A_{ij} - \lambda z_i z_j / |\boldsymbol{z}|^2$. We can verify that for this matrix, the eigenvalue for $\boldsymbol{z}$ is set to zero

$$B_{ij} z_j = A_{ij} z_j - \lambda z_i \frac{z_j}{|\boldsymbol{z}|^2} z_j = \lambda z_i - \lambda z_i = 0. \tag{6.55}$$

With this matrix, the equation (6.54) becomes

$$x_i - \frac{\lambda \kappa \boldsymbol{x} \cdot \boldsymbol{z}}{|\boldsymbol{z}|^2} z_i = \kappa B_{ij} x_j + b_i, \tag{6.56}$$

[2] If the droplet's boundary is a level surface $\zeta(\boldsymbol{x}) = 0$, then the normal vector is $\boldsymbol{n} = \boldsymbol{\nabla}\zeta / |\boldsymbol{\nabla}\zeta|$. But we can construct another function $f = \zeta / |\boldsymbol{\nabla}\zeta|$. $f = 0$ clearly still describes the droplet's boundary, and we have $\boldsymbol{\nabla} f = \boldsymbol{\nabla}\zeta / |\boldsymbol{\nabla}\zeta| + \zeta \boldsymbol{\nabla}(|\boldsymbol{\nabla}\zeta|^{-1}) = \boldsymbol{n}$, since the second term vanishes on the surface.

Since $B_{ij}z_j = 0$, we are motivated to introduce a new unknown vector $\boldsymbol{y}$

$$y_i = x_i - \frac{\lambda\kappa \boldsymbol{x}\cdot\boldsymbol{z}}{|\boldsymbol{z}|^2} z_i = x_i - \lambda\kappa x_i', \tag{6.57}$$

where with "prime" we denote the projection $\boldsymbol{x}' = \boldsymbol{z}(\boldsymbol{x}\cdot\boldsymbol{z})/(\boldsymbol{z}\cdot\boldsymbol{z})$ on the eigenvector $\boldsymbol{z}$. The equation (6.56) then becomes

$$\begin{gathered} y_i = \kappa B_{ij} y_j + b_i, \\ \text{or} \\ y_i = \kappa A_{ij} y_j - \lambda\kappa y_i' + b_i. \end{gathered} \tag{6.58}$$

Scalar multiplying $\boldsymbol{z}$ with (6.57), we get $\boldsymbol{x}\cdot\boldsymbol{z} = \boldsymbol{y}\cdot\boldsymbol{z} + \lambda\kappa\boldsymbol{x}\cdot\boldsymbol{z}$. Expressing $\boldsymbol{x}\cdot\boldsymbol{z}$ and plugging it back into (6.57) we get an equation to retrieve $\boldsymbol{x}$ once $\boldsymbol{y}$ is found

$$x_i = y_i + \frac{\lambda\kappa}{1-\lambda\kappa}\frac{\boldsymbol{y}\cdot\boldsymbol{z}}{|\boldsymbol{z}|^2} z_i = y_i + \frac{\lambda\kappa}{1-\lambda\kappa} y_i' \tag{6.59}$$

The "deflated" equation (6.58) is no longer ill-posed when $\kappa \approx 1/\lambda$ and can accurately be solved numerically for $\boldsymbol{y}$. Afterwards, the original unknown $\boldsymbol{x}$ can be found (6.59). This deflation should be done for each eigenvector and eigenvalue that would hinder accurate solution of (6.54).

Analogously, for boundary integral equations we can use a similar procedure. In vector function space, the scalar product is defined as [77]

$$(\boldsymbol{u}, \boldsymbol{v}) = \int_S \boldsymbol{u}(\boldsymbol{x})\cdot\boldsymbol{v}(\boldsymbol{x}) dS_x. \tag{6.60}$$

Instead of solving for $\boldsymbol{v}$ using (6.41), we first solve for an auxiliary field $\boldsymbol{w}$ using a "deflated" boundary integral equation (analogous to (6.58))

$$w_k(\boldsymbol{y}) = F_k(\boldsymbol{y}) + \kappa\frac{1}{4\pi}\int_S w_i(\boldsymbol{x}) T_{ikj}(\boldsymbol{x},\boldsymbol{y}) n_{xj} dS_x - \kappa w_k'^{(1)}(\boldsymbol{y}) + \kappa w_k'^{(-1)}(\boldsymbol{y}), \tag{6.61}$$

where now $\kappa = (1-\lambda)(1+\lambda)$, λ is the viscosity ratio, and $\boldsymbol{F}(\boldsymbol{y})$ (analogous to b_i) is the forcing function - it contains all the terms without $\boldsymbol{v}$ in (6.41).

$\boldsymbol{w}'^{(1)}$ is the projection of $\boldsymbol{w}$ onto the eigensolution $C\boldsymbol{n}$ with the eigenvalue 1

$$\boldsymbol{w}'^{(1)}(\boldsymbol{y}) = \boldsymbol{n}_y \frac{(\boldsymbol{w},\boldsymbol{n})}{(\boldsymbol{n},\boldsymbol{n})} = \frac{\boldsymbol{n}_y}{S}\int_S \boldsymbol{w}(\boldsymbol{x})\cdot\boldsymbol{n}_x dS_x, \tag{6.62}$$

where we noticed that the constant C does not influence the projection.

$\boldsymbol{w}'^{(-1)}$ is the projection of $\boldsymbol{w}$ onto the eigensolution of rigid body motion $\boldsymbol{V} + \boldsymbol{\Omega} \times \boldsymbol{x}$ with the eigenvalue -1. A simple way to find it was given by [123]. Here we show a marginally even simpler way. Let us look at the translation and rotation separately

$$\boldsymbol{w}'^{(-1)} = \boldsymbol{w}'^{(t)} + \boldsymbol{w}'^{(r)}. \tag{6.63}$$

First, the projection on the translational motion is

$$\boldsymbol{w}'^{(t)}(\boldsymbol{y}) = \hat{\boldsymbol{V}} \frac{(\boldsymbol{w}, \hat{\boldsymbol{V}})}{(\hat{\boldsymbol{V}}, \hat{\boldsymbol{V}})} = \frac{\hat{\boldsymbol{V}}}{S} \hat{\boldsymbol{V}} \cdot \int_S \boldsymbol{w}(\boldsymbol{x}) dS_x, \tag{6.64}$$

where $\hat{\boldsymbol{V}}$ is an arbitrary constant unit vector. There are three linearly independent possibilities for $\hat{\boldsymbol{V}}$, all of which should be spanned for the full projection to the translational motion. Choosing $\hat{\boldsymbol{V}}$ to be the unit basis vectors $\boldsymbol{e}_x$, $\boldsymbol{e}_y$ and $\boldsymbol{e}_z$, we see that the full projection is

$$\boldsymbol{w}'^{(t)}(\boldsymbol{y}) = \frac{1}{S} \int_S \boldsymbol{w}(\boldsymbol{x}) dS_x. \tag{6.65}$$

Next we consider the projection on the rotational motion

$$\begin{aligned} \boldsymbol{w}'^{(r)}(\boldsymbol{y}) &= \hat{\boldsymbol{\Omega}} \times \boldsymbol{y} \frac{(\boldsymbol{w}, \hat{\boldsymbol{\Omega}} \times \boldsymbol{x})}{(\hat{\boldsymbol{\Omega}} \times \boldsymbol{x}, \hat{\boldsymbol{\Omega}} \times \boldsymbol{x})} \\ &= \left(\frac{\hat{\boldsymbol{\Omega}}}{\int_S |\boldsymbol{x}|^2 dS_x - \int_S (\hat{\boldsymbol{\Omega}} \cdot \boldsymbol{x})^2 dS_x} \hat{\boldsymbol{\Omega}} \cdot \int_S \boldsymbol{x} \times \boldsymbol{w}(\boldsymbol{x}) dS_x \right) \times \boldsymbol{y}, \end{aligned} \tag{6.66}$$

where again $\hat{\boldsymbol{\Omega}}$ is an arbitrary constant unit vector, and we arrived at the expression on the right hand side after some algebraic manipulation of vector products. Again there are three linearly independent choices of $\hat{\boldsymbol{\Omega}}$. Setting them to $\boldsymbol{e}_x$, $\boldsymbol{e}_y$ and $\boldsymbol{e}_z$, we arrive at the full projection on the rotational motion

$$\boldsymbol{w}'^{(r)}(\boldsymbol{y}) = \boldsymbol{\Omega}^{(w)} \times \boldsymbol{y}, \tag{6.67}$$

where

$$\boldsymbol{\Omega}^{(w)} = \mathbf{M} \cdot \int_S \boldsymbol{x} \times \boldsymbol{w}(\boldsymbol{x}) dS_x, \tag{6.68}$$

and $\mathbf{M}$ is a diagonal matrix

$$\mathbf{M} = \operatorname{diag} \left(\frac{1}{\int_S |\boldsymbol{x}|^2 dS_x - \int_S (\boldsymbol{e_i} \cdot \boldsymbol{x})^2 dS_x} \right), \quad i = 1 \ldots 3, \tag{6.69}$$

where $\boldsymbol{e_i}$ takes up the values $\boldsymbol{e}_x$, $\boldsymbol{e}_y$ and $\boldsymbol{e}_z$.

Once we have solved the "deflated" boundary integral equation (6.61), we find the velocity field by an analogous formula to (6.59)

$$\boldsymbol{v}(\boldsymbol{y}) = \boldsymbol{w}(\boldsymbol{y}) + \frac{\kappa}{1-\kappa}\frac{\boldsymbol{n}_y}{S}\int_S \boldsymbol{w}(\boldsymbol{x})\cdot\boldsymbol{n}_x dS_x - \frac{\kappa}{1+\kappa}\boldsymbol{w}'^{(-1)}(\boldsymbol{y}). \tag{6.70}$$

But since we require for $\boldsymbol{\nabla}\cdot\boldsymbol{v} = 0$, the term proportional to $\boldsymbol{n}_y$ should vanish, leaving us with

$$\boldsymbol{v}(\boldsymbol{y}) = \boldsymbol{w}(\boldsymbol{y}) - \frac{\kappa}{1+\kappa}\boldsymbol{w}'^{(-1)}(\boldsymbol{y}). \tag{6.71}$$

6.3.4 Regularization of singular integrals

There are several integrals in the "deflated" boundary integral equation (6.61) that scale as $O(|\boldsymbol{X}|^{-1})$ as $\boldsymbol{x}\to\boldsymbol{y}$. However it is possible to remove these singularities to facilitate their numerical evaluation.

Using the identity (6.47) multiplied with $f_M(\boldsymbol{y})$, we see that the following is true

$$\int_S f_M(\boldsymbol{x})G_{ik}(\boldsymbol{x},\boldsymbol{y})n_{xi}dS_x = \int_S [f_M(\boldsymbol{x}) - f_M(\boldsymbol{y})]G_{ik}(\boldsymbol{x},\boldsymbol{y})n_{xi}dS_x, \tag{6.72}$$

where the left-hand side integral has a $O(|\boldsymbol{X}|^{-1})$ singularity, but the right-hand side integral has a $O(1)$ behavior as $\boldsymbol{x}\to\boldsymbol{y}$.

Next, we can also subtract the singularity from the $\mathbf{T}$ integral by using the identity[77] (derivation is in the appendix A.12)

$$\int_S T_{ijk}(\boldsymbol{x},\boldsymbol{y})n_{xk}dS_x = \begin{cases} -8\pi\delta_{ij}, \text{ if } \boldsymbol{y}\in V^{(i)} \\ -4\pi\delta_{ij}, \text{ if } \boldsymbol{y}\in S \\ 0, \text{ if } \boldsymbol{y}\in V^{(e)} \end{cases}, \tag{6.73}$$

where we take the case when $\boldsymbol{y}\in S$.

$$\int_S w_i(\boldsymbol{x})T_{ikj}(\boldsymbol{x},\boldsymbol{y})n_{xj}dS_x = \int_S [w_i(\boldsymbol{x}) - w_i(\boldsymbol{y})]\,T_{ikj}(\boldsymbol{x},\boldsymbol{y})n_{xj}dS_x - 4\pi w_k(\boldsymbol{y}), \tag{6.74}$$

where again the left-hand side integral has a $O(|\boldsymbol{X}|^{-1})$ singularity, but the right-hand side integral has a $O(1)$ behavior as $\boldsymbol{x}\to\boldsymbol{y}$.

6.3.5 Removal of curvature from the boundary integral equation

The determination of the mean curvature by fitting the paraboloids is much less precise than the determination of the normal vectors, which can introduce errors in the calculation [125]. However, since the integral containing the mean curvature

$$\mathcal{K}_k = \int_S \left(k_1(\boldsymbol{x}) + k_2(\boldsymbol{x})\right) G_{ik}(\boldsymbol{x},\boldsymbol{y}) n_{xi} dS_x \tag{6.75}$$

is over a closed surface, it is possible to reformulate it in a curvatureless form as shown by Zinchenko and Davis [123, 125](derivation is in appendix A.13 and A.14)

$$\boldsymbol{\mathcal{K}} = -\mathcal{P}\int_S \frac{\boldsymbol{X}}{X^3}\left(1 - 3\frac{(\boldsymbol{n}_x\cdot\boldsymbol{X})^2}{X^2}\right) dS_x, \tag{6.76}$$

where it is reminded that $\boldsymbol{X} = \boldsymbol{x} - \boldsymbol{y}$. The integrand scales as $O(|\boldsymbol{X}|^{-2})$, when $\boldsymbol{X} \to \boldsymbol{0}$. Zinchenko and Davis also show how $\boldsymbol{\mathcal{K}}$ can be regularized to have $O(1)$ behavior when $\boldsymbol{X} \to \boldsymbol{0}$ [125].

First, we note that the integral can be written with different Green functions we have looked at previously

$$\mathcal{K}_k = \mathcal{P}\int_S \left(4\pi\frac{\partial\Gamma(\boldsymbol{x},\boldsymbol{y})}{\partial x_k} - \frac{1}{2}T_{ijk}(\boldsymbol{x},\boldsymbol{y}) n_{xi} n_{xj}\right) dS_x. \tag{6.77}$$

Let us first look at the normal component of $\boldsymbol{\mathcal{K}}$

$$\boldsymbol{\mathcal{K}}\cdot\boldsymbol{n}_y = \int_S \left(4\pi\boldsymbol{n}_y\cdot\boldsymbol{\nabla}_x\Gamma(\boldsymbol{x},\boldsymbol{y}) - \frac{1}{2}T_{ijk}(\boldsymbol{x},\boldsymbol{y}) n_{xi} n_{xj} n_{yk}\right) dS_x, \tag{6.78}$$

which now has a $O(|\boldsymbol{X}|^{-1})$ singularity, as $\boldsymbol{X} \to \boldsymbol{0}$, hence $\mathcal{P}$ is omitted. The singularity can be further reduced using the equations (6.9) and (6.73) to get the identity

$$\int_S \left(4\pi\boldsymbol{n}_x\cdot\boldsymbol{\nabla}_x\Gamma(\boldsymbol{x},\boldsymbol{y}) - \frac{1}{2}T_{ijk}(\boldsymbol{x},\boldsymbol{y}) n_{yi} n_{yj} n_{xk}\right) dS_x = 0, \tag{6.79}$$

which we add to the normal component of $\boldsymbol{\mathcal{K}}$ to get

$$\boldsymbol{\mathcal{K}}\cdot\boldsymbol{n}_y = \int_S \left(4\pi(\boldsymbol{n}_x + \boldsymbol{n}_y)\cdot\boldsymbol{\nabla}_x\Gamma(\boldsymbol{x},\boldsymbol{y}) - \frac{1}{2}T_{ijk}(\boldsymbol{x},\boldsymbol{y}) n_{xi} n_{yj} (\boldsymbol{n}_x + \boldsymbol{n}_y)_k\right) dS_x, \tag{6.80}$$

whose integrand is now $O(1)$, as $\boldsymbol{X} \to \boldsymbol{0}$. It is worth noting that $\boldsymbol{X}\cdot(\boldsymbol{n}_x + \boldsymbol{n}_y) = O(|\boldsymbol{X}|^3)$, as $\boldsymbol{X} \to \boldsymbol{0}$.

Next we look at the tangential component of $\boldsymbol{\mathcal{K}}$. We note that

$$\boldsymbol{n}_y \times (\boldsymbol{\mathcal{K}} \times \boldsymbol{n}_y) = \boldsymbol{\mathcal{K}}(\boldsymbol{n}_y \cdot \boldsymbol{n}_y) - \boldsymbol{n}_y(\boldsymbol{\mathcal{K}} \cdot \boldsymbol{n}_y) = \boldsymbol{\mathcal{K}} - \boldsymbol{\mathcal{K}}_n = \boldsymbol{\mathcal{K}}_t, \tag{6.81}$$

where $\boldsymbol{\mathcal{K}}_n$ and $\boldsymbol{\mathcal{K}}_t$ are the normal and tangential component of $\boldsymbol{\mathcal{K}}$, respectively. Therefore tangential component of $\boldsymbol{\mathcal{K}}$ is

$$\boldsymbol{\mathcal{K}}_t = \mathcal{P} \int_S \boldsymbol{n}_y \times \left(4\pi \boldsymbol{\nabla}_x \Gamma(\boldsymbol{x}, \boldsymbol{y}) \times \boldsymbol{n}_y - \frac{1}{2} (\boldsymbol{n}_x \cdot \mathbf{T}(\boldsymbol{x}, \boldsymbol{y}) \cdot \boldsymbol{n}_x) \times \boldsymbol{n}_y \right) dS_x. \tag{6.82}$$

Again, the singularity can be removed using the equations (6.22) and (6.73) to get the identity

$$\mathcal{P} \int_S \boldsymbol{n}_y \times \left(-4\pi \boldsymbol{\nabla}_x \Gamma(\boldsymbol{x}, \boldsymbol{y}) \times \boldsymbol{n}_x - \frac{1}{2} (\boldsymbol{n}_y \cdot \mathbf{T}(\boldsymbol{x}, \boldsymbol{y}) \cdot \boldsymbol{n}_x) \times \boldsymbol{n}_y \right) dS_x = \mathbf{0}, \tag{6.83}$$

which we add to $\boldsymbol{\mathcal{K}}_t$ to get

$$\boldsymbol{\mathcal{K}}_t = \int_S \boldsymbol{n}_y \times \left(4\pi \boldsymbol{\nabla}_x \Gamma(\boldsymbol{x}, \boldsymbol{y}) \times (\boldsymbol{n}_y - \boldsymbol{n}_x) - \frac{1}{2} ([\boldsymbol{n}_x + \boldsymbol{n}_y] \cdot \mathbf{T}(\boldsymbol{x}, \boldsymbol{y}) \cdot \boldsymbol{n}_x) \times \boldsymbol{n}_y \right) dS_x. \tag{6.84}$$

This integrand is now $O(1)$, as $\boldsymbol{X} \to \mathbf{0}$.

The regularized form of $\boldsymbol{\mathcal{K}} = (\boldsymbol{\mathcal{K}} \cdot \boldsymbol{n}_y)\boldsymbol{n}_y + \boldsymbol{\mathcal{K}}_t$ is found after some algebraic work as [125]

$$\boldsymbol{\mathcal{K}} = -\int_S \left((\boldsymbol{X} \cdot \boldsymbol{n}_x)\boldsymbol{n}_y + (\boldsymbol{X} \cdot \boldsymbol{n}_y)\boldsymbol{n}_x + (1 - \boldsymbol{n}_y \cdot \boldsymbol{n}_x)\boldsymbol{X} - 3[\boldsymbol{X} \cdot (\boldsymbol{n}_x + \boldsymbol{n}_y)][\boldsymbol{X} \cdot \boldsymbol{n}_x] \frac{\boldsymbol{X}}{X^2} \right) \frac{dS_x}{X^3}, \tag{6.85}$$

which is $O(1)$, as $\boldsymbol{X} \to \mathbf{0}$.

6.4 Summary of steps used for calculating droplet velocity

The steps for calculating the magnetic droplet's surface velocity are the following:

1. We find the magnetic potential from the regularized boundary integral equation

$$\psi(\boldsymbol{y}) = \psi_\infty(\boldsymbol{y}) - (\mu_r - 1) \int_S [\psi(\boldsymbol{x}) - \psi(\boldsymbol{y})] \, \boldsymbol{\nabla}_x \Gamma(\boldsymbol{x}, \boldsymbol{y}) \cdot \boldsymbol{n}_{\boldsymbol{x}} dS_x. \tag{6.86}$$

2. We find the tangential magnetic field by numerical differentiation on the surface

mesh

$$\boldsymbol{H_t^{(i)}} = \mathbf{P}_{\parallel} \cdot \boldsymbol{\nabla}\psi. \tag{6.87}$$

From it we find the normal magnetic field by the integral

$$H_n^{(i)}(\boldsymbol{y}) = \frac{\boldsymbol{H_\infty}(\boldsymbol{y}) \cdot \boldsymbol{n_y}}{\mu_r} - \frac{\mu_r - 1}{\mu_r} \int_S \boldsymbol{n_y} \cdot \Bigg[\Big[\boldsymbol{H_t^{(i)}}(\boldsymbol{x}) - \boldsymbol{H_t^{(i)}}(\boldsymbol{y})\Big] (\boldsymbol{n_x} \cdot \boldsymbol{\nabla}_x \Gamma(\boldsymbol{x}, \boldsymbol{y})) - \Big[\boldsymbol{H_t^{(i)}}(\boldsymbol{x}) - \boldsymbol{H_t^{(i)}}(\boldsymbol{y})\Big] \times (\boldsymbol{n_x} \times \boldsymbol{\nabla}_x \Gamma(\boldsymbol{x}, \boldsymbol{y})) \Bigg] dS_x. \tag{6.88}$$

Then we find the effective magnetic surface force (3.31)

$$f_M(\boldsymbol{y}) = \frac{\gamma}{R_0} \frac{Bm}{8\pi} (\mu_r - 1) \left(\mu_r \left(\frac{H_n^{(i)}(\boldsymbol{y})}{H_\infty} \right)^2 + \left(\frac{H_t^{(i)}(\boldsymbol{y})}{H_\infty} \right)^2 \right) \tag{6.89}$$

3. Before calculating the velocity, we first find an auxiliary field $\boldsymbol{w}$ from the regularized boundary integral equation

$$\begin{aligned} w_k(\boldsymbol{y}) = {} & v_{\infty k}(\boldsymbol{y}) \\ & + \frac{1}{8\pi\eta^{(e)}} \int_S [f_M(\boldsymbol{x}) - f_M(\boldsymbol{y})] G_{ik}(\boldsymbol{x}, \boldsymbol{y}) n_{xi} dS_x \\ & + \frac{\gamma}{8\pi\eta^{(e)}} \int_S \Bigg((\boldsymbol{X} \cdot \boldsymbol{n}_x) n_{yk} + (\boldsymbol{X} \cdot \boldsymbol{n}_y) n_{xk} + (1 - \boldsymbol{n}_y \cdot \boldsymbol{n}_x) X_k \\ & \qquad - 3[\boldsymbol{X} \cdot (\boldsymbol{n}_x + \boldsymbol{n}_y)][\boldsymbol{X} \cdot \boldsymbol{n}_x] \frac{X_k}{X^2} \Bigg) \frac{dS_x}{X^3} \\ & + \frac{1 - \lambda}{8\pi} \int_S [w_i(\boldsymbol{x}) - w_i(\boldsymbol{y})] T_{ikj}(\boldsymbol{x}, \boldsymbol{y}) n_{xj} dS_x \\ & - \frac{(1 - \lambda) n_{yk}}{2S} \int_S \boldsymbol{w}(\boldsymbol{x}) \cdot \boldsymbol{n}_x dS_x \\ & + \frac{1 - \lambda}{2} w_k'^{(-1)}(\boldsymbol{y}), \end{aligned} \tag{6.90}$$

where $\boldsymbol{w}'^{(-1)}$ is the $\boldsymbol{w}$ projection on the rigid body motion calculated as

$$\begin{aligned} \boldsymbol{w}'^{(-1)}(\boldsymbol{y}) &= \boldsymbol{V}^{(w)} + \boldsymbol{\Omega}^{(w)} \times \boldsymbol{y}, \\ \boldsymbol{V}^{(w)} &= \frac{1}{S} \int_S \boldsymbol{w}(\boldsymbol{x}) dS_x, \\ \boldsymbol{\Omega}^{(w)} &= \mathbf{M} \cdot \int_S \boldsymbol{x} \times \boldsymbol{w}(\boldsymbol{x}) dS_x, \\ \mathbf{M} = \operatorname{diag} & \left(\frac{1}{\int_S |\boldsymbol{x}|^2 dS_x - \int_S (\boldsymbol{e_i} \cdot \boldsymbol{x})^2 dS_x} \right), \quad i = 1 \ldots 3, \end{aligned} \tag{6.91}$$

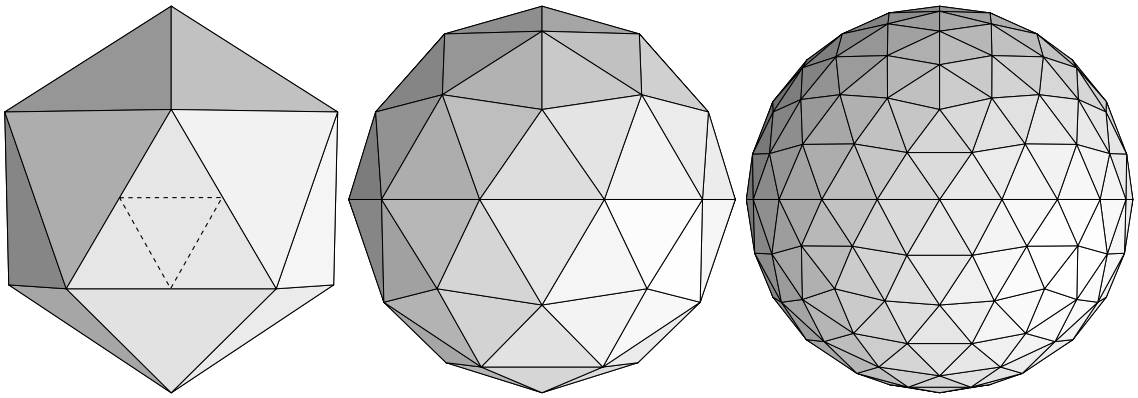

Figure 6.3: Mesh refining starting from an icosahedron.

where $\boldsymbol{e_i}$ takes up the values $\boldsymbol{e}_x$, $\boldsymbol{e}_y$ and $\boldsymbol{e}_z$.

4. Finally, the velocity field is found using eq. (6.71)

$$\boldsymbol{v}(\boldsymbol{y}) = \boldsymbol{w}(\boldsymbol{y}) - \frac{1-\lambda}{2}\boldsymbol{w}'^{(-1)}(\boldsymbol{y}). \tag{6.92}$$

6.5 Numerical implementation

6.5.1 Surface discretization

To solve the equations numerically we first need to discretize the droplet's surface. We mesh the surface with flat triangular elements. Two ordered arrays are created: one contains the coordinates (x_i, y_i, z_i) of the vertices, the other contains the vertex numbers (i, j, k) belonging to a given face. The vertex numbers are stored in a fixed order to indicate the orientation of the face i.e. which side is facing the exterior of the droplet. The true droplet's shape is retrievable by a smooth interpolation of the mesh points.

To generate the initial mesh, we start with an icosahedron, whose faces are recursively split into 4 equilateral triangles. All the vertices are projected onto a unit sphere. This results in a highly regular mesh - all triangles are nearly equilateral (figure 6.3). The coordination number of a vertex is equal to the number of neighboring vertices. For the recursively split icosahedron the coordination numbers are nearly all 6, except for 12 points corresponding to the initial icosahedron, whose coordination numbers are 5.

A good surface discretization allows for the accurate calculation of the true droplet's surface properties, such as its shape, normal vector, curvature etc. To achieve it, more points need to be located in regions of large curvature, and the triangles should be as regular as possible. However, the algorithm complexity is proportional to $O(N^2)$, where N is the number of surface points, therefore the total number of points should be kept

as low as possible. Some mesh upkeep procedures are therefore needed as the droplet changes shape.

6.5.2 Determining the normal vector and curvature

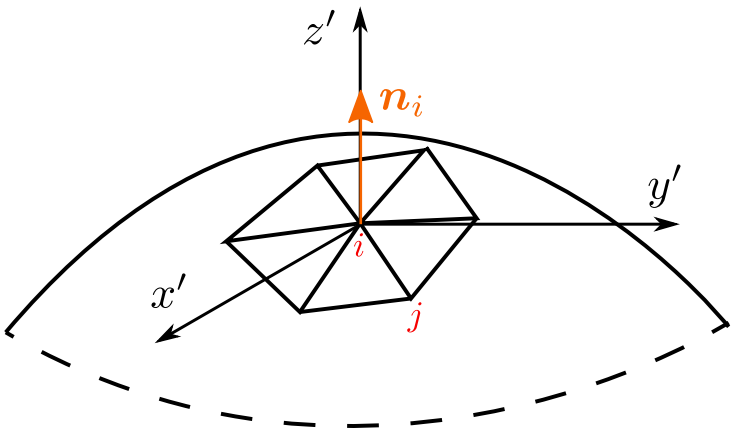

Figure 6.4: Local coordinates on the surface of the droplet at the point i.

The normal vector on each vertex i is found by fitting a paraboloid on the vertex i and its neighboring vertices. The fitting scheme is taken from the work by Zinchenko and Davis [123].

For each vertex we find an initial approximation for the normal vector. When the number of vertices on the droplet's surface remains unchanged in subsequent time iterations, this initial approximation is taken as the normal vector of the vertex in the previous time step. If it is the first time step or the number of vertices has changed, the initial approximation is calculated as [126]

$$\boldsymbol{n}(i) \propto \sum_{\Delta \text{ next to } i} \alpha_\Delta \boldsymbol{n}_\Delta, \tag{6.93}$$

where $\boldsymbol{n}_\Delta$ is the normal vector of the triangle, α_Δ is the angle adjacent to the vertex i of the triangle, and the summation is done over all the triangles containing the vertex i.

Then the following procedure is utilized: [123]

1. Move to the local coordinate system (x', y', z') centered on the vertex i such that the z' axis is pointing at the current approximation of the normal vector $\boldsymbol{n}^\nu(i)$ (figure 6.4), where ν denotes the iteration number.

2. Minimize with respect to A, B, C, D, E the cost function

$$G_{cost} = \sum_{j \text{ next to } i} \frac{(Ax'_j + By'_j + Cx'^2_j + Dx'_j y'_j + Ey'^2_j - z'_j)^2}{x'^2_j + y'^2_j + z'^2_j}, \tag{6.94}$$

where the summation is over vertices j adjacent to i, and the denominator gives larger weight to the points closer to i.

3. The next approximation of the normal vector in the (x', y', z') coordinates is given by

$$\boldsymbol{n}^{\nu+1}(i) = \frac{\{-A, -B, 1\}}{\sqrt{1 + A^2 + B^2}}. \tag{6.95}$$

4. If $|\boldsymbol{n}^{\nu+1}(i) - \boldsymbol{n}^{\nu}(i)| > \varepsilon$, proceed to 1 with the current approximation of $\boldsymbol{n}(i)$. In simulations $\varepsilon = 10^{-8}$.

5. The normal vector on the vertex i is the current approximation of $\boldsymbol{n}(i)$. The principal curvatures[3] on the vertex i are

$$k_1(i) = -C - E + \sqrt{(C-E)^2 + D^2}, \quad k_2(i) = -C - E - \sqrt{(C-E)^2 + D^2}. \tag{6.96}$$

The cost function G_{cost} is minimized by the simultaneous solution of five equations

$$\frac{\partial G_{cost}}{\partial A} = \frac{\partial G_{cost}}{\partial B} = \frac{\partial G_{cost}}{\partial C} = \frac{\partial G_{cost}}{\partial D} = \frac{\partial G_{cost}}{\partial E} = 0 \tag{6.97}$$

to get the five unknowns. The minimum can always be found since the coordination number of all vertices (number of neighboring vertices) is ensured to be no smaller than 5.

6.5.3 Non-singular integral quadrature

Since all of the integrals to be solved (section 6.4) except for the one for H_n calculation (6.88) are $O(1)$ as $\boldsymbol{X} \to \boldsymbol{0}$, we can use a trapezoidal rule [127] for their quadrature. Furthermore, with trapezoidal rule it is possible to efficiently reformulate the summation over triangles to summation over vertices [123, 128]

$$\int_S f(\boldsymbol{x}) dS_x \approx \sum_{\Delta} \frac{1}{3}(f_{1\Delta} + f_{2\Delta} + f_{3\Delta})\Delta S = \sum_i f(\boldsymbol{x}_i)\Delta S_i, \tag{6.98}$$

[3]Principal curvatures are not used in the calculation of the magnetic field and velocity, but they will be useful in the mesh upkeep procedures.

where $f_{j\Delta}$ is the function value at the vertices of a given triangle, ΔS is the area of said triangle, $\boldsymbol{x}_i$ is the radiusvector pointing at the i-th vertex, and ΔS_i is found as the average area of the triangles adjacent to the i-th vertex

$$\Delta S_i = \frac{1}{3}\sum \Delta S. \tag{6.99}$$

To solve the integral equations, we reformulate them into linear systems of equations. We write the magnetic potential to be solved on the N vertex points as a vector of length N, and

$$\boldsymbol{\psi} = (\psi(1)\ \psi(2)\ \cdots\ \psi(N))^T, \tag{6.100}$$

where T denotes the transpose. And since the field $\boldsymbol{w}$ is a vector function, we write it as a vector of length $3N$

$$\boldsymbol{w} = (w_1(1)\ w_2(1)\ w_3(1)\ \cdots\ w_1(N)\ w_2(N)\ w_3(N))^T. \tag{6.101}$$

In that case the integral equation (6.86) becomes

$$\boldsymbol{\psi} = \mathbf{A}\boldsymbol{\psi} + \boldsymbol{\psi_\infty}, \tag{6.102}$$

where $\boldsymbol{\psi}_\infty$ is a vector of length N, whose components contain the background magnetic potential $\psi_\infty(j) = \psi_\infty(\boldsymbol{x}_j)$, and $\mathbf{A}$ is a square $N \times N$ matrix

$$\mathbf{A} = \begin{pmatrix} -\sum_{i\neq 1} K^{(\psi)}(i,1) & K^{(\psi)}(2,1) & \cdots & K^{(\psi)}(N,1) \\ K^{(\psi)}(1,2) & -\sum_{i\neq 2} K^{(\psi)}(i,2) & \cdots & K^{(\psi)}(N,2) \\ \vdots & \vdots & \ddots & \vdots \\ K^{(\psi)}(1,N) & K^{(\psi)}(2,N) & \cdots & -\sum_{i\neq N} K^{(\psi)}(i,N) \end{pmatrix}. \tag{6.103}$$

$K^{(\psi)}(i,j)$ denotes the discretized integral kernel of (6.86), such that i corresponds to the integration variable $\boldsymbol{x}$, and j corresponds to the free variable $\boldsymbol{y}$

$$K^{(\psi)}(i,j) = -(\mu_r - 1)\boldsymbol{\nabla}_x \Gamma(\boldsymbol{x}_i, \boldsymbol{y}_j) \cdot \boldsymbol{n}(\boldsymbol{x}_i)\Delta S_i. \tag{6.104}$$

And the integral for $\boldsymbol{w}$ (6.90) becomes

$$\boldsymbol{w} = \mathbf{B}\boldsymbol{w} + \mathbf{D}\boldsymbol{w} + \mathbf{E}\boldsymbol{w} + \boldsymbol{f}, \tag{6.105}$$

where the $3N \times 3N$ matrix $\mathbf{B}$ corresponds to the $\mathbf{T}$ integral

$$\mathbf{B} = \begin{pmatrix} \mathbf{K^{(w)}}(1,1) & \mathbf{K^{(w)}}(2,1) & \cdots & \mathbf{K^{(w)}}(N,1) \\ \mathbf{K^{(w)}}(1,2) & \mathbf{K^{(w)}}(2,2) & \cdots & \mathbf{K^{(w)}}(N,2) \\ \vdots & \vdots & \ddots & \vdots \\ \mathbf{K^{(w)}}(1,N) & \mathbf{K^{(w)}}(2,N) & \cdots & \mathbf{K^{(w)}}(N,N) \end{pmatrix}, \tag{6.106}$$

where $\mathbf{K^{(w)}}(i,j)$ is a 3×3 matrix

$$K_{kl}^{(w)}(i,j) = \begin{cases} \dfrac{1-\lambda}{8\pi} T_{lkm}(\boldsymbol{x}_i, \boldsymbol{y}_j) n_m(\boldsymbol{x}_i) \Delta S_i, \text{ if } i \neq j \\ -\displaystyle\sum_{i' \neq j} \dfrac{1-\lambda}{8\pi} T_{lkm}(\boldsymbol{x}_{i'}, \boldsymbol{y}_j) n_m(\boldsymbol{x}_{i'}) \Delta S_{i'}, \text{ if } i = j \end{cases}. \tag{6.107}$$

Next, the $3N \times 3N$ matrix $\mathbf{D}$ corresponds to the term with $\boldsymbol{w}'^{(1)}$: the projection on the eigensolution proportional to the surface normal

$$D_{kl}(i,j) = -\frac{1-\lambda}{2S} n_k(j) n_l(i) \Delta S_i. \tag{6.108}$$

And the $3N \times 3N$ matrix $\mathbf{E}$ corresponds to the term with $\boldsymbol{w}'^{(-1)}$: the projection on the eigensolution of rigid body motion. It is written as a sum of two parts $\mathbf{E} = \mathbf{E}^{trans} + \mathbf{E}^{rot}$. $\mathbf{E}^{trans}$ is simply

$$E_{kl}^{trans}(i,j) = \frac{1-\lambda}{2S} \Delta S_i. \tag{6.109}$$

But $\mathbf{E}^{rot}$ is found by first calculating the 3×3 matrix

$$\mathbf{M} = \operatorname{diag}\left(\frac{1}{\sum_i |\boldsymbol{x}_i|^2 \Delta S_i - \sum_i (\boldsymbol{e_k} \cdot \boldsymbol{x}_i)^2 \Delta S_i} \right), \quad k = 1 \ldots 3, \tag{6.110}$$

where $\boldsymbol{e_i}$ takes up the values $\boldsymbol{e}_x$, $\boldsymbol{e}_y$ and $\boldsymbol{e}_z$. Then we get

$$E_{kl}^{rot}(i,j) = \frac{1-\lambda}{2} M_{km} \varepsilon_{mnl} (\boldsymbol{x}_i)_n \Delta S_i, \tag{6.111}$$

where ε_{mnl} is the Levi-Civita symbol and $(\boldsymbol{x}_i)_n$ is the n-th component of the vector $\boldsymbol{x}_i$.

Finally, $\boldsymbol{f}$ contains the terms without $\boldsymbol{w}$. Also it is split into parts for ease of expression $\boldsymbol{f} = \boldsymbol{v}^\infty + \boldsymbol{f}^{mag} + \boldsymbol{f}^{st}$. $\boldsymbol{v}^\infty$ is simply the contribution by the background flow $v_k^\infty(j) = v_{\infty k}(\boldsymbol{x}_j)$ written as a vector of length $3N$

$$\boldsymbol{v}^\infty = (v_{\infty 1}(1)\ v_{\infty 2}(1)\ v_{\infty 3}(1)\ \cdots\ v_{\infty 1}(N)\ v_{\infty 2}(N)\ v_{\infty 3}(N))^T. \tag{6.112}$$

The $3N$ vector corresponding to the magnetic force integral is

$$f_k^{mag}(j) = \frac{1}{8\pi\eta^{(e)}} \sum_{i \neq j} [f_M(\boldsymbol{x}_i) - f_M(\boldsymbol{y}_j)] G_{lk}(\boldsymbol{x}_i, \boldsymbol{y}_j) n_l(\boldsymbol{x}_i) \Delta S_i. \tag{6.113}$$

And the $3N$ vector corresponding to the surface tension integral is

$$\begin{aligned} f_k^{st}(j) = & \frac{\gamma}{8\pi\eta^{(e)}} \sum_{i \neq j} \Bigg((\boldsymbol{X} \cdot \boldsymbol{n}(\boldsymbol{x}_i)) n_k(\boldsymbol{y}_j) + (\boldsymbol{X} \cdot \boldsymbol{n}(\boldsymbol{y}_j)) n_k(\boldsymbol{x}_i) + (1 - \boldsymbol{n}(\boldsymbol{y}_j) \cdot \boldsymbol{n}(\boldsymbol{x}_i)) X_k \\ & - 3[\boldsymbol{X} \cdot (\boldsymbol{n}(\boldsymbol{x}_i) + \boldsymbol{n}(\boldsymbol{y}_j))][\boldsymbol{X} \cdot \boldsymbol{n}(\boldsymbol{x}_i)] \frac{X_k}{X^2} \Bigg) \frac{\Delta S_i}{X^3}, \end{aligned} \tag{6.114}$$

where $\boldsymbol{X} = \boldsymbol{x}_i - \boldsymbol{y}_j$.

Having written the discretized integral equations in a form of linear system of equations (6.102) and (6.105), we efficiently solve for $\boldsymbol{w}$ using the standard `LinearAlgebra` library in Julia programming language [129]. Finally, the $3N$ vector containing velocities is obtained by

$$\boldsymbol{v} = \boldsymbol{w} - \mathbf{E}\boldsymbol{w}. \tag{6.115}$$

6.5.4 Weakly singular integral quadrature

The integral for the normal component of the magnetic field (6.88) contains an $O(|\boldsymbol{X}|^{-1})$ singularity as $\boldsymbol{X} \to \mathbf{0}$. The triangles that do not contain the singularity are evaluated using the trapezoidal rule, however some additional steps need to be taken to evaluate the triangles with one vertex on the singularity.

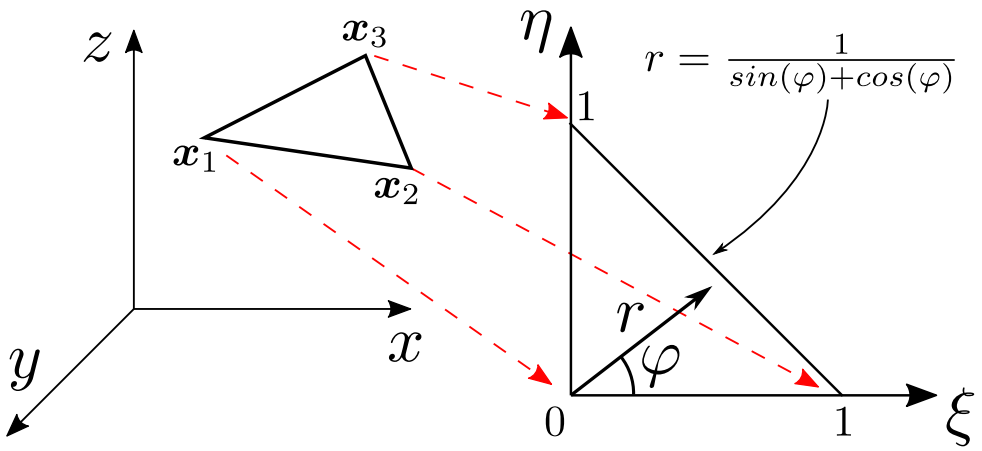

Figure 6.5: Mapping of a triangle in 3D space to the coordinates ξ, η.

Let us introduce parametric coordinates ξ, η as shown in figure 6.5. The physical parameters known on the triangle vertices can be linearly interpolated over the triangle

surface [78]. We do this with the radiusvector, normal vector and the tangential magnetic field

$$\begin{aligned}\boldsymbol{x}(\xi,\eta) &= \zeta\boldsymbol{x}_1 + \xi\boldsymbol{x}_2 + \eta\boldsymbol{x}_3,\\ \boldsymbol{n}(\xi,\eta) &= \zeta\boldsymbol{n}(\boldsymbol{x}_1) + \xi\boldsymbol{n}(\boldsymbol{x}_2) + \eta\boldsymbol{n}(\boldsymbol{x}_3),\\ \boldsymbol{H}_t(\xi,\eta) &= \zeta\boldsymbol{H}_t(\boldsymbol{x}_1) + \xi\boldsymbol{H}_t(\boldsymbol{x}_2) + \eta\boldsymbol{H}_t(\boldsymbol{x}_3),\end{aligned} \tag{6.116}$$

where $\zeta = 1 - \xi - \eta$. A surface integral over the triangle in the parametric coordinates is then [78]

$$\int_\Delta f(\boldsymbol{x})dS_x = \int_0^1 d\xi \int_0^{1-\xi} f(\xi,\eta)\left|\frac{\partial \boldsymbol{x}}{\partial \xi} \times \frac{\partial \boldsymbol{x}}{\partial \eta}\right| d\eta = h_S \int_0^1 d\xi \int_0^{1-\xi} f(\xi,\eta)d\eta, \tag{6.117}$$

where $h_S = |(\boldsymbol{x}_2 - \boldsymbol{x}_1) \times (\boldsymbol{x}_3 - \boldsymbol{x}_1)|$ is a constant and can be moved outside the integral.

If a function has a $O(|\boldsymbol{X}|^{-1})$ singularity at $\boldsymbol{x}_1$, it can be integrated in the following way. Let the function be $f(\boldsymbol{x}) = g(\boldsymbol{x})/|\boldsymbol{x} - \boldsymbol{x}_1|$, where $g(\boldsymbol{x})$ is bounded. Then the integral becomes

$$\int_\Delta f(\boldsymbol{x})dS_x = h_S \int_0^1 d\xi \int_0^{1-\xi} \frac{g(\xi,\eta)}{|(\boldsymbol{x}_2 - \boldsymbol{x}_1)\xi + (\boldsymbol{x}_3 - \boldsymbol{x}_1)\eta|} d\eta. \tag{6.118}$$

We can remove the singularity by introducing polar coordinates $\xi = r\cos\varphi$, $\eta = r\sin\varphi$ (see figure 6.5). The differential area element in ξ, η plane is $d\xi d\eta = r dr d\varphi$ and the integral becomes

$$\int_\Delta f(\boldsymbol{x})dS_x = h_S \int_0^{\frac{\pi}{2}} \frac{d\varphi}{|(\boldsymbol{x}_2 - \boldsymbol{x}_1)\cos\varphi + (\boldsymbol{x}_3 - \boldsymbol{x}_1)\sin\varphi|} \int_0^{\frac{1}{\sin\varphi + \cos\varphi}} g(r,\varphi)dr. \tag{6.119}$$

Over singular triangles the integral in (6.88) is solved by multiplying the integrand by $|\boldsymbol{x} - \boldsymbol{y}|$, where $\boldsymbol{y}$ is the point of singularity, and then using the formula (6.119). The integral over the singular triangle is evaluated with a 10 point Gauss-Legendre quadrature for the variables r and φ [62].

6.5.5 Magnetic potential numerical differentiation

To get the tangential magnetic field, we need to differentiate the obtained magnetic potential. It is done by formulating a system of equations for each vertex i [62]

$$(\boldsymbol{\nabla}\psi)_i \cdot (\boldsymbol{x}_j - \boldsymbol{x}_i) = \psi_j - \psi_i, \tag{6.120}$$

where j are the neighboring vertices to i. Since there are always 5 or more neighbors to a given vertex, the system is overdetermined for the three components of $\boldsymbol{\nabla}\psi$. It is solved

by the method of minimum-norm least squares as implemented in the matrix division function in the `LinearAlgebra` library of the Julia programming language [129].

To get the tangential magnetic field, $\boldsymbol{\nabla}\psi$ is projected on the tangential plane

$$\boldsymbol{H}_t = \mathbf{P}_{||} \cdot \boldsymbol{\nabla}\psi. \tag{6.121}$$

The estimate of the normal field with this method is imprecise since the droplet is meshed only on the surface.

6.5.6 Time stepping

The change in droplet shape is found by moving the vertices with their velocity. Simplest way to find the vertex position in the subsequent time step is the Euler method [127]

$$\boldsymbol{x}^{\nu+1} = \boldsymbol{x}^{\nu} + \boldsymbol{v}^{\nu}\Delta t, \tag{6.122}$$

where Δt is a small time step. The Euler method proved to be sufficient since the dominant source of error is the surface triangulation as will be shown later and as has been reported in the literature [79, 130]. Higher order methods would increase the computation time without significant improvements in precision.

An adaptive time step was chosen to ensure precision and computational efficiency

$$\Delta t = \min\left\{\tau_Z, 0.05\frac{2\pi}{\omega}, 0.07\frac{R_0\eta^{(e)}}{\gamma}\right\}, \tag{6.123}$$

where ω is the angular frequency of the rotating magnetic field, and τ_Z is inspired by the work of Zinchencko and Davis [130]

$$\tau_Z = 7.4\frac{\eta^{(e)}}{R_0\gamma}\min_i\left\{\left(\frac{\Delta x_{min}}{|k|_{max}}\right)_i\right\}, \tag{6.124}$$

where Δx_{min} is the smallest edge connected to the vertex i and $|k|_{max}$ is the largest of the two principal curvatures measured by their absolute value. This time step ensures that the triangles do not get distorted too much in each time step, and that smaller steps are taken when there are rapid spatial changes in the droplet shape i.e. large curvature. Furthermore, when a rotating field is applied, the time steps need to be small enough to resolve this rotation. Therefore to calculate the motion of a droplet in a fast-rotating field, we use the period-averaged magnetic surface force (6.29).

A limitation of the Euler method is that the volume of the droplet is not conserved. This is mitigated by rescaling the droplet after each time step

$$\boldsymbol{x}_{rescaled} = \left(\frac{V}{V_0}\right)^{-\frac{1}{3}} (\boldsymbol{x} - \boldsymbol{x}_{cm}) + \boldsymbol{x}_{cm}, \tag{6.125}$$

where V_0 is the initial droplet volume, $\boldsymbol{x}_{cm}$ is the center of mass expressed as an integral over the surface using a corollary of the divergence theorem ($\int_V \boldsymbol{\nabla} f dV = \int_S f \boldsymbol{n} dS$)

$$\boldsymbol{x}_{cm} = \frac{1}{V}\int_V \boldsymbol{x} dV_x = \frac{1}{2V}\int_V \boldsymbol{\nabla} x^2 dV_x = \frac{1}{2V}\int_S x^2 \boldsymbol{n}_x dS_x, \tag{6.126}$$

and V is the droplet volume, also expressed as an integral over the surface

$$V = \int_V dV_x = \frac{1}{3}\int_V \boldsymbol{\nabla}\cdot\boldsymbol{x} dV_x = \frac{1}{3}\int_S \boldsymbol{x}\cdot\boldsymbol{n}_x dS_x. \tag{6.127}$$

6.5.7 Tangential velocity optimization

Since the mesh is moving with the velocity of the droplet, it quickly gets distorted, for example, the triangles stretch out in the direction of an elongating flow. This can be somewhat mitigated by noticing that only the normal component of the velocity changes the droplet shape. This idea is the basis of stabilization techniques that work by adding a velocity component in the tangential plane meant to decrease the mesh degradation as much as possible in a given time step [131, 123].

In this work, we use an optimization algorithm that minimizes a cost function with respect to the tangential components of the velocity [79]

$$F = \sum_{\substack{\boldsymbol{x}_{ij} \\ i<j}} \left[\frac{d}{dt}\left(\frac{|\boldsymbol{x}_{ij}|^2}{h_{ij}^2} + \frac{h_{ij}^2}{|\boldsymbol{x}_{ij}|^2}\right)\right]^2 + 0.4\sum_{\Delta}\frac{1}{C_\Delta^2}\left(\frac{dC_\Delta}{dt}\right)^2, \tag{6.128}$$

where the first sum is over the edges and the second sum is over the triangles. The edge vector $\boldsymbol{x}_{ij} = \boldsymbol{x}_j - \boldsymbol{x}_i$ is a vector pointing from the vertex $\boldsymbol{x}_i$ to the neighboring vertex $\boldsymbol{x}_j$. h_{ij} is a target edge length ensuring finer mesh in large curvature regions. It is defined by [79]

$$\begin{aligned} h_{ij}^2 &= \frac{1}{2}(h_i^2 + h_j^2), \quad h_i^2 = K\Lambda_i^{-0.25}, \\ \Lambda_i &= k_1^2(i) + k_2^2(i) + \frac{0.004}{R_0^2}, \\ K &= \frac{4}{\sqrt{3}N_\Delta}\sum_i \Lambda_i^{0.25}\Delta S_i, \end{aligned} \tag{6.129}$$

where N_Δ is the number of triangles in the mesh. $C_\Delta = S_\Delta/(a^2+b^2+c^2)$ is the "compactness" of the triangle, where a, b, c are its side lengths, and S_Δ is its area. Large C_Δ corresponds to triangles close to equilateral. The first sum in (6.128) ensures that the measure of how close the edge lengths are to their target values changes little. Second sum in (6.128) ensures that the triangles retain their compactness i.e. they do not collapse.

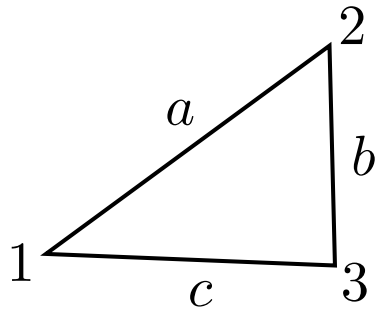

Figure 6.6: Triangle side and vertex notation.

Approximating h_{ij} as time independent, the function F can be written in terms of the vertex velocities [132]

$$\begin{aligned} F(\boldsymbol{v}_1,\ \ldots,\ \boldsymbol{v}_N) = &\sum_{\substack{\boldsymbol{x}_{ij} \\ i<j}} \left[2(\boldsymbol{x}_{ij}\cdot(\boldsymbol{v}_j-\boldsymbol{v}_i))\left(\frac{1}{h_{ij}^2}-\frac{h_{ij}^2}{|\boldsymbol{x}_{ij}|^4}\right)\right]^2 \\ &+ 0.4\sum_\Delta \frac{1}{C_\Delta^2}\left[-A\boldsymbol{x}_{12}\cdot(\boldsymbol{v}_2-\boldsymbol{v}_1) - B\boldsymbol{x}_{23}\cdot(\boldsymbol{v}_3-\boldsymbol{v}_2) - C\boldsymbol{x}_{31}\cdot(\boldsymbol{v}_1-\boldsymbol{v}_3)\right]^2, \end{aligned} \tag{6.130}$$

where

$$\begin{aligned} A &= \frac{a^2(a^2+b^2+c^2)-a^4-b^4-c^4}{4C_\Delta(a^2+b^2+c^2)^3} \\ B &= \frac{b^2(a^2+b^2+c^2)-a^4-b^4-c^4}{4C_\Delta(a^2+b^2+c^2)^3} \\ C &= \frac{c^2(a^2+b^2+c^2)-a^4-b^4-c^4}{4C_\Delta(a^2+b^2+c^2)^3}. \end{aligned} \tag{6.131}$$

The meaning of a, b, c and $1, 2, 3$ in the second sum is shown in the figure 6.6.

To avoid numerical gradient approximation when minimizing F, it is written in explicit form [132]

$$\begin{aligned} \boldsymbol{\nabla}_{\boldsymbol{v}_i} F = &-\sum_{\substack{j \\ \text{next to } i}} 8(\boldsymbol{x}_{ij}\cdot(\boldsymbol{v}_j-\boldsymbol{v}_i))\left(\frac{1}{h_{ij}^2}-\frac{h_{ij}^2}{|\boldsymbol{x}_{ij}|^4}\right)^2 \boldsymbol{x}_{ij} \\ &+ \sum_{\substack{\Delta \\ \text{contains } i}} \frac{0.2}{C_\Delta^2}\left[-A\boldsymbol{x}_{i2}\cdot(\boldsymbol{v}_2-\boldsymbol{v}_i) - B\boldsymbol{x}_{23}\cdot(\boldsymbol{v}_3-\boldsymbol{v}_2) - C\boldsymbol{x}_{3i}\cdot(\boldsymbol{v}_i-\boldsymbol{v}_3)\right](A\boldsymbol{x}_{i2} - C\boldsymbol{x}_{3i}), \end{aligned} \tag{6.132}$$

where the gradient is taken with respect to the velocity of the i-th vertex. In the triangle notation (figure 6.6) i is chosen to be the vertex 1. Since we want to change only the tangential component of the velocity, the gradient is projected on the tangential plane

$$\boldsymbol{\nabla}^{||}_{\boldsymbol{v}_i} F = \mathbf{P}_{||} \cdot \boldsymbol{\nabla}_{\boldsymbol{v}_i} F. \tag{6.133}$$

For each vertex i the optimal velocity is found by the BFGS (Broyden – Fletcher – Goldfarb – Shanno) method provided by the `Optim` library [133] for Julia programming language. Since the tangential gradient is provided, the normal component of the resulting velocity field is unchanged, but the tangential component is adjusted to minimize the mesh degradation. The tangential velocity is optimized in each simulation time step.

6.5.8 Mesh restructuring: vertex sliding

The adjustment of tangential velocity decreases but does not remove the mesh degradation completely. Therefore, periodically some active mesh restructuring is necessary between the time iterations. One such restructuring method is the sliding of vertices on the droplet surface to minimize a cost function describing the desired mesh properties.

In this work we use a cost function [79] that is to be minimized with respect to the vertex positions

$$E(\boldsymbol{x}_1, \ \dots \ , \boldsymbol{x}_N) = \sum_{\substack{\boldsymbol{x}_{ij} \\ i<j}} \left[\frac{1}{2} \left(\frac{|\boldsymbol{x}_{ij}|^2}{h_{ij}^2} + \frac{h_{ij}^2}{|\boldsymbol{x}_{ij}|^2} \right) \right]^{50} + \sum_{\Delta} \left(\frac{C_\Delta^{et}}{C_\Delta} \right)^{100}, \tag{6.134}$$

where again the first sum is over the vertices and the second sum is over the triangles. $C_\Delta^{et} = \sqrt{3}/12$ is the "compactness" of an equilateral triangle. The cost function E takes up large values if the edge lengths differ greatly from h_{ij}, and when the triangles are far from equilateral.

Again, approximating $\boldsymbol{h}_{ij}$ as constant, we can write a gradient with respect to the coordinates of the i-th vertex [132]

$$\begin{aligned} \boldsymbol{\nabla}_{\boldsymbol{x}_i} E = -50 \sum_{\substack{j \\ \text{next to } i}} & \left[\frac{1}{2} \left(\frac{|\boldsymbol{x}_{ij}|^2}{h_{ij}^2} + \frac{h_{ij}^2}{|\boldsymbol{x}_{ij}|^2} \right) \right]^{49} \left(\frac{1}{h_{ij}^2} - \frac{h_{ij}^2}{|\boldsymbol{x}_{ij}|^4} \right) \boldsymbol{x}_{ij} \\ - 100 \sum_{\substack{\Delta \\ \text{contains } i}} & \left(\frac{C_\Delta^{et}}{C_\Delta} \right)^{99} \left(\frac{C_\Delta^{et}}{C_\Delta^2} \right) \boldsymbol{\nabla}_{\boldsymbol{x}_i} C_\Delta, \end{aligned} \tag{6.135}$$

and $\boldsymbol{\nabla}_{\boldsymbol{x}_i} C_\Delta = A\boldsymbol{x}_{i2} + C\boldsymbol{x}_{i3}$, where A and C are defined in (6.131), the triangle edge indices are shown in figure (6.6), and 1 is relabeled to i.

The vertices are moved by a modified gradient descent method to ensure that they always remain on the droplet's surface [79]:

1. The vertices are moved according to

$$\boldsymbol{x}_i^* = \boldsymbol{x}_i^\nu - \delta \boldsymbol{\nabla}_{\boldsymbol{x}_i^\nu} E, \tag{6.136}$$

   where $\delta = 0.01\min\{(\Delta x_{min}/|\boldsymbol{\nabla}_{\boldsymbol{x}} E|)_i\}$, and Δx_{min} is the smallest edge length next to a given vertex.

2. For each x_i^*, the closest original vertex (before the vertex sliding was initiated) is found and x_i^* is projected on to the local paraboloid fitted around the original vertex. After projection, x_i^* becomes the vertex for the next iteration $x_i^{\nu+1}$

3. h_{ij} is updated with the new k_1 and k_2 values calculated from the locally fitted paraboloids on the original vertices [132].

The mesh quality is characterized by two parameters [79]

$$Sc = \frac{\max\left(\frac{|\boldsymbol{x}_{ij}|}{h_{ij}}\right)}{\min\left(\frac{|\boldsymbol{x}_{ij}|}{h_{ij}}\right)}, \quad C_{\Delta\ min} = \min C_\Delta. \tag{6.137}$$

The first parameter describes the scatter of $|\boldsymbol{x}_{ij}|/h_{ij}$, which ideally would be uniform. We seek to decrease Sc and increase $C_{\Delta\ min}$. The iterations are done for 100 times to see if they result in significant mesh improvements. If for any iteration $\nu \leq 100$, $Sc^\nu < 0.75Sc^0$ and $C^\nu_{\Delta\ min} > 1.15C^0_{\Delta\ min}$, the vertex sliding iterations are done 900 more times. Otherwise, the mesh is returned to the original state.

Vertex sliding is performed after every 100 time steps in the simulation.

6.5.9 Mesh restructuring: edge flipping

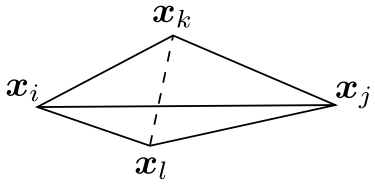

Figure 6.7: Edge flipping notation.

A simple mesh restructuring procedure is edge flipping. Say there are two adjacent triangles $[\boldsymbol{x}_i, \boldsymbol{x}_j, \boldsymbol{x}_k]$ and $[\boldsymbol{x}_i, \boldsymbol{x}_l, \boldsymbol{x}_j]$ (see figure 6.7). Then if [79, 134]

$$|\boldsymbol{x}_l - \boldsymbol{x}_k|^2 < |(\boldsymbol{x}_k - \boldsymbol{O}_k) \cdot (\boldsymbol{x}_l - \boldsymbol{x}_k)| + |(\boldsymbol{x}_l - \boldsymbol{O}_l) \cdot (\boldsymbol{x}_l - \boldsymbol{x}_k)|, \tag{6.138}$$

the edge $[\boldsymbol{x}_i, \boldsymbol{x}_j]$ can be replaced with $[\boldsymbol{x}_l, \boldsymbol{x}_k]$. $\boldsymbol{O}_k$ and $\boldsymbol{O}_l$ are the centers of the circumscribed circles around the triangles $[\boldsymbol{x}_i, \boldsymbol{x}_j, \boldsymbol{x}_k]$ and $[\boldsymbol{x}_i, \boldsymbol{x}_l, \boldsymbol{x}_j]$, respectively. The criterion (6.138) is equivalent to Delaunay triangulation on a flat surface, and if the triangles on the droplet surface are sufficiently small (so that the surface seems locally flat), it should increase the regularity of the triangles. Edges are not flipped if they would result in vertices with fewer than 5 connected edges. This is done to ensure that a paraboloid can always be fitted centered on said vertex.

The algorithm iterates through all edges until (6.138) is satisfied, and an edge gets flipped. It then iterates through the edges again from the start until no more flips are possible. Afterwards vertex sliding is performed to further improve the mesh.

Edge flipping is attempted on each time step in the simulation.

6.5.10 Mesh restructuring: vertex addition

Finally, it was found that the above mentioned mesh stabilization techniques are not satisfactory, when the droplet's curvature becomes too large. Therefore, we performed a vertex addition routine, where we split triangles in regions of large curvature.

For each triangle we calculate the "magnitude" of the curvature (as the average of its vertices)

$$\mathcal{H}_\Delta = \frac{1}{3} \sum_{i \in \Delta} \mathcal{H}_i, \quad \mathcal{H}_i = \left(\sqrt{k_1^2 + k_2^2} \right)_i . \tag{6.139}$$

And we compare it with the length scale of the triangle $\sqrt{S_\Delta}$. If

$$\mathcal{H}_\Delta \sqrt{S_\Delta} > \varepsilon_{split}, \tag{6.140}$$

the triangle is marked for splitting. Additionally, a triangle is marked for splitting, if at least two neighboring triangles are marked. An empiric threshold of $\varepsilon_{split} = 0.2$ is used in this work.

New vertices are added in edge mid-points of the marked triangles (figure 6.8). Each new vertex is projected to the local paraboloid fitted on the nearest original vertex. The

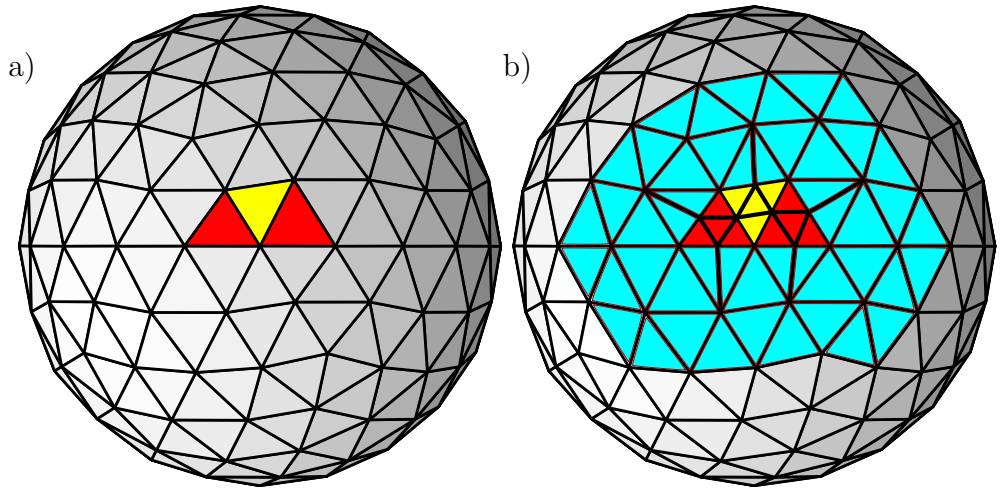

Figure 6.8: An illustrative example of vertex addition. a) First, the red triangles are marked for splitting. Then since the yellow triangle now has two marked neighbors, it also is marked. b) The edges of the marked triangles acquire new vertices that are connected in such a way to ensure at least 5 neighbors for each vertex. The split marked triangles and the neighborhood in blue "two edges deep" is treated with the vertex sliding procedure.

new vertices are connected in such a way that ensures at least 5 neighbors for each resulting vertex. Finally, the vertex sliding procedure is performed on the neighborhood of the newly created vertices [134] (see figure 6.8).

Vertex addition is carried out no more often than every 5 time steps in the simulation.

6.6 Algorithm tests

6.6.1 Time integration precision

It is reported in the literature that currently the limiting factor for free surface calculations using the boundary element methods is the surface discretization, and therefore more complex time integration schemes than the simple Euler method seem to be unnecessary [79]. To asses this, we elongated a droplet in a constant field (figure 6.9) for 350 time steps of $\Delta t = 0.03 R_0 \eta^{(e)}/\gamma$ using the Euler method and the second order Runge-Kutta method [127]. The simulation parameters were $\lambda = 1$, $\mu_r = 22$, $Bm = 5.8$, which correspond to a droplet that would strongly elongate reaching aspect ratio of $a/b = 5.8$ [75]. The vertex addition was turned off, and three different initial meshes generated from the refinement of an icosahedron were used resulting in number of vertices $N = 162$, $N = 642$ and $N = 2562$.

The discrepancy between the second order Runge-Kutta method and the Euler method is around 1% independent on the number of vertices on the discretized droplet's surface.

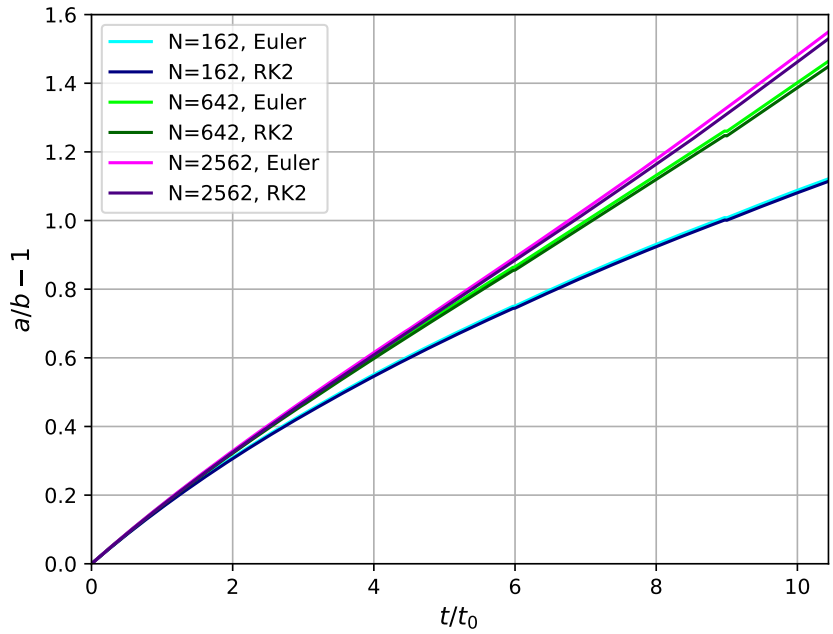

Figure 6.9: Elongation of droplets with $\lambda = 1$, $\mu_r = 22$, $Bm = 5.8$. The time scale is $t_0 = R_0\eta^{(e)}/\gamma$. N indicates the number of vertices describing the droplet, RK2 indicates the second order Runge-Kutta method. a and b are the semiaxes of an ellipsoid fitted to the vertices.

Yet the computation time doubles since the velocities need to be calculated for the intermediate time step. And indeed in figure 6.9 we see the importance of the mesh fineness. Therefore we chose to use only the Euler method, but with rescaling the volume after each time step.

6.6.2 Space integration precision

Figure 6.9 shows that the number of vertices N on the droplet's surface strongly affects the computation precision. However, the algorithm complexity is $O(N^2)$, therefore increasing N quickly makes it prohibitively slow. By adding the vertices in the regions of high curvature, we seek to find the minimal number of vertices that are needed to accurately calculate the droplet's dynamics.

Just as previously, we elongated a droplet in a constant field for 350 time steps of $\Delta t = 0.03R_0\eta^{(e)}/\gamma$ with the Euler method. The simulation parameters were $\lambda = 1$, $\mu_r = 22$, $Bm = 5.8$. We started with a mesh with $N = 162$ and had different triangle splitting thresholds ε_{split}.

We see in figure 6.10 that for $\varepsilon_{split} = 0.2$, the error is below 0.1% compared to the stricter $\varepsilon_{split} = 0.15$. Therefore, $\varepsilon_{split} = 0.2$ was chosen for the simulations in this work. Larger values of ε_{split} could be used, but the reduction in the result precision should be

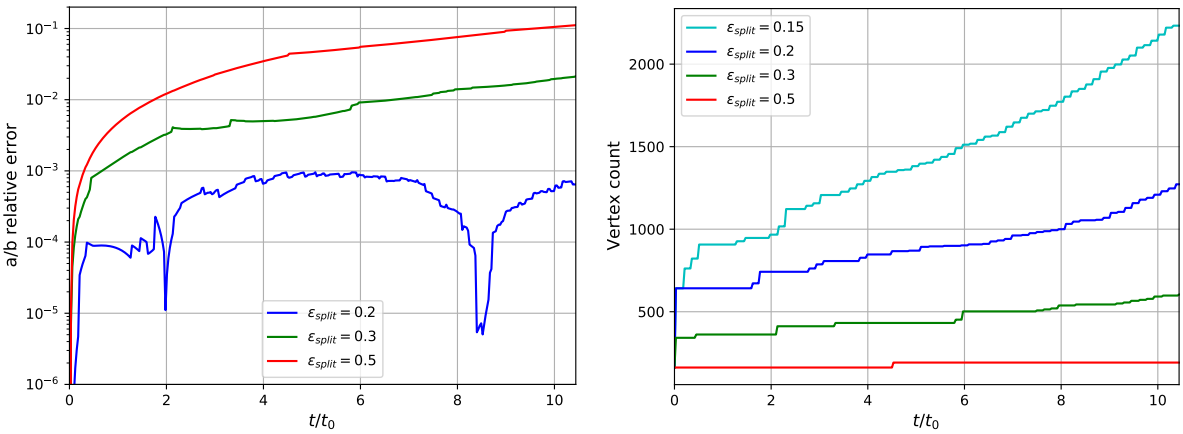

Figure 6.10: Elongation of droplets with $\lambda = 1$, $\mu_r = 22$, $Bm = 5.8$. The time scale is $t_0 = R_0\eta^{(e)}/\gamma$. a and b are the semiaxes of an ellipsoid fitted to the vertices. Left graph compares the simulations with different triangle splitting thresholds ε_{split} to the simulation with $\varepsilon_{split} = 0.15$. We see that for $\varepsilon_{split} = 0.2$ error is below 10^{-3}. The right graph shows how the number of vertices increases as the simulation progresses.

taken into the account.

6.6.3 Test case: droplet contraction to a sphere

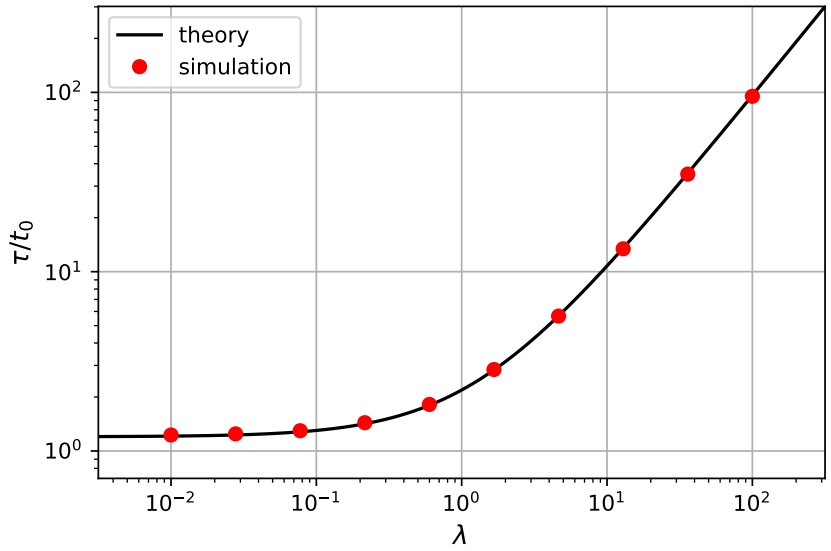

Figure 6.11: Characteristic contraction time a slightly elongated droplet as a function of the viscosity ratio λ. The time scale is $t_0 = R_0\eta^{(e)}/\gamma$. The theoretical curve corresponds to (6.142).

According to the small deformation theory described in section 5, in absence of magnetic field an elongated spheroidal droplet with semiaxes $a > b$ exponentially relaxes to a spherical shape

$$\epsilon_1(t) = \epsilon_1(0)e^{-\frac{t}{\tau}}, \tag{6.141}$$

where $\epsilon_1 = (a-b)/b$ and

$$\tau = \frac{R_0 \eta^{(e)}}{\gamma} \frac{(3+2\lambda)(16+19\lambda)}{40(1+\lambda)}. \tag{6.142}$$

To test it, in simulations we slightly elongated the droplet in magnetic field and then set it to zero. The droplet relaxed to a sphere and we fitted ellipsoids in each time step to determine $\epsilon_1(t)$. Since

$$\ln \epsilon_1(t) = \ln \epsilon_1(0) - \frac{t}{\tau}, \tag{6.143}$$

we determined τ by a linear fit and plotted it in figure 6.11. Excellent agreement can be seen for a large range of λ between the simulation results and the theoretical curve. The deviations are less than 1%.

6.6.4 Test case: droplet elongation in a shear flow

Another test case for the algorithm is a viscous drop in a shear flow in absence of any magnetic fields. Consider a droplet placed at the origin subjected to a flow

$$\boldsymbol{v}_\infty = Gz\boldsymbol{e}_x, \tag{6.144}$$

where G is the shear rate. The effects of such a flow on the droplet is characterized by the dimensionless capillary number - the ratio of viscous to capillary forces [101]

$$Ca = \frac{\eta^{(e)} R_0 G}{\gamma} \tag{6.145}$$

G. I. Taylor calculated the equilibrium shape of a droplet subject to such a flow in the limit of small Ca [135]. For small Ca, the droplets are prolate spheroids. The angle θ the droplet's long axis makes with the z axis (figure 6.12) in the equilibrium is

$$\theta = \frac{\pi}{4} + Ca \frac{(19\lambda+16)(2\lambda+3)}{80(1+\lambda)}. \tag{6.146}$$

And the nowadays named Taylor deformation parameter $D = (a-b)/(a+b)$ in the equilibrium is

$$D = Ca \frac{19\lambda+16}{16\lambda+16}. \tag{6.147}$$

We ran simulations with $\lambda = 1.4$ and varied Ca from 0.03 to 0.3. The figure 6.13 shows a good agreement between theoretical curves and simulation results.

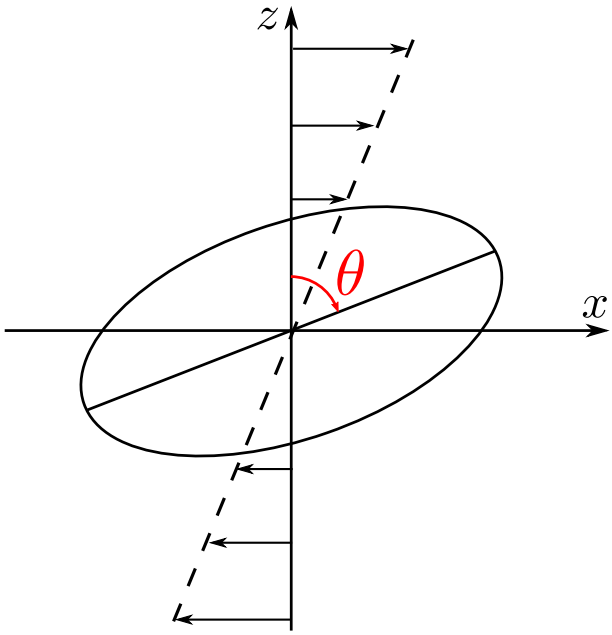

Figure 6.12: Schematic of a droplet in a shear flow.

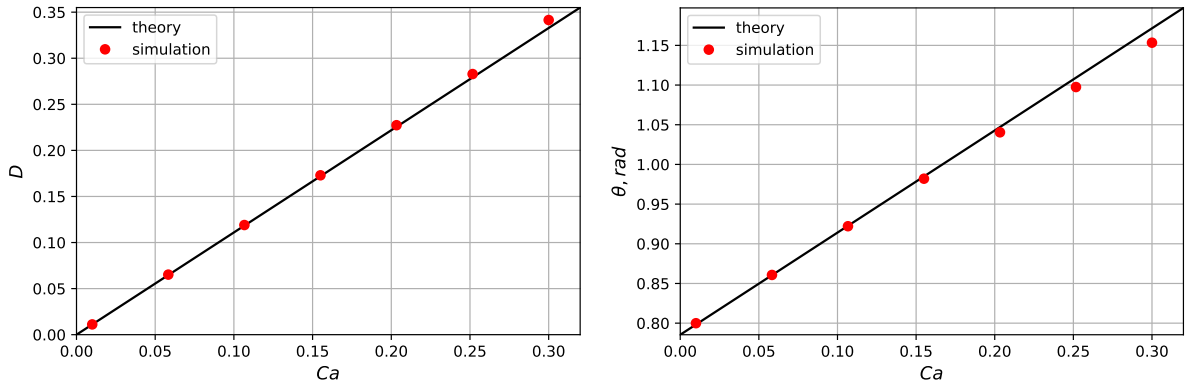

Figure 6.13: Equilibrium shape of non-magnetic droplets with $\lambda = 1.4$ in a shear flow with the capillary number Ca. D is the Taylor deformation parameter and θ is the angle the droplet makes with the z axis. The theoretical curves correspond to the equations (6.147) and (6.146).

6.6.5 Test case: droplet motion in a weak rotating magnetic field

To test the magnetic field induced dynamics, we examine the motion of a droplet subjected to a rotating magnetic field. The governing equations in the limit of a weak field and small deformations were derived in section 5. The droplet is an ellipsoid with semiaxes $a \geq b \geq c$. Additionally the angle β between the droplet's largest axis and the magnetic field is needed to describe its motion. The angle β is negative if the droplet lags behind the field.

We ran a simulation with $\lambda = 100$, $\mu_r = 10$, $Bm = 1$ and the magnetic field angular frequency $\omega = 0.05$. We fitted an ellipsoid to the vertices of the droplet to obtain the semiaxes', and the angle β. We compared it with the numerically evaluated solution to

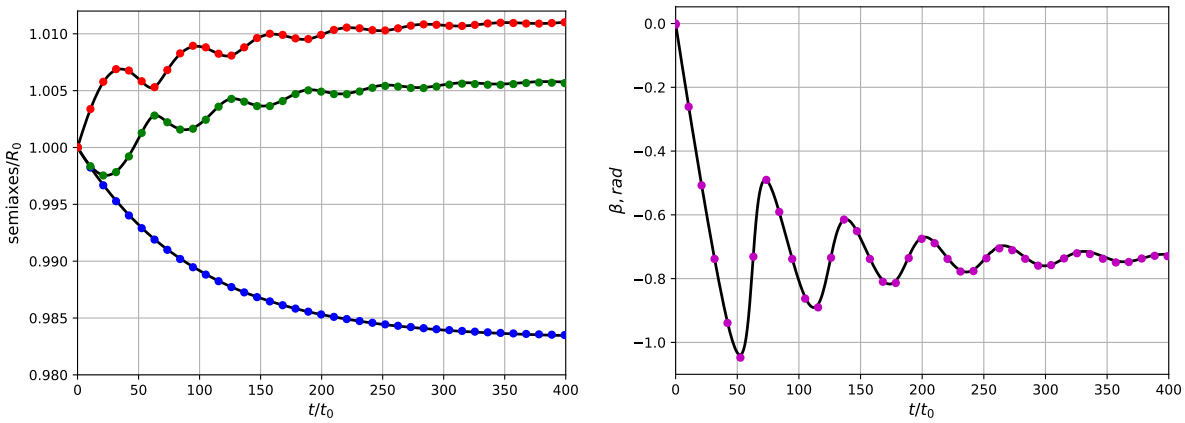

Figure 6.14: The dynamics of an initially spherical droplet subjected to a weak rotating magnetic field. The simulation was done with the $\lambda = 100$, $\mu_r = 10$, $Bm = 1$ and the magnetic field angular frequency $t_0\omega = 0.05$. The times scale is $t_0 = R_0\eta^{(e)}/\gamma$. The points indicate the simulation results (for clarity only every 100th time step is shown). The black curves correspond to the small deformation theory. They are calculated from the numerical integration of the system of ordinary differential equations (5.25).

the system of ordinary differential equations of the deformation parameters ϵ_1, ϵ_2 and the angle β (5.25). The system is stiff and therefore was solved with the `LSODA` algorithm as implemented in the Python `SciPy` library [136]. The comparison between the BEM simulation and the solution to (5.25) can be seen in figure 6.14. There is an excellent correspondence between the two.

6.6.6 Wielandt's deflation effects

When $\lambda \gg 1$, it was show that the integral equations for velocity are ill-posed and can be approximately augmented by the velocity of a rigid body motion. The Wielandt's deflation is a technique that was used to remove the nonphysical rotation and translation of the droplet.

To test its effectiveness, a droplet of $\lambda = 100$, was subjected to a shear flow with $Ca = 2$. The droplet was initially spherical and centered on the origin. The calculations were done with Wielandt's deflation turned on and off (figure 6.15). When the deflation was not implemented, after some time, when the droplet had elongated somewhat, its center of mass started drifting seemingly at random. The drift is not large, however, by implementing the deflation the algorithm does become more robust. There is a small monotone drift also when the deflation is on. This is not surprising since the origin is not a stable fixed point for a shear flow and a small shape asymmetry can result in the drift.

It might be noted that the drift of the center of mass was examined also for the case when the droplet with $\lambda = 100$, $\mu_r = 10$, $Bm = 2$ was elongating in a constant magnetic

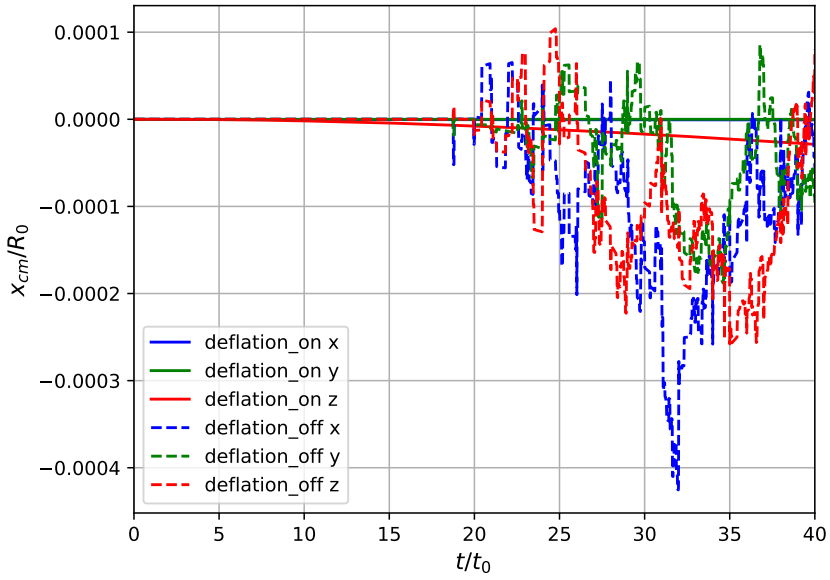

Figure 6.15: The center of mass change for a droplet with $\lambda = 100$ in a shear flow with $Ca = 2$. The solid lines show the center of mass coordinates when Wielandt's deflation was implemented, whereas the dashed lines do so when it was not implemented. The time scale is $t_0 = R_0\eta^{(e)}/\gamma$.

field. There, both when the Wielandt's deflation was active and inactive, the observed drift of the center of mass was close to the floating-point precision. Therefore it seems that whether the ill-posedness of the velocity integral equation plays a role is dependent not only on λ, but also on the setup of the problem.

When $\lambda \ll 1$, the velocity integral equations also become ill-posed. This time a flow proportional to the surface normal might be added to the solution. This would lead to an nonphysical expansion or contraction of the droplet. This nonphysical solution is also eliminated using the Wielandt's deflation.

To test it, we did simulations with a droplet of $\lambda = 0.05$ in a shear flow of $Ca = 0.1$ (figure 6.16). We did not rescale the volume after each time step. Significant volume change was observed when the deflation was not implemented. Interestingly, this time the effects of the nonphysical solution were monotone, as opposed to the random drift of the center of mass. The Euler time stepping scheme might introduce some changes in volume. To examine its effects, the second order Runge-Kutta method was also used. It can be seen that the nonphysical solution produces a roughly 4.4% change in the volume. Whereas, the use of the Euler method results only in 0.4% change to the volume compared to the second order Runge-Kutta method.

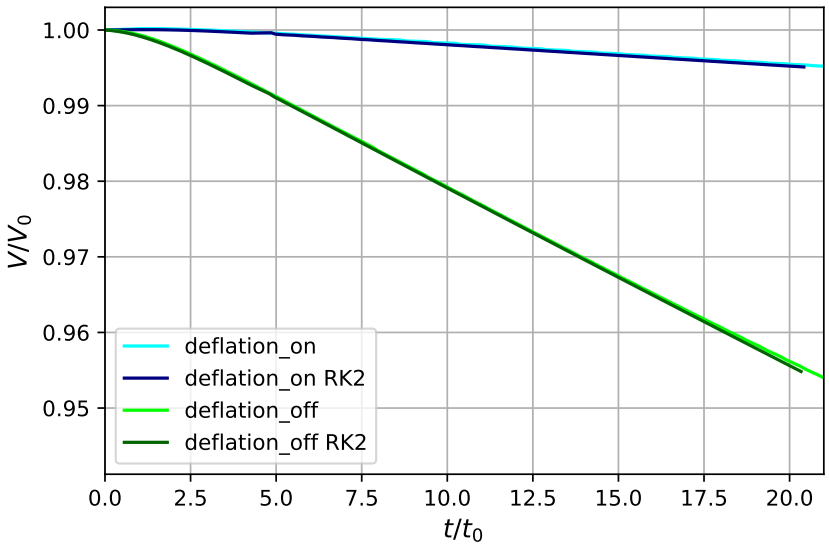

Figure 6.16: The volume V of a droplet with $\lambda = 0.05$ in a shear flow with $Ca = 0.1$. The volume is scaled by the initial volume V_0 of the droplet. Blue lines correspond to the case when the Wielandt's deflation is on, green lines show the case when it is off. Light lines show the simple Euler time stepping, and the dark lines show second order Runge-Kutta methods. The time scale is $t_0 = R_0\eta^{(e)}/\gamma$.

6.6.7 Limits of the algorithm: stretching of a droplet in a constant field

A magnetic droplet in a constant field elongates parallel to it until surface tension forces balance the magnetic forces. When μ_r is above a critical value, and Bm is large, in equilibrium the droplets form conical tips, as was seen experimentally [24]. Theoretical treatment of the problem places the critical magnetic permeability at $\mu_r \gtrsim 15 \ldots 18$, when the droplets can develop sharp tips [56]. Axi-symmetric simulations have been able to reproduce the conical tips [60, 61, 75]. For a full three dimensional simulation the mesh refinement near the sharp tips is a significant challenge.

To test the limits of our algorithm, we stretched a droplet with $\lambda = 100$, $\mu_r = 30$ and $Bm = 5$ (figure (6.17)). This is well within the range of parameters, where conical tips should be forming. If the droplet is assumed to be an ellipsoid, with these parameters in the equilibrium we would expect an aspect ratio of $a/b = 13$ [24]. The addition of vertices in the regions of high curvature can be seen. As the droplet elongates, the radius of curvature of the tips decreases and the number of vertices grows quickly. At $t = 81$ the simulation breaks down without reaching equilibrium. The droplet managed to achieve an aspect ratio of $a/b = 5.4$, measured from tip to tip, since the droplet clearly is no longer an ellipsoid. We can infer that the algorithm can feasibly calculate droplet shapes up to moderate deformations.

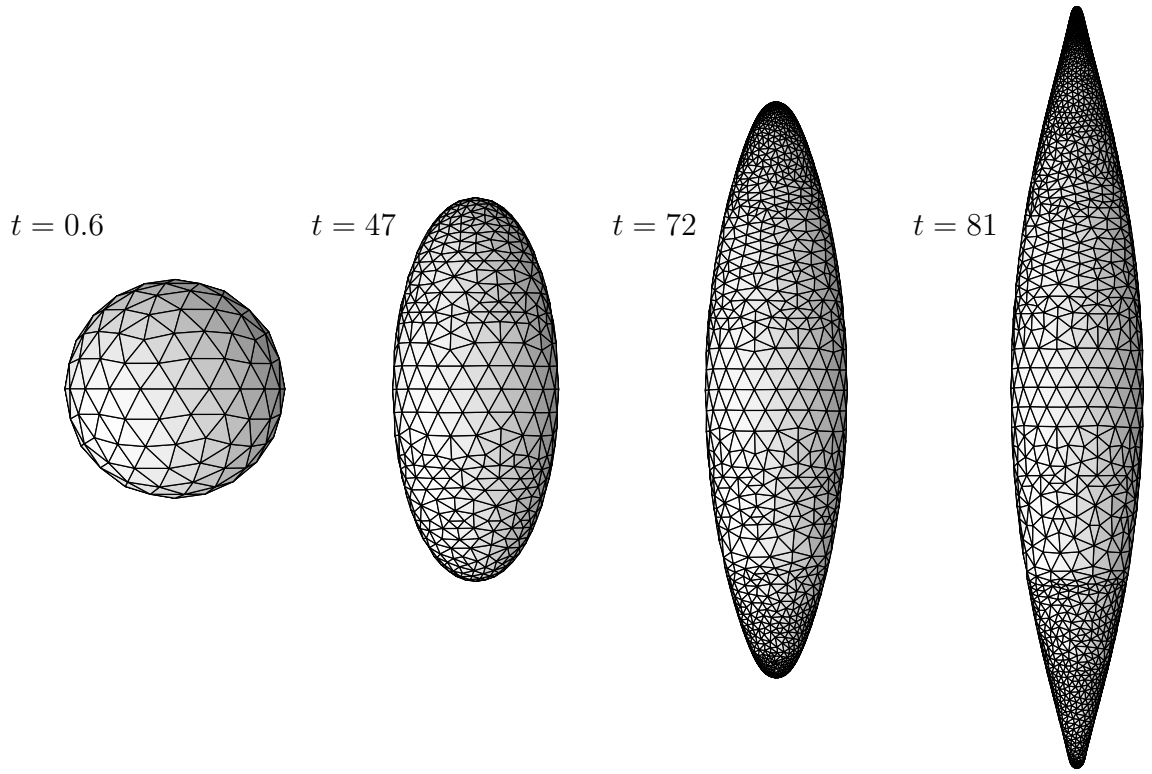

Figure 6.17: The mesh of an elongating droplet in a constant magnetic field. The simulation parameters are $\lambda = 100$, $\mu_r = 30$ and $Bm = 5$. Time of the snapshots are given next to the droplets. The need to refine the sharp tips causes the number of vertices to grow quickly and the simulation breaks down at $t = 81$ without reaching equilibrium.

6.7 Results

6.7.1 Phase diagram of droplets in a rotating field

Depending on the rotating magnetic field frequency ω and strength H_∞, the droplets take up different interesting shapes (see figure 4 in the experimental work [71]). For small H_∞, the droplets are nearly spherical regardless of the frequency. For small ω and large H_∞, the droplets form elongated shapes. For large ω and large H_∞, the droplets are flattened pancake-like shapes, and if the field is not too large, a crown of fingers can be seen on its perimeter. For intermediate range of ω and H_∞ non-stationary shapes can be seen, such as whirling "S" and "8" shaped droplets. In the intermediate range the droplets can break and reform.

Here we explore numerically the dynamics of a magnetic droplet depending on $t_0\omega$ and Bm, where $t_0 = R_0\eta^{(e)}/\gamma$ is the time scale in the simulations. Obviously, the whole range of this motion is beyond the scope of this work. For instance, droplet topology changes and large deformations as of yet can not be tackled with the present algorithm. Furthermore,

the authors of the experimental work [71] explain the intermediate range behavior with the interplay between the normal surface forces arising from the ferrofluid magnetization and tangential surface forces arising from the rotation of magnetic nanoparticles. The latter is not taken into the account in our problem setup.

The simulations were done with the parameters $\mu_r = 10$ and $\lambda = 100$. The characteristic shape deformation time (6.142) is $\tau = 96.3t_0$, where $t_0 = R_0\eta^{(e)}/\gamma$. The simulations halted when the time reached $t = 400t_0$ - several times the characteristic shape deformation time τ, or they halted when the deformations became too large. The μ_r value is the same as in the work by Erdmanis et al. [62], where the droplet equilibrium shapes were explored experimentally and with simulations in the limit $\omega \to \infty$. The λ value is typical for droplets generated by phase separation [62, 68, 71, 96]. Three dimensional ellipsoids were fitted onto the droplet vertices and the time evolution of the ellipsoid semi-axes depending on ω and Bm are shown in a phase diagram (figure 6.18).

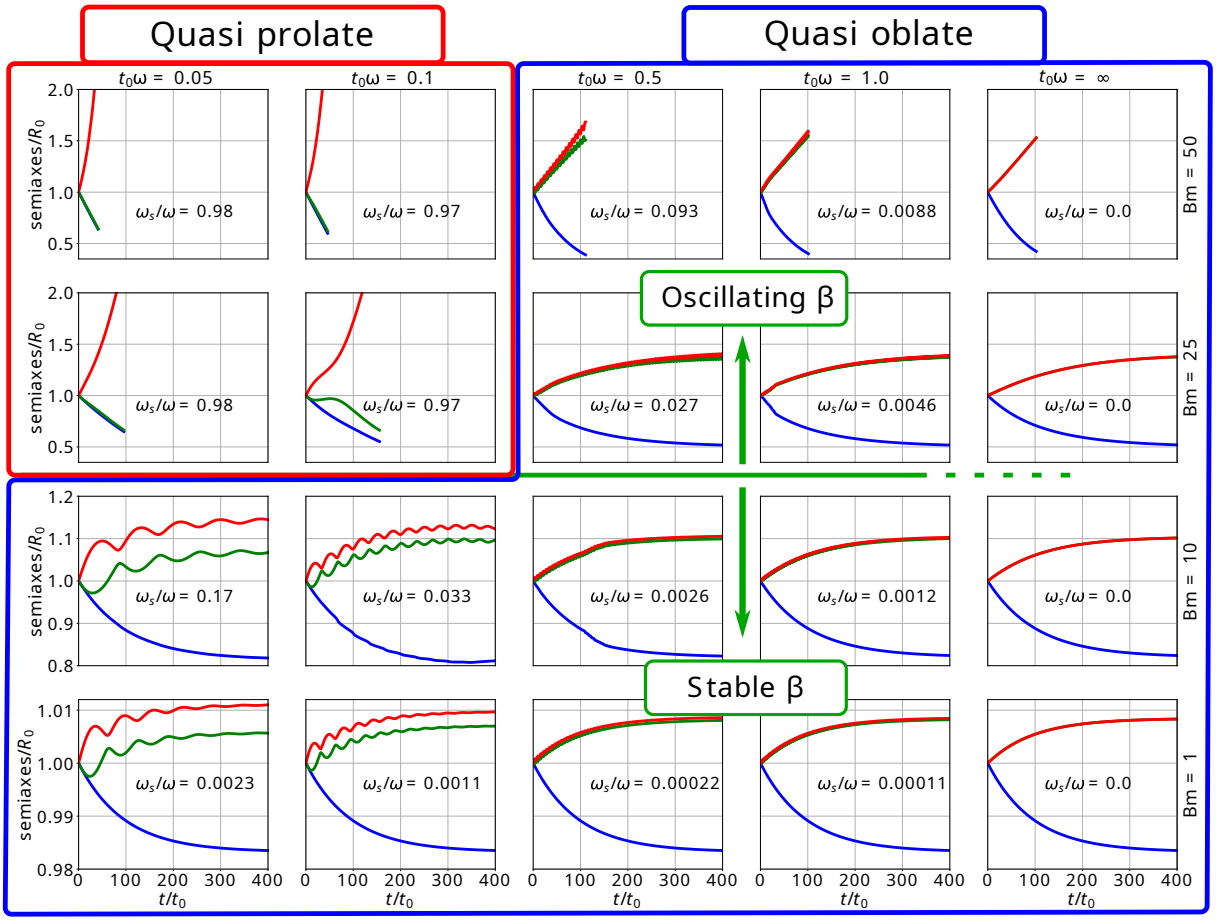

Figure 6.18: Phase diagram showing the evolution of droplet semi-axes depending on ω and Bm. The simulation parameters are $\mu_r = 10$, $\lambda = 100$. The time scale is $t_0 = R_0\eta^{(e)}/\gamma$. The ratio ω_s/ω characterizes to what extent the droplets rotate as a rigid body on the last simulation step. Values closer to 1 mean the motion is close to the rotation as rigid body. Values close to 0 mean that the droplet changes orientation due to surface deformations. ω_s is calculated using the equation (6.148).

We see that in a rotating field, the droplets in general form a tri-axial shape. The phase diagram can be divided into two qualitatively different regions depending on the droplet shape: quasi-prolate, quasi oblate. Just like in the experimental phase diagram (see figure 4 in [71]), for weak fields, the droplets are nearly spherical. However, with the simulations we can notice their quasi oblate shapes and the oscillations of the semi-axes. When $\omega = 1/t_0$, or $\tau\omega = 96.3$ the semi-axes' oscillations are almost imperceptible and the time evolution is nearly that of the period-averaged calculations ($t_0\omega = \infty$).

Increasing the magnetic field, for small ω the droplets elongate forming quasi prolate shapes. For or larger ω, the droplets again are prolate, but with noticeably large deformations. The Bm values are such that in an infinitely fast rotating field, the droplet would take up an elongated shape [62, 70]. And indeed the initial quasi-oblate shape seems to be unstable. The two longest axes start to diverge in lengths, as can be seen for $t_0\omega = 0.5$ and $Bm = 25$, $Bm = 50$. No symmetry breaking perturbations were introduced for the period-averaged calculations ($t_0\omega = \infty$), but as was shown in the work of Erdmanis et al. [62], such perturbations are essential to induce the transition to an elongated shape. Therefore, the droplets remained oblate. The simulations of the droplet dynamics provide a prediction that the initially spherical droplets first flatten out before elongating in a fast-rotating field.

6.7.2 Do the droplets rotate?

As the droplets undergo motion in the rotating magnetic field, their orientation changes direction i.e. they seem to rotate. Since the droplets are liquid, there are two mechanisms for the change of orientation (figure 6.19). The droplets can rotate as rigid bodies, they can change orientation by surface deformation or a mix of both.

To determine which mechanism is dominant, we calculate the average surface angular velocity

$$\omega_s = \left\langle \frac{|\boldsymbol{x}_p \times \boldsymbol{v}|}{x_p^2} \right\rangle, \tag{6.148}$$

where $\boldsymbol{x}_p$ is the radius vector of a given vertex projected on the rotation plane of the magnetic field (with the center of mass being at the origin), $\boldsymbol{v}$ is the velocity of said vertex. Averaging is done over all the vertices on the droplet. If the droplet takes up a shape that rotates as a rigid body following the magnetic field, the ratio ω_s/ω would be 1. This ratio was calculated for the last simulation step and is shown in the phase diagram (figure 6.18).

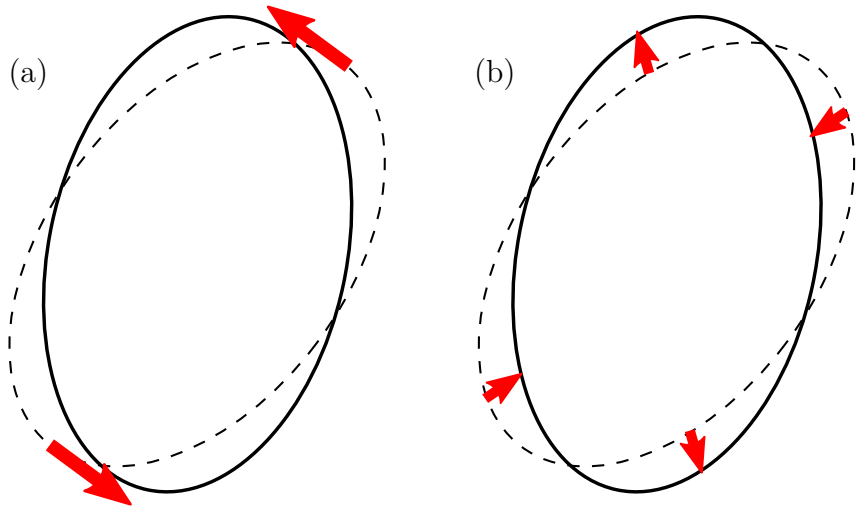

Figure 6.19: The droplets can change their orientation either by (a) rotation as a rigid body, or by (b) surface deformation, or a combinations of both.

When the droplet is quasi-oblate, the ratio $\omega_s/\omega \ll 1$ and the change of orientation cannot be described as a rigid body rotation; the surface deformations dominate. The ratio ω_s/ω grows with increasing Bm and shrinks with increasing ω. Just as was analytically shown in the section 5, below some critical Bm value, the droplets take up equilibrium shapes that follow the magnetic field lagging behind by a constant angle β. However, this motion is a pseudo-rotation caused by surface deformations. For larger Bm, the shapes do not (within the simulation time) reach equilibrium and β remains oscillatory, therefore the motion is more complex, but it still seems to be dominated by surface deformations.

When the droplet is quasi-prolate, the ratio $\omega_s/\omega \approx 1$ and the droplet rotates more or less like a rigid body. Nonetheless, it keeps elongating. It might be noted that for small Bm and small ω we expect for nearly spherical quasi-prolate droplets to be achievable with $\omega_s/\omega \ll 1$. This was shown in section 5.

6.7.3 Examples of motion

Let us examine some cases from the phase diagram (figure 6.18).

An illustrative example for an oblate droplet with stable β is shown in figure 6.20. The droplet is well described by an ellipsoid. Both the axes lengths and the angle undergo oscillations before settling to equilibrium. The angle β always stays negative, meaning that the droplet always follows behind the field. The surface angular velocity is smaller than the angular velocity of the magnetic field, therefore the droplet pseudo-rotates. This type of motion was described analytically in section 5.

A qualitatively different motion can be seen for oblate droplets with oscillating β. A

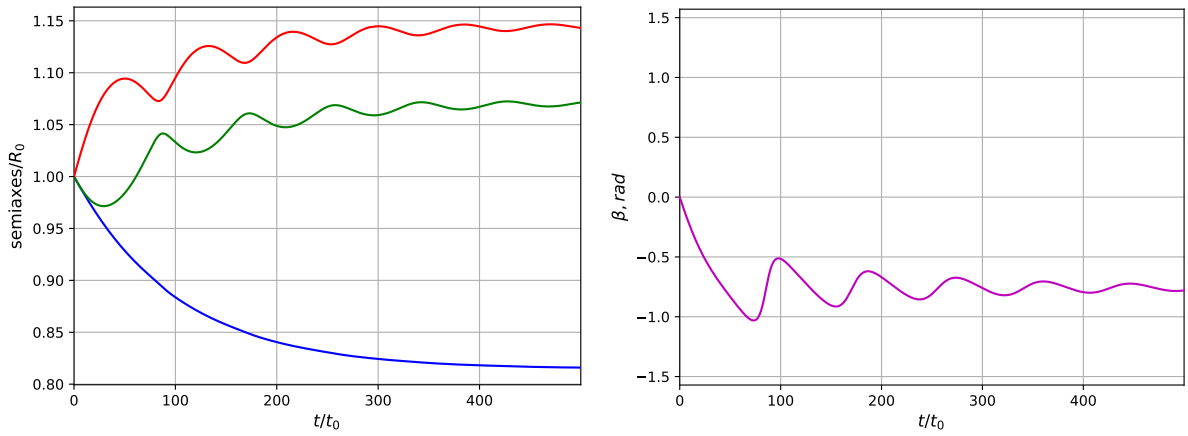

Figure 6.20: Time evolution of the droplet semi-axes (left) and the angle β between the longest axis and the magnetic field (right). Negative β means that the droplet lags behind the field. Simulation parameters are $\lambda = 100$, $\mu_r = 10$, $Bm = 10$, $t_0\omega = 0.05$. The time scale is $t_0 = R_0\eta^{(e)}/\gamma$.

sample case is shown in figure 6.21. Just as before, the droplets in this regime can be well described by an ellipsoid. The axes lengths oscillate, but in contrast with the regime of stable β, the two long axes diverge in length one from the other. Furthermore, the angle β is no longer settling to an equilibrium value. The droplet's longest axis cannot keep up with the rotating magnetic field. After reaching $\beta = -\pi/2$ due to the symmetry of the droplet, β becomes positive indicating that the droplet is leading the field. The positive β quickly decreases to negative values since as the droplet "tries" to align itself with the field. This is reminiscent of the back and forth motion observed in systems of rigid particles rotating under the action of a magnetic field [137, 138].

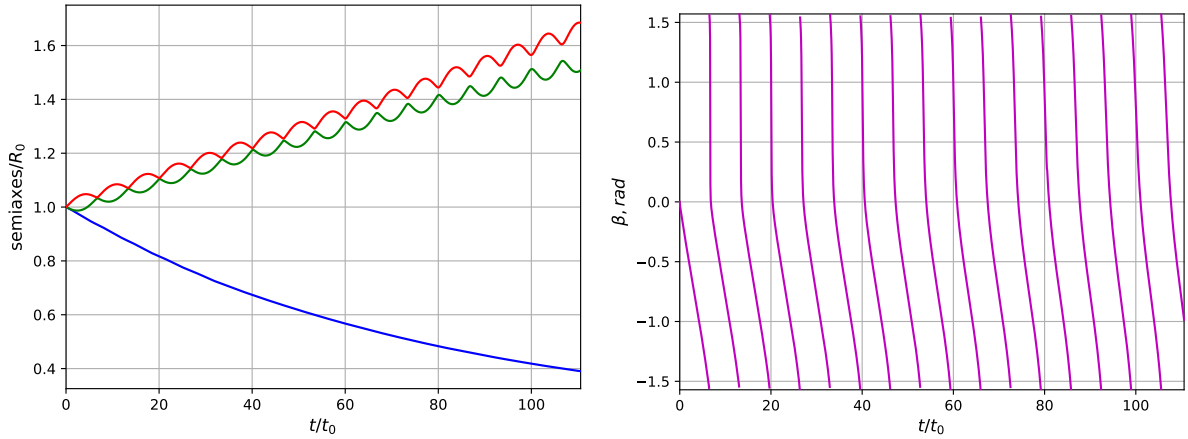

Figure 6.21: Time evolution of the droplet semi-axes (left) and the angle β between the longest axis and the magnetic field (right). Negative β means that the droplet lags behind the field. Simulation parameters are $\lambda = 100$, $\mu_r = 10$, $Bm = 50$, $t_0\omega = 0.5$. The time scale is $t_0 = R_0\eta^{(e)}/\gamma$.

Finally, an example from the quasi-oblate droplet region is shown in figure 6.22. The

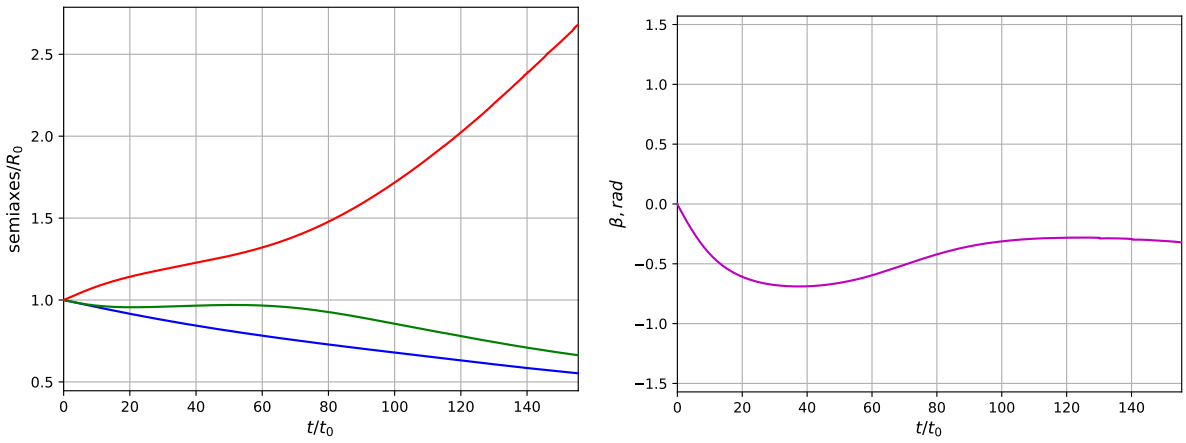

Figure 6.22: Time evolution of the droplet semi-axes (left) and the angle β between the longest axis and the magnetic field (right). Negative β means that the droplet lags behind the field. Simulation parameters are $\lambda = 100$, $\mu_r = 10$, $Bm = 25$, $t_0\omega = 0.1$. The time scale is $t_0 = R_0\eta^{(e)}/\gamma$.

graphs show that with these parameters, the droplet elongates and follows the field with some initial oscillations in both the axes lengths and the angle β. Unlike with the previous cases, here the droplet ceases to be an ellipsoid as shown in figure 6.23. Notably, the tips of the droplet start to bend due to the viscous friction and the droplet forms ”S” like shape in the rotating field.

6.8 Summary and discussion

The model used to describe the droplet (the Stokes equations for velocity and the Laplace equation for the magnetic potential) can be we written in integral equation form, where the integral is over the droplet's surface. This allows us to use the boundary element methods (BEM), where we mesh only the surface of the droplet with triangular elements. We calculate the velocity on the droplet's surface, which is sufficient to determine its deformation in time. The integrals used in BEM are singular and regularization techniques need to be used. They include singularity subtraction, rewriting of the integrals to a less singular form, and the change of basis to local spherical coordinates to calculate weakly singular integrals.

If we move the mesh points with the calculated velocity, the mesh quality rapidly deteriorates. To mitigate it we used several upkeep routines. In each time step, we optimized the tangential component of the velocity to minimize mesh distortion. This alone was not sufficient, and we found it necessary to improve the mesh between the simulation time steps. The simulation software that was created can flip the edges of

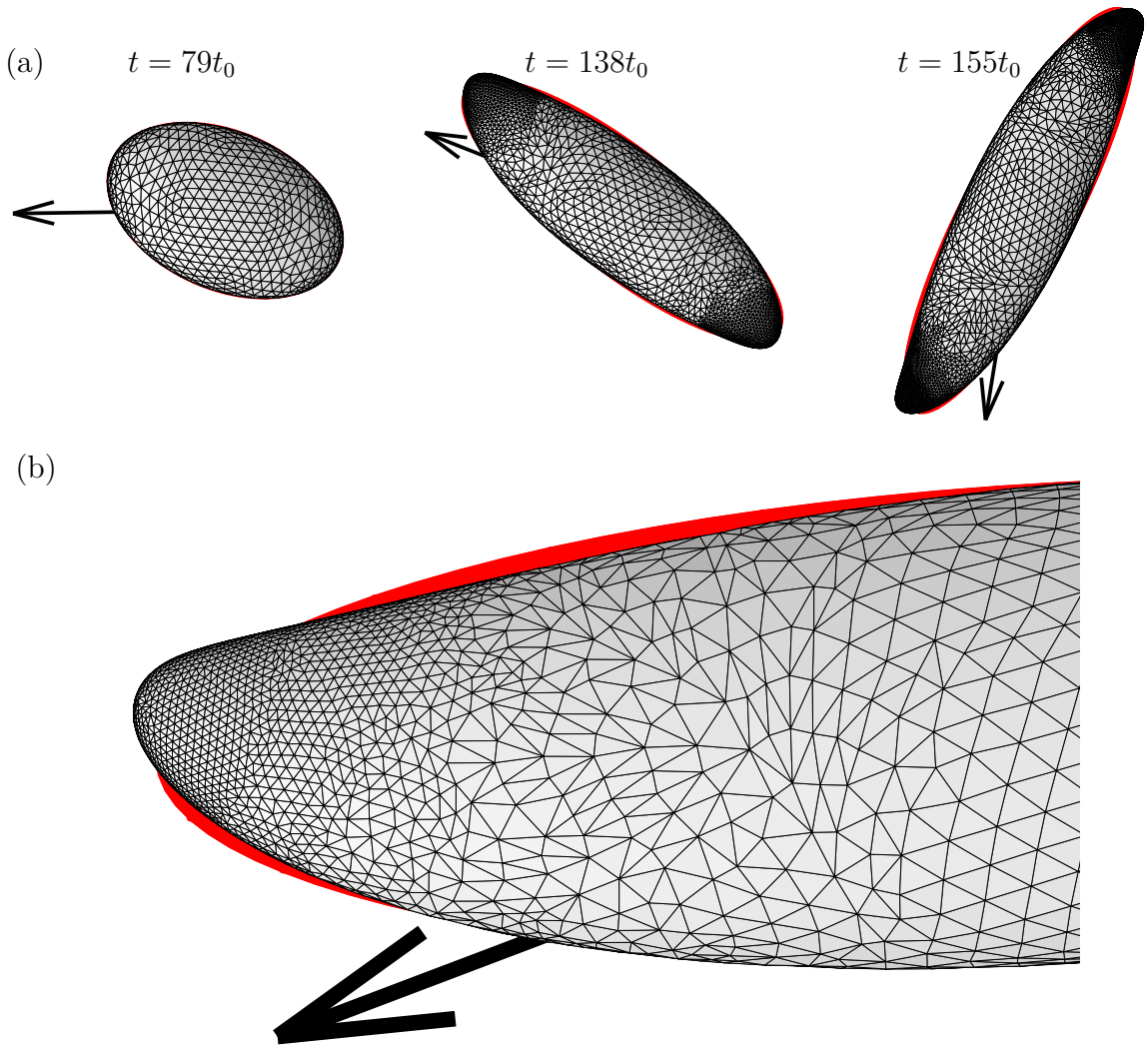

Figure 6.23: The mesh of a droplet with $\lambda = 100$, $\mu_r = 10$, $Bm = 25$, $t_0\omega = 0.1$ in a magnetic field rotating counter-clockwise. The time scale is $t_0 = R_0\eta^{(e)}/\gamma$. The mesh is drawn over a red best-fit ellipsoid do illustrate how similar the droplet shapes are to an ellipsoid. The black arrow denotes the momentary magnetic field direction. (a) shows a snapshot at different times during the simulation. (b) shows a zoomed in part of the mesh at $t = 155t_0$.

triangles, it can slide the mesh points around the droplet, and it can add new mesh points. Particularly the new point addition was crucial to achieve accurate results, however, each new point significantly increases the computation time. The algorithm complexity scales roughly as $O(N^2)$, where N is the number of mesh points.

There exists an unwanted eigensolution to the homogeneous integral equation for the magnetic potential when $\mu/\mu_0 \to \infty$. This eigensolution is just an arbitrary constant, which does not impact the solution when $\mu/\mu_0 \gg 1$, since only the derivatives of the magnetic potential are necessary. There are also unwanted eigensolutions to the homogeneous integral equation for velocity when $\lambda = 0$ and $\lambda \to \infty$. These eigensolutions to

the homogeneous integral equation can distort the solution when $\lambda \ll 1$ or $\lambda \gg 1$. When $\lambda \ll 1$ the true solution can be approximately augmented by a velocity proportional to the surface normal $C\boldsymbol{n}$. When $\lambda \gg 1$ the true solution can be approximately augmented by the velocity corresponding to a solid body motion $\boldsymbol{V} + \boldsymbol{\Omega} \times \boldsymbol{x}$. The accurate convergence of the equations can be ensured by the use of Wielandt's deflation. We show how its use removes seemingly random center of mass fluctuation when $\lambda = 100$, and it improves the volume conservation when $\lambda = 0.05$.

We have produced an algorithm to calculate the magnetic droplet dynamics in the general three dimensional case without the restrictions of axisymmetric shape of the droplet. This is crucial for droplets in a rotating field, since as was shown, the shapes they take up are tri-axial. The simulations are feasible only for moderate droplet deformations, for example, a drop stretching in a constant stationary field can reach the aspect ratio $a/b = 5.4$.

The algorithm allows us to explore with simulations the behavior of magnetic droplets depending on the magnetic field rotation frequency and strength. We find that large frequencies suppress the elongation of the droplet and they form quasi oblate shapes. These quasi oblate shapes, however, have an axis that is slightly longer than others, and this axis follows behind the field. This motion is a pseudo-rotation, since the apparent rotation of the droplet is the result of surface deformations. Whereas if the field is strong and rotation frequency low, the droplets elongate and rotate behind the magnetic field similar to rigid bodies. In this regime, their shape can deviate from an ellipsoidal shape - the tips of elongated droplets can bend due to viscous friction.

There are still some notable limitations to the algorithm. It is unable to calculate the splitting and merger of droplets - something that has been observed experimentally [71]. For this additional mesh restructuring methods would be necessary. Several such methods can be found in the literature [79, 134, 139]. The algorithm could feasibly be extended to work with multiple magnetic and non-magnetic droplets. It could also be extended to take into account a rigid boundary around the solution domain (such as the droplets above an infinite no-slip wall), provided that we can write the appropriate Green's functions.

7 Magnetic droplet collective dynamics

7.1 Introduction

An interesting phenomenon that has received the attention of researchers in the recent years is the field-driven self-assembly of colloids [140]. It has been shown that in a rotating field, solid magnetic particles can self-organize into two dimensional rotating crystals [83, 85, 141]. Another work considered the self-assembly in a precessing field on the surface of a liquid of droplets containing magnetic chains [91]. In this section we present a new kind of two dimensional rotating crystals, where the magnetic droplets self-organize in a rotating field. First, we observe them experimentally. Afterwards, we seek to elucidate the motion of droplets in these crystals using a simple model, that takes into account the hydrodynamic drop-drop interactions and the fact that the droplets are close to the bottom of the microscope cell.

7.2 Experimental observation of droplet ensembles in a rotating field

When placed under the microscope, even the smallest magnetic droplets lie on the bottom glass, as can be seen from the comparison of gravitational and thermal energies. We assume the volume fraction of nanoparticles in the drop $\phi_{drop} \approx 30\%$ [23]. The density of the maghemite nanoparticles is $\rho_{NP} = 4.86\rho_{H_2O}$ [142], where $\rho_{H_2O} = 1000kg/m^3$ is the density of water. This means that the density of the drop is

$$\rho_{drop} = \phi_{drop}\rho_{NP} + (1 - \phi_{drop})\rho_{H_2O} = 2200kg/m^3 \tag{7.1}$$

We take a very small droplet radius $R_0 = 1\mu m$. With these parameters, the characteristic height at which the droplet hovers from the bottom of the cell due to thermal fluctuations is

$$h_0 = \frac{k_B T}{(\rho_{drop} - \rho_{H_2O}) g \frac{4}{3}\pi R_0^3} \approx 80nm, \tag{7.2}$$

where $k_B = 1.38{\cdot}10^{-23}J/K$ is the Boltzmann constant, $T = 293K$ is the room temperature and $g = 9.8m/s^2$ is the free fall acceleration. And we assumed that the density of the dilute phase is nearly that of water.

When a rotating magnetic field ($f = 15Hz$, $\mu_0 H_\infty = 6mT$) is applied, if the droplets are above a critical volume $V_{crit} \approx \pi(3.5\mu m)^3/6$, the droplet takes up a flattened oblate

shape. This flattened drop rotates and sucks in smaller droplets in its immediate neighborhood. If the droplet is smaller than V_{crit}, it elongates to a needle like shape and rotates with the angular velocity of the magnetic field without coalescing, except when sometimes random collisions happen. This behavior is depicted in figure 7.1.

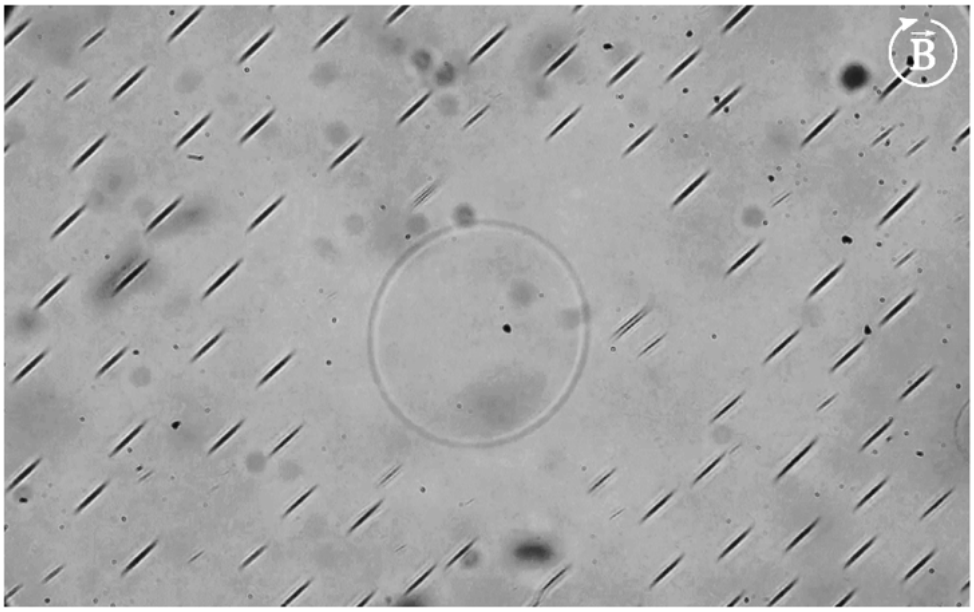

Figure 7.1: A view of droplets after a rotating magnetic field is turned on. Field of view $= 400\mu m \times 250\mu m$. Magnetic field ($f = 15Hz$, $\mu_0 H_\infty = 6mT$) is rotating in the plane of observation. Figure is from [96].

Interestingly, by adjusting the microscope focus, we determined that the elongated droplets are rotating in the same focal plane a distance of $h = (9 \pm 1)\mu m$ above the bottom of the sample cell. And the flattened droplets rotate a couple of μm lower. This is far larger than h_0 expected from the thermal agitation. Other authors also report that when the droplets are rotating, they migrate away from the walls of the microscope cell [71, 143]. The mechanism for this repulsion from the wall remains an open question. In fact, the opposite effect is in place for a rigid sphere rotating close to a wall, where due to inertial effects a force appears that pushes the sphere towards the wall [144].

After some time under the rotating field (couple of minutes) the small elongated droplets arrange themselves in regular structures - two dimensional rotating crystals (see figure 7.2 (a)). The droplets form a lattice with triangular order that itself rotates as a rigid body in the direction of the magnetic field, however, more slowly than it. There is some drift of droplets observed in the outermost layer. The individual droplets within the crystal still rotate with the angular velocity of the field. It was observed that 2 droplets rotate in a stable manner around a common center of mass. 4 droplets form a quadrilateral whose diagonals oscillate in length as the ensemble rotates (see figure 7.2 (b)).

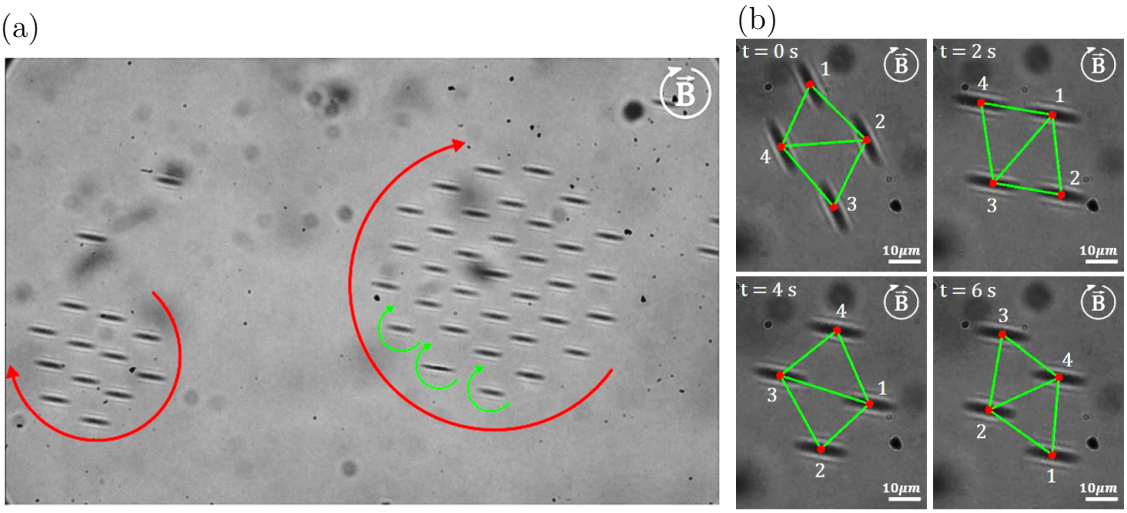

Figure 7.2: Ensembles of rotating magnetic droplets. Magnetic field ($f = 15Hz$, $\mu_0 H_\infty = 6mT$) is rotating in the plane of observation. (a) Shows rotating crystals of needle-like droplets. Field of view = $400\mu m \times 250\mu m$. (b) Shows how four droplets form a rotating quadrilateral with oscillating diagonal lengths. The droplets are labeled 1-4, and are Delaunay triangulated to better illustrate their motion. Snapshots are taken with 2 second increments. Figure is from [96].

If the density of droplets is large, the droplets form crystals that are too large to noticeably rotate (see figure 7.3.). The droplets form a highly regular stationary structure even if the system is non stationary and there is a flow between the droplets produced by their rotation. This can be seen by observing a smaller droplet meandering between the lattice points. By Delaunay triangulating the centers of the droplets, it becomes easier to visualize the crystalline structure. We can observe different grains of the crystal separated by a boundary of dislocations.

Interestingly within the rotating crystal the droplets are much more equal in length than they were at the beginning. We observed how this equilibration of lengths takes place. A small droplet was located between the lattice points of a large crystal of rotating droplets. In time its length (and therefore presumably its volume) increased. The resolution was not good enough to confidently discern how exactly this increase of length occurred. However, it seemed that some small collisions happened between the small droplet and the neighboring droplets that caused the exchange of their material thus growing the small droplet (figure 7.4).

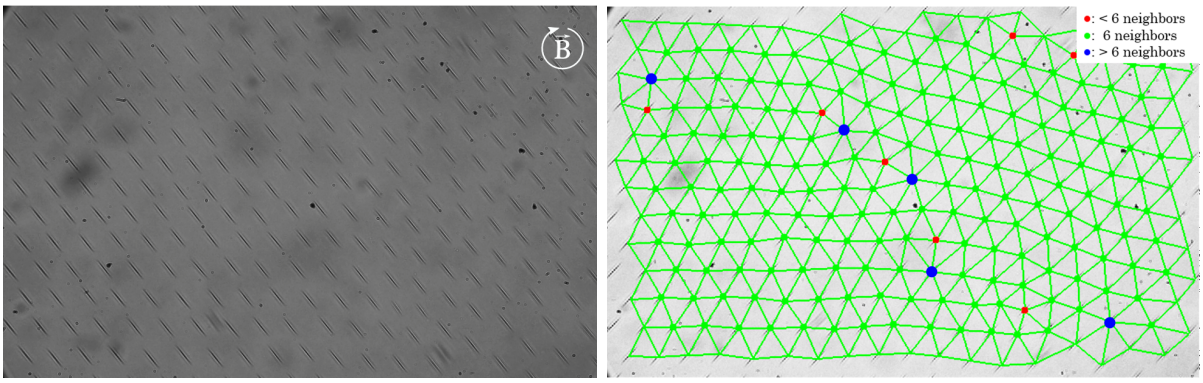

Figure 7.3: If the droplets are densely situated, they organize themselves in a large 2D triangular lattice. Each droplet still rotates in the direction and with the frequency of the magnetic field, but the whole crystal is stationary. On the right side the droplet centers are Delaunay triangulated to illustrate the crystalline structure. Field of view = $400\mu m \times 250\mu m$. Magnetic field ($f = 15Hz$, $\mu_0 H_\infty = 6mT$) and the droplets are rotating in the plane of observation. Figure is from [96].

7.3 Simple model: droplets as point torques

7.3.1 Model formulation

The full dynamics of the ensembles of magnetic droplets are complicated and presently beyond the capabilities of the BEM algorithm. The droplets are highly elongated ($a/b \approx 18$), and there are several of them. Furthermore, the algorithm would need the capability to simulate coalescence and splitting of droplets. Nonetheless we can propose simplified models to see what aspects of the experiment they can replicate.

In this model droplets are treated as point torques acting on the fluid at the center of their mass. Because the droplets are rotating near the bottom of the cell, it is important to take into account the wall effects. The velocity of a viscous fluid vanishes on the wall, which slows down the motion of droplet ensembles.

Consider a no-slip wall located at $z = 0$ ((a) in figure 7.5). The velocity field (called a rotlet) produced by a point torque $\boldsymbol{\mathcal{T}} = \{0, 0, \mathcal{T}\}$ located at $\boldsymbol{y} = \{y_1, y_2, h\}$ is given by [96, 145]

$$\boldsymbol{u}(\boldsymbol{x}) = \frac{1}{8\pi\eta^{(e)}} \left(\frac{\boldsymbol{\mathcal{T}} \times \boldsymbol{X}}{|\boldsymbol{X}|^3} - \frac{\boldsymbol{\mathcal{T}} \times \tilde{\boldsymbol{X}}}{|\tilde{\boldsymbol{X}}|^3} \right), \tag{7.3}$$

where $\boldsymbol{X} = \boldsymbol{x} - \boldsymbol{y}$, and $\tilde{\boldsymbol{X}} = \boldsymbol{x} - \tilde{\boldsymbol{y}}$. $\tilde{\boldsymbol{y}} = \{y_1, y_2, -h\}$ is the location of the image system that insures the no-slip boundary condition at $z = 0$. We will only need to evaluate the rotlet velocity at the centers of mass of the droplets. And since all the droplets are rotating in the same plane a height h above the bottom, $\boldsymbol{x}$ becomes $\{x_1, x_2, h\}$, and the

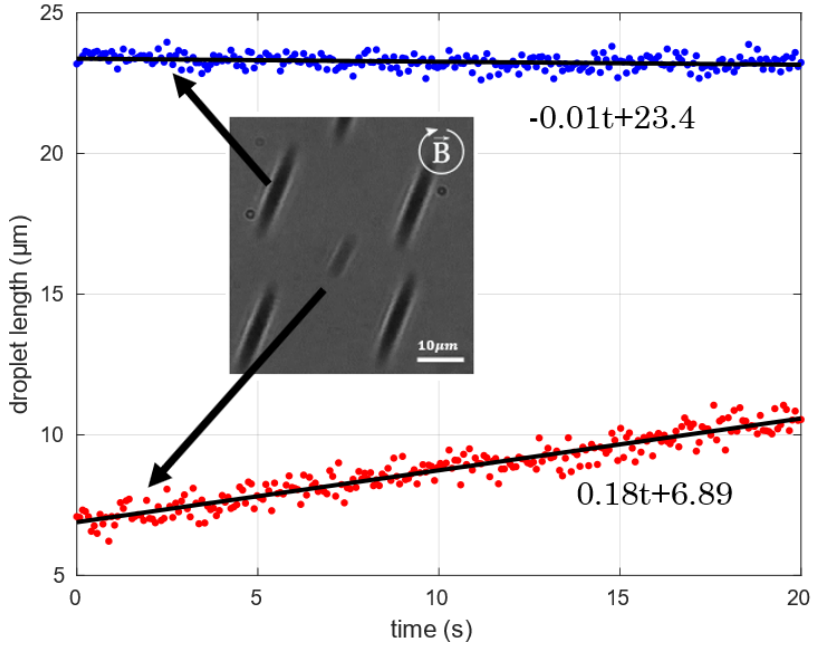

Figure 7.4: The lengths of two droplets within a large stationary crystal. The small droplet finds itself between bigger droplets that form the lattice. The length of the small droplet (red points) increases over time. The length of the large droplet (blue points) remains relatively static. The equations describe a linear fit. Figure is from [96].

expression simplifies

$$\boldsymbol{u}(x_1, x_2) = \frac{\mathcal{T}}{8\pi\eta^{(e)}} \left(\frac{1}{|\boldsymbol{X}|^3} - \frac{1}{(|\boldsymbol{X}|^2 + 4h^2)^{3/2}} \right) \{-(x_2 - y_2), x_1 - y_1, 0\} \,. \tag{7.4}$$

The center of mass velocity of the k-th droplet can be found by summing the rotlet velocities produced by all other rotating droplets evaluated at the center of mass $\boldsymbol{x}_k$ of the k-th droplet ((b) in figure 7.5)

$$\boldsymbol{v}_k = \sum_{j \neq k} \boldsymbol{u}_j(\boldsymbol{x}_k). \tag{7.5}$$

7.3.2 Rotation frequencies of simple configurations of droplets

Since the motion is in a plane, we can denote a droplet's position as a complex number

$$z_k = x_{k1} + i x_{k2}. \tag{7.6}$$

Then according to equations (7.4) and (7.5) the droplet positions evolve as

$$\frac{dz_k}{dt} = i \frac{\mathcal{T}}{8\pi\eta^{(e)}} \sum_{j \neq k} \left(\frac{1}{|z_k - z_j|^3} - \frac{1}{(|z_k - z_j|^2 + 4h^2)^{3/2}} \right) (z_k - z_j). \tag{7.7}$$

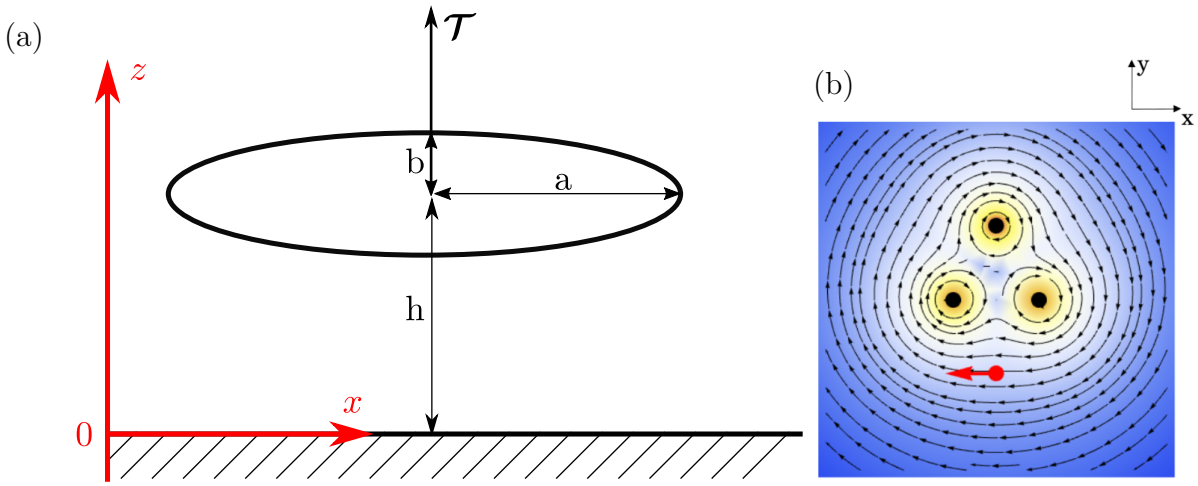

Figure 7.5: (a) shows a schematic of a droplet rotating in the direction perpendicular to the no-slip wall. (b) illustrates how the droplet center of mass velocities are calculated. If there are four droplets in the ensemble, the velocity of the fourth drop (shown in red) is found by adding the velocities produced by the other three droplets (shown in black). The streamlines show the flow produced by the three black droplets.

Numerical solutions show that simple symmetrical configurations of droplets rotate as a rigid body with an angular velocity Ω. Examples of such configurations include two droplets some distance apart, and four droplets positioned on the vertices of a square. In a reference frame that rotates with Ω around the center of mass of the droplet ensemble these solutions would be stationary. This motivates us to replace $z_k \leftarrow (z_k - z_{cm})e^{i\Omega t}$ to arrive at the differential equations for z_k in the rotating frame of reference

$$\frac{dz_k}{dt} = i\left[-\Omega(z_k - z_{cm}) + \frac{\mathcal{T}}{8\pi\eta^{(e)}}\sum_{j\neq k}\left(\frac{1}{|z_k - z_j|^3} - \frac{1}{(|z_k - z_j|^2 + 4h^2)^{3/2}}\right)(z_k - z_j)\right], \tag{7.8}$$

where z_{cm} is the center of mass of the droplet ensemble.

Let us look at the case of two droplets with the inter-drop distance R orbiting one another. We can choose their coordinates such that the center of mass is zero

$$z_1 = \frac{R}{2}e^{i\Omega t}, \quad z_2 = -\frac{R}{2}e^{i\Omega t}. \tag{7.9}$$

By inserting them in equation (7.8), we arrive at the angular frequency of the two droplet orbiting motion

$$\Omega_{2d} = \frac{\mathcal{T}}{8\pi\eta^{(e)}}\left(\frac{2}{R^3} - \frac{2}{(R^2 + 4h^2)^{3/2}}\right) \tag{7.10}$$

Now let us look at the case of four droplets in the configuration of a square with the

diagonal R. Again we can choose their coordinates such that the center of mass is zero

$$z_1 = \frac{R}{2}e^{i\Omega t}, \quad z_2 = i\frac{R}{2}e^{i\Omega t}, \quad z_3 = -\frac{R}{2}e^{i\Omega t}, \quad z_4 = -i\frac{R}{2}e^{i\Omega t}. \tag{7.11}$$

By inserting them in equation (7.8), we arrive at the angular frequency of four droplets in square configuration orbiting their center of mass

$$\Omega_{4d} = \frac{\mathcal{T}}{8\pi\eta^{(e)}}\left(\frac{2+4\sqrt{2}}{R^3} - \frac{2}{(R^2+4h^2)^{3/2}} - \frac{4\sqrt{2}}{(R^2+8h^2)^{3/2}}\right). \tag{7.12}$$

A similar procedure can be carried out to get the orbiting frequencies of other number of droplets arranged symmetrically on a circle.

7.3.3 Evaluation of the torque exerted by the droplet

To calculate the torque exerted on the fluid by the droplet as it rotates, we treat the droplet as a rigid elongated ellipsoid. Such an approximation is justified since the viscosity of the droplet over the viscosity of the surrounding fluid was measured to be $\lambda \approx 1460$. Furthermore, from the simulations we conclude that the droplet rotates nearly like a rigid body when it is strongly elongated.

When a slender rigid body rotates perpendicular to the no-slip wall, the torque it exerts is similar to that of the body rotating in an infinite fluid (figure 15 in [146]). And the droplets in the ensembles can be considered slender (their aspect ratio is $a/b \approx 15$). Therefore for simplicity we used the expression for a torque of a rotating ellipsoid in an infinite fluid (page 56 of [116])

$$\mathcal{T} = \frac{16\pi ab^2}{3(a^2\alpha_0 + b^2\beta_0)}(a^2+b^2)\left(\omega - \omega_{\text{fluid}}\right), \tag{7.13}$$

where $a > b$ are the semiaxes of the prolate spheroidal droplet, ω is the angular frequency of the rotating droplet (or the magnetic field), ω_{fluid} is the z component of the local rotation angular velocity of the fluid $\boldsymbol{\nabla} \times \boldsymbol{v}/2$. Finally, the constants α_0 and β_0 are given by

$$\alpha_0 = ab^2\int_0^\infty \frac{dt}{(a^2+t)\Delta(t)}, \quad \beta_0 = ab^2\int_0^\infty \frac{dt}{(b^2+t)\Delta(t)}, \quad \Delta(t) = \sqrt{(a^2+t)(b^2+t)^2}. \tag{7.14}$$

Inserting the droplet parameters from an experiment $a = (9.0 \pm 0.3)\mu m$, $b = (0.6 \pm$

$0.2)\mu m$, $\omega = 2\pi \cdot 14.5 Hz$ and assuming that the surrounding fluid is water $\eta^{(e)} = 10^{-3} Pa{\cdot}s$, we get a characteristic torque that a droplet exerts

$$\mathcal{T} = (1.9 \pm 0.4) \cdot 10^{-16} N \cdot m. \tag{7.15}$$

We find that the z component of $\omega_{\text{fluid}} \ll \omega$ for the experimental inter-droplet distances, therefore it was omitted from the evaluation of $\mathcal{T}$.

7.3.4 Comparison with experiment

Since the ensembles of droplets can rotate while the inter-drop distances change (see (b) in figure 7.2), we define the angular velocity of an ensemble as

$$\Omega = \left\langle \frac{|(\boldsymbol{x}_k - \boldsymbol{x}_{cm}) \times \boldsymbol{v}_k|}{|\boldsymbol{x}_k - \boldsymbol{x}_{cm}|^2} \right\rangle, \tag{7.16}$$

where the the average is taken over all the droplets k, $\boldsymbol{x}_k$ is the position of k-th droplet, $\boldsymbol{v}_k$ is its velocity, and $\boldsymbol{x}_{cm}$ is the location of the center of mass of the droplet ensemble.

	Experiment	Theory
2 drops $\Omega, rad/s$	0.66 ± 0.04	0.6 ± 0.1
4 drops $\Omega, rad/s$	0.47 ± 0.04	0.6 ± 0.1
4 drops $\Omega_{\text{diag}}, rad/s$	0.95 ± 0.02	1.1 ± 0.2
4 drops $\Omega_{\text{diag}}/\Omega$	2.0 ± 0.2	1.71 ± 0.02

Table 4: Comparison between the experimental and theoretical values of the rotation frequencies of small ensembles of droplets. For ensemble of four droplets also the angular frequency of diagonal length oscillation is shown.

First, we experimentally observe two droplets orbiting a common center of mass. We use the formula (7.16) to calculate the experimental angular orbiting velocity Ω. Then we can use the formula (7.10) to calculate the theoretical Ω. The results are shown in table 4. The errors in the theoretical values are obtained by varying the measured input parameters within their error bounds. We see that for 2 droplets, the simple model replicates the experimental orbiting frequency.

Second, we calculate the experimental Ω for the ensemble of four droplets (see (b) in figure 7.2). However, since the droplets do not form a rectangle, but rather a quadrilateral whose diagonals oscillate, we cannot use the formula (7.12) to calculate the theoretical

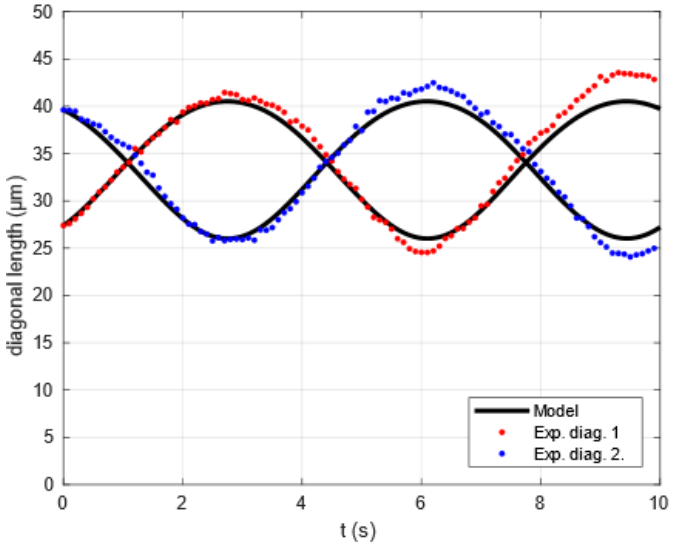

Figure 7.6: Diagonal oscillations in an ensemble of four droplets. The blue and red points are experimental values. The black lines show the solution of model (7.7), where input parameters were adjusted within the margins of error to produce a good agreement with the experimental oscillations. Figure is from [96].

Ω. We therefore numerically solve equation (7.7) with the initial positions of the droplets taken from the experiment. And we calculate the theoretical Ω also with the formula (7.16). Interestingly, in the solution of the simple model, the diagonal oscillation is replicated (figure 7.6). The diagonal oscillations Ω_{diag} were fitted with a sinusoidal function to determine their frequencies. Both the angular velocity of the ensemble and the diagonal oscillation frequency are shown in table 4. We see that for 4 droplets, the simple model replicates both Ω and Ω_{diag} within the margins of error. However, the ratio of the two is not captured accurately by the model. Interestingly, while the error in the length and width of the droplet is the main source of uncertainty in the theoretical values of Ω and Ω_{diag}, the error in height h from the bottom of the cell produces the most uncertainty in their ratio $\Omega_{\text{diag}}/\Omega$.

The model cannot replicate the motion of larger ensembles of droplets (for example (a) in figure 7.2). Since there is nothing enforcing the equilibrium distance between the droplets, large ensembles of droplets do not rotate as rigid crystals, but instead quickly disintegrate.

7.4 Summary and discussion

When placed under a rotating field, the microscopic magnetic droplets obtained by phase separation of ferrofluid can arrange themselves in regular rotating ensembles - two

dimensional rotating crystals. This happens with small enough droplets, whose volume is below the critical volume $V_{crit} \approx \pi(3.5\ \mu m)^3/6$. Interestingly even though the droplets are much denser than the surrounding dilute phase, after the rotating field is turned on they migrate to around 9 μm above the bottom of the microscope cell. The individual droplets themselves rotate in the field direction, and additionally they drive the rotation of the crystal. Except for the outermost layer, the droplets in a crystal rotate as a rigid body. When the density of the droplets in the sample is large, they form large crystals, who do not noticeably rotate.

We introduced a simple model, which states that each droplet moves with the flow produced by all the other droplets in the ensemble. The droplets concentrate the torque in a single point in their center of mass, which produces a rotlet flow around them. In this rotlet flow we take into account that the droplets are all 9 μm above a no-slip wall. This simple model worked well to quantitatively describe the motion of small ensembles of droplets. Since in the model there are no forces determining the equilibrium between the droplets, the ensembles are not rigid. In our paper, where we first described the ensemble behavior of magnetic droplets [96], we proposed an attractive magnetic force between the droplets. It would have to be counteracted by a sufficiently large repulsive force. In the paper [96] we proposed a hydrodynamic repulsion due to finite Reynolds number [147], which unfortunately was too small by two orders of magnitude. The mechanism which determines the equilibrium distance between the droplets remains an open question.

8 Conclusions

In this work we studied the dynamics of magnetic fluid droplets under a rotating field. The droplets were buoyant in an external liquid medium, whose viscosity is significantly smaller than the viscosity of the droplets themselves. We first studied these droplets as single and isolated deforming objects, second as self-organized ensembles of objects with collective dynamics. Several complementary approaches were used to describe the dynamics of the isolated droplets. For the simple case of a nearly spherical droplet, we produced analytic expressions that are easy to analyze. We then developed simulations to be able to calculate the dynamics of droplets with larger deformations. Finally, we examined experimentally a magnetic droplet obtained by phase separation to see to what extent the magnetic fluid model used in the previous two approaches can describe their behavior in a rotating field. Concerning the collective behavior of magnetic droplets in a rotating field, we first observed it experimentally and then a simple model was proposed to capture their dynamics.

When the magnetic field and thus the deformation of an individual droplet is small, we showed how a phenomenological equation for the anisotropy tensor that describes the droplet's shape can be used to calculate its dynamics in a rotating or precessing field. By modeling the droplet as region of magnetic fluid in a nonmagnetic carrier liquid, we can use the Lamb's solution for the Stokes equations in spherical coordinates to calculate the dynamics of the droplets in the limit of small deformations. We showed that this hydrodynamic solution coincides with the solution of the phenomenological equations up to the first order in magnetic Bond number Bm and deformation amplitude ε. In this limit, the motion of the magnetic droplet in a rotating field is governed by a single dimensionless parameter $\tau\omega$ - the product of the characteristic small deformation decay time and the field rotation angular frequency. $\tau\omega$ determines whether the droplet will be more elongated or more flattened and whether its shape will undergo oscillations as it settles to an equilibrium. The droplet pseudo-rotates: it appears to follow the rotating magnetic field, but this motion is due to surface deformations and no torque is exerted by the droplet on the fluid. According to the small deformation theory, the value of the small deformation decay time τ should be the same in a rotating field and in a stationary or zero field. Experimentally the value τ_{rel} describing the exponential approach to the equilibrium shape is a couple of orders of magnitude larger than the τ_{rot} obtained from the equilibrium shape of the droplet in a rotating field. Therefore, the magnetic fluid model

that takes into account only the normal surface force due to Maxwell stress tensor needs to be improved to be able to quantitatively describe the motion of magnetic droplets in a rotating field.

We were able to model a droplet without the limitation of small deformations of our analytical description, using a simulation based on the boundary element method (BEM). We can use the BEM simulation to calculate the three-dimensional dynamics of a droplet in external magnetic and flow fields up to moderate droplet deformations. Significant mesh upkeep is required to accurately simulate the droplet dynamics. It was shown by the BEM simulations that in a rotating magnetic field the droplets take up a tri-axial shape that can slightly deviate from an ellipsoid. For example, the tips of an elongated droplet become bent due to viscous friction, which is something observed experimentally. We see that for large Bm and small magnetic field rotation frequency ω, droplets elongate and rotate similar to rigid bodies following the rotating magnetic field. However, large magnetic field rotation frequency ω suppresses the elongation of droplets, and their shape is close to oblate. In this regime the droplets pseudo-rotate: they follow the rotating magnetic field due to surface deformations. According to the simulations, other important observations are recovered, for example, in a fast-rotating field with the field strength above the oblate-prolate shape instability [68, 62], an initially spherical droplet first flattens before elongating. And indeed, using the BEM simulations it was possible to determine the limits of applicability of the small deformation theory.

For ensembles of droplets, we observed for the first time rotating ordered out-of-equilibrium structures of magnetic droplets in a rotating field - for certain field parameters, the elongated needle-like droplets form two-dimensional rotating crystals of triangular order. The droplets in the crystals rotate with the frequency of the magnetic field, however, the crystals themselves rotate slower. The rotation frequency of the crystal decreases with its size, and very large crystals seemed to be stationary in the experiment. The ensembles of droplets exhibit typical features of two-dimensional crystal, such as different grains connected by a boundary of dislocations. The droplets in the crystal all organize themselves into a single plane rotating about 9 μm above the bottom of the experimental cell. The model that treats the droplets as point torques above a no-slip wall is able to quantitatively reproduce the motion of small ensembles of droplets. However, the model ceases to be accurate when the size of the ensembles increases. Since in the model there are no forces that determine the equilibrium distance between the droplets, large ensembles of droplets do not form rotating crystals, but instead disintegrate.

In summary we can conclude the following. Magnetic fluid model is able to qualitatively describe the motion in a rotating field of individual magnetic fluid droplets obtained by phase separation. BEM simulations can be used to effectively study the complicated shape dynamics of such magnetic fluid droplets. Rotating magnetic fluid droplets can collectively produce intricate non-equilibrium structures, which are not yet fully understood.

A Derivations

A.1 Magnetostatics equations

Equations of magnetostatics

$$\boldsymbol{\nabla} \times \boldsymbol{H} = \boldsymbol{0}, \quad \boldsymbol{\nabla} \cdot \boldsymbol{B} = 0 \tag{A.1}$$

are an approximation of Maxwell's equations in media.

Let us illustrate what is assumed in employing this approximation. For simplicity let us look at an unmoving medium. The full Maxwell's equations in media read [2]

$$\begin{aligned} \boldsymbol{\nabla} \times \boldsymbol{H} &= \boldsymbol{j} + \frac{\partial \boldsymbol{D}}{\partial t}, \quad \boldsymbol{\nabla} \cdot \boldsymbol{B} = 0, \\ \boldsymbol{\nabla} \times \boldsymbol{E} &= -\frac{\partial \boldsymbol{B}}{\partial t}, \quad \boldsymbol{\nabla} \cdot \boldsymbol{D} = \rho, \end{aligned} \tag{A.2}$$

where $\boldsymbol{E}$ and $\boldsymbol{D} = \epsilon \boldsymbol{E}$ are the electric field intensity and induction, ϵ is the permittivity of the medium. ρ is the free charge density, $\boldsymbol{j}$ is the free current density in the medium.

The equation $\boldsymbol{\nabla} \cdot \boldsymbol{B} = 0$ already holds. A current arises in the body described by the Ohm's law

$$\boldsymbol{j} = \sigma \boldsymbol{E}, \tag{A.3}$$

where σ is the conductivity of the medium. The droplets are electrically neutral and there is no free charge $\rho = 0$. Therefore, we assume that the only way electric field arises is because of the changing magnetic field. This leaves us with two coupled equations

$$\begin{cases} \boldsymbol{\nabla} \times \boldsymbol{H} = \sigma \boldsymbol{E} + \epsilon \dfrac{\partial \boldsymbol{E}}{\partial t} \\ \boldsymbol{\nabla} \times \boldsymbol{E} = -\mu \dfrac{\partial \boldsymbol{H}}{\partial t} \end{cases}. \tag{A.4}$$

Let the system have a characteristic time scale t_0, a characteristic length scale R_0, a characteristic magnetic field intensity scale H_0, and a characteristic electric field intensity scale E_0. Then from the second equation in (A.4) we can relate them

$$\frac{E_0}{H_0} = \mu \frac{R_0}{t_0}. \tag{A.5}$$

Writing the first equation in dimensionless variables $\tilde{t} = t/t_0$, $\tilde{x} = x/R_0$, $\tilde{\boldsymbol{H}} = \boldsymbol{H}/H_0$,

$\tilde{\boldsymbol{E}} = \boldsymbol{E}/E_0$, we have

$$\tilde{\boldsymbol{\nabla}} \times \tilde{\boldsymbol{H}} = \frac{\mu\sigma R_0^2}{t_0}\tilde{\boldsymbol{E}} + \epsilon\mu\frac{R_0^2}{t_0^2}\frac{\partial\tilde{\boldsymbol{E}}}{\partial\tilde{t}}. \tag{A.6}$$

The following holds $\epsilon\mu = \epsilon_r\mu_r/c^2$, where the index r denotes the relative permittivity and permeability, and c is the speed of light. But for the droplets $\mu_r \approx 30$ and $\epsilon_r \approx 80$ (water relative electric permittivity). We equate R_0 with the droplet's radius $R_0 = 10\ \mu m$ and t_0 with the reciprocal of the maximum rotating field frequency $t_0 = 1/(1000Hz) = 0.1ms$. Therefore the coefficient in front of the second term is

$$\epsilon\mu\frac{R_0^2}{t_0^2} = 10^{-16}. \tag{A.7}$$

And taking an extreme value for the electric conductivity $\sigma = 20S/m$ (which is the conductivity of 4M NaCl solution [148]), we have the coefficient in front of the first term on the right-hand side

$$\frac{\mu\sigma R_0^2}{t_0} = 10^{-9}. \tag{A.8}$$

Therefore, on the scale of the magnetic droplets the magnetostatic equations are an excellent approximation.

A.2 Magnetic pressure

We can write the body force density due to the Maxwell stress tensor $T_{ik} = -\mu_0 H^2\delta_{ik}/2 + H_i B_k$ as

$$\begin{aligned} f_i &= \frac{\partial T_{ik}}{\partial x_k} \\ &= -\mu_0\frac{1}{2}\frac{\partial H_k H_k}{\partial x_i} + \frac{\partial H_i B_k}{\partial x_k} \\ &= -\mu_0 H_k\frac{\partial H_k}{\partial x_i} + B_k\frac{\partial H_i}{\partial x_k} \\ &= \mu_0 M_k\frac{\partial H_i}{\partial x_k}, \end{aligned} \tag{A.9}$$

where we used the fact that $\partial_k B_k = 0$ and $\partial_k H_i = \partial_i H_k$ as follows from Maxwell's equations.

When magnetization is linear ($\boldsymbol{M} = (\mu/\mu_0 - 1)\boldsymbol{H}$), we can write the body force density

as a negative gradient of the magnetic pressure

$$\begin{aligned} f_i &= \mu_0 M_k \frac{\partial H_i}{\partial x_k} \\ &= \mu_0 \left(\frac{\mu}{\mu_0} - 1 \right) H_k \frac{\partial H_k}{\partial x_i} \\ &= \frac{1}{2} \mu_0 \left(\frac{\mu}{\mu_0} - 1 \right) \frac{\partial H_k H_k}{\partial x_i} \stackrel{def}{=} -\frac{\partial p_M}{\partial x_i}. \end{aligned} \tag{A.10}$$

A.3 Magnetic surface force

The normal force due to the Maxwell stress tensor acting on a surface element is

$$\begin{aligned} f_n = n_i T_{ik} n_k &= n_i (-\mu_0 \frac{1}{2} H^2 \delta_{ik} + H_i B_k) n_k \\ &= -\mu_0 \frac{1}{2} H^2 + H_n B_n \\ &= -\mu_0 \frac{1}{2} H_n^2 + H_n B_n - \mu_0 \frac{1}{2} H_t^2 \\ &= -\mu_0 \frac{1}{2} (\frac{B_n^2}{\mu_0^2} - 2 \frac{B_n^{(i)}}{\mu_0} M_n^{(i)} + M_n^2) + (\frac{B_n^{(i)}}{\mu_0} - M_n^{(i)}) B_n^{(i)} - \mu_0 \frac{1}{2} H_t^2 \\ &= \frac{B_n^2}{2\mu_0} - \frac{\mu_0}{2} M_n^2 - \frac{\mu_0}{2} H_t^2 \end{aligned} \tag{A.11}$$

where the index n denotes the normal component and t the tangential component. On the droplet's surface H_t is continuous and B_n is continuous. Therefore the normal force difference on the boundary due to the Maxwell stress tensor is

$$f_n^{(e)} - f_n^{(i)} = \frac{\mu_0}{2} {M_n^{(i)}}^2, \tag{A.12}$$

since the magnetization of the surrounding fluid is zero.

The tangential force due to the Maxwell stress tensor acting on a surface element is

$$\begin{aligned} f_t = t_i T_{ik} n_k &= t_i (-\mu_0 \frac{1}{2} H^2 \delta_{ik} + H_i B_k) n_k \\ &= H_t B_n, \end{aligned} \tag{A.13}$$

where $\boldsymbol{t}$ is a unit tangential vector. But since both H_t and B_n are continuous, the tangential force difference on the boundary due to the Maxwell stress tensor is

$$f_t^{(e)} - f_t^{(i)} = 0. \tag{A.14}$$

A.4 Effective magnetic surface force

The forces acting on the droplet's boundary in the normal direction are

$$\boldsymbol{n} \cdot (\tilde{\boldsymbol{\sigma}}^{(e)} - \tilde{\boldsymbol{\sigma}}^{(i)}) \cdot \boldsymbol{n} + \frac{\mu_0}{2} {M_n^{(i)}}^2 - \gamma(k_1 + k_2) = 0. \tag{A.15}$$

We want to write the equation in terms of the effective hydrodynamic stress tensor

$$\begin{aligned} \boldsymbol{\sigma} &= \tilde{\boldsymbol{\sigma}} - p_M \mathbf{I} \\ &= \tilde{\boldsymbol{\sigma}} + \frac{1}{2}\mu_0 \left(\frac{\mu}{\mu_0} - 1 \right) H^2 \mathbf{I}, \end{aligned} \tag{A.16}$$

where $\mathbf{I}$ is the identity tensor. To achieve this, we add and subtract $p_M^{(i)}$ from (A.15) to get (there is no need to do the same with $p_M^{(e)}$ since it is 0)

$$\boldsymbol{n} \cdot (\boldsymbol{\sigma}^{(e)} - \boldsymbol{\sigma}^{(i)}) \cdot \boldsymbol{n} + f_M - \gamma(k_1 + k_2) = 0, \tag{A.17}$$

where f_M is the effective magnetic surface force

$$\begin{aligned} f_M &= \frac{\mu_0}{2} {M_n^{(i)}}^2 + \frac{1}{2}\mu_0 \left(\frac{\mu}{\mu_0} - 1 \right) {H^{(i)}}^2 \\ &= \frac{1}{2}\mu_0 \left(\frac{\mu}{\mu_0} - 1 \right)^2 {H_n^{(i)}}^2 + \frac{1}{2}\mu_0 \left(\frac{\mu}{\mu_0} - 1 \right) {H_n^{(i)}}^2 + \frac{1}{2}\mu_0 \left(\frac{\mu}{\mu_0} - 1 \right) {H_t^{(i)}}^2 \\ &= \frac{1}{2}\mu_0 \left(\frac{\mu}{\mu_0} - 1 \right) {H_n^{(i)}}^2 \left(\frac{\mu}{\mu_0} - 1 + 1 \right) + \frac{1}{2}\mu_0 \left(\frac{\mu}{\mu_0} - 1 \right) {H_t^{(i)}}^2 \\ &= \frac{1}{2}\mu_0 \left(\frac{\mu}{\mu_0} - 1 \right) \left(\frac{\mu}{\mu_0} {H_n^{(i)}}^2 + {H_t^{(i)}}^2 \right). \end{aligned} \tag{A.18}$$

A.5 Integral of Green's second identity

Like stated in the equation (6.5), the following identity holds when $\boldsymbol{y} \in S$

$$\int_S \Gamma(\boldsymbol{x}, \boldsymbol{y}) \boldsymbol{\nabla}_x \psi^{(i)}(\boldsymbol{x}) \cdot \boldsymbol{n}_{\boldsymbol{x}} dS_x - \int_S \psi^{(i)}(\boldsymbol{x}) \boldsymbol{\nabla}_x \Gamma(\boldsymbol{x}, \boldsymbol{y}) \cdot \boldsymbol{n}_{\boldsymbol{x}} dS_x = \frac{\psi^{(i)}(\boldsymbol{y})}{2}. \tag{A.19}$$

A naive way to justify the equation (A.19) would be the following. The integral $\int_V \psi(\boldsymbol{x}) \delta(\boldsymbol{x} - \boldsymbol{y}) dV_x$ has value of $\psi(\boldsymbol{y})$ if $\boldsymbol{y} \in V$ and 0 if $\boldsymbol{y} \notin V$, therefore it should have an intermediate value of $\psi(\boldsymbol{y})/2$ as $\boldsymbol{y}$ lies directly on S. However, the Dirac delta function is defined for integrals that do not contain $\boldsymbol{y}$ as one of its bounds [113].

Let us then evaluate (A.19) in a different manner. When $\boldsymbol{y} \in V^{(i)}$, we have

$$\int_S [\Gamma(\boldsymbol{x},\boldsymbol{y})\boldsymbol{\nabla}_x\psi^{(i)}(\boldsymbol{x})\cdot\boldsymbol{n}_{\boldsymbol{x}} - \psi^{(i)}(\boldsymbol{x})\boldsymbol{\nabla}_x\Gamma(\boldsymbol{x},\boldsymbol{y})\cdot\boldsymbol{n}_{\boldsymbol{x}}]dS_x = \psi^{(i)}(\boldsymbol{y}), \tag{A.20}$$

where we wrote everything under one integral for convenience. To evaluate it when $\boldsymbol{y}$ approaches S from the inside, we deform the surface S with a small half-sphere with the radius ε centered on $\boldsymbol{y}$ (figure A.1 (a)). The integral can be split into two parts one over the undeformed surface excluding the small half-sphere an one over the half-sphere

$$\int_S = \int_{S-\varepsilon} + \int_\varepsilon = \psi^{(i)}(\boldsymbol{y}). \tag{A.21}$$

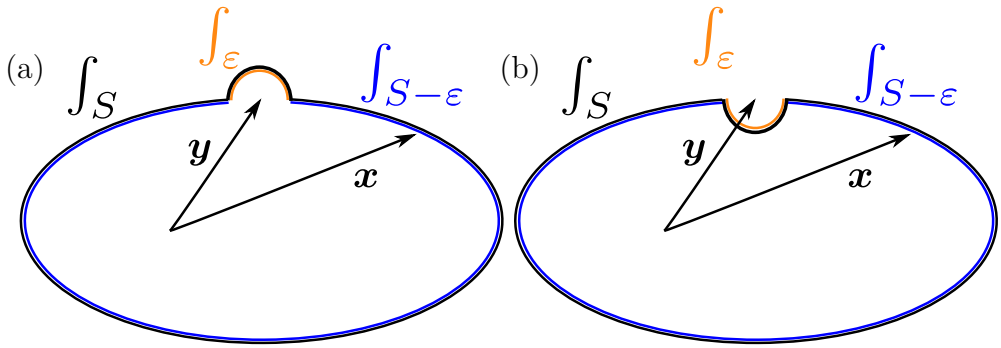

Figure A.1: Deformation of the droplet's surface S to evaluate an integral as $\boldsymbol{y}$ approaches it from (a) inside, (b) outside.

When ε goes to zero,

$$\lim_{\varepsilon\to 0}\int_{S-\varepsilon} = \mathcal{P}\int_S \tag{A.22}$$

becomes the Cauchy principal value integral since the singular point is approached equally rapidly from all directions [120].

Whereas $\int_\varepsilon$ can be evaluated analytically in spherical coordinates centered on $\boldsymbol{y}$. On the small half sphere $\psi^{(i)}(\boldsymbol{x})$ and $\boldsymbol{\nabla}_x\psi^{(i)}(\boldsymbol{x})$ become constant $\psi^{(i)}(\boldsymbol{y})$, and $[\boldsymbol{\nabla}_x\psi^{(i)}(\boldsymbol{x})]_{\boldsymbol{x}=\boldsymbol{y}}$. The normal vector becomes $\boldsymbol{n}_x = \boldsymbol{e}_r$, and the radius vector becomes $\boldsymbol{X} = \varepsilon\boldsymbol{e}_r$. The gradient of Γ can be written in spherical coordinates as $\boldsymbol{\nabla}_x\Gamma(\boldsymbol{x},\boldsymbol{y}) = -\boldsymbol{e_r}/(4\pi\varepsilon^2)$. The integral becomes

$$\begin{aligned}&\int_\varepsilon [\Gamma(\boldsymbol{x},\boldsymbol{y})\boldsymbol{\nabla}_x\psi^{(i)}(\boldsymbol{x})\cdot\boldsymbol{n}_{\boldsymbol{x}} - \psi^{(i)}(\boldsymbol{x})\boldsymbol{\nabla}_x\Gamma(\boldsymbol{x},\boldsymbol{y})\cdot\boldsymbol{n}_{\boldsymbol{x}}]dS_x = \\ &\psi^{(i)}(\boldsymbol{y})\int_\varepsilon \left(\frac{\boldsymbol{e}_r}{4\pi\varepsilon^2}\right)\cdot\boldsymbol{e}_r\varepsilon^2\sin(\theta)d\theta d\phi = \frac{\psi^{(i)}(\boldsymbol{y})}{2},\end{aligned} \tag{A.23}$$

since the integration happens over a half-sphere. The first term does not contribute to

the integral's value since $\varepsilon \to 0$, $\Gamma \propto 1/\varepsilon$ and the area of the small half-sphere $S_\varepsilon \propto \varepsilon^2$,

Combining the equations (A.20), (A.21), and (A.23), we get the expression for the integral of Green's second identity when $\boldsymbol{y} \in S$

$$\mathcal{P}\int_S [\Gamma(\boldsymbol{x},\boldsymbol{y})\boldsymbol{\nabla}_x\psi^{(i)}(\boldsymbol{x})\cdot\boldsymbol{n}_{\boldsymbol{x}} - \psi^{(i)}(\boldsymbol{x})\boldsymbol{\nabla}_x\Gamma(\boldsymbol{x},\boldsymbol{y})\cdot\boldsymbol{n}_{\boldsymbol{x}}]dS_x = \frac{\psi^{(i)}(\boldsymbol{y})}{2}. \tag{A.24}$$

But since the integral is convergent, and the Cauchy principal value of a convergent integral is just its value, we can omit it and therefore (A.19) holds when $\boldsymbol{y} \in S$. The same value is obtained by allowing $\boldsymbol{y}$ to approach from the outside.

A.6 Identity for regularizing magnetic potential integral equation

When $\boldsymbol{y} \in S$, the following holds

$$\int_S \boldsymbol{\nabla}_x\Gamma(\boldsymbol{x},\boldsymbol{y})\cdot\boldsymbol{n}_{\boldsymbol{x}}dS_x = -\frac{1}{2}. \tag{A.25}$$

To prove it we notice that when $\boldsymbol{y}$ is inside the droplet, we have

$$\int_S \boldsymbol{\nabla}_x\Gamma(\boldsymbol{x},\boldsymbol{y})\cdot\boldsymbol{n}_{\boldsymbol{x}}dS_x = \int_{V^{(i)}} \Delta_x\Gamma(\boldsymbol{x},\boldsymbol{y})dV_x = -1, \tag{A.26}$$

where we used Γ definition (6.1) and the properties of Dirac delta function.

When $\boldsymbol{y}$ approaches the droplet's surface from inside, we split the integral in two parts ($\int_S = \int_{S-\varepsilon} + \int_\varepsilon = -1$) like shown in figure A.1. When ε goes to zero,

$$\lim_{\varepsilon\to 0}\int_{S-\varepsilon} = \mathcal{P}\int_S \tag{A.27}$$

becomes the Cauchy principal value integral since the singular point is approached equally rapidly from all directions [120]. Whereas $\int_\varepsilon$ can be evaluated analytically in spherical coordinates centered on $\boldsymbol{y}$. On the small half sphere $\psi^{(i)}(\boldsymbol{x})$ becomes constant $\psi^{(i)}(\boldsymbol{y})$, and hence $\boldsymbol{\nabla}_x\psi^{(i)}(\boldsymbol{y}) = \boldsymbol{0}$. The normal vector becomes $\boldsymbol{n}_x = \boldsymbol{e}_r$, and the radius vector becomes $\boldsymbol{X} = \varepsilon\boldsymbol{e}_r$. The gradient of Γ can be written in spherical coordinates as $\boldsymbol{\nabla}_x\Gamma(\boldsymbol{x},\boldsymbol{y}) =$

$-\boldsymbol{e_r}/(4\pi\varepsilon^2)$. Therefore the integral becomes

$$\begin{aligned}&\int_\varepsilon \boldsymbol{\nabla}_x \Gamma(\boldsymbol{x},\boldsymbol{y})\cdot \boldsymbol{n_x} dS_x = \\ &-\int_\varepsilon \Big(\frac{\boldsymbol{e}_r}{4\pi\varepsilon^2}\Big)\cdot \boldsymbol{e}_r \varepsilon^2 \sin(\theta) d\theta d\phi = -\frac{1}{2},\end{aligned} \tag{A.28}$$

Combining the results we get that when $\boldsymbol{y} \in S$

$$\mathcal{P}\int_S \boldsymbol{\nabla}_x \Gamma(\boldsymbol{x},\boldsymbol{y})\cdot \boldsymbol{n_x} dS_x = -\frac{1}{2}. \tag{A.29}$$

But since the integral is convergent, and the Cauchy principal value of a convergent integral is just its value, we can omit it and therefore (A.25) holds when $\boldsymbol{y} \in S$. The same value is obtained by allowing $\boldsymbol{y}$ to approach from the outside.

A.7 Limit of surface current integral

When $\boldsymbol{y}$ is approaching the droplet's surface from the outside, the following expression holds

$$\begin{aligned}&\int_S \Big(\boldsymbol{n_x}\times \boldsymbol{B_t^{(e)}}(\boldsymbol{x})\Big)\times \boldsymbol{\nabla}_x \Gamma(\boldsymbol{x},\boldsymbol{y}) dS_x = \\ &\mathcal{P}\int_S \Big(\boldsymbol{n_x}\times \boldsymbol{B_t^{(e)}}(\boldsymbol{x})\Big)\times \boldsymbol{\nabla}_x \Gamma(\boldsymbol{x},\boldsymbol{y}) dS_x + \frac{\boldsymbol{B_t^{(e)}}(\boldsymbol{y})}{2}.\end{aligned} \tag{A.30}$$

To prove it and to assign a value to the singular integral when $\boldsymbol{y}$ approaches the droplet from the outside, we deform the droplet with a half-sphere with a radius ε around $\boldsymbol{y}$ (figure A.1 (b)) and then let $\varepsilon \to 0$. The integral can be split into two parts one over the undeformed surface excluding the small half-sphere an one over the half-sphere ($\int_S = \int_{S-\varepsilon} + \int_\varepsilon$).

When ε goes to zero,

$$\lim_{\varepsilon\to 0}\int_{S-\varepsilon} = \mathcal{P}\int_S \tag{A.31}$$

becomes the Cauchy principal value integral since the singular point is approached equally rapidly from all directions [120].

Whereas $\int_\varepsilon$ can be evaluated analytically in spherical coordinates centered on $\boldsymbol{y}$. On the small half-sphere magnetic field is constant $\boldsymbol{B_t^{(e)}}(\boldsymbol{x}) = \boldsymbol{B_t^{(e)}}(\boldsymbol{y})$, the normal vector

becomes $\boldsymbol{n_x} = -\boldsymbol{e_r}$, and $\boldsymbol{\nabla}_x\Gamma(\boldsymbol{x},\boldsymbol{y}) = -\boldsymbol{r}/(4\pi r^3) = -\boldsymbol{e_r}/(4\pi r^2)$

$$\begin{aligned}&\int_\varepsilon \left(\boldsymbol{n_x}\times\boldsymbol{B_t^{(e)}}(\boldsymbol{x})\right)\times\boldsymbol{\nabla}_x\Gamma(\boldsymbol{x},\boldsymbol{y})dS_x = \\ &\frac{1}{4\pi}\int_\varepsilon \left(\boldsymbol{e_r}\times\boldsymbol{B_t^{(e)}}(\boldsymbol{y})\right)\times\boldsymbol{e_r}d\Omega_x = \frac{\boldsymbol{B_t^{(e)}}(\boldsymbol{y})}{2},\end{aligned} \tag{A.32}$$

where $d\Omega$ is the differential solid angle.

A.8 Identity for regularizing magnetic field normal component

The identity holds

$$\mathcal{P}\int_S \boldsymbol{n_x}\times\boldsymbol{\nabla}_x\Gamma(\boldsymbol{x},\boldsymbol{y})dS_x = \boldsymbol{0}. \tag{A.33}$$

To prove it we notice that when $\boldsymbol{y}$ is not on the surface, using a corollary of the divergence theorem ($\int_S \boldsymbol{n}\times\boldsymbol{f}dS = \int_V \boldsymbol{\nabla}\times\boldsymbol{f}dV$[113]), the following identity holds

$$\int_S \boldsymbol{n_x}\times\boldsymbol{\nabla}_x\Gamma(\boldsymbol{x},\boldsymbol{y})dS_x = \int_V \boldsymbol{\nabla}_x\times\boldsymbol{\nabla}_x\Gamma(\boldsymbol{x},\boldsymbol{y})dS_x = \boldsymbol{0}. \tag{A.34}$$

When $\boldsymbol{y}$ approaches the droplet's surface either from inside or outside, we split the integral in two parts ($\int_S = \int_{S-\varepsilon} + \int_\varepsilon = 0$) like shown in figure A.1. The integral over the small half-sphere is zero as $\varepsilon \to 0$ since both $\boldsymbol{n_x}$ and $\boldsymbol{\nabla}_x\Gamma$ are collinear and their cross product is identically zero.

$\int_{S-\varepsilon}$ becomes the Cauchy principal value integral, which is zero. Therefore, when $\boldsymbol{y}$ is on the surface, we have (A.33) where the integral should be evaluated with the Cauchy principal value, since as $\boldsymbol{x}\to\boldsymbol{y}$, the integrand scales as $O(|\boldsymbol{X}|^{-2})$, where $\boldsymbol{X} = \boldsymbol{x}-\boldsymbol{y}$.

A.9 Generalized Lorentz reciprocal identity

The identity

$$\frac{\partial}{\partial x_k}(v_i'\sigma_{ik} - v_i\sigma_{ik}') = v_i'\frac{\partial\sigma_{ik}}{\partial x_k} - v_i\frac{\partial\sigma_{ik}'}{\partial x_k} \tag{A.35}$$

holds.

To prove it, we differentiate using the chain rule

$$\frac{\partial}{\partial x_k}(v_i'\sigma_{ik} - v_i\sigma_{ik}') = \sigma_{ik}\frac{\partial v_i'}{\partial x_k} + v_i'\frac{\partial\sigma_{ik}}{\partial x_k} - v_i\frac{\partial\sigma_{ik}'}{\partial x_k} - \sigma_{ik}'\frac{\partial v_i}{\partial x_k}. \tag{A.36}$$

We see that (A.35) is proven, if $D = \sigma_{ik}\partial_k v_i' - \sigma_{ik}'\partial_k v_i = 0$. Let us examine this difference

$$\begin{aligned} D &= \sigma_{ik}\frac{\partial v_i'}{\partial x_k} - \sigma_{ik}'\frac{\partial v_i}{\partial x_k} \\ &= \left(-p\delta_{ik} + \eta\left[\frac{\partial v_i}{\partial x_k} + \frac{\partial v_k}{\partial x_i}\right]\right)\frac{\partial v_i'}{\partial x_k} - \left(-p'\delta_{ik} + \eta\left[\frac{\partial v_i'}{\partial x_k} + \frac{\partial v_k'}{\partial x_i}\right]\right)\frac{\partial v_i}{\partial x_k}. \end{aligned} \tag{A.37}$$

The terms in blue vanish, because their summation with $\partial_k v_i$ results in the divergence of velocity, which is zero. And the terms in red cancel each other. What remains is

$$D = \eta\left(\frac{\partial v_k}{\partial x_i}\frac{\partial v_i'}{\partial x_k} - \frac{\partial v_k'}{\partial x_i}\frac{\partial v_i}{\partial x_k}\right) = 0, \tag{A.38}$$

where we see that the second term is the negative of the first one by relabeling the summation indices.

A.10 Integral of Lorentz reciprocal identity

Like stated in the equation (6.38), the following identity holds when $\boldsymbol{y} \in S$

$$\frac{1}{8\pi\eta^{(i)}}\int_S G_{ik}(\boldsymbol{x},\boldsymbol{y})\sigma_{ij}^{(i)}(\boldsymbol{x})n_{xj}dS_x - \frac{1}{8\pi}\int_S v_i^{(i)}(\boldsymbol{x})T_{ikj}(\boldsymbol{x},\boldsymbol{y})n_{xj}dS_x = \frac{v_k^{(i)}(\boldsymbol{y})}{2}. \tag{A.39}$$

The proof is identical to the one outline in the appendix A.5. When $\boldsymbol{y} \in V^{(i)}$, we have

$$\frac{1}{8\pi}\int_S \left[\frac{1}{\eta^{(i)}}G_{ik}(\boldsymbol{x},\boldsymbol{y})\sigma_{ij}^{(i)}(\boldsymbol{x})n_{xj} - v_i^{(i)}(\boldsymbol{x})T_{ikj}(\boldsymbol{x},\boldsymbol{y})n_{xj}\right]dS_x = v_k^{(i)}(\boldsymbol{y}), \tag{A.40}$$

where we wrote everything under one integral for convenience. To evaluate it when $\boldsymbol{y}$ approaches S from the inside, we deform the surface S with a small half-sphere with the radius ε centered on $\boldsymbol{y}$ (figure A.1 (a)). The integral can be split into two parts one over the undeformed surface excluding the small half-sphere an one over the half-sphere

$$\int_S = \int_{S-\varepsilon} + \int_\varepsilon = v_k^{(i)}(\boldsymbol{y}). \tag{A.41}$$

When ε goes to zero,

$$\lim_{\varepsilon\to 0}\int_{S-\varepsilon} = \mathcal{P}\int_S \tag{A.42}$$

becomes the Cauchy principal value integral since the singular point is approached equally rapidly from all directions [120]. Whereas $\int_\varepsilon$ can be evaluated analytically in spherical coordinates centered on $\boldsymbol{y}$. On the small half sphere $\sigma_{ij}^{(i)}(\boldsymbol{x})$ and $v_i^{(i)}(\boldsymbol{x})$ become constant

$\sigma_{ij}^{(i)}(\boldsymbol{y})$, and $v_i^{(i)}(\boldsymbol{y})$. The normal vector becomes $\boldsymbol{n}_x = \boldsymbol{e}_r$, and the radius vector becomes $\boldsymbol{X} = \varepsilon \boldsymbol{e}_r$. The tensor $\mathbf{T}$ components can be written in spherical coordinates as $T_{ijk} = -6\frac{(\hat{\boldsymbol{r}})_i(\hat{\boldsymbol{r}})_j(\hat{\boldsymbol{r}})_k}{\varepsilon^2}$, where $\hat{\boldsymbol{r}} = \{\sin(\theta)\cos(\phi), \sin(\theta)\sin(\phi), \cos(\theta)\}$. The integral over the small half-sphere is

$$\begin{aligned}
&\frac{1}{8\pi}\int_\varepsilon \left[\frac{1}{\eta^{(i)}} G_{ik}(\boldsymbol{x},\boldsymbol{y})\sigma_{ij}^{(i)}(\boldsymbol{x})n_{xj} - v_i^{(i)}(\boldsymbol{x})T_{ikj}(\boldsymbol{x},\boldsymbol{y})n_{xj}\right] dS_x = \\
&-\frac{v_i^{(i)}(\boldsymbol{y})}{8\pi}\int_\varepsilon T_{ikj} n_{xj}\varepsilon^2 \sin(\theta) d\theta d\phi = \\
&-\frac{v_i^{(i)}(\boldsymbol{y})}{8\pi}(-4\pi\delta_{ik}) = \frac{v_k^{(i)}(\boldsymbol{y})}{2},
\end{aligned} \tag{A.43}$$

since the integration happens over a half-sphere. The first term does not contribute to the integral's value since $\varepsilon \to 0$, $\mathbf{G} \propto 1/\varepsilon$ and the area of the small half-sphere $S_\varepsilon \propto \varepsilon^2$,

Combining the equations (A.40), (A.41), and (A.43), we get the expression for the integral of Green's second identity when $\boldsymbol{y} \in S$

$$\frac{1}{8\pi}\mathcal{P}\int_S \left[\frac{1}{\eta^{(i)}} G_{ik}(\boldsymbol{x},\boldsymbol{y})\sigma_{ij}^{(i)}(\boldsymbol{x})n_{xj} - v_i^{(i)}(\boldsymbol{x})T_{ikj}(\boldsymbol{x},\boldsymbol{y})n_{xj}\right] dS_x = \frac{v_k^{(i)}(\boldsymbol{y})}{2}. \tag{A.44}$$

But since the integral is convergent, and the Cauchy principal value of a convergent integral is just its value, we can omit it and therefore (A.39) holds when $\boldsymbol{y} \in S$. The same value is obtained by allowing $\boldsymbol{y}$ to approach from the outside.

A.11 Integral of velocity Green tensor

The following identity holds

$$\int_S G_{ik}(\boldsymbol{x},\boldsymbol{y}) n_{xi} dS_x = 0. \tag{A.45}$$

To prove it, we can notice that from the definition of G_{ij} (6.32),

$$v_i = \frac{1}{8\pi\eta} G_{ij} b_j$$

is a solution to the Stokes equations. But then

$$\frac{\partial v_i}{\partial x_i} = 0 = \frac{1}{8\pi\eta}\frac{\partial G_{ij}}{\partial x_i} b_j.$$

Since $\boldsymbol{b}$ is arbitrary, it implies that $\partial_i G_{ij} = 0$, which by the divergence theorem means

that (A.45) holds when $\boldsymbol{y}$ is not on the surface. Alternatively for the particular case of infinite domain Green functions (6.34), we can just differentiate $\partial_i G_{ij}$ to find that it is identically zero.

When $\boldsymbol{y}$ approaches the surface S either from inside or outside, we split the integral in two parts just like in figure A.1. The integral over the small half-sphere is zero as $\varepsilon \to 0$ since $G_{ik}(\boldsymbol{x}, \boldsymbol{y}) n_{xi} \propto 1/\varepsilon$, but $S_\varepsilon \propto \varepsilon^2$. Therefore (A.45) holds also when $\boldsymbol{y} \in S$. The integral (A.45) is convergent since the integrand scales as $O(|\boldsymbol{X}|^{-1})$ when $\boldsymbol{x} \to \boldsymbol{y}$.

A.12 Integral of stress Green tensor

The following identity holds

$$\int_S T_{ijk}(\boldsymbol{x}, \boldsymbol{y}) n_{xk} dS_x = \begin{cases} -8\pi\delta_{ij}, \text{ if } \boldsymbol{y} \in V^{(i)} \\ -4\pi\delta_{ij}, \text{ if } \boldsymbol{y} \in S \\ 0, \text{ if } \boldsymbol{y} \in V^{(e)} \end{cases}. \tag{A.46}$$

To prove it we start with the the stress tensor due to $\mathbf{T}$ (6.32)

$$\sigma_{ik} = \frac{1}{8\pi} T_{ijk} b_j. \tag{A.47}$$

We calculate its divergence

$$\frac{\partial \sigma_{ik}}{\partial x_k} = \frac{1}{8\pi} b_j \frac{\partial T_{ijk}}{\partial x_k} = -b_i \delta(\boldsymbol{x} - \boldsymbol{y}), \tag{A.48}$$

where we used the equation (6.31). Integrating it over the droplet's volume $V^{(i)}$, and using the divergence theorem and properties of Dirac delta function, we get

$$b_j \int_S T_{ijk}(\boldsymbol{x}, \boldsymbol{y}) n_{xk} dS_x = \begin{cases} -8\pi b_i, \text{ if } \boldsymbol{y} \in V^{(i)} \\ 0, \text{ if } \boldsymbol{y} \in V^{(e)} \end{cases}. \tag{A.49}$$

To evaluate the integral when $\boldsymbol{y} \in S$, we observe the case when $\boldsymbol{y} \in V^{(i)}$ and let $\boldsymbol{y}$ approach S from the inside. We deform the surface S with a small half-sphere with the radius ε centered on $\boldsymbol{y}$ (figure A.1 (a)). The integral can be split into two parts one over the undeformed surface excluding the small half-sphere an one over the half-sphere

$$\int_S = \int_{S-\varepsilon} + \int_\varepsilon = -8\pi b_i. \tag{A.50}$$

When ε goes to zero,

$$\lim_{\varepsilon \to 0} \int_{S-\varepsilon} = \mathcal{P} \int_S \tag{A.51}$$

becomes the Cauchy principal value integral since the singular point is approached equally rapidly from all directions [120]. Whereas $\int_\varepsilon$ can be evaluated analytically in spherical coordinates centered on $\boldsymbol{y}$. The normal vector becomes $\boldsymbol{n}_x = \boldsymbol{e}_r$, and the radius vector becomes $\boldsymbol{X} = \varepsilon \boldsymbol{e}_r$. The tensor $\mathbf{T}$ components can be written in spherical coordinates as $T_{ijk} = -6\frac{(\hat{\boldsymbol{r}})_i (\hat{\boldsymbol{r}})_j (\hat{\boldsymbol{r}})_k}{\varepsilon^2}$, where $\hat{\boldsymbol{r}} = \{\sin(\theta)\cos(\phi), \sin(\theta)\sin(\phi), \cos(\theta)\}$. The integral over the small half-sphere is

$$\begin{aligned} &b_j \int_\varepsilon T_{ijk}(\boldsymbol{x}, \boldsymbol{y}) n_{xk} dS_x = \\ &b_j \int_\varepsilon T_{ikj} n_{xk} \varepsilon^2 \sin(\theta) d\theta d\phi = \\ &b_j(-4\pi\delta_{ij}) = -4\pi b_i, \end{aligned} \tag{A.52}$$

since the integration happens over a half-sphere.

Combining the equations (A.50) and (A.52), we get the expression for the integral when $\boldsymbol{y} \in S$

$$b_j \mathcal{P} \int_S T_{ijk}(\boldsymbol{x}, \boldsymbol{y}) n_{xk} dS_x = -4\pi b_i. \tag{A.53}$$

But since the integral is convergent, and the Cauchy principal value of a convergent integral is just its value, we can omit it. Finally, (A.46) holds, since $\boldsymbol{b}$ is arbitrary in equations (A.49) and (A.53).

A.13 Surface divergence theorem

It will prove useful to define a surface divergence of a vector field, which would allow us to use a formula on the surface analogous to the divergence theorem in $\mathbb{R}^3$. Let S be a surface enclosed by the curve C. S has a unit normal vector $\boldsymbol{n}$, and the curve C has a unit tangent vector $\boldsymbol{t}$ oriented counter-clockwise as viewed from the direction of the normal vector (see figure A.2). Vector $\boldsymbol{m}$ is defined to be pointing "out" of S along the enclosing curve C

$$\boldsymbol{m} = \boldsymbol{t} \times \boldsymbol{n} \tag{A.54}$$

We want to find the operator $\tilde{\boldsymbol{\nabla}}_S$ such that for some vector function $\boldsymbol{f}$

$$\int_S \tilde{\boldsymbol{\nabla}}_S \cdot \boldsymbol{f} dS = \int_C \boldsymbol{f} \cdot \boldsymbol{m} dl. \tag{A.55}$$

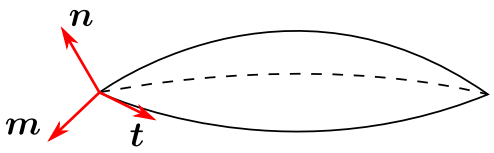

Figure A.2: Illustration of the surface normal vector $\boldsymbol{n}$, the tangent vector $\boldsymbol{t}$ on the enclosing curve, and the vector $\boldsymbol{m}$ tangent to the surface, but normal to the enclosing curve.

We can use the curl theorem ($\int_S (\boldsymbol{\nabla} \times \boldsymbol{g}) \cdot \boldsymbol{n} dS = \int_C \boldsymbol{g} \cdot \boldsymbol{t} dl$) to get the expression for $\tilde{\boldsymbol{\nabla}}_{\boldsymbol{S}}$ [149]. Setting $\boldsymbol{g} = \boldsymbol{n} \times \boldsymbol{f}$, we arrive at

$$\tilde{\boldsymbol{\nabla}}_S \cdot \boldsymbol{f} = \boldsymbol{n} \cdot (\boldsymbol{\nabla} \times (\boldsymbol{n} \times \boldsymbol{f})), \tag{A.56}$$

which satisfies (A.55). Opening up the cross products and writing the expression in component form, we get

$$\tilde{\boldsymbol{\nabla}}_S \cdot \boldsymbol{f} = \frac{\partial f_i}{\partial x_i} - \frac{\partial f_i}{\partial x_j} n_i n_j - \frac{\partial n_j}{\partial x_j} f_i n_i, \tag{A.57}$$

where we used $n_j \partial_i n_j = 0$. Rewriting the expression some more, we have

$$\tilde{\boldsymbol{\nabla}}_S \cdot \boldsymbol{f} = \boldsymbol{\nabla}_S \cdot \boldsymbol{f} - (k_1 + k_2) \boldsymbol{f} \cdot \boldsymbol{n}, \tag{A.58}$$

where $(k_1 + k_2) = \boldsymbol{\nabla} \cdot \boldsymbol{n}$ is the sum of principal curvatures at a point on the surface [150] and

$$\boldsymbol{\nabla}_S = (\mathbf{I} - \boldsymbol{n}\boldsymbol{n}) \cdot \boldsymbol{\nabla} \tag{A.59}$$

is the commonly known surface divergence operator ($\mathbf{I}$ is the identity tensor).

The divergence theorem on the surface is then written as (page 239 in [150])

$$\int_S \boldsymbol{\nabla}_S \cdot \boldsymbol{f} dS = \int_C \boldsymbol{f} \cdot \boldsymbol{m} dl + \int_S (k_1 + k_2) \boldsymbol{f} \cdot \boldsymbol{n} dS. \tag{A.60}$$

A.14 Curvatureless capillary force integral

The following identity holds

$$\int_S (k_1(\boldsymbol{x}) + k_2(\boldsymbol{x})) \, G_{ik}(\boldsymbol{x}, \boldsymbol{y}) n_{xi} dS_x = -\mathcal{P} \int_S \frac{X_k}{X^3} \left(1 - 3\frac{(\boldsymbol{n}_x \cdot \boldsymbol{X})^2}{X^2}\right) dS_x. \tag{A.61}$$

To prove it, we first note that the left-hand side is reminiscent of the last term in the surface divergence theorem (A.60) with $\boldsymbol{f} = \boldsymbol{G}_k$. We divide the surface of the droplet in

two parts: a small circular area with radius ε centered on $\boldsymbol{y}$, and the rest of the surface area not containing $\boldsymbol{y}$ (figure A.3). We denote the former by S_ε and the latter by $S_{\not\ni}$. The curve separating the two areas is labeled C_ε.

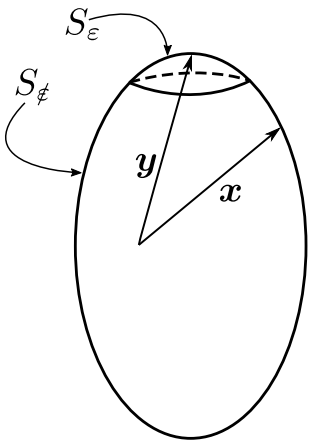

Figure A.3: Division of the droplet's surface S into two areas S_ε and $S_{\not\ni}$.

From (A.60) noting that $\partial_j G_{jk} = 0$ we have

$$\int_{S_{\not\ni}} (k_1(\boldsymbol{x}) + k_2(\boldsymbol{x}))\, G_{ik}(\boldsymbol{x},\boldsymbol{y}) n_{xi} dS_x = -\int_{S_{\not\ni}} n_{xi} n_{xj} \frac{\partial G_{ik}(\boldsymbol{x},\boldsymbol{y})}{\partial x_j} dS_x - \int_{C_\varepsilon} G_{ik}(\boldsymbol{x},\boldsymbol{y}) m_i(\boldsymbol{x}) dl_x. \tag{A.62}$$

The integral $\int_{C_\varepsilon} G_{ik}(\boldsymbol{x},\boldsymbol{y}) m_i(\boldsymbol{x}) dl_x$ can be evaluated in local polar coordinates (ρ, ϕ) centered on $\boldsymbol{y}$. Since the surface is locally flat for small enough ε, $\boldsymbol{m} = \boldsymbol{e}_\rho$, $\boldsymbol{X} = \rho \boldsymbol{e}_\rho$, $dl = \rho d\phi$ and the integral becomes

$$\int_{C_\varepsilon} \boldsymbol{G}_k(\boldsymbol{x},\boldsymbol{y}) \cdot \boldsymbol{m}(\boldsymbol{x}) dl_x = \int_0^{2\pi} 2\boldsymbol{e}_\rho d\phi = \boldsymbol{0}. \tag{A.63}$$

As $\varepsilon \to 0$, the integral over $S_{\not\ni}$ becomes the Cauchy principal value integral over the whole surface

$$\mathcal{P} \int_S (k_1(\boldsymbol{x}) + k_2(\boldsymbol{x}))\, G_{ik}(\boldsymbol{x},\boldsymbol{y}) n_{xi} dS_x = -\mathcal{P} \int_S n_{xi} n_{xj} \frac{\partial G_{ik}(\boldsymbol{x},\boldsymbol{y})}{\partial x_j} dS_x. \tag{A.64}$$

Finally, since the left-hand side is convergent also without taking the Cauchy principal value, and the value of a convergent integral is the same as its Cauchy principal value, we can omit it. Whereas for the right-hand side can be further simplified after differentiation of G_{ik}, leaving us with (A.61), which concludes the proof.

B Author's publications

The results of this work have been published in three papers:

- [96] - A. P. Stikuts, R. Perzynski, A. Cēbers, "Spontaneous order in ensembles of rotating magnetic droplets", *Journal of Magnetism and Magnetic Materials*, **500**, 2020, 166304, https://doi.org/10.1016/j.jmmm.2019.166304.
- [109] - A. P. Stikuts, R. Perzynski, and A. Cēbers, "Small deformation theory for a magnetic droplet in a rotating field", *Physics of Fluids*, **34**, 052010 (2022), https://doi.org/10.1063/5.0091453
- [59] - A. Langins, A. P. Stikuts, and A. Cēbers , "A three-dimensional boundary element method algorithm for simulations of magnetic fluid droplet dynamics", *Physics of Fluids*, **34**, 062105 (2022), https://doi.org/10.1063/5.0092532

The full text copies are provided hereafter.

Journal of Magnetism and Magnetic Materials 500 (2020) 166304

Contents lists available at ScienceDirect

Journal of Magnetism and Magnetic Materials

journal homepage: www.elsevier.com/locate/jmmm

Research articles

Spontaneous order in ensembles of rotating magnetic droplets

A.P. Stikuts[a,b,*], R. Perzynski[b], A. Cēbers[a,c]

[a] MMML Lab, Faculty of Physics and Mathematics, University of Latvia, Jelgavas iela 3 – 014, Riga LV-1004, Latvia
[b] Sorbonne University, CNRS, UMR 8234, PHENIX, Paris F-75005, France
[c] Chair of Theoretical Physics, University of Latvia, Jelgavas iela 3, Riga LV-1004, Latvia

ARTICLE INFO

Keywords:
Magnetic
Colloid
Droplet
Self assembly

ABSTRACT

Ensembles of elongated magnetic droplets in a rotating field are studied experimentally. In a given range of field strength and frequency the droplets form rotating structures with a triangular order – rotating crystals. A model is developed to describe ensembles of several droplets, taking into account the hydrodynamic interactions between the rotating droplets in the presence of a solid wall below the rotating ensemble. A good agreement with the experimentally observed periodic dynamics for an ensemble of four droplets is obtained. During the rotation, the tips of the elongated magnetic droplets approach close to one another. An expression is derived that gives the magnetic interaction between such droplets by taking into account the coulombian forces between magnetic charges on the droplet tips.

1. Introduction

In recent years, systems based on out-of-equilibrium assemblies have gained considerable attention, see for example the recent review on field driven self-assemblies of colloids [1].

In particular, the formation of dynamical structures of spinning particles under rotating magnetic fields, leading to 2D rotating-crystals, have been studied in a series of works [2–5], showing mechanisms of their formation and their properties. Ref. [2,3] study a system of millimeter-sized magnetized disks, floating above a liquid-gas interface under the action of an inhomogeneous field (created by rotating permanent magnets). The repulsion between disks at finite Reynolds number results from a lift force between the rotating particles [2,3]. The formation of rotating crystals of magnetic Janus colloids is described in [4]. There, a significant role is played by lubrication effects between rotating colloids. These effects are responsible for the dependence of the crystal angular velocity on its size. In [5], an ensemble of magnetic droplets at the liquid-air interface is observed to form ordered dynamical structures under rotating field. Each droplet contains magnetic micron-sized particles which are chaining under magnetic field. The precessing field induces the rotation of the chains inside the droplets, which results in the global rotation of the droplets, which, in turn, auto-organize in a dynamical crystal.

Such 2D rotating crystals are also considered in the broader context of active matter. Let us mention here the rotating crystals formed by fast moving sulfur oxidizing bacteria Thiovolum Majus where the formation of the rotating crystals is due to the hydrodynamic and steric interactions between cells [6]. Moreover, a spontaneous breaking of the internal chirality leads to the development of rotational motion of self-propelling particles [7].

Here 2D rotating crystals of a new kind – ensembles of rotating needle-like magnetic droplets (micron-sized and resulting from a phase separation [8]) – are observed and described. The shapes of such droplets in rotating field are analysed in [8,9], where, according to parameters such as magnetic field strength and rotation frequency, the shape of the droplet can change from oblate to prolate, to oblate again. Here we choose the parameters such that the droplets are prolate. For densely packed needle-like droplets in a rotating field, the axis ratios resulting from an interplay between the droplet breakup and coalescence have been examined in [10]. We present below the experimental observations of ensembles of such droplets under rotating field and describe them with a simple model in order to elucidate the underlying mechanisms of their behavior.

2. Experiment

2.1. Experimental setup

In the experiments we use a water-based ferrofluid made of maghemite nanoparticles (diameter $d = 7$ nm, volume fraction $\varphi = 5\%$) that are stabilized with a citrate coating. A demixing in two coexisting phases can be induced in the ferrofluid by increasing its ionic strength,

* Corresponding author at: MMML Lab, Faculty of Physics and Mathematics, University of Latvia, Jelgavas iela 3 – 014, Riga LV-1004, Latvia.
E-mail address: andris_pavils.stikuts@lu.lv (A.P. Stikuts).

https://doi.org/10.1016/j.jmmm.2019.166304
Received 8 August 2019; Received in revised form 2 December 2019; Accepted 13 December 2019
Available online 17 December 2019

adding NaCl [11,12]. In this way, droplets of highly concentrated phase are obtained coexisting with a surrounding medium at extremely low concentration of magnetic nanoparticles. These droplets exhibit under rather low static and dynamic fields, a series of shape instabilities as described in [8,9].

We introduce ≈ 15 μl of the phase separated ferrofluid into a closed volume between two microscope slides separated by a double-sided tape of height $H \approx 130\,\mu m$, and we observe it with a Leica DMI3000B microscope that is supplied with a home built coil setup. Droplets are filmed with a Basler acA1920-155um camera attached to the microscope, and the images are recorded in 8-bit gray-scale format. We track the droplet shape and position using a custom written program in MATLAB.

2.2. Determination of the magnetic droplet parameters

As in [9], we measure the properties of a few droplets (typically 10 microns in diameter) by elongating them along a magnetic field (of a few tens of gauss) and assuming an axisymmetric ellipsoidal shape fitted with the theoretical relation from [13,14]. From this we find that the relative magnetic permeability of the magnetic droplets is $\mu = 34 \pm 2$ and the surface tension is $\gamma = (8.2 \pm 0.4)\cdot 10^{-4}$ erg/cm^2.

To determine their viscosity, the elongated droplets are let to relax in zero field, under their surface tension. The exponential relaxation of the droplet deformation parameter $D = (a - b)/(a + b)$ (a and b are the semi-axes of the droplet) is fitted as a function of time using the expression from [15] assuming small deformations $D \ll 1$ and an axisymmetric ellipsoidal shape. We get that the ratio of the droplet viscosity η^i over the viscosity of the surrounding liquid η^e is $\lambda = \eta^i/\eta^e = 10.1 \pm 2.5$.

2.3. Droplet behavior under a rotating magnetic field

When the phase separated ferrofluid sample is first placed under a microscope, some droplets are located close to the bottom of the cell due to their size and to their density being larger than that of the surrounding fluid, but with a distribution of heights. When a rotating magnetic field of magnitude $B = 60$ G and frequency $f = 15$ Hz is applied, we observe that the droplets arrange themselves in the same focal plane. By adjusting the focus of the microscope, we determined that the droplets are around $h = (9 \pm 1)\,\mu m$ above the bottom of the sample-cell.

In this applied rotating field, there is a critical volume $V_{crit} \approx \frac{\pi}{6}(3.5\,\mu m)^3$ for the droplets. If the volume of a particular droplet is larger than V_{crit} the droplet flattens out into an oblate shape [8,9] that sucks in and merges with smaller droplets in its immediate vicinity. However, if the droplet volume is below this critical value, they elongate and rotate with the same frequency as the field without coalescing. This is illustrated in Fig. 1.

Once the at first unsteady motion has settled, the small-enough elongated droplets arrange themselves into crystal like structures (Fig. 2) rotating in the direction of the magnetic field, albeit more slowly. The droplets in these crystals experience some oscillations around their lattice points, however the crystal structure remains intact and it rotates like a solid body (except sometimes for the most outer layer, where some drift is observed).

In regions where the droplet concentration is larger, the droplets form 2D triangular crystals that are too large to noticeably rotate. The centers of the droplets are Delaunay triangulated to clearly see the lattice structure. Fig. 3 illustrates that the 2D structure is polycrystalline with a grain boundary marked by an array of dislocations.

The droplet lengths are more similar within a stationary single crystal than they were at first. Fig. 4 illustrates a mechanism by which the droplets could achieve this. The length (and presumably also the volume) of a small droplet situated in between the lattice points of a large crystal increases over time. It is hard to assess the change of the

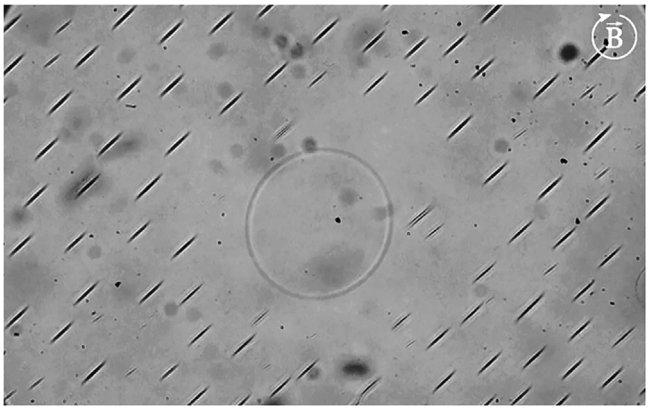

Fig. 1. A view of droplets right after a rotating magnetic field is turned on. If a droplet's volume is below a critical value, it elongates and rotates with the field. If a droplet's volume is above a critical value, it flattens out into an oblate shape that also rotates with the field (seen at the center of the image). Field of view = 400 × 250 μm^2. Magnetic field ($B = 60$ G and $f = 15$ Hz) is rotating in the plane of observation.

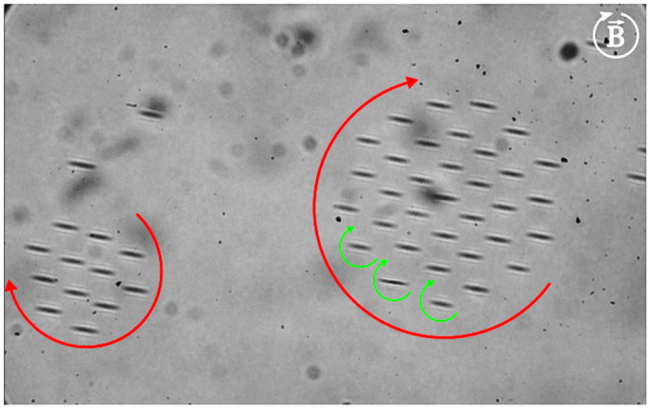

Fig. 2. In time droplets organize themselves in 2D rotating crystals. Each individual droplet is rotating in the direction and with the frequency of the magnetic field. The crystal is also rotating in the direction of the magnetic field, but more slowly. Field of view = 400 × 250 μm^2. Magnetic field ($B = 60$ G and $f = 15$ Hz) is rotating in the plane of observation.

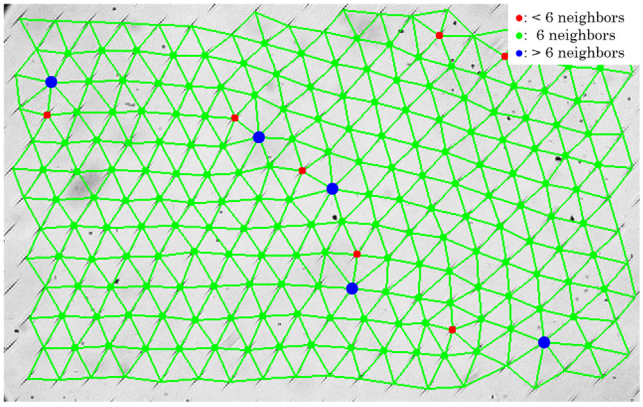

Fig. 3. If the droplets are densely situated, they organize themselves in a large stationary 2D triangular lattice. Each droplet still rotates in the direction and with the frequency of the magnetic field, but the whole crystal is stationary. Field of view = 400 × 250 μm^2. Magnetic field ($B = 60$ G and $f = 15$ Hz) and the droplets are rotating in the plane of observation.

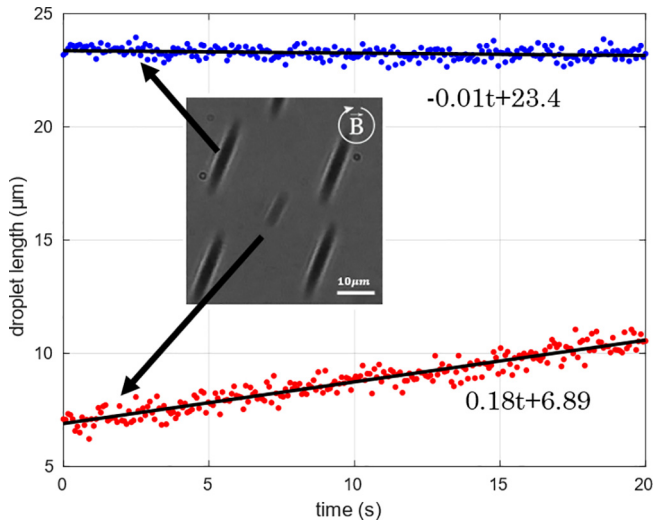

Fig. 4. The lengths of two droplets within a large stationary crystal. The small droplet finds itself between bigger droplets that form the lattice. The length of the small droplet (red points) increases over time. The length of the large droplet (blue points) remains relatively static. The equations describe a linear fit used to illustrate the average rate of change of the droplet length. (For interpretation of the references to colour in this figure legend, the reader is referred to the web version of this article.)

droplet's width since it is close to the microscope spatial resolution and its determination is sensitive to errors from an ellipsoidal fit during the image processing.

3. Proposed model

3.1. Description of the proposed model

To understand the underlying interactions that lead to this ordering of the rotating elongated droplets, we develop a model below. The motion of the rotating droplet crystals is described by taking into account the flow each droplet produces. In our model, we assume that a droplet exerts a point torque at its center of mass producing a so called rotlet flow around it. Since the droplets are spinning close to the bottom of the sample, it is important to take into account the effects of the wall on the flow field. As the velocity of a viscous fluid is 0 on the wall, it significantly slows down the motion of the rotating crystals.

We use the rotlet expression taking into account an infinite no-slip wall from [16]. In the case where the plane is located at $z = 0$ and a torque $\vec{\tau} = (0, 0, \tau)$ is applied at the point (X, Y, Z), the velocity at (x, y, z) simplifies and is given by

$$\vec{u} = \frac{1}{8\pi\eta}\left(\frac{\vec{\tau}\times\vec{r}}{|\vec{r}|^3} - \frac{\vec{\tau}\times\vec{R}}{|\vec{R}|^3}\right), \tag{1}$$

where $\vec{r} = (x - X, y - Y, z - Z)$ and $\vec{R} = (x - X, y - Y, z + Z)$, the viscosity η here equals η^e. The velocity of the j-th droplet is calculated as the sum of rotlet fields produced by all other droplets at the location of the center of mass of j-th droplet, i.e. $\vec{v_j} = \sum_{i\neq j}\vec{u_i}$.

To determine the torque a rotating droplet exerts, we treat it as a rigid body. Even though the droplets are liquid and contract to spherical shapes if the magnetic field is removed, the approximation of a rigid particle is justified because the internal viscosity η^i is 10 times larger than the viscosity η^e of the surrounding medium. Since the droplets are well described by a slender body approximation (the aspect ratio is typically 18:1), and because they rotate with their rotational axis perpendicular to the infinite wall, the torque they produce is close to that of a slender body rotating in an infinite fluid (see Fig. 15 in [17]). Therefore for simplicity, we use the expression given by [18] (page 56) for the torque of a rotating ellipsoid where the flow is in an infinite space.

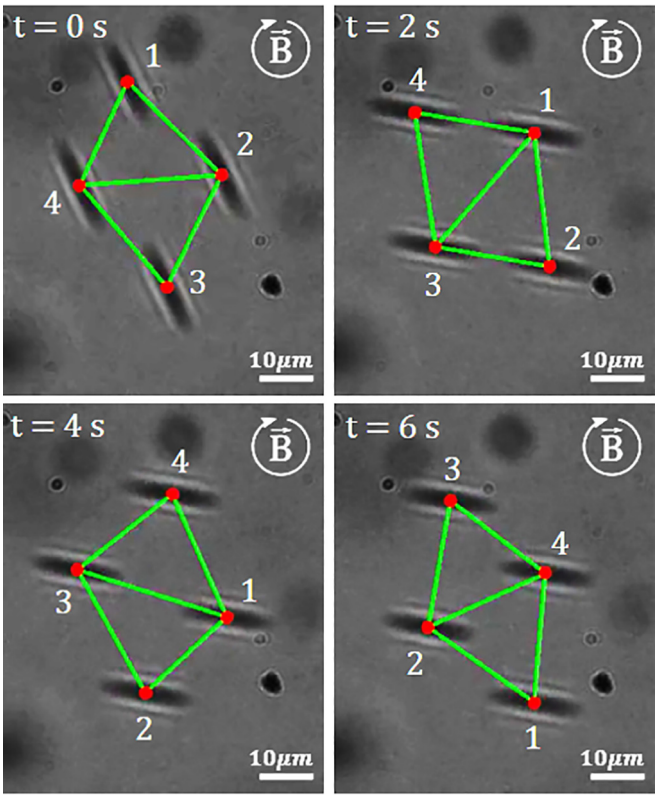

Fig. 5. Four droplets form a quadrilateral rotating crystal with oscillating diagonal lengths. The droplets are labeled 1–4, and are Delaunay triangulated to better illustrate their motion. Snapshots are taken with 2 s increments. Magnetic field ($B = 60$ G and $f = 15$ Hz) is rotating in the plane of observation.

Since this model does not take into account any radial forces or flows between two droplets, it does not impose an equilibrium distance between two droplets. Therefore, as an initial condition in the calculations, we place the droplets at positions taken from an experiment. We then let their positions evolve according to this model.

We expect this model to reproduce the angular velocity of the rotating crystals if the rotational flows produced by the droplets do not disrupt the distances between the droplets. This is the case for small ensembles of 2 or 3 droplets.

However, it was found that 4 droplets produce periodically oscillating inter-drop distances (Fig. 5), which is something that could be reproduced by this model even without radial forces between the droplets.

3.2. Tests of the proposed model

To test the model, let us first look at the case of two droplets orbiting around a common center of mass. Experimentally the droplets are rotating with an angular velocity $\omega_{rot}^{exp} = (0.66 \pm 0.04)$ rad/s. Using in the model the droplet length and starting with coordinates from the experimental images (as said above), we get a value for the angular velocity $\omega_{rot}^{theor} = (0.6 \pm 0.1)$ rad/s which is in good agreement with the experiment. We calculate the angular velocity of the rotating crystal by taking the average between all droplets of

$$\omega_{rot} = \frac{|\vec{r}\times\vec{v}|}{|\vec{r}|^2}, \tag{2}$$

where $\vec{r}$ is the vector from the center of mass of the crystal to that of the droplet and $\vec{v}$ is the droplet's velocity. The error for the model value is determined by varying input parameters within measurement

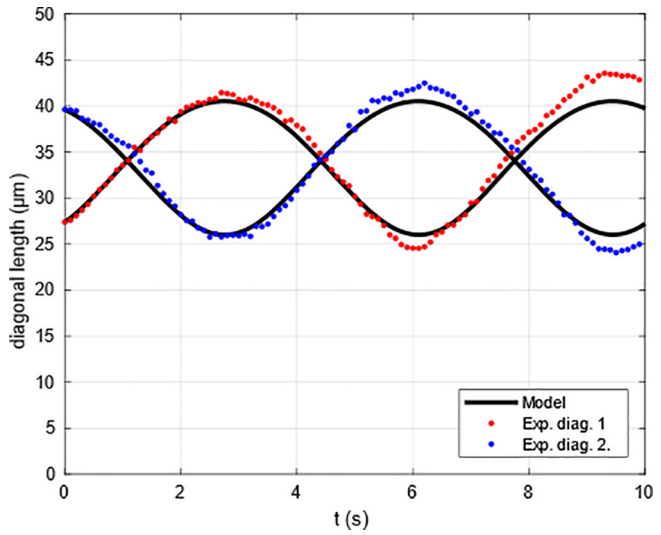

Fig. 6. The diagonal lengths of the four droplet rotating crystal over time. The blue and red points are taken from experimental fits of the droplet positions. The black lines are the model results, which used the droplet position at $t = 0$ that were taken from the experiment and the droplet dimensions that were taken from the experiment within the margins of error such that the model best fits the experiment points.

error boundaries. The two droplets rotate around a common center of mass significantly slower than an individual droplet rotating with the magnetic field (15 Hz). This is because the speed of the rotational flow produced by a single droplet decreases roughly as $1/r^2$, where r is the distance from the droplet's center.

As shown in Fig. 5 four magnetic droplets form a quadrilateral that rotates in the direction of the field and additionally its diagonal lengths oscillate. Again using droplet parameters from the experiment, we calculate the motion of the droplets and see that the rotation of the quadrilateral and the oscillation of the diagonal lengths is nicely reproduced as shown in Fig. 6. The angular oscillation frequency of the experiment is found to be $\omega_{diag}^{exp} = (0.95 \pm 0.02)$ rad/s which coincides with the value from the model $\omega_{diag}^{theor} = (1.1 \pm 0.2)$ rad/s. The experimental angular velocity of the crystal $\omega_{rot}^{exp} = (0.47 \pm 0.04)$ rad/s just barely coincides with the model value $\omega_{rot}^{theor} = (0.60 \pm 0.09)$ rad/s. However, the ratio of the two cannot be described with the current model: $\omega_{diag}^{exp}/\omega_{rot}^{exp} = 2.0 \pm 0.2$ and $\omega_{diag}^{theor}/\omega_{rot}^{theor} = 1.71 \pm 0.02$. Interestingly, in our model, while the uncertainty in the droplet length is the primary source of error both for ω_{diag} and ω_{rot}, the error in their ratio comes mostly from the uncertainty of the droplet position above the horizontal wall.

When calculating the motion of a large rotating crystal of droplets, we soon find that because there is nothing that forces an equilibrium distance between the droplets, the 2D crystal does not retain its regular shape and quickly disintegrates.

3.3. Suggestions for further improvement of the model

To reproduce the "crystallization" of droplets, the modelling needs both an attractive and a repulsive force between them. We propose that the equilibrium distance between the droplets is given by a balance between a magnetic attractive force and a radially outward secondary flow, as described in [19] for a rotating spherical particle. Note that some further work is still needed to write the secondary flow expression for a rotating elongated droplet near a wall.

Approximating the droplets as rotating spheres and using the expression from [19] does not suffice. We see that the force produced by the outward flow is two orders of magnitude smaller than the attractive force between the droplets due to a rotating magnetic dipole

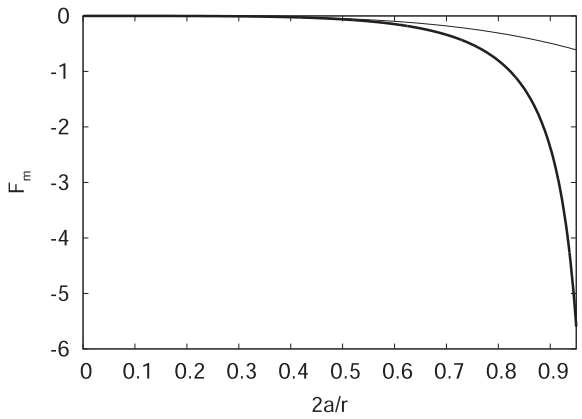

Fig. 7. Dimensionless magnetic force as a function of the inverse distance between droplets. Exact relation – thick line, dipolar approximation – thin line.

interaction. We do, however, propose an expression for the magnetic attraction for elongated rotating particles (in Gaussian units), which turns out to be around 4 times larger than the simple magnetic dipole interaction. This is something that a suitable repulsive force would have to compensate.

Since the tips of two rotating elongated magnetic droplets with opposite magnetic charges $\pm \pi b^2 M$ (M is the magnetization of the droplet) may come rather close to each other, the magnetic interaction between the droplets is given by a coulumbian interaction of the charges on their tips. We approximate the droplets as elongated cylinders with a length of $2a$ and a cross section radius b. Time-averaged magnetic interaction energy in that case reads as follows (for the full derivation see Appendix A):

$$U = \frac{2(\pi b^2 M)^2}{r}\left(1 - \frac{1}{2\pi}\int_0^{2\pi} \frac{dt}{\sqrt{(1 + 2a\cos(t)/r)^2 + 4a^2\sin^2(t)/r^2}}\right). \tag{3}$$

If $r \gg 2a$, then we obtain $U = -\frac{m^2}{2r^3}$, where $m = 2a\pi b^2 M$ is the magnetic moment of the droplet. Thus at large distances between droplets, the magnetic interaction energy is given by the time averaged dipolar interaction energy.

The magnetic force between droplets is obtained by differentiation. It is shown in Fig. 7, scaled by $m^2/8a^4$. Fig. 7 shows that at close distance between droplets the dipolar interaction force is smaller by an order of magnitude than the force calculated using coulombian interaction between effective magnetic charges. It is this strong attraction that balances the hydrodynamic flows in the formation of the 2D crystals of magnetic droplets.

4. Conclusions

Ensembles of magnetic microdroplets in a rotating magnetic field form structures with a regular triangular order – rotating crystals. The distance between the droplets results from a balance between the magnetic attraction and the repulsion associated with the flow arising from inertial effects. Ensembles of several droplets (2,4) are well described by the model taking into account the hydrodynamic interactions between the droplets in the presence of a solid wall underneath. In large arrays, rows of dislocations are observed at the grain boundaries. It is shown that for an accurate description of the magnetic interaction between the droplets, the coulombian interaction between the magnetic charges on the tips of the elongated droplets must be considered.

CRediT authorship contribution statement

A.P. Stikuts: Conceptualization, Investigation, Software, Methodology, Writing - original draft. **R. Perzynski:** Supervision,

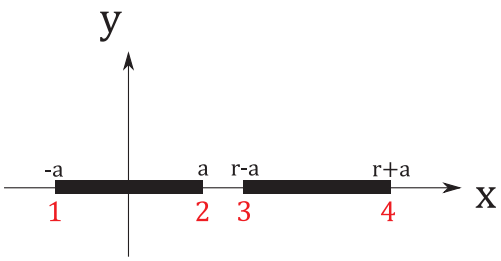

Fig. 8. Schematic of two elongated droplets (the black rectangles) at $t = 0$. Their centers are a distance r apart and they are rotating about them. The tips of the droplets are labeled with numbers 1–4 shown in red.

Writing - review & editing. **A. Cēbers:** Supervision, Writing - review & editing, Methodology.

Declaration of Competing Interest

The authors declare that they have no known competing financial interests or personal relationships that could have appeared to influence the work reported in this paper.

Acknowledgments

We express gratitude to D. Talbot for the ferrofluid sample, and G. Kitenbergs for helpful experimental insights. The research was helped by the funding from the Embassy of France in Latvia, SIA "Mikrotīkls" and the French-Latvian bilateral program "Osmose" FluMaMi (n°40033SJ; LV-FR/2019/5).

Appendix A. Magnetic interaction of elongated droplets

To derive the time-averaged magnetic interactions between the elongated droplets, we treat them as elongated cylinders with cross-section radius b and length $2a$. Two droplets rotate with a frequency of Ω about their center-points that are a distance r apart. We set the origin at the center of one of the drops and let the center of the other be located on the x axis. To keep track of the rotating tips of the droplets, we label them from 1 to 4 as seen in Fig. 8. The radius vectors pointing to the tips are then

$$\begin{aligned}
\vec{r_1} &= (a\cos(\Omega t),\, a\sin(\Omega t)) \\
\vec{r_2} &= (-a\cos(\Omega t),\, -a\sin(\Omega t)) \\
\vec{r_3} &= (r + a\cos(\Omega t),\, a\sin(\Omega t)) \\
\vec{r_4} &= (r - a\cos(\Omega t),\, -a\sin(\Omega t))
\end{aligned} \tag{4}$$

If the droplets are magnetized with a volume magnetization M and they are slender, we can approximately describe them with point magnetic charges $\pm \pi b^2 M$ at their tips. Then we can write the energy of coulombian interaction between the tips as the sum of pairwise energies $U = U_{13} + U_{24} + U_{14} + U_{23}$. We omit energies U_{12} and U_{34} as they are constant and do not contribute to the force. The expressions for the pairwise energies are

$$\begin{aligned}
U_{13} &= U_{24} = \frac{(\pi b^2 M)^2}{r} \\
U_{23}(t) &= -\frac{(\pi b^2 M)^2}{\sqrt{(r + 2a\cos(\Omega t))^2 + 4a^2\sin^2(\Omega t)}} \\
U_{14}(t) &= U_{23}\left(t + \frac{\pi}{\Omega}\right)
\end{aligned} \tag{5}$$

where in the last line we noticed that U_{14} is equal to U_{23} after rotation by angle π. We sum all the energies and average over a rotation period $2\pi/\Omega$ and obtain Eq. (3).

References

[1] V. Liljeström, C. Chen, P. Dommersnes, J.O. Fossum, A.H. Gröschel, Active structuring of colloids through field-driven self-assembly, Curr. Opin. Colloid Interface Sci. 40 (2019) 25–41.
[2] B. Grzybowski, H. Stone, G. Whitesides, Dynamic self-assembly of magnetized, millimetre-sized objects rotating at a liquid-air interface, Nature 405 (2000) 1033–1036.
[3] B. Grzybowski, X. Jiang, H. Stone, G. Whitesides, Dynamic, self-assembled aggregates of magnetized, millimeter-sized objects rotating at the liquid-air interface: macroscopic, two-dimensional classical artificial atoms and molecules, Phys. Rev. E 64 (2001) 011603.
[4] Y. Yan, S. Bae, S. Granick, Rotating crystals of magnetic janus colloids, Soft Matter. 11 (2015) 147–153.
[5] Q. Wang, L. Yang, B. Wang, E. Yu, J. Yu, L. Zhang, Collective behavior of reconfigurable magnetic droplets via dynamic self-assembly, ACS Appl. Mater. Interfaces 11 (2019) 1630–1637.
[6] A. Petroff, X.-L. Wu, A. Libchaber, Fast-moving bacteria self-organize into active two-dimensional crystals of rotating cells, Phys. Rev. Lett. 114 (2015) 158102.
[7] A. Shen, A. Wurger, J. Lintuvuori, Hydrodynamic self-assembly of active colloids: chiral spinners and dynamic crystals, Soft Matter. 15 (2019) 1508–1521.
[8] J. Bacri, A. Cebers, R. Perzynski, Behavior of a magnetic microdrop in a rotating magnetic field, Phys. Rev. Lett. 72 (1994) 2705–2708.
[9] J. Erdmanis, G. Kitenbergs, R. Perzynski, A. Cēbers, Magnetic micro-droplet in rotating field: numerical simulation and comparison with experiment, J. Fluid Mech. 821 (2017) 266–295.
[10] O. Sandre, J. Browaeys, R. Perzynski, J.-C. Bacri, V. Cabuil, R. Rosensweig, Assembly of microscopic highly magnetic droplets: magnetic alignment versus viscous drag, Phys. Rev. E 59 (1999) 1736–1746.
[11] F. Cousin, E. Dubois, V. Cabuil, Approach of the critical point of gas-liquid transitions in an electrostatically stabilized colloidal suspension, J. Chem. Phys. 115 (2001) 6051–6057.
[12] F. Cousin, E. Dubois, V. Cabuil, Tuning the interactions of a magnetic colloidal suspension, Phys. Rev. E 68 (2003) 021405.
[13] J. Bacri, D. Salin, Instability of ferrofluid magnetic drops under magnetic field, J. Phys. 43 (1982) L771–L777.
[14] A. Cebers, Virial method of investigation of statics and dynamics of drops of magnetizable liquids, Magnetohydrodynamics 21 (1985) 19–26.
[15] Y. Dikansky, A. Cebers, V.P. Shatsky, Magnetic emulsion properties in electric and magnetic fields. 1. Statics, Magnetohydrodynamics 26 (1990) 25–30.
[16] J. Blake, A. Chwang, Fundamental singularities of viscous flow. Part I: The image systems in the vicinity of a stationary no-slip boundary, J. Eng. Math. 8 (1974) 23–29.
[17] S.-M. Yang, L. Leal, Particle motion in stokes flow near a plane fluid-fluid interface. Part 1. Slender body in a quiescent fluid, J. Fluid. Mech. 136 (1983) 393–421.
[18] S. Kim, S. Karrila, Microhydrodynamics: Principles and Selected Applications, Butterworth-Heinemann, 1991.
[19] W. Bickley, The secondary flow due to a sphere rotating in a viscous fluid, The London, Edinburgh, Dublin Philos. Mag. J. Sci. 25 (1938) 746–752.

Physics of Fluids

Small deformation theory for a magnetic droplet in a rotating field

Cite as: Phys. Fluids **34**, 052010 (2022); https://doi.org/10.1063/5.0091453
Submitted: 15 March 2022 • Accepted: 06 May 2022 • Accepted Manuscript Online: 07 May 2022 • Published Online: 19 May 2022

A. P. Stikuts, R. Perzynski and A. Cēbers

Physics of Fluids ARTICLE scitation.org/journal/phf

Small deformation theory for a magnetic droplet in a rotating field

Cite as: Phys. Fluids **34**, 052010 (2022); doi: 10.1063/5.0091453
Submitted: 15 March 2022 · Accepted: 6 May 2022 ·
Published Online: 19 May 2022

View Online Export Citation CrossMark

A. P. Stikuts,[1,2,a)] R. Perzynski,[2] and A. Cēbers[1]

AFFILIATIONS

[1]MMML Lab, Faculty of Physics, Mathematics and Optometry, University of Latvia, Jelgavas iela 3-014, Riga LV-1004, Latvia
[2]Sorbonne Université, CNRS, Laboratoire PHENIX, 4 place Jussieu, case 51, F-75005 Paris, France

[a)]Author to whom correspondence should be addressed: andris_pavils.stikuts@lu.lv

ABSTRACT

A three-dimensional small deformation theory is developed to examine the motion of a magnetic droplet in a uniform rotating magnetic field. The equations describing the droplet's shape evolution are derived using two different approaches—a phenomenological equation for the tensor describing the anisotropy of the droplet and the hydrodynamic solution using the perturbation theory. We get a system of ordinary differential equations for the parameters describing the droplet's shape, which we further analyze for the particular case when the droplet's elongation is in the plane of the rotating field. The qualitative behavior of this system is governed by a single dimensionless quantity $\tau\omega$—the product of the characteristic relaxation time of small perturbations and the angular frequency of the rotating magnetic field. Values of $\tau\omega$ determine whether the droplet's equilibrium will be closer to an oblate or a prolate shape, as well as whether its shape will undergo oscillations as it settles to this equilibrium. We show that for small deformations, the droplet pseudo-rotates in the rotating magnetic field—its long axis follows the field, which is reminiscent of a rotation; nevertheless, the torque exerted on the surrounding fluid is zero. We compare the analytic results with boundary element simulation to determine their accuracy and the limits of the small deformation theory.

I. INTRODUCTION

Due to a combination of responsiveness to external magnetic fields and their deformability, magnetic droplets make an interesting material that has found many applications. They are widely used in microfluidics,[1] where an external magnetic field can be used for their formation, transport, and sorting. Magnetic droplets have been used as microrobots that scale obstacles and transport cargo.[2,3] Using time varying external fields, it is possible to induce dynamic self-assembled structures in magnetic droplet systems.[4–6] Biologically compatible magnetic droplets have found applications in biomedical context such as a proposed method for treating retinal detachment[7] and the measurement of mechanical properties of growing tissues.[8]

The behavior of magnetic fluid droplets in constant magnetic field has been widely researched. Such droplets elongate in the external field direction until the capillary forces balance out the magnetic forces. Assuming a spheroidal shape, theoretical equilibrium elongation depending on the magnetic field can be found.[9–11] The development of the theoretical equilibrium curves allows for the experimental measurement of the droplet surface tension and magnetic permeability.[9,11,12] For large elongations, the droplets cease to be ellipsoidal and develop sharp tips,[13] and numerical studies are required to describe their shape,[11,14,15] which have shown that the ellipsoidal approximation is valid when the aspect ratio is $a/b \lesssim 4$.[15] Recently, a semi-analytic relation has been proposed to describe the droplet elongation even in the large deformation regime.[16] The dynamics of a droplet in constant field can also be theoretically described with the ellipsoidal approximation.[10,17]

In a rotating magnetic field, magnetic droplets show a large variety of complex behaviors depending on the magnetic field parameters.[18,19] For low frequencies, the droplets elongate and follow the field; viscous friction can cause the droplets to break.[20] For high frequencies (much larger than the reciprocal of the characteristic time for surface deformations), the magnetic field forcing can be averaged over the rotation period. In this regime, the droplet takes up interesting equilibrium shapes. At low magnetic field strengths, the droplets are oblate spheroids flattened in the plane of the rotating field; increasing the field strength, a spontaneous symmetry breaking occurs, and they elongate tangential to the plane of rotation; increasing the field further, the droplets become flattened again in the rotation plane, and a crown of fingers can be seen on their perimeter.[18] This oblate–prolate–oblate transition has been described theoretically assuming spheroidal

shapes,[18] later it was extended to the case of an ellipsoid with three different axes.[21] Recently, an algorithm based on boundary element methods (BEMs) was used to calculate the equilibrium shapes in high-frequency fields without the constraint of the ellipsoidal approximation.[12] However, the time-dependent dynamics of magnetic droplets in rotating fields has not been yet thoroughly theoretically investigated.

An approach often used to calculate droplet dynamics in external flows is phenomenological models for the anisotropy tensor, which describes the droplet's shape. There are several definitions for the tensor quantity. For example, models based on the Doi–Ohta theory[22] up to a constant factor and summand use $\boldsymbol{q} = \int_S \boldsymbol{nn} dS$, where $\boldsymbol{n}$ is the droplet's normal vector and the integral is over the droplet's surface.[23] The Maffetone–Minale model[24] and others based on it describe the evolution of a tensor quantity $\boldsymbol{S}$, whose eigenvalues are the squared semiaxes of the ellipsoidal droplet. Such phenomenological models have proven useful in predicting the experimentally observed droplet shapes in external flows.[25] For a more thorough description of different models for an ellipsoidal droplet, we refer to a review article.[26] The phenomenological nature of the models allows for their extension to more complicated situations, for example, non-Newtonian fluids, taking into account wall effects and in our case—magnetic interaction. It is important, however, to verify these models against experiments, microscopic theories, and simulations.

In this paper, our goal is to derive analytic formulas for droplet shape dynamics in weak rotating magnetic fields, well below the measured threshold of shape instabilities. We showcase a phenomenological model for droplet anisotropy tensor and show how it can be used in the case of a rotating (or precessing) field. By solving the full hydrodynamic problem, we show that its solution is exact for droplets with small deformations in weak fields. Furthermore, we explore the dynamics of magnetic droplets in rotating magnetic fields observing interesting effects such as nonlinear shape oscillations and droplet pseudo-rotation without torque exertion. We provide the velocity and pressure fields in and around the droplet valid for weak fields and small droplet deformations. Finally, we determine the applicability limits of the analytic expressions in comparison to numerical boundary element calculations.

II. PROBLEM FORMULATION

We consider a superparamagnetic magnetic droplet with magnetic permeability μ, surface tension coefficient γ, viscosity $\eta^{(i)}$, and volume $4\pi R_0^3/3$ suspended in an infinite carrier fluid whose viscosity is $\eta^{(e)}$ and magnetic permeability equal to the vacuum magnetic permeability μ_0. A rotating external field is applied $\boldsymbol{H}_\infty = H_\infty(\boldsymbol{e}_y \cos(\omega t) + \boldsymbol{e}_z \sin(\omega t))$ with angular velocity $\boldsymbol{\omega} = \omega \boldsymbol{e}_x$. $\boldsymbol{H}$ is the magnetic field intensity, $\boldsymbol{B} = \mu_0(\boldsymbol{H} + \boldsymbol{M})$ is the magnetic field induction, and $\boldsymbol{M}$ is the magnetization. Magnetization is assumed to be linearly dependent on the magnetic field intensity $\boldsymbol{M} = \chi \boldsymbol{H}$ and, therefore, is the magnetic field induction $\boldsymbol{B} = \mu \boldsymbol{H}$, where the susceptibility is $\chi = \mu/\mu_0 - 1$.

The fluid both inside and outside the droplet obeys the Stokes equations

$$-\frac{\partial \tilde{p}}{\partial x_i} + \eta \frac{\partial^2 v_i}{\partial x_j \partial x_j} + \frac{\partial T_{ij}}{\partial x_j} = 0, \quad \frac{\partial v_j}{\partial x_j} = 0, \tag{1}$$

where v_i is the fluid velocity and $\tilde{p}$ is its pressure. $T_{ij} = -\mu_0 H^2 \delta_{ij}/2 + H_i B_j$ is the Maxwell stress tensor such that $\partial_j T_{ij} = \mu_0 M_j \partial_j H_i$.[27,28]

For linearly magnetizable fluids, its action in the bulk fluid can be represented by a magnetic pressure term

$$p_M = -\frac{1}{2}\mu_0 \left(\frac{\mu}{\mu_0} - 1\right) H^2, \quad \frac{\partial T_{ij}}{\partial x_j} = -\frac{\partial p_M}{\partial x_i}. \tag{2}$$

This allows us to formulate the Stokes equations of motion with an effective pressure $p = \tilde{p} + p_M$ taking into account p_M in the boundary conditions.

They are as follows. On the droplet surface, the velocity is continuous

$$\boldsymbol{v}^{(e)} - \boldsymbol{v}^{(i)} = 0. \tag{3}$$

The total force on the surface element in the normal direction is zero

$$n_i(\sigma_{ij}^{(e)} - \sigma_{ij}^{(i)})n_j + f_M - \gamma(k_1 + k_2) = 0. \tag{4}$$

$\sigma_{ij} = -p\delta_{ij} + \eta(\partial v_i/\partial x_j + \partial v_j/\partial x_i)$ is the effective hydrodynamic stress tensor (including the magnetic pressure), n_i is the droplet's outward unit normal, k_1 and k_2 are the principal curvatures, and f_M is the effective magnetic surface force

$$f_M = \frac{1}{2}\mu_0 \left(\frac{\mu}{\mu_0} - 1\right)\left(\frac{\mu}{\mu_0} H_n^{(i)2} + H_t^{(i)2}\right), \tag{5}$$

where H_n and H_t are the normal and tangential field components, respectively, on the surface of the droplet. The total force in the tangential direction on the surface element is zero

$$P_{ki}(\sigma_{ij}^{(e)} - \sigma_{ij}^{(i)})n_j = 0, \tag{6}$$

where $P_{ki} = \delta_{ki} - n_k n_i$ is the projection operator on the tangent plane of the surface.

To find the magnetic field, we solve the equations of magnetostatics

$$\nabla \times \boldsymbol{H} = 0, \quad \nabla \cdot \boldsymbol{B} = 0. \tag{7}$$

Introducing the magnetic potential ψ such that $\boldsymbol{H} = \nabla\psi$, Eq. (7) is satisfied if it satisfies the Laplace equation

$$\Delta\psi = 0. \tag{8}$$

The boundary conditions for the magnetostatic problem are as follows. On the surface of the droplet, the normal component of $\boldsymbol{B}$ is continuous

$$\mu_0 n_i \frac{\partial \psi^{(e)}}{\partial x_i} - \mu n_i \frac{\partial \psi^{(i)}}{\partial x_i} = 0, \tag{9}$$

and, if there is no distribution of magnetic dipoles on the surface, the potential itself is continuous

$$\psi^{(e)} - \psi^{(i)} = 0, \tag{10}$$

which also automatically satisfies the requirement that the tangential component of $\boldsymbol{H}$ is continuous. Finally, far away from the droplet

$$\frac{\partial \psi^{(e)}}{\partial x_i} = H_{\infty i}. \tag{11}$$

A. Dimensionless parameters

Three dimensionless parameters naturally arise in the solution of the problem

- the viscosity ratio $\lambda = \eta^{(i)}/\eta^{(e)}$,
- the relative magnetic permeability $\mu_r = \mu/\mu_0$, and
- the magnetic Bond number $Bm = 4\pi\mu_0 R_0 H_\infty^2/\gamma$, which is the ratio of a characteristic magnetic force and a characteristic surface tension force.

It is worth mentioning that different authors define different dimensionless groups as the magnetic Bond number. For example, some definitions are without the 4π factor[20] $Bm = \mu_0 R_0 H_\infty^2/\gamma$, and others have two in the denominator[11] $Bm = \mu_0 R_0 H_\infty^2/(2\gamma)$, whereas some call this ratio the magnetic capillary number Ca_m,[29] analogous to a similar quantity for droplets in electric fields—the electric capillary number Ca_{el}.[30] Our choice corresponds to the one used in the work of Erdmanis *et al.*[12] Care should be exercised when comparing results between them.

B. Description of droplet's shape

In the limit of the weak field ($Bm \ll 1$) when the deformation of the magnetic droplet is small, we may represent it as a triaxial ellipsoid with semiaxes $a \geq b \geq c$ (Fig. 1). Equivalently, we can use two deformation parameters, the elongation

$$\epsilon_1 = \frac{a-b}{b} \tag{12}$$

and the flatness

$$\epsilon_2 = \frac{b-c}{b} \tag{13}$$

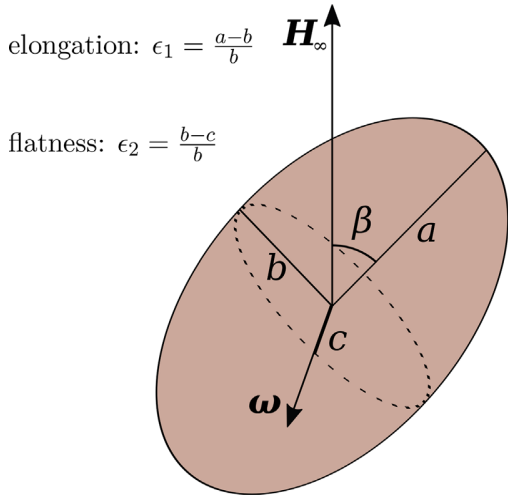

FIG. 1. In the limit of small deformations, the droplet can be described as an ellipsoid with semiaxes $a \geq b \geq c$ and with an angle β between the longest axis and the field in the case when the motion is in the rotation plane of the magnetic field. $\beta < 0$ if the droplet lags behind the field. The magnetic field $\boldsymbol{H}_\infty$ rotates with the angular velocity $\boldsymbol{\omega}$.

of the droplet, which together with the incompressibility condition $abc = R_0^3$ fully determine all three semiaxes. These deformation parameters are related to the commonly used[15,30–32] Taylor deformation parameter D in the limit where the droplet is a prolate spheroid as

$$D = \frac{\epsilon_1}{\epsilon_1 + 2} = \frac{\epsilon_1}{2} + O(\epsilon_1^2) \tag{14}$$

and in the limit where the droplet is an oblate spheroid as

$$D = \frac{\epsilon_2}{\epsilon_2 - 2} = -\frac{\epsilon_2}{2} + O(\epsilon_2^2). \tag{15}$$

When the droplet deforms in the plane of the rotating magnetic field, the smallest axis c is in the direction of $\boldsymbol{\omega}$, and another parameter arises—the angle β between the droplet's longest axis and the external magnetic field direction. It is chosen such that $\beta < 0$ if the droplet's axis is lagging behind the field. In general, two more angles would be necessary to describe the out-of-plane motion of the droplet; however, we do not examine it in this work.

III. ANISOTROPY TENSOR APPROACH

Ellipsoidal droplet's shape is described by a quadratic form

$$x_i A_{ij} x_j = 1. \tag{16}$$

Unperturbed spherical shape corresponds to $A_{ij} = \delta_{ij}/R_0^2$, where δ_{ij} is the Kronecker delta. For deformed droplets, we may write $A_{ij} = (\delta_{ij} + \zeta_{ij})/R_0^2$, where ζ_{ij} is the symmetric anisotropy tensor. Eigenvalues of ζ_{ij} are $\lambda_i = (R_0^2/a_i^2 - 1)$, where a_i are the semiaxes of the droplet. For small deformations, the eigenvalues can be written as

$$\begin{cases} \lambda_1 = -2\left(\dfrac{c}{R_0} - 1\right), \\ \lambda_2 = -2\left(\dfrac{b}{R_0} - 1\right), \\ \lambda_3 = -2\left(\dfrac{a}{R_0} - 1\right). \end{cases} \tag{17}$$

Conservation of volume requires $\prod_{i=1}^{3}(1+\lambda_i) = 1$. For small deformations, it means that

$$\lambda_1 + \lambda_2 + \lambda_3 = 0. \tag{18}$$

Let us consider a rotating coordinate frame $(\boldsymbol{e}'_x, \boldsymbol{e}'_y, \boldsymbol{e}'_z)$ such that

$$\begin{cases} \boldsymbol{e}'_x = \boldsymbol{e}_x, \\ \boldsymbol{e}'_y = \boldsymbol{e}_y \sin(\omega t) - \boldsymbol{e}_z \cos(\omega t), \\ \boldsymbol{e}'_z = \boldsymbol{e}_y \cos(\omega t) + \boldsymbol{e}_z \sin(\omega t). \end{cases} \tag{19}$$

In this rotating frame, the magnetic field is stationary, and in the $\boldsymbol{e}'_z$ direction, there is an additional constant fluid flow rotating with angular velocity $\boldsymbol{\Omega} = -\omega \boldsymbol{e}'_x$.

In the static case when $\omega = 0$, the droplet elongates in the $\boldsymbol{e}'_z$ direction to an axisymmetric equilibrium shape characterized by its elongation

$$\delta = [\epsilon_1]_{\omega=0} = \left[\frac{a-b}{b}\right]_{\omega=0}. \tag{20}$$

In that case, we can write the equilibrium anisotropy tensor

$$\boldsymbol{\zeta}^0 = \begin{pmatrix} \frac{2\delta}{3} & 0 & 0 \\ 0 & \frac{2\delta}{3} & 0 \\ 0 & 0 & -\frac{4\delta}{3} \end{pmatrix}. \tag{21}$$

A phenomenological equation for the tensor ζ_{ij} in the rotating frame reads[33]

$$\frac{d\zeta_{ij}}{dt} - e_{ipr}\Omega_p\zeta_{rj} - e_{jpr}\Omega_p\zeta_{ir} = -\frac{1}{\tau}(\zeta_{ij} - \zeta^0_{ij}), \tag{22}$$

where τ is the relaxation time of droplet's shape perturbations and e_{ipr} is the Levi–Civita symbol. A brief justification of Eq. (22) might be appropriate here. The left-hand side of the equation is the Jaumann derivative, which takes into account that the components of the tensor can change due to rotation. On the contrary, the right-hand side states that the droplet's shape exponentially approaches an equilibrium described by $\boldsymbol{\zeta}^0$ with characteristic time τ. It might be noted that an additional term can be added to describe the effect of a shear flow on the droplet's shape and, thus, describe their rheology, but it is outside of the scope of this work. See, for example, the Maffettone–Minale model[24] for ellipsoidal droplets in a viscous flow, which uses a tensor $\boldsymbol{S}$ close to the inverse of the one used here $\boldsymbol{S} = R_0^2(\boldsymbol{\zeta} + \boldsymbol{I})^{-1}$, where $\boldsymbol{I}$ is the identity tensor.

For the components of the anisotropy tensor, Eq. (22) gives three independent sets of equations

$$\frac{d\zeta_{11}}{dt} = -\frac{1}{\tau}\left(\zeta_{11} - \frac{2\delta}{3}\right), \tag{23}$$

$$\begin{cases} \frac{d\zeta_{12}}{dt} = -\frac{1}{\tau}\zeta_{12} + \omega\zeta_{13}, \\ \frac{d\zeta_{13}}{dt} = -\frac{1}{\tau}\zeta_{13} - \omega\zeta_{12}, \end{cases} \tag{24}$$

$$\begin{cases} \frac{d\zeta_{22}}{dt} = -\frac{1}{\tau}\left(\zeta_{22} - \frac{2\delta}{3}\right) + 2\omega\zeta_{23}, \\ \frac{d\zeta_{23}}{dt} = -\frac{1}{\tau}\zeta_{23} - \omega\zeta_{22} + \omega\zeta_{33}, \\ \frac{d\zeta_{33}}{dt} = -\frac{1}{\tau}\left(\zeta_{33} + \frac{4\delta}{3}\right) - 2\omega\zeta_{23}. \end{cases} \tag{25}$$

When the droplet moves in the plane of the magnetic field, only the system of equations (25) is relevant. Equation (23) is just needed to satisfy the incompressibility condition for the droplet, and it gives no new information since the trace of ζ_{ij} is zero as follows from Eq. (18). Equations (24) describe the out-of-plane motion of the droplet, their solutions decay exponentially to zero, and therefore, the in-plane motion is stable.

Since ζ_{ij} is symmetric, it has three real eigenvalues and mutually orthogonal eigenvectors $(\boldsymbol{n}^1, \boldsymbol{n}^2, \boldsymbol{n}^3)$. We can write

$$\zeta_{ij} = \lambda_1 n^1_i n^1_j + \lambda_2 n^2_i n^2_j + \lambda_3 n^3_i n^3_j. \tag{26}$$

The eigenvectors are aligned with the axes of the ellipsoid; hence, they are

$$\begin{cases} \boldsymbol{n}^1 = \boldsymbol{e}'_x, \\ \boldsymbol{n}^2 = \boldsymbol{e}'_y \cos(\beta) + \boldsymbol{e}'_z \sin(\beta), \\ \boldsymbol{n}^3 = -\boldsymbol{e}'_y \sin(\beta) + \boldsymbol{e}'_z \cos(\beta). \end{cases} \tag{27}$$

We then see that

$$\begin{cases} \zeta_{22} = \lambda_2 \cos^2(\beta) + \lambda_3 \sin^2(\beta), \\ \zeta_{23} = (\lambda_2 - \lambda_3)\cos(\beta)\sin(\beta), \\ \zeta_{33} = \lambda_2 \sin^2(\beta) + \lambda_3 \cos^2(\beta). \end{cases} \tag{28}$$

Inserting Eq. (28) in Eq. (25), we find the equations for the time evolution of the eigenvalues of the anisotropy tensor and the angle β

$$\begin{cases} \frac{d\lambda_2}{dt} = -\frac{1}{\tau}\left(\lambda_2 + \frac{\delta}{3} - \delta\cos(2\beta)\right), \\ \frac{d\lambda_3}{dt} = -\frac{1}{\tau}\left(\lambda_3 + \frac{\delta}{3} + \delta\cos(2\beta)\right), \\ \frac{d\beta}{dt} = -\omega + \frac{\delta\sin(2\beta)}{\tau(\lambda_3 - \lambda_2)}. \end{cases} \tag{29}$$

Finally, from Eq. (17), it follows that for small deformations, the droplet deformation parameters [defined in Eqs. (12) and (13)] are connected with λ_i by

$$\epsilon_1 = \frac{1}{2}(\lambda_2 - \lambda_3), \quad \epsilon_2 = \frac{1}{2}(\lambda_1 - \lambda_2). \tag{30}$$

Combining Eqs. (29), (30), and (18), we get the time evolution of the deformation parameters

$$\begin{cases} \frac{d\epsilon_1}{dt} = -\frac{1}{\tau}(\epsilon_1 - \delta\cos(2\beta)), \\ \frac{d\epsilon_2}{dt} = -\frac{1}{\tau}(\epsilon_2 - \delta\sin^2(\beta)), \\ \frac{d\beta}{dt} = -\omega - \frac{\delta\cos(\beta)\sin(\beta)}{\tau\epsilon_1}. \end{cases} \tag{31}$$

Equation (22) used to derive the system (31) can be considered phenomenological, where the constants δ and τ may be determined experimentally or on the basis of some microscopic models considered in Sec. IV.

Note that the same anisotropy tensor equation (22) can be used to calculate the droplet dynamics in a precessing field. One just has to change the reference frame such that the field is stationary.

IV. HYDRODYNAMIC APPROACH

We solve the problem formulated in Sec. II asymptotically for small deformations using the perturbation theory. The droplet shape is slightly deviated from a sphere, which is described in spherical coordinates

$$\begin{cases} x = r\cos(\phi)\sin(\theta), \\ y = r\sin(\phi)\sin(\theta), \\ z = r\cos(\phi), \end{cases} \tag{32}$$

by

$$r = R_0(1 + \varepsilon f(\theta, \phi)), \tag{33}$$

where ε is a small parameter and we use x, y, z to denote the coordinates in the basis of $\boldsymbol{e}'_x, \boldsymbol{e}'_y, \boldsymbol{e}'_z$. We assume that all the physical parameters can be expressed as a power series of ε

$$\begin{aligned} \boldsymbol{v} &= \boldsymbol{v}_0 + \varepsilon \boldsymbol{v}_1 + O(\varepsilon^2), \\ p &= p_0 + \varepsilon p_1 + O(\varepsilon^2), \\ f_M &= f_{M0} + \varepsilon f_{M1} + O(\varepsilon^2). \end{aligned} \tag{34}$$

In the solution, we identify ε with the elongation and flatness parameters $\epsilon_1 = O(\varepsilon)$, $\epsilon_2 = O(\varepsilon)$. Furthermore, similarly to how it was done in paper by Vlahovska,[30] we assume that the magnetic bond number is small. Therefore, we omit from the solution the terms which are $O(\varepsilon^2)$ and $O(\varepsilon Bm)$.

Variables with the index 0 are the solutions to the spherical droplet, and they correspond to the flow arising from the magnetic forcing. Next order corrections $\varepsilon \boldsymbol{v}_1, \varepsilon p_1$ arise from the effects of surface deformation such as the flow due to surface tension. $\boldsymbol{v}, p$ and $\boldsymbol{v}_0, p_0$ satisfy the Stokes equations [Eq. (1)], therefore, do $\varepsilon \boldsymbol{v}_1, \varepsilon p_1$.

First, we find the solution for a non-rotating magnetic field. Then to get the solution for a rotating field, instead of having the magnetic field rotate, we add a flow field rotating in the opposite direction.

A. Solution for a spherical droplet

The expression for the magnetic field inside a spherical magnetic (or equivalently dielectric) droplet placed in a homogeneous external field $\boldsymbol{H}_\infty = H_\infty \boldsymbol{e}'_z$ is well known[34]

$$\boldsymbol{H}_0^{(i)} = \frac{3H_\infty}{\mu + 2}\boldsymbol{e}'_z, \tag{35}$$

which leads to the effective magnetic surface force [Eq. (5)] of

$$f_{M0} = \frac{\gamma}{R_0}\frac{9Bm}{8\pi}\frac{\mu_r - 1}{(\mu_r + 2)^2}\left(\mu_r \cos^2(\theta) + \sin^2(\theta)\right). \tag{36}$$

To find the velocity, we use Lamb's solution for the Stokes equations in spherical harmonics.[35,36] For the flow outside and inside the droplet, it reads

$$\begin{aligned} \boldsymbol{v}^{(e)} =& \sum_{l=1}^{\infty}\frac{1}{\eta^{(e)}}\left[-\frac{(l-2)r^2\nabla p_{-l-1}^{(e)}}{2l(2l-1)} + \frac{(l+1)\boldsymbol{r}p_{-l-1}^{(e)}}{l(2l-1)}\right] \\ &+ \sum_{l=0}^{\infty}\left[\nabla\phi_{-l-1}^{(e)} + \nabla\times\left(\boldsymbol{r}\chi_{-l-1}^{(e)}\right)\right], \end{aligned} \tag{37}$$

$$\begin{aligned} \boldsymbol{v}^{(i)} =& \sum_{l=0}^{\infty}\frac{1}{\eta^{(i)}}\left[\frac{(l+3)r^2\nabla p_l^{(i)}}{2(l+1)(2l+3)} - \frac{l\boldsymbol{r}p_l^{(i)}}{(l+1)(2l+3)}\right] \\ &+ \sum_{l=0}^{\infty}\left[\nabla\phi_l^{(i)} + \nabla\times\left(\boldsymbol{r}\chi_l^{(i)}\right)\right], \end{aligned} \tag{38}$$

and the corresponding effective pressure reads

$$p^{(e)} = \sum_{l=1}^{\infty} p_{-l-1}^{(e)}, \quad p^{(i)} = \sum_{l=0}^{\infty} p_l^{(i)}, \tag{39}$$

where $p_l^{(i)}$, $p_{-l-1}^{(e)}$, $\phi_l^{(i)}$, $\phi_{-l-1}^{(e)}$, $\chi_l^{(i)}$, and $\chi_{-l-1}^{(e)}$ are a sum of spherical harmonics of degree l multiplied by an appropriate power of r

$$\begin{aligned} p_l^{(i)} &= r^l\sum_{m=-l}^{l} a_l^m Y_l^m, \quad p_{-l-1}^{(e)} = r^{-l-1}\sum_{m=-l}^{l} A_l^m Y_l^m, \\ \phi_l^{(i)} &= r^l\sum_{m=-l}^{l} b_l^m Y_l^m, \quad \phi_{-l-1}^{(e)} = r^{-l-1}\sum_{m=-l}^{l} B_l^m Y_l^m, \\ \chi_l^{(i)} &= r^l\sum_{m=-l}^{l} c_l^m Y_l^m, \quad \chi_{-l-1}^{(e)} = r^{-l-1}\sum_{m=-l}^{l} C_l^m Y_l^m. \end{aligned}$$

The coefficients a, A, b, B, c, C are to be found from the boundary conditions. The spherical harmonics are

$$Y_l^m(\theta, \phi) = \sqrt{\frac{2l+1}{4\pi}\frac{(l-m)!}{(l+m)!}}P_l^m(\cos(\theta))e^{im\phi}, \tag{40}$$

where P_l^m is the associated Legendre polynomial. It is worth noting that the spherical harmonics are orthonormal with respect to integration over the whole solid angle[37]

$$\int_0^{2\pi} d\phi \int_0^{\pi} Y_l^m(\theta, \phi)\bar{Y}_{l'}^{m'}(\theta, \phi)\sin\theta d\theta = \delta_{ll'}\delta_{mm'}, \tag{41}$$

where the bar denotes the complex conjugate. Therefore, the coefficients in the spherical harmonic series of function $f(\theta, \phi) = \sum_{l=0}^{\infty}\sum_{m=-l}^{l} A_l^m Y_l^m(\theta, \phi)$ can be found by $A_l^m = \int_0^{2\pi} d\phi \int_0^{\pi} f(\theta, \phi)\bar{Y}_l^m(\theta, \phi)\sin\theta d\theta$.

The normal force on the spherical droplet boundary ($r = R_0$), that is, due to the magnetic field and surface tension is

$$f_M - \gamma(k_1 + k_2) = \frac{\gamma}{R_0}\left(\frac{9Bm}{8\pi}\frac{\mu_r - 1}{(\mu_r + 2)^2}\left(\mu_r \cos^2(\theta) + \sin^2(\theta)\right) - 2\right). \tag{42}$$

It must be counteracted by an effective hydrodynamic stress such that Eq. (4) is satisfied. Similarly to the work by Das and Saintillan,[38] we can see which summands in Lamb's solution [Eqs. (37) and (38)] need to be retained to produce the effective hydrodynamic stress of the right form. The normal force contains only harmonics of degree $l = 0$ and $l = 2$, and there is a symmetry around ϕ. Therefore, the only non-zero coefficients in Lamb's solution that are needed are a_0^0, B_0^0, a_2^0, b_2^0, A_2^0, B_2^0.

Now that there is a finite number of unknown variables, the further calculations are straightforward, albeit cumbersome, therefore, were done in Wolfram Mathematica. Lamb's solution with the non-zero coefficients is substituted in the boundary equations [Eqs. (3), (4), and (6)]. We write the boundary conditions on the spherical drop ($r = R_0$) and expand them in spherical harmonics. For the boundary conditions to be satisfied for arbitrary angles θ and ϕ, we require that each coefficient of expansion in spherical harmonics is zero, which leads to six equations for the six unknown coefficients in Lamb's solution.

The resulting velocities and effective pressures for the case of a spherical droplet can be found in Appendix A.

B. Solution for a deformed droplet

We assume that the droplet is ellipsoidal. Such an assumption is justified since the magnetic force induces changes in shape of the

droplet corresponding to spherical harmonic Y_2^0, which for small deformations means an ellipsoidal shape. As can be seen further, in a rotational flow, initially ellipsoidal droplets remain ellipsoidal. For small deformation parameters ϵ_1 and ϵ_2 in Cartesian coordinates, the equation for an ellipsoid, whose largest axis is rotated by an angle β from $\boldsymbol{e}_z'$ (magnetic field direction) is

$$\frac{\epsilon_1-\epsilon_2}{3}+(1+2\epsilon_2)\frac{x^2}{R_0^2}+\frac{(y\cos(\beta)+z\sin(\beta))^2}{R_0^2}+(1-2\epsilon_1)\frac{(z\cos(\beta)-y\sin(\beta))^2}{R_0^2}=1. \tag{43}$$

In spherical coordinates, the equation becomes

$$\begin{aligned} r&=R_0(1+\varepsilon f(\theta,\phi))\\ &=R_0\left(1+\alpha_2^2Y_2^{-2}+\alpha_2^1Y_2^{-1}+\alpha_2^0Y_2^0+\alpha_2^1Y_2^1+\alpha_2^2Y_2^2\right), \end{aligned} \tag{44}$$

where we expressed $\varepsilon f(\theta,\phi)$ in spherical harmonics. For an ellipsoid, the coefficients in front of harmonics Y_2^1 and Y_2^2 are the same as the coefficients in front of Y_2^{-1} and Y_2^{-2}, respectively. The coefficients are

$$\begin{aligned} \alpha_2^0&=\sqrt{\frac{\pi}{45}}(\epsilon_1(1+3\cos(2\beta))+2\epsilon_2),\\ \alpha_2^1&=-2i\sqrt{\frac{2\pi}{15}}\epsilon_1\cos(\beta)\sin(\beta),\\ \alpha_2^2&=-\sqrt{\frac{\pi}{30}}(\epsilon_1(1-\cos(2\beta))+2\epsilon_2). \end{aligned} \tag{45}$$

Note that all $\alpha_2^m=O(\varepsilon)$.

The normal vector and curvature are found by describing the droplet as a level surface $\xi=r-R_0(1+\varepsilon f(\theta,\phi))=0$, then

$$\boldsymbol{n}=\left[\frac{\nabla\xi}{|\nabla\xi|}\right]_{r=R_0(1+\varepsilon f)} \tag{46}$$

and

$$k_1+k_2=[\nabla\cdot\boldsymbol{n}]_{r=R_0(1+\varepsilon f)}, \tag{47}$$

which we then expand in ε and Bm keeping only the first order terms. Up to the first order in ε and Bm, f_M remains unchanged from the spherical case.

Just as in the zeroth order solution (for the spherical droplet), the first order correction fields $\varepsilon\boldsymbol{v}_1^{(i)},\varepsilon p_1^{(i)},\varepsilon\boldsymbol{v}_1^{(e)},\varepsilon p_1^{(e)}$ are written in the form of Lamb's solution. The boundary conditions for the full fields $(\boldsymbol{v}_0+\varepsilon\boldsymbol{v}_1,\ p_0+\varepsilon p_1)$ are enforced on the deformed surface $r=R_0(1+\varepsilon f)$ up to the first order of ε and Bm.

Again examining the normal force on the droplet boundary, it becomes evident that the only non-zero coefficients in Lamb's solution for the first order correction fields are the ones with $l=2$. However, now all $m=-l,\ldots,l$ are needed since there is no longer a symmetry along ϕ. Now there is only a finite number of coefficients, who can be found just as in the spherical case. We plug the solution with the non-zero coefficients in the boundary conditions [Eqs. (3), (4), and (6)] enforced on the deformed surface $r=R_0(1+\varepsilon f)$ and expand them in power series of ε and Bm up to the first order. We then expand the expressions in spherical harmonics and require all the coefficients in front of them to be 0 to satisfy the boundary conditions for all θ,ϕ.

This leads to somewhat long expressions for the velocity and pressure fields inside and outside the droplet. (They are provided in Appendix B.) To get the solution for the case when the magnetic field is rotating, we add $\boldsymbol{v}_{rot}=-\omega\boldsymbol{e}_x'\times\boldsymbol{r}$ to the velocity field.

To describe the change in shape of the droplet, only the velocity on its boundary $\boldsymbol{v}^{(b)}=[\boldsymbol{v}]_{r=R_0(1+\varepsilon f)}$ is needed. If the droplet's shape is described by $r=\rho(\theta,\phi,t)=R_0(1+\varepsilon f(\theta,\phi,t))$, then the kinematic boundary condition dictates that

$$\frac{\partial\rho}{\partial t}=v_r^{(b)}-\frac{1}{r}\left(v_\theta^{(b)}\frac{\partial\rho}{\partial\theta}+\frac{v_\phi^{(b)}}{\sin(\theta)}\frac{\partial\rho}{\partial\phi}\right), \tag{48}$$

where again we keep only the terms up to first power of ε and Bm. If we expand the droplet's shape in spherical harmonics $r=\rho(\theta,\phi,t)=R_0\sum_{l=0}^{\infty}\sum_{m=-l}^{l}\alpha_l^m(t)Y_l^m(\theta,\phi)$ and plug them in Eq. (48), we get the differential equations for the expansion coefficients

$$\begin{cases} \dfrac{d\alpha_2^2}{dt}=i\omega\alpha_2^1-\dfrac{\alpha_2^2}{\tau},\\ \dfrac{d\alpha_2^1}{dt}=\dfrac{i\omega}{2}\left(\sqrt{6}\alpha_2^0+2\alpha_2^2\right)-\dfrac{\alpha_2^1}{\tau},\\ \dfrac{d\alpha_2^0}{dt}=i\sqrt{6}\omega\alpha_2^1+\dfrac{4\sqrt{5\pi}\delta}{15\tau}-\dfrac{\alpha_2^0}{\tau}. \end{cases} \tag{49}$$

We also see that the coefficients with opposite signs in m evolve with the same rate $d\alpha_l^m/dt=d\alpha_l^{-m}/dt$. The derivatives of the coefficients with $l\neq2$ are zero, which means that an initially ellipsoidal droplet stays ellipsoidal.

If we insert the ellipsoid expansion coefficients from Eq. (45) into Eq. (49), we retrieve the system of equations for the time evolution of the ellipsoid deformation parameters [Eq. (31)]. Furthermore, from the hydrodynamic approach, we also get the expressions for the phenomenological constants in the anisotropy tensor approach. The elongation of the droplet in a non-rotating field is

$$\delta=\frac{9Bm}{32\pi}\frac{(\mu_r-1)^2}{(\mu_r+2)^2}, \tag{50}$$

and the characteristic relaxation time for small perturbations from equilibrium is

$$\tau=\frac{R_0\eta^{(e)}}{\gamma}\frac{(3+2\lambda)(16+19\lambda)}{40(1+\lambda)}. \tag{51}$$

The values obtained here for δ agree in the limit of small deformations with the equilibrium values of an ellipsoidal droplet in a homogeneous static field.[9–11] τ is the same as described in other works on small deformations of droplets.[31,33]

V. ANALYSIS AND COMPARISON WITH NUMERICAL SIMULATIONS

A. Fixed points and their stability

The fixed points for Eq. (31) are

$$\begin{cases} \epsilon_1^*=\dfrac{\delta}{\sqrt{1+4\tau^2\omega^2}},\\ \epsilon_2^*=\dfrac{\delta}{2}\left(1-\dfrac{1}{\sqrt{1+4\tau^2\omega^2}}\right),\\ \beta^*=-\dfrac{1}{2}\arctan(2\tau\omega)+n\pi, \end{cases} \tag{52}$$

where n is a whole number. We see that for non-rotating field $\tau\omega = 0$, the droplet becomes prolate $\epsilon_2^* = 0$ and aligns with the field $\beta^* = n\pi$, whereas for large field rotation frequencies $\tau\omega \to \infty$, the droplet becomes nearly oblate $\epsilon_1^* \to 0$, it flattens to a value of $\epsilon_2^* \to \delta/2$ and lags the field by an angle $\beta^* \to -\pi/4 + n\pi$.

It is interesting to investigate the stability of the fixed point. Linearizing Eq. (31) for small perturbations $\Delta\epsilon_1$, $\Delta\epsilon_2$, $\Delta\beta$ around the fixed point, we get

$$\frac{d}{dt}\begin{pmatrix}\Delta\epsilon_1\\ \Delta\epsilon_2\\ \Delta\beta\end{pmatrix} = \begin{pmatrix} -\frac{1}{\tau} & 0 & \frac{4\delta\omega}{\sqrt{1+4\tau^2\omega^2}} \\ 0 & -\frac{1}{\tau} & -\frac{2\delta\omega}{\sqrt{1+4\tau^2\omega^2}} \\ -\frac{\omega\sqrt{1+4\tau^2\omega^2}}{\delta} & 0 & -\frac{1}{\tau} \end{pmatrix}\begin{pmatrix}\Delta\epsilon_1\\ \Delta\epsilon_2\\ \Delta\beta\end{pmatrix}. \tag{53}$$

The eigenvalues of this matrix are $-1/\tau, -1/\tau - 2i\omega, -1/\tau + 2i\omega$, meaning that the fixed points are stable foci, and there is an oscillation with twice the angular frequency of the magnetic field as the perturbations decay.

B. Qualitative behavior of the system

We can scale the deformation parameters by the deformation parameter in a non-rotating field δ [Eq. (50)] and time by the characteristic decay time τ [Eq. (51)], setting $\tilde{\epsilon}_1 = \epsilon_1/\delta$, $\tilde{\epsilon}_2 = \epsilon_2/\delta$, and $\tilde{t} = t/\tau$. We then see that up to a constant scaling factor, the system is governed only by a single free parameter $\tau\omega$, which is proportional to the capillary number—the ratio of viscous forces to the surface tension forces.[39] In this form, system (31) is written as

$$\begin{cases} \frac{d\tilde{\epsilon}_1}{d\tilde{t}} = -\tilde{\epsilon}_1 + \cos(2\beta), \\ \frac{d\tilde{\epsilon}_2}{d\tilde{t}} = -\tilde{\epsilon}_2 + \sin^2(\beta), \\ \frac{d\beta}{d\tilde{t}} = -\tau\omega - \frac{\cos(\beta)\sin(\beta)}{\tilde{\epsilon}_1}. \end{cases} \tag{54}$$

The variables ϵ_1 and β form a closed system. We can use that to visualize their evolution by drawing a phase portrait (Fig. 2). Similarities can be seen with the behavior of a damped pendulum, where if the initial elongation is large enough, the droplet overshoots its equilibrium angle β several times before settling. Unlike the damped pendulum, in this system, there is no inertia—it is completely dissipative. However, similarly to the pendulum, there is an interplay between two characteristic times—the oscillatory period $T = \pi/\omega$ (the shape oscillates with twice the frequency of the magnetic field) and the small deformation decay time τ.

The transient behavior of an initially spherical droplet when placed in a rotating magnetic field illustrates the interplay between the two characteristic times of the system (Fig. 3). If the oscillatory period

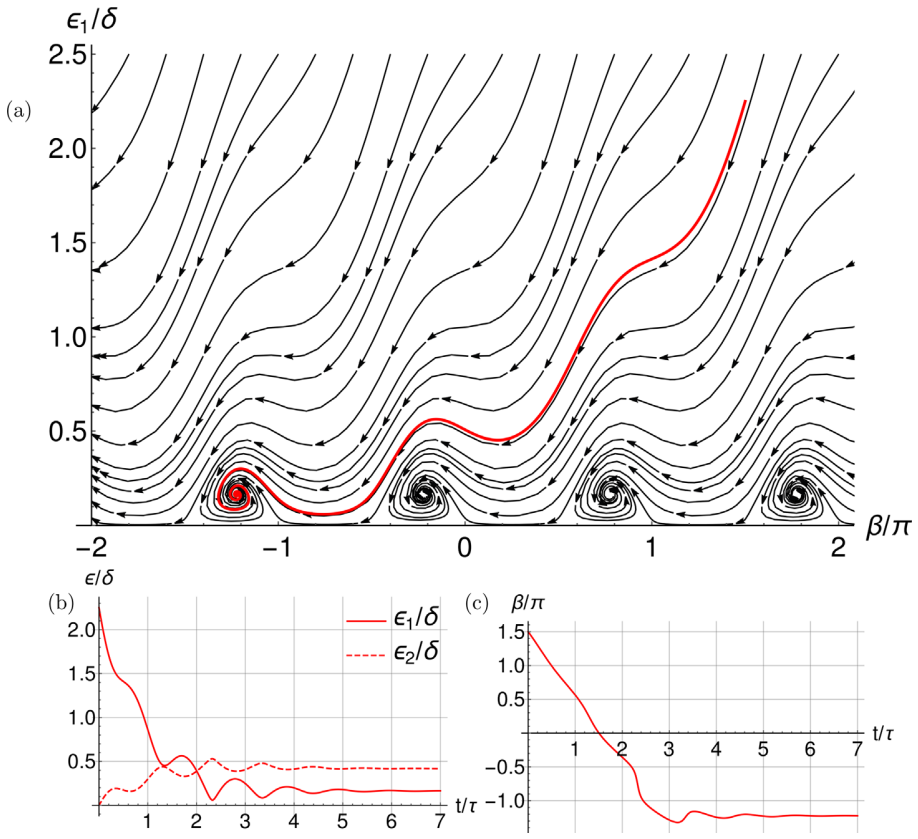

FIG. 2. (a) The phase portrait of the parameter describing the droplet elongation relative to its deformation under non-rotating field ϵ_1/δ and the angle between the droplet and the magnetic field β. The field frequency is such that $\tau\omega = 3$. (b) and (c) The time evolution of the variables ϵ_1/δ, ϵ_2/δ, and β corresponding to the red trajectory in (a).

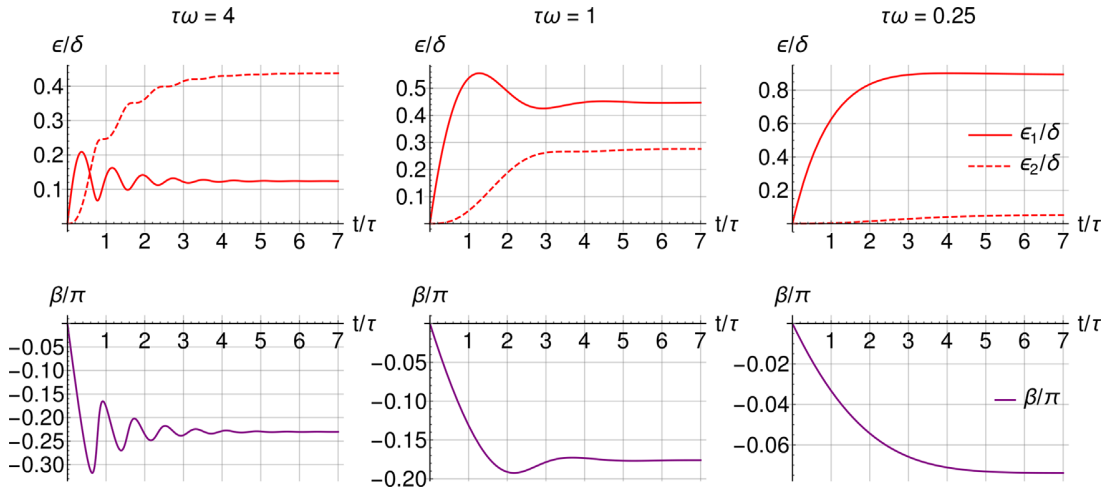

FIG. 3. Relaxation to an equilibrium shape of an initially spherical droplet when a rotating magnetic field of different frequencies $\tau\omega$ is applied. The top row shows the deformation parameters ϵ_1 and ϵ_2, and the bottom row shows the angle β between the droplet's largest axis and the field.

T is small compared to the relaxation time τ ($\tau\omega \gg 1$), there is enough time for the droplet to make several oscillations before settling; however, if the opposite is the case, the droplet relaxes to the equilibrium before a single oscillation can occur.

C. Flow fields around the droplet

The solution using the hydrodynamic approach allows us to visualize the flow fields inside and outside the droplets. Figure 4 shows the velocity streamlines in the stationary frame of reference for different droplet equilibrium shapes.

A visual inspection of the flow fields shows that the droplets are not in a rigid body rotation, but rather are changing their orientation due to surface deformations. Indeed if we integrate the outer velocity and pressure field over the droplet surface, we get that the net torque the droplet exerts on the fluid is identically zero up to the first order in ε.

The magnetic torque exerted by the droplet is $\mu_0(4\pi R_0^3/3)\boldsymbol{M}\times\boldsymbol{H}_\infty$, which is proportional to the deformation of the droplet (ϵ_1, ϵ_2) multiplied by Bm. From Eq. (52), it can be seen that the deformation of the droplet is proportional to Bm. However, it then follows that the magnetic torque is proportional to Bm^2. To consider a real rotation of the droplet that imparts a torque, we must go beyond the first order terms in the solution.

A similar result was found in a work that experimentally and with simulations examined sessile water droplets in a rotating electric field.[40] It was found that just as here, the droplets appear to rotate with the angular velocity of the rotating field, but the internal flow fields produce this apparent rotation by deforming the droplet's surface. The authors of said work called this motion "pseudo-rotation." This result can be contrasted with the Quincke rotation (or electrorotation) of weakly conducting droplets, where rotational Rotlet-like velocity fields emerge as the rotation starts.[38,41]

D. Comparison with numerical calculations

We use a numerical algorithm based on the boundary element method (BEM) that calculates the 3D evolution of a magnetic droplet's shape in an arbitrary magnetic field. The algorithm (outlined in

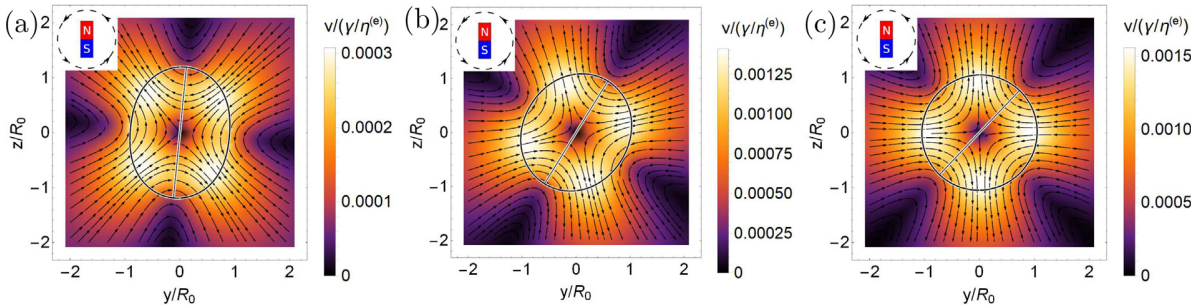

FIG. 4. The velocity field cross section at $x = 0$ inside and outside the magnetic droplets in the laboratory reference frame. The magnetic field is momentarily pointing in the z axis direction and rotating counterclockwise. The plots are made with equilibrium shapes of the droplets with $\delta = 0.3$ and (a) $\tau\omega = 0.1$, (b) $\tau\omega = 1$, and (c) $\tau\omega = 10$. The droplet shapes and their longest axis are outlined. The flow is such that it turns the longest axis of the droplet counterclockwise. The velocity magnitude in units of $\gamma/\eta^{(e)}$ is shown with a color gradient.

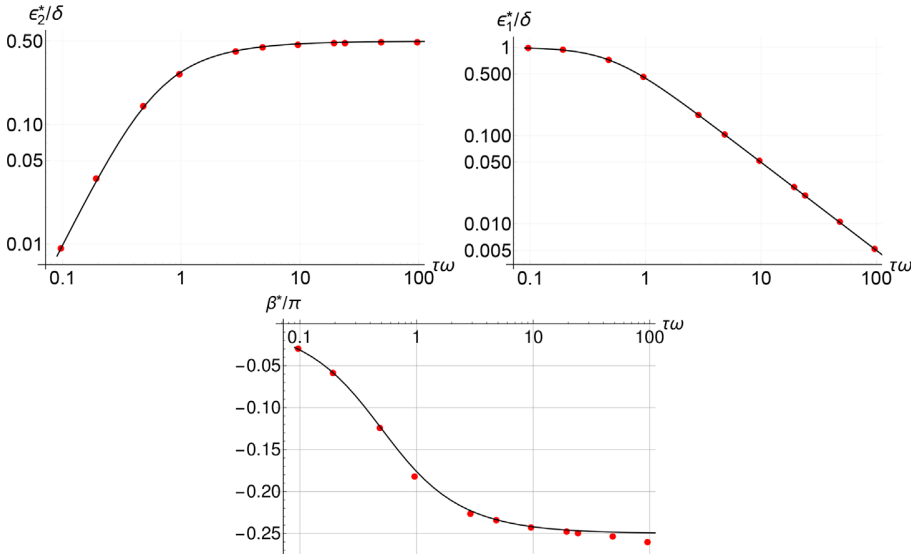

FIG. 5. The equilibrium values of the elongation ϵ_1^*, flatness ϵ_2^*, and the angle between the field and the droplet's largest axis β^* depending on the field rotation frequency. The droplet elongation in the non-rotating field is $\delta = 0.005$. The red dots are BEM simulation results and the black lines are from (52).

Appendix C) is an extension of the work by Erdmanis *et al.*[12] to be able to capture the dynamics of droplets with $\lambda \neq 1$.

To validate the results of the small deformation theory, we calculate the equilibrium shapes using the BEM algorithm and compare them with the analytic expressions [Eq. (52)] for the fixed points (Fig. 5). The dimensionless input parameters for simulation are chosen as follows: $Bm = 0.1$, $\lambda = 100$, $\mu_r = 10$, and $\omega/(\gamma/(R_0\eta^{(e)}))$ varied. These parameters correspond to $\delta = 0.005$ and $\tau = 96.3/(R_0\eta^{(e)}/\gamma)$. To get the deformation parameters and the angle between the field and the droplet's largest axis, we fit a 3D ellipsoid to the vertices of the mesh triangles. We see excellent agreement for both deformation parameters ϵ_1^* and ϵ_2^*, and good agreement for β^*. Possibly, the discrepancy between the theoretical curve of β and simulation results for large ω is due to elongation ϵ_1 tending to 0, and thus, the angle between the largest axis and the field β becomes ill-defined.

To determine the limits of the small deformation theory, we numerically calculate the equilibrium shapes for increasing values of Bm [proportional to the parameter δ as given in Eq. (50)] and compare them to Eq. (52) (Fig. 6). The simulation parameters are $\omega = 0.05/(\gamma/(R_0\eta^{(e)}))$, $\lambda = 100$, and $\mu_r = 10$, and Bm is varied from 0.1 to 13. These parameters correspond to $\tau = 96.3/(R_0\eta^{(e)}/\gamma)$. We see that the error is roughly below 10%, if $\delta < 0.3$. Indeed, we see that although $Bm \propto \delta$, instead of $Bm \ll 1$, the criterion which should be assessed to determine if the small deformation theory is applicable for a particular case is $\delta \ll 1$.

In this comparison between simulations and the theory, the droplet is quasi oblate $\epsilon_2 > \epsilon_1$. There is qualitative agreement in droplet's behavior between the theory and simulations also for values of $Bm \lesssim 12$ ($\delta \lesssim 0.6$). However, for these simulation parameters, at around $Bm \approx 13$ ($\delta \approx 0.65$), the droplet ceases to be quasi oblate and strongly elongates ($\epsilon_1 \approx 2.7, \epsilon_2 \approx 0.03$) in roughly the field direction and rotates more or less like a rigid body. Such a bifurcation is not captured by the $O(\varepsilon)$ small deformation theory, but it has been observed experimentally (the left column of Fig. 1 in the work by Bacri *et al.*[18]).

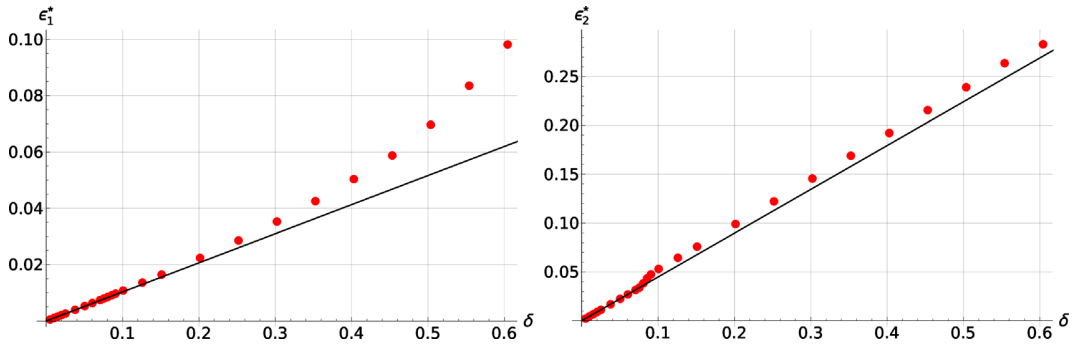

FIG. 6. The equilibrium values of the elongation ϵ_1^*, flatness ϵ_2^* depending on the scaled magnetic field characterized by the parameter δ as calculated from Eq. (50). The droplet's characteristic deformation time multiplied by the field rotation frequency is $\tau\omega = 4.8$. The red dots are BEM simulation results, and the black lines are from Eq. (52).

VI. CONCLUSIONS

We have produced an analytic 3D solution for the magnetic droplet shape dynamics in a rotating field valid for small deformations and small Bm in the leading order. In particular, the parameter $\delta \lesssim 0.3$ as expressed in Eq. (50) is what determines the limit of this small deformation theory. When the droplet is elongated in the plane of the rotating field, its shape evolution is governed by a system of three nonlinear differential equations [Eq. (31)]. Its solution is determined up to a scaling by a single parameter $\tau\omega$—the product of the decay time of small deformations and the magnetic field rotation frequency.

The hydrodynamic equations governing the droplet are completely dissipative; nonetheless, a droplet in a rotating field can experience nonlinear damped oscillations before reaching an equilibrium shape. The interplay of two characteristic times (the field rotation period and the droplet relaxation time) leads to a phase portrait similar to that of a damped pendulum. Interestingly, for weak fields, the droplets pseudo-rotate in the direction of the magnetic field—their surface deforms such that the long axis follows the field; nonetheless, no torque is exerted by the droplet.

We have showcased how the anisotropy tensor description can be used to calculate the droplet shape in the rotating (or precessing) magnetic field. The phenomenological model was validated with numerical simulations and by solving the full hydrodynamic problem. In the limit of small deformations, the phenomenological equation of motion [Eq. (22)] is exact.

Our results could be used for the verification of numerical algorithms and could serve as a basis for more complex models, for example, ones that incorporate a shear flow,[24] which could be then used to analytically calculate the rheological properties of magnetic droplets, which have so far been tackled numerically.[29,42]

ACKNOWLEDGMENTS

A.P.S. is thankful to SIA "Mikrotīkls" and the Embassy of France in Latvia for financially supporting cotutelle studies.

A.P.S. acknowledges the financial support of "Strengthening of the capacity of doctoral studies at the University of Latvia within the framework of the new doctoral model," Identification No. 8.2.2.0/20/I/006.

A.C. and A.P.S. acknowledge the financial support of grant of the Scientific Council of Latvia via Grant No. lzp-2020/1-0149.

AUTHOR DECLARATIONS

Conflict of Interest

The authors have no conflicts to disclose.

DATA AVAILABILITY

The data that support the findings of this study are available from the corresponding author upon reasonable request.

APPENDIX A: VELOCITY AND EFFECTIVE PRESSURE OF A SPHERICAL DROPLET

In spherical coordinates

$$\begin{cases} x = r\cos(\phi)\sin(\theta), \\ y = r\sin(\phi)\sin(\theta), \\ z = r\cos(\phi), \end{cases} \tag{A1}$$

if the magnetic field is pointing in the $\boldsymbol{e}'_z$ axis direction, the velocity and effective pressure inside (i) and outside (e) a spherical magnetic droplet read

$$\boldsymbol{v}_0^{(i)} = \frac{\gamma}{\eta^{(e)}} M_2 \left[\left(\frac{L_4}{L_2 L_3} \left(\frac{r}{R_0}\right) - \frac{3}{L_3}\left(\frac{r}{R_0}\right)^3 \right) (1 + 3\cos(2\theta))\boldsymbol{e}_r + \left(-\frac{3L_4}{L_2 L_3}\left(\frac{r}{R_0}\right) + \frac{15}{L_3}\left(\frac{r}{R_0}\right)^3 \right) \sin(2\theta)\boldsymbol{e}_\theta \right], \tag{A2}$$

$$\boldsymbol{v}_0^{(e)} = \frac{\gamma}{\eta^{(e)}} M_2 \left[\left(\frac{1}{L_2}\left(\frac{r}{R_0}\right)^{-2} - \frac{3L_1}{L_2 L_3}\left(\frac{r}{R_0}\right)^{-4} \right) (1 + 3\cos(2\theta))\boldsymbol{e}_r + \left(-\frac{6L_1}{L_2 L_3}\left(\frac{r}{R_0}\right)^{-4} \right) \sin(2\theta)\boldsymbol{e}_\theta \right], \tag{A3}$$

$$p_0^{(i)} = \frac{\gamma}{R_0}\left(2 - M_1 - \frac{21\lambda M_2}{L_3}(1 + 3\cos(2\theta)) \left(\frac{r}{R_0}\right)^2 \right), \tag{A4}$$

$$p_0^{(e)} = \frac{\gamma}{R_0}\frac{2M_2}{L_2}(1 + 3\cos(2\theta))\left(\frac{r}{R_0}\right)^{-3}, \tag{A5}$$

where

$$M_1 = \frac{3Bm}{8\pi}\frac{\mu_r - 1}{\mu_r + 2}, \quad M_2 = \frac{3Bm}{16\pi}\frac{(\mu_r - 1)^2}{(\mu_r + 2)^2}, \quad L_1 = (2 + 3\lambda), \quad L_2 = (3 + 2\lambda), \quad L_3 = (16 + 19\lambda), \quad L_4 = (19 + 16\lambda). \tag{A6}$$

APPENDIX B: VELOCITY AND EFFECTIVE PRESSURE OF A DEFORMED DROPLET

The velocity and effective pressure fields in and around a slightly deformed droplet are written as power series

$$\begin{aligned} \boldsymbol{v}^{(i)} &= \boldsymbol{v}_0^{(i)} + \varepsilon \boldsymbol{v}_1^{(i)} + O(\varepsilon^2), \\ \boldsymbol{v}^{(e)} &= \boldsymbol{v}_0^{(e)} + \varepsilon \boldsymbol{v}_1^{(e)} + O(\varepsilon^2), \\ p^{(i)} &= p_0^{(i)} + \varepsilon p_1^{(i)} + O(\varepsilon^2), \\ p^{(e)} &= p_0^{(e)} + \varepsilon p_1^{(e)} + O(\varepsilon^2), \end{aligned} \tag{B1}$$

where the first order correction terms are as follows:

$$\varepsilon \boldsymbol{v}_1^{(i)} = \frac{\gamma}{\eta^{(e)}}\left(-\frac{L_4}{L_2 L_3}\left(\frac{r}{R_0}\right) + \frac{3}{L_3}\left(\frac{r}{R_0}\right)^3 \right) E_1 \boldsymbol{e}_r + \frac{\gamma}{\eta^{(e)}}\left(\frac{L_4}{L_2 L_3}\left(\frac{r}{R_0}\right) - \frac{5}{L_3}\left(\frac{r}{R_0}\right)^3 \right) E_2 \boldsymbol{e}_\theta + \frac{\gamma}{\eta^{(e)}}\left(\frac{L_4}{L_2 L_3}\left(\frac{r}{R_0}\right) - \frac{5}{L_3}\left(\frac{r}{R_0}\right)^3 \right) E_3 \boldsymbol{e}_\phi, \tag{B2}$$

$$\varepsilon \boldsymbol{v}_1^{(e)} = \frac{\gamma}{\eta^{(e)}}\left(-\frac{1}{L_2}\left(\frac{r}{R_0}\right)^{-2}+\frac{3L_1}{L_2L_3}\left(\frac{r}{R_0}\right)^{-4}\right)E_1\boldsymbol{e}_r + \frac{\gamma}{\eta^{(e)}}\frac{2L_1}{L_2L_3}E_2\boldsymbol{e}_\theta\left(\frac{r}{R_0}\right)^{-4}+\frac{\gamma}{\eta^{(e)}}\frac{2L_1}{L_2L_3}E_3\boldsymbol{e}_\phi\left(\frac{r}{R_0}\right)^{-4}, \quad \text{(B3)}$$

$$\varepsilon p_1^{(i)} = \frac{\gamma}{R_0}\frac{21\lambda E_1}{L_3}\left(\frac{r}{R_0}\right)^{2}, \quad \text{(B4)}$$

$$\varepsilon p_1^{(e)} = -\frac{\gamma}{R_0}\frac{2E_1}{L_2}\left(\frac{r}{R_0}\right)^{-3}, \quad \text{(B5)}$$

where

$$E_1 = -2\epsilon_1\sin(2\beta)\sin(2\theta)\sin(\phi) + \sin^2(\theta)\cos(2\phi)(\epsilon_1\cos(2\beta)-\epsilon_1-2\epsilon_2) + \frac{1}{6}(3\cos(2\theta)+1)(3\epsilon_1\cos(2\beta)+\epsilon_1+2\epsilon_2), \quad \text{(B6)}$$

$$E_2 = -\frac{1}{2}\epsilon_1\cos(2\beta)\sin(2\theta)(\cos(2\phi)-3) + 2\epsilon_1\sin(2\beta)\cos(2\theta)\sin(\phi) + \sin(2\theta)(\epsilon_1+2\epsilon_2)\cos^2(\phi), \quad \text{(B7)}$$

$$E_3 = 2\cos(\phi)[\epsilon_1\sin(2\beta)\cos(\theta)+\sin(\theta)\sin(\phi) \times (\epsilon_1\cos(2\beta)-\epsilon_1-2\epsilon_2)]. \quad \text{(B8)}$$

The above expressed solution is for a droplet in a stationary magnetic field pointing in the $\boldsymbol{e}_z'$ direction. To get the solution for a rotating field with the angular velocity $\boldsymbol{\omega}=\omega\boldsymbol{e}_x'$, we can change the reference such that the rotating magnetic field is pointing in the $\boldsymbol{e}_z'$ direction by adding a background rotating velocity field $\boldsymbol{v}_{rot}=-\omega\boldsymbol{e}_x'\times\boldsymbol{r}$ to both internal and external velocity fields.

APPENDIX C: BOUNDARY ELEMENT METHOD

The governing equations presented in Sec. II are written in the boundary integral form. The Laplace equation for the magnetic potential [Eq. (8)] in the integral form reads[12,43]

$$\psi(\boldsymbol{y}) = \frac{2\boldsymbol{y}\cdot\boldsymbol{H}_\infty(\boldsymbol{y})}{1+\mu_r}+\frac{1-\mu_r}{1+\mu_r}\frac{1}{2\pi}\int_S\psi(\boldsymbol{x})\frac{\partial}{\partial x_i}\left(\frac{1}{|\boldsymbol{X}|}\right)n_i(\boldsymbol{x})dS_x, \quad \text{(C1)}$$

where the integration is over the droplet's surface, and we have introduced $\boldsymbol{X}=\boldsymbol{x}-\boldsymbol{y}$. The Stokes equations [Eq. (1)] in the integral form read[44]

$$v_k(\boldsymbol{y}) = \frac{2v_k^\infty(\boldsymbol{y})}{1+\lambda}-\frac{1}{1+\lambda}\frac{\gamma}{4\pi\eta^{(e)}} \times\int_S(k_1(\boldsymbol{x})+k_2(\boldsymbol{x}))n_i(\boldsymbol{x})G_{ik}(\boldsymbol{x},\boldsymbol{y})dS_x + \frac{1}{1+\lambda}\frac{1}{4\pi\eta^{(e)}}\int_S f_M(\boldsymbol{x})n_i(\boldsymbol{x})G_{ik}(\boldsymbol{x},\boldsymbol{y})dS_x + \frac{1-\lambda}{1+\lambda}\frac{1}{4\pi}\int_S v_i(\boldsymbol{x})T_{ijk}(\boldsymbol{x},\boldsymbol{y})n_j(\boldsymbol{x})dS_x, \quad \text{(C2)}$$

where $G_{ik}(\boldsymbol{x},\boldsymbol{y})=\delta_{ij}/|\boldsymbol{X}|+X_iX_j/|\boldsymbol{X}|^3$, $T_{ijk}(\boldsymbol{x},\boldsymbol{y})=-6X_iX_jX_k/|\boldsymbol{X}|^5$, and $v_k^\infty(\boldsymbol{y})$ is the background flow far away from the droplet. The boundary conditions are automatically satisfied if we solve the integral equations.

For smooth droplets, all the integrands in Eqs. (C1) and (C2) scale as $1/|\boldsymbol{X}|$ as $\vec{x}\to\vec{y}$, and some steps need to be taken to facilitate their numerical evaluation. Details for calculating the magnetic potential [Eq. (C1)] and from that the effective magnetic surface force can be found in the work by Erdmanis *et al.*[12] Some notes may be appropriate on the way we tackled the velocity integral equation [Eq. (C2)].

To regularize the integral and avoid introducing numerical errors from calculating the curvature, the first term on the right hand side was expressed in a curvaturless form[45]

$$\int_S(k_1(\boldsymbol{x})+k_2(\boldsymbol{x}))n_i(\boldsymbol{x})G_{ik}(\boldsymbol{x},\boldsymbol{y})dS_x = -\int_S\left[X_in_i(\boldsymbol{x})n_k(\boldsymbol{y})+X_in_i(\boldsymbol{y})n_k(\boldsymbol{x})+[1-n_i(\boldsymbol{x})n_i(\boldsymbol{y})]X_k - \frac{3X_k(n_i(\boldsymbol{x})+n_i(\boldsymbol{y}))X_iX_jn_j(\boldsymbol{x})}{|\boldsymbol{X}|^2}\right]\frac{dS_x}{|\boldsymbol{X}|^3}, \quad \text{(C3)}$$

where the expression in square brackets is proportional to $|\boldsymbol{X}|^3$ as $\vec{x}\to\vec{y}$. The second integral can be regularized using singularity subtraction.[44] We employ the identity $\int_S n_i(\boldsymbol{x})G_{ik}(\boldsymbol{x},\boldsymbol{y})dS_x=0$ to get

$$\int_S f_M(\boldsymbol{x})n_i(\boldsymbol{x})G_{ik}(\boldsymbol{x},\boldsymbol{y})dS_x = \int_S[f_M(\boldsymbol{x})-f_M(\boldsymbol{y})]n_i(\boldsymbol{x})G_{ik}(\boldsymbol{x},\boldsymbol{y})dS_x, \quad \text{(C4)}$$

where the integrand is now $O(1)$ as $\vec{x}\to\vec{y}$, if $f_M(\boldsymbol{x})$ is smooth. Finally, singularity subtraction is used also on the third term.[44] The identity $\int_S T_{ijk}(\boldsymbol{x},\boldsymbol{y})n_j(\boldsymbol{x})dS_x=-4\pi\delta_{ik}$ leads to

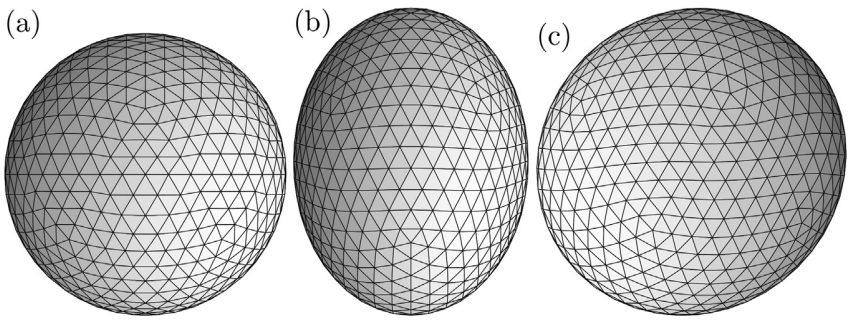

FIG. 7. The triangular mesh on the droplet's surface. (a) The initial ($t=0$) mesh of a spherical droplet. (b) and (c) The views of the mesh at $t=500/(R_0\eta^{(e)}/\gamma)$ perpendicular and along the angular velocity of the magnetic field, respectively. The simulation parameters are $Bm=9$, $\mu_r=10, \lambda=100, \omega=0.05/(\gamma/(R_0\eta^{(e)}))$.

$$\int_S v_i(\boldsymbol{x}) T_{ijk}(\boldsymbol{x},\boldsymbol{y}) n_j(\boldsymbol{x}) dS_x = \int_S [v_i(\boldsymbol{x}) - v_i(\boldsymbol{y})] T_{ijk}(\boldsymbol{x},\boldsymbol{y}) n_j(\boldsymbol{x}) dS_x - 4\pi v_k(\boldsymbol{y}), \quad \text{(C5)}$$

where the integrand is now $O(1)$ as $\vec{x} \to \vec{y}$, if $\boldsymbol{v}(\boldsymbol{x})$ is smooth.

We mesh the surface of the droplet with triangular elements (Fig. 7) and efficiently solve the now regularized integral equations with the trapezoidal rule. First, we find the magnetic potential, then we compute the effective magnetic surface force f_M, which we use to find the velocity on the surface of the droplet. We move the mesh points with this velocity using the Euler method and repeat the calculation for the next time step. A manuscript with a full description of the numerical algorithm is in preparation.

REFERENCES

[1]E. Al-Hetlani and M. O. Amin, "Continuous magnetic droplets and microfluidics: Generation, manipulation, synthesis and detection," Microchim. Acta **186**, 55 (2019).
[2]X. Fan, X. Dong, A. C. Karacakol, H. Xie, and M. Sitti, "Reconfigurable multifunctional ferrofluid droplet robots," Proc. Natl. Acad. Sci. **117**, 27916–27926 (2020).
[3]X. Fan, M. Sun, L. Sun, and H. Xie, "Ferrofluid droplets as liquid microrobots with multiple deformabilities," Adv. Funct. Mater. **30**, 2000138 (2020).
[4]J. V. I. Timonen, M. Latikka, L. Leibler, R. H. A. Ras, and O. Ikkala, "Switchable static and dynamic self-assembly of magnetic droplets on superhydrophobic surfaces," Science **341**, 253–257 (2013).
[5]Q. Wang, L. Yang, B. Wang, E. Yu, J. Yu, and L. Zhang, "Collective behavior of reconfigurable magnetic droplets via dynamic self-assembly," ACS Appl. Mater. Interfaces **11**, 1630–1637 (2019).
[6]A. Stikuts, R. Perzynski, and A. Cēbers, "Spontaneous order in ensembles of rotating magnetic droplets," J. Magn. Magn. Mater. **500**, 166304 (2020).
[7]O. T. Mefford, R. C. Woodward, J. D. Goff, T. Vadala, T. G. St. Pierre, J. P. Dailey, and J. S. Riffle, "Field-induced motion of ferrofluids through immiscible viscous media: Testbed for restorative treatment of retinal detachment," J. Magn. Magn. Mater. **311**, 347–353 (2007).
[8]F. Serwane, A. Mongera, P. Rowghanian, D. A. Kealhofer, A. A. Lucio, Z. M. Hockenbery, and O. Campàs, "In vivo quantification of spatially varying mechanical properties in developing tissues," Nat. Methods **14**, 181–186 (2017).
[9]J. Bacri and D. Salin, "Instability of ferrofluid magnetic drops under magnetic field," J. Phys. Lett. **43**, 649–654 (1982).
[10]A. O. Tsebers, "Virial method of investigation of statics and dynamics of drops of magnetizable liquids," Magnetohydrodynamics **21**, 19–26 (1985).
[11]S. Afkhami, A. J. Tyler, Y. Renardy, M. Renardy, T. G. St. Pierre, R. C. Woodward, and J. S. Riffle, "Deformation of a hydrophobic ferrofluid droplet suspended in a viscous medium under uniform magnetic fields," J. Fluid Mech. **663**, 358–384 (2010).
[12]J. Erdmanis, G. Kitenbergs, R. Perzynski, and A. Cēbers, "Magnetic microdroplet in rotating field: Numerical simulation and comparison with experiment," J. Fluid Mech. **821**, 266–295 (2017).
[13]H. A. Stone, J. R. Lister, and M. P. Brenner, "Drops with conical ends in electric and magnetic fields," Proc. R. Soc. London, Ser. A **455**, 329–347 (1999).
[14]O. Lavrova, G. Matthies, T. Mitkova, V. Polevikov, and L. Tobiska, "Numerical treatment of free surface problems in ferrohydrodynamics," J. Phys.: Condens. Matter **18**, S2657–S2669 (2006).
[15]P. Rowghanian, C. D. Meinhart, and O. Campàs, "Dynamics of ferrofluid drop deformations under spatially uniform magnetic fields," J. Fluid Mech. **802**, 245–262 (2016).
[16]K. Misra, "Magnetic (electric) drop deformation in uniform external fields: Volume averaged methods and formation of static and dynamic conical tips," Phys. Fluids **32**, 107104 (2020).
[17]J.-C. Bacri and D. Salin, "Dynamics of the shape transition of a magnetic ferrofluid drop," J. Phys. Lett. **44**, 415–420 (1983).
[18]J.-C. Bacri, A. O. Cebers, and R. Perzynski, "Behavior of a magnetic fluid microdrop in a rotating magnetic field," Phys. Rev. Lett. **72**, 2705–2708 (1994).
[19]E. Janiaud, F. Elias, J.-C. Bacri, V. Cabuil, and R. Perzynski, "Spinning ferrofluid microscopic droplets," Magnetohydrodynamics **36**, 300–378 (2000).
[20]O. Sandre, J. Browaeys, R. Perzynski, J.-C. Bacri, V. Cabuil, and R. E. Rosensweig, "Assembly of microscopic highly magnetic droplets: Magnetic alignment versus viscous drag," Phys. Rev. E **59**, 1736–1746 (1999).
[21]K. I. Morozov and A. V. Lebedev, "Bifurcations of the shape of a magnetic fluid droplet in a rotating magnetic field," J. Exp. Theor. Phys. **91**, 1029–1032 (2000).
[22]M. Doi and T. Ohta, "Dynamics and rheology of complex interfaces. I," J. Chem. Phys. **95**, 1242–1248 (1991).
[23]A. S. Almusallam, R. G. Larson, and M. J. Solomon, "A constitutive model for the prediction of ellipsoidal droplet shapes and stresses in immiscible blends," J. Rheol. **44**, 1055–1083 (2000).
[24]P. Maffettone and M. Minale, "Equation of change for ellipsoidal drops in viscous flow," J. Non-Newtonian Fluid Mech. **78**, 227–241 (1998).
[25]E. Boonen, P. Van Puyvelde, and P. Moldenaers, "Droplet dynamics in mixed flow conditions: Effect of shear/elongation balance and viscosity ratio," J. Rheol. **54**, 1285–1306 (2010).
[26]M. Minale, "Models for the deformation of a single ellipsoidal drop: A review," Rheol. Acta **49**, 789–806 (2010).
[27]R. E. Rosensweig, *Ferrohydrodynamics* (Dover Publications, 2014).
[28]E. Blūms, A. Cēbers, and M. M. Maiorov, *Magnetic Fluids* (Walter de Gruyter, 1997).
[29]L. H. P. Cunha, I. R. Siqueira, F. R. Cunha, and T. F. Oliveira, "Effects of external magnetic fields on the rheology and magnetization of dilute emulsions of ferrofluid droplets in shear flows," Phys. Fluids **32**, 073306 (2020).
[30]P. M. Vlahovska, "On the rheology of a dilute emulsion in a uniform electric field," J. Fluid Mech. **670**, 481–503 (2011).
[31]J. M. Rallison, "The deformation of small viscous drops and bubbles in shear flows," Annu. Rev. Fluid Mech. **16**, 45–66 (1984).
[32]D. Das and D. Saintillan, "A nonlinear small-deformation theory for transient droplet electrohydrodynamics," J. Fluid Mech. **810**, 225–253 (2017).
[33]Y. I. Dikanskii, A. O. Tsebers, and V. P. Shatskii, "Magnetic emulsion properties in electric and magnetic fields. I. Statics" Magnetohydrodynamics **26**, 25–30 (1990).
[34]J. A. Stratton, *Electromagnetic Theory* (McGraw Hill Book Company, 1941).
[35]H. Lamb, *Hydrodynamics*, 6th ed. (Cambridge University Press, 1975).
[36]S. Kim and S. J. Karrila, *Microhydrodynamics: Principles and Selected Applications*, Butterworth-Heinemann Series in Chemical Engineering (Butterworth-Heinemann, 1991).
[37]J. D. Jackson, *Classical Electrodynamics* (John Wiley and Sons, 1998).
[38]D. Das and D. Saintillan, "A three-dimensional small-deformation theory for electrohydrodynamics of dielectric drops," J. Fluid Mech. **914**, A22 (2021).
[39]H. A. Stone, "Dynamics of drop deformation and breakup in viscous fluids," Annu. Rev. Fluid Mech. **26**, 65–102 (1994).
[40]O. Ghazian, K. Adamiak, G. P. Castle, and Y. Higashiyama, "Oscillation, pseudo-rotation and coalescence of sessile droplets in a rotating electric field," Colloids Surf., A **441**, 346–353 (2014).
[41]P. M. Vlahovska, "Electrohydrodynamics of drops and vesicles," Annu. Rev. Fluid Mech. **51**, 305–330 (2019).
[42]S. Ishida and D. Matsunaga, "Rheology of a dilute ferrofluid droplet suspension in shear flow: Viscosity and normal stress differences," Phys. Rev. Fluids **5**, 123603 (2020).
[43]C. Pozrikidis, *A Practical Guide to Boundary Element Methods with the Software Library BEMLIB* (Chapman and Hall/CRC, 2002).
[44]C. Pozrikidis, *Boundary Integral and Singularity Methods for Linearized Viscous Flow* (Cambridge University Press, 1992).
[45]A. Z. Zinchenko, M. A. Rother, and R. H. Davis, "Cusping, capture, and breakup of interacting drops by a curvatureless boundary-integral algorithm," J. Fluid Mech. **391**, 249–292 (1999).

Physics of Fluids

A three-dimensional boundary element method algorithm for simulations of magnetic fluid droplet dynamics

Cite as: Phys. Fluids **34**, 062105 (2022); https://doi.org/10.1063/5.0092532
Submitted: 23 March 2022 • Accepted: 18 May 2022 • Accepted Manuscript Online: 20 May 2022 • Published Online: 02 June 2022

Aigars Langins, Andris Pāvils Stikuts and Andrejs Cēbers

Physics of Fluids ARTICLE scitation.org/journal/phf

A three-dimensional boundary element method algorithm for simulations of magnetic fluid droplet dynamics

Cite as: Phys. Fluids **34**, 062105 (2022); doi: 10.1063/5.0092532
Submitted: 23 March 2022 · Accepted: 18 May 2022 ·
Published Online: 2 June 2022

Aigars Langins,[1,a)] Andris Pāvils Stikuts,[1,2] and Andrejs Cēbers[1]

AFFILIATIONS

[1]MMML Lab, Department of Physics, Mathematics and Optometry, University of Latvia, Jelgavas st. 3-014, Riga LV-1002, Latvia
[2]Laboratoire PHENIX, Sorbonne Université, CNRS, 4 Place Jussieu, Case 51, F-75005 Paris, France

[a)]Author to whom correspondence should be addressed: aigars.langins@lu.lv

ABSTRACT

This paper outlines a numerical algorithm capable of simulating the full three-dimensional dynamics of magnetic fluid droplets in external magnetic fields by solving boundary integral equations. The algorithm works with arbitrary droplet and carrier fluid viscosity ratios. It is validated with known theoretical relationships. It also enables evaluating various approximations often used to describe ellipsoidal droplets by comparing the droplet dynamics calculated from such approximations to the results obtained from first principles using our numerical algorithm. The algorithm may be used to investigate droplet configurations in arbitrary magnetic fields and to indirectly calculate the physical properties of magnetic fluid droplets and predicting the magnetic field thresholds above which the droplet shape can develop instabilities in the form of various spikes.

I. INTRODUCTION

Figures of equilibrium of self-gravitating masses are a classical problem in mathematical physics,[1] where different bifurcations of shapes are described. Since the classical paper by Taylor,[2] the equilibrium shapes and their dynamics under the action of electromagnetic fields have been investigated in many publications. A significant breakthrough in the research of droplets under the action of an electromagnetic field arose with the synthesis of magnetic liquids,[3] allowing many interesting effects to be observed and described, such as the droplet deformation and its dynamics under the action of static magnetic fields,[4–6] rotating fields,[7,8] labyrinthine pattern formation in the Hele–Shaw cells,[9] and adjustable rheological properties of magnetic fluids with external magnetic fields.[10] To describe these effects, different approximate methods[11–13] (under assumptions of ellipsoidal shape, satisfaction of boundary conditions on average, and others) have been employed that need to be tested. Yet more observed phenomena have still not been described theoretically or sufficiently explored numerically, such as the dynamics of hysteresis of droplet deformation,[14] reentrant transition of figures of equilibrium of magnetic droplets in a high frequency rotating field,[7] and spike formation on the droplet poles.[15] It should be noted that magnetic fluids under the action of an electromagnetic field have many uses, including biomechanics,[16] biochemical assays,[17] dynamic self-assembly,[15] magnetohydrodynamic induction pumps,[18] microfluidics,[19] and many others, thus, providing information about the physical properties of the concentrated phase of magnetic colloids. These colloids may possess very interesting properties due to their highly magnetic nature—such as field dependent surface tension or dependence of rheological properties on the magnetic field.

In parallel with the experimental investigation of magnetic droplets, significant efforts in the development of numerical methods for their simulation have been undertaken. Efficient tools for the simulation of the free boundary phenomena may be developed on the basis of the boundary integral equations.[20,21] These methods have also been applied in the axisymmetric case.[22,23] Among the phenomena predicted is, for example, the formation of the spikes on the droplet poles if the magnetic permeability is high enough.[23–25] Other complicated free boundary problems, for example, the formation of the labyrinthine patterns in the Hele–Shaw cells, have also been tackled by boundary integral equation techniques.[26] The application of the boundary integral equation algorithm for the full three dimensional case is a real challenge since special care should be applied to retain

the quality of the mesh on the droplet's surface.[27–29] Modeling such dynamics can also be approached via the immersed boundary method,[30] which is sensitive to precise boundary description[31] or lattice Boltzmann methods, which can handle complex fluid configurations and the coexistence of multiple fluid phases well.[32] A further review of magnetic fluid modeling and simulations is also available.[33] In parallel with the development of the numerical tools for the simulation of magnetic droplets, corresponding elaborations are taking place for the simulation of droplets in leaky dielectrics where in addition to the usual terms, the convective surface charge transfer by the liquid motion should be taken into account.[34]

Recently, one of the first attempts to simulate magnetic droplets in the three dimensional case has been made with the condition that both the droplet and the surrounding fluid have equal viscosities.[35] Since the viscosities of the concentrated phase of strongly magnetic droplets obtained by the demixing of magnetic colloids are significantly larger than the viscosity of the carrier liquid (usually water),[36] it is crucial to take that into account in the numerical models.

At present, there do not exist exact solutions of magnetic droplet behavior under the simultaneous action of viscous, magnetic, and capillary forces, which could be used as benchmarks for validating numerical models. In this situation, the validation of the numerical models is carried out by the comparison of the numerical results with some approximate solutions. It is our aim here to carry out these comparisons using the simple model of a magnetic fluid droplet[3] with a generalization of the recently published numerical algorithm.[35]

The paper is organized as follows. The mathematical model and the relevant equations are outlined in Sec. II. Next, Sec. III introduces the numerical algorithm, which is then validated with known theoretical relationships, as can be seen in Sec. IV. Finally, simulations of droplet behavior in different situations by the developed algorithm are presented in Sec. V, concluding with a short discussion.

II. MATHEMATICAL MODEL

A. Equations of motion

We consider a droplet of magnetic fluid suspended in an infinite non-magnetic carrier fluid. We look at the case where the inertia of the fluid is negligible. Then, the motion is governed by the Stokes equations for a magnetic fluid,[3,37]

$$-\nabla p + \eta \Delta \boldsymbol{v} + \boldsymbol{f_M} = \boldsymbol{0}, \quad \nabla \cdot \boldsymbol{v} = 0, \tag{1}$$

where p is the pressure, η is the dynamic viscosity, $f_{Mi} = \partial_k T_{ik}$ is the volume force due to magnetic field, and $T_{ik} = -\frac{1}{2}\mu_0 H^2 \delta_{ik} + H_i B_k$ is the Maxwell stress tensor, where $\boldsymbol{H}$ is the magnetic field intensity, $\boldsymbol{B} = \mu_0(\boldsymbol{H} + \boldsymbol{M})$ is the magnetic field induction, and $\boldsymbol{M}$ is the magnetization. The boundary conditions for forces on the droplet surface read

$$(\sigma_{ik}^{(e)} - \sigma_{ik}^{(i)})n_k + (T_{ik}^{(e)} - T_{ik}^{(i)})n_k - \gamma(k_1 + k_2)n_i = 0, \tag{2}$$

where $\sigma_{ik} = -p\delta_{ik} + \eta(\partial_i v_k + \partial_k v_i)$ is the stress tensor of the fluid, $\gamma(k_1 + k_2)$ is the capillary force due to the surface tension, with γ being the surface tension and k_1, k_2 being the principal surface curvatures, and $\boldsymbol{n}$ is the unit normal vector pointing out of the droplet. The superscripts (e) and (i) denote the parameters outside and inside of the droplet, respectively.

B. Equations of motion in integral form

It is possible to write an integral equation for the velocity of the points on the droplet's surface, which automatically satisfies the boundary conditions,[21]

$$\begin{aligned} v_k(\boldsymbol{y}) = &\frac{1}{4\pi(\eta^{(e)} + \eta^{(i)})}\int_S f(\boldsymbol{x}) n_i(\boldsymbol{x}) G_{ik}(\boldsymbol{x}, \boldsymbol{y}) dS_x \\ &+ \frac{1}{4\pi}\frac{\eta^{(e)} - \eta^{(i)}}{\eta^{(e)} + \eta^{(i)}}\int_S v_i(\boldsymbol{x}) T_{ijk}(\boldsymbol{x}, \boldsymbol{y}) n_j(\boldsymbol{x}) dS_x \\ &+ \frac{2\eta^{(e)}}{\eta^{(e)} + \eta^{(i)}} v_{0k}(\boldsymbol{y}), \end{aligned} \tag{3}$$

where the integral is over the surface of the droplet, the integral kernels are the Stokeslet $G_{ik}(\boldsymbol{x}, \boldsymbol{y}) = \frac{\delta_{ij}}{|\boldsymbol{x}-\boldsymbol{y}|} + \frac{(x_i - y_i)(x_j - y_j)}{|\boldsymbol{x}-\boldsymbol{y}|^3}$, and the stresslet $T_{ijk}(\boldsymbol{x}, \boldsymbol{y}) = -6\frac{(x_i - y_i)(x_j - y_j)(x_k - y_k)}{|\boldsymbol{x}-\boldsymbol{y}|^5}$, $f(\boldsymbol{x})$ is the combined normal force of surface tension and magnetic forces on the droplet's surface, and $\boldsymbol{v_0}(\boldsymbol{y})$ is the ambient flow to which the droplet is subjected. The normal force on the surface can be written as[35]

$$f = \left(\frac{1}{2}\mu_0\mu(\mu - 1){H^{(i)}}_n^2 + \frac{1}{2}\mu_0(\mu - 1){H^{(i)}}_t^2 - \gamma(k_1 + k_2)\right), \tag{4}$$

where H_t and H_n are the tangential and normal components of the magnetic field on the surface and μ is the relative permeability of the droplet.

C. Dimensionless variables

We introduce the length scale as the radius of a spherical droplet R_0, timescale $t_0 = R_0\eta^{(e)}/\gamma$, a magnetic field scale H_0, a magnetic permeability scale μ_0, a viscosity parameter $\lambda = \eta^{(i)}/\eta^{(e)}$, and the Bond magnetic number $Bm = 4\pi\mu_0 R_0 H_0^2/\gamma$.

Then, the integral equations can be rewritten in a dimensionless form,

$$\begin{aligned} v_k(\boldsymbol{y}) = &-\frac{1}{1+\lambda}\frac{1}{4\pi}\int_S (k_1(\boldsymbol{x}) + k_2(\boldsymbol{x}))n_i(\boldsymbol{x})G_{ik}(\boldsymbol{x}, \boldsymbol{y})dS_x \\ &+ \frac{1}{1+\lambda}\frac{1}{4\pi}\int_S f_M(\boldsymbol{x})n_i(\boldsymbol{x})G_{ik}(\boldsymbol{x}, \boldsymbol{y})dS_x \\ &+ \frac{1-\lambda}{1+\lambda}\frac{1}{4\pi}\int_S v_i(\boldsymbol{x})T_{ijk}(\boldsymbol{x}, \boldsymbol{y})n_j(\boldsymbol{x})dS_x \\ &+ \frac{2}{1+\lambda}v_{0k}(\boldsymbol{y}). \end{aligned} \tag{5}$$

The magnetic part of the normal force was separated out and in a dimensionless form reads

$$f_M = \frac{Bm}{8\pi}\left(\mu(\mu - 1){H^{(i)}}_n^2 + (\mu - 1){H^{(i)}}_t^2\right). \tag{6}$$

D. Regularization of the boundary integral equations

All of the integrands in (5) are weakly singular, they scale as $O(1/r)$ as $\boldsymbol{x} \to \boldsymbol{y}$ and are convergent ($\boldsymbol{r} = \boldsymbol{x} - \boldsymbol{y}$). The asymptotic behavior can easily be seen by writing out the integrands in Taylor series for small $\boldsymbol{r}$ in local coordinates centered at $\boldsymbol{y}$. It may be noted that $\boldsymbol{r} \cdot \boldsymbol{n} = O(r^2)$ as $\boldsymbol{x} \to \boldsymbol{y}$. The integrals can be tackled numerically,

for example, by calculating them on the singular elements in polar coordinates, where a factor of r arises from the differential area element.[20] Nonetheless, easier implementation and greater precision of the numerical scheme can be achieved by removing these singularities, which for these integrals is possible.

Since the first integral in (5) is over a closed surface, it can be transformed in the following form:[38]

$$\int_S (k_1(\boldsymbol{x}) + k_2(\boldsymbol{x}))n_i(\boldsymbol{x})G_{ik}(\boldsymbol{x},\boldsymbol{y})dS_x = -\int_S \left(r_i n_i(\boldsymbol{x})n_k(\boldsymbol{y}) + r_i n_i(\boldsymbol{y})n_k(\boldsymbol{x}) + (1 - n_i(\boldsymbol{x})n_i(\boldsymbol{y}))r_k - \frac{3r_k(n_i(\boldsymbol{x}) + n_i(\boldsymbol{y}))r_i r_j n_j(\boldsymbol{x})}{|\boldsymbol{r}|^2} \right) \frac{dS_x}{|\boldsymbol{r}|^3}. \tag{7}$$

Note that the term in the brackets of the integral scales as $|\boldsymbol{r}|^3$ and the whole integrand scales as $O(1)$, as $\boldsymbol{x} \to \boldsymbol{y}$. Furthermore, calculating the sum of principal curvatures $(k_1 + k_2) = \nabla \cdot \boldsymbol{n}$ in the first term on the right hand side of (5) notoriously introduces large errors from the surface discretization,[27,38] which in this form is not necessary.

The singularity in the second integral in (5) can be reduced by an order using singularity subtraction.[21] We use the identity[35] $\int_S n_i(\boldsymbol{x})G_{ik}(\boldsymbol{x},\boldsymbol{y})dS_x = 0$, which we multiply by $f_M(\boldsymbol{y})$ and subtract from the second integral in (5) to get

$$\int_S f_M(\boldsymbol{x})n_i(\boldsymbol{x})G_{ik}(\boldsymbol{x},\boldsymbol{y})dS_x = \int_S [f_M(\boldsymbol{x}) - f_M(\boldsymbol{y})]n_i(\boldsymbol{x})G_{ik}(\boldsymbol{x},\boldsymbol{y})dS_x, \tag{8}$$

where the integrand on the right hand side is $O(1)$ as $\boldsymbol{x} \to \boldsymbol{y}$, if $f_M(\boldsymbol{x})$ is smooth.

The third integral in (5) is also treated by singularity subtraction using the identity[21] $\int_S T_{ijk}(\boldsymbol{x},\boldsymbol{y})n_j(\boldsymbol{x})dS_x = -4\pi\delta_{ik}$ and is replaced by

$$\int_S v_i(\boldsymbol{x})T_{ijk}(\boldsymbol{x},\boldsymbol{y})n_j(\boldsymbol{x})dS_x = \int_S [v_i(\boldsymbol{x}) - v_i(\boldsymbol{y})]T_{ijk}(\boldsymbol{x},\boldsymbol{y})n_j(\boldsymbol{x})dS_x - 4\pi v_k(\boldsymbol{y}). \tag{9}$$

As a result, the singularity has been reduced by one order, and the integrand stays bounded as $\boldsymbol{x} \to \boldsymbol{y}$, if $v_i(\boldsymbol{x})$ is smooth.

We can write integral equation (5) for $\boldsymbol{v}$ in the form

$$v_k(\boldsymbol{y}) = \frac{\kappa}{4\pi}\int_S v_i(\boldsymbol{x})T_{ijk}(\boldsymbol{x},\boldsymbol{y})n_j(\boldsymbol{x})dS_x + F_k(\boldsymbol{y}), \tag{10}$$

where $\boldsymbol{F}$ is independent of and $\kappa = \frac{1-\lambda}{1+\lambda}$. It is known[39] that the homogeneous part of this integral equation has an eigensolution with eigenvalues $\kappa = \pm 1$. The $\kappa = 1$ eigensolution is a uniform expansion of the droplet, and the $\kappa = -1$ eigensolution is an arbitrary rigid body motion of it. Therefore, for cases where $\lambda \gg 1$ or $\lambda \ll 1$, the integral equation is poorly conditioned. Magnetic droplets obtained by demixing of magnetic colloids are observed to have large viscosities ($\lambda \approx 100$).[7] Hence, we use Wielandt's deflation,[39] a procedure where we formulate an equivalent integral equation does not have the unwanted eigensolutions. The regularized integral equations and Wielandt's deflation are further explained in Appendix A.

E. Magnetic part

We consider equations of magnetostatics in the absence of electric currents,

$$\nabla \times \boldsymbol{H} = 0, \quad \nabla \cdot \boldsymbol{B} = 0. \tag{11}$$

The magnetostatic approximation is valid as long as $R_0/t_0 \ll c$, where R_0 is the characteristic scale of the problem, t_0 is the characteristic time of the problem, and c is the speed of light. Even a fast rotating field ($f_0 = 10^5$Hz) and a large droplet ($R_0 = 1$ cm) would fall well within the application limits of magnetostatics.

The magnetic field can be expressed as a gradient of magnetic scalar potential $\boldsymbol{H} = \nabla\psi$. Since $\nabla \cdot \boldsymbol{H} = 0$ by the virtue of Maxwell's equation for $\boldsymbol{B}$ and assumed uniform magnetization $\boldsymbol{M}$, the magnetic potential satisfies the Laplace equation $\Delta\psi = 0$.

Taking into account the continuity of the scalar potential $\psi^{(i)} = \psi^{(e)}$ and of the normal field component $\mu\nabla\psi^{(i)} \cdot \boldsymbol{n} = \nabla\psi^{(e)} \cdot \boldsymbol{n}$ on the fluid interface S, Laplace's equation can be recast in an integral equation form:[21]

$$\psi(\boldsymbol{y}) = \frac{2\boldsymbol{H_0} \cdot \boldsymbol{y}}{\mu + 1} - \frac{1}{2\pi}\frac{\mu - 1}{\mu + 1}\int_S \psi(\boldsymbol{x})\nabla_x\left(\frac{1}{r}\right) \cdot \boldsymbol{n}(\boldsymbol{x})\, \mathrm{d}S_x, \tag{12}$$

where the $\boldsymbol{H_0}$ term represents an unperturbed background field.

The magnetic potential is calculated on discrete points describing the droplet; this allows us to calculate the tangential field component at each node $\boldsymbol{H_t} = |(I - \boldsymbol{n} \otimes \boldsymbol{n})\nabla\psi|$.

Since the nodes are on the surface of the droplet, it is not possible to directly calculate the normal component of the gradient of the magnetic potential. Therefore, to calculate the normal component of the field, we use the relation, where the normal field is expressed entirely in terms of the tangential field component,[35]

$$\boldsymbol{H_n}(\boldsymbol{y}) = \frac{\boldsymbol{H_0} \cdot \boldsymbol{n}(\boldsymbol{y})}{\mu} - \frac{\mu - 1}{4\pi\mu}\boldsymbol{n}(\boldsymbol{y}) \cdot \mathcal{P}\int_S \left[(\boldsymbol{n}(\boldsymbol{x}) \times \boldsymbol{H_t}(\boldsymbol{x})) \times \nabla_x\left(\frac{1}{r}\right) \right] \mathrm{d}S_x. \tag{13}$$

The integrand in (13) has a $O(1/r^2)$ singularity when $\boldsymbol{y} \to \boldsymbol{x}$; therefore, it should be evaluated as a Cauchy principal value integral denoted by $\mathcal{P}$. Similarly as before with velocity integral equations, singularity subtraction is applied, making use of identities

$$\int_S \frac{1}{4\pi}\nabla_x\left(\frac{1}{r}\right) \cdot \boldsymbol{n}(\boldsymbol{x})\, \mathrm{d}S_x = -\frac{1}{2}, \tag{14}$$

$$\int_S \frac{\boldsymbol{n}(\boldsymbol{x}) \times \boldsymbol{r}}{r^3}\, \mathrm{d}S_x = \boldsymbol{0}, \tag{15}$$

where $\boldsymbol{y}$ lies on the boundary of the region of integration.

The equation for magnetic potential can be cast in a regularized form by means of (14),

$$\psi(\boldsymbol{y}) = \boldsymbol{H_0}(\boldsymbol{y}) \cdot \boldsymbol{y} - \frac{\mu - 1}{4\pi}\int_S [\psi(\boldsymbol{x}) - \psi(\boldsymbol{y})]\nabla_x\left(\frac{1}{r}\right) \cdot \boldsymbol{n}(\boldsymbol{x})\, \mathrm{d}S_x. \tag{16}$$

Relation for the normal field component is regularized by using (14) and (15) (Ref. 35) [here, the sign is opposite in front of the integral term as compared to that in Eq. (3.9) of Ref. 35],

$$H_n(\boldsymbol{y}) = \frac{\boldsymbol{H_0}\cdot\boldsymbol{n}(\boldsymbol{y})}{\mu} - \frac{\mu-1}{4\pi\mu}\boldsymbol{n}(\boldsymbol{y}) \times \int_S \left[[\boldsymbol{H_t}(\boldsymbol{x}) - \boldsymbol{H_t}(\boldsymbol{y})]\,\nabla_x\left(\frac{1}{r}\right)\cdot\boldsymbol{n}(\boldsymbol{x}) - [\boldsymbol{H_t}(\boldsymbol{x}) - \boldsymbol{H_t}(\boldsymbol{y})] \times \left(\boldsymbol{n}(\boldsymbol{x}) \times \nabla_x\left(\frac{1}{r}\right)\right)\right] \mathrm{d}S_x.$$

Similarly as in the case of the velocity calculation, the integrands in the regularized equations are now bounded for $\boldsymbol{y} \to \boldsymbol{x}$ and can easily be integrated numerically. Singular integrands are calculated using local polar coordinates centered at $\boldsymbol{y}$ for the singular elements.[20,35]

We also derived an alternative approach for calculating the normal and tangential field components from normal field differences on the surface, but it was observed to be less precise and slower and consequently was not used in further calculations. For details, refer to Appendixes B and III.

Having solved these boundary integral equations for the magnetic field, we can obtain the forces acting of the droplet surface (6) and subsequently calculate the velocity of each mesh node.

F. Infinitely fast rotating field

Let the magnetic field rotate in the z axis direction with the angular frequency ω,

$$\boldsymbol{H_0} = H_0 \cos(\omega t)\boldsymbol{e}_x + H_0 \sin(\omega t)\boldsymbol{e}_y. \tag{17}$$

Then, if the period $T = 2\pi/\omega$ is much smaller than the characteristic time of shape deformations τ [for small deformations given later in the paper in (24)], the magnetic forcing can be averaged over the rotation period. The period-averaged normal surface force (6) is given by[35]

$$\langle f_M \rangle = \frac{Bm}{16\pi}(\mu-1)\left(\mu\left[H_{xn}^2 + H_{yn}^2\right] + \left[H_{xt}^2 + H_{yt}^2\right]\right), \tag{18}$$

where $\boldsymbol{H}_x$ and $\boldsymbol{H}_y$ are the magnetic field intensity distribution on the droplet's surface, when it is placed in a stationary background field $\boldsymbol{H_0} = \boldsymbol{e}_x$ and $\boldsymbol{H_0} = \boldsymbol{e}_y$, respectively.

III. NUMERICAL ALGORITHM

The numerical approach is an extension of Ref. 35, where only equilibrium droplet configurations were calculated at equal fluid viscosities.

The magnetic fluid droplet surface is triangulated by a mesh of boundary elements (BEM) with collocation points or nodes. The integrals are solved using the trapezoid integration scheme using only the function values on the nodes. This allows us to conveniently reformulate the summation over the flat triangles to the summation over nodes[27]

$$\int_S f(\boldsymbol{x})dS \approx \sum_i f(\boldsymbol{x}_i)\Delta S_i, \tag{19}$$

where the summation is done over all nodes i and $\Delta S_i = 1/3\sum \Delta S$ is the average area of the three triangles adjacent to the node i. This way the integral equations become linear systems of equations that can be solved using common numerical libraries, for example, velocity integral equation (10) can be represented as $\boldsymbol{v} = A\boldsymbol{v} + \boldsymbol{F}$, where is the unknown vector of length $3N$ containing the velocities on the nodes, A is a $3N \times 3N$ matrix corresponding to the T_{ijk} integral containing the interactions between the nodes, and $\boldsymbol{F}$ is a $3N$ vector corresponding to the terms in (10) without $\boldsymbol{v}$. In practice, most of the time is spent in populating these matrices A and $\boldsymbol{F}$. Solution of the integral equations of Sec. II gives the velocities of nodes and allows us to calculate the dynamics of droplet shapes.

The original spherical mesh is generated by iteratively splitting an icosahedron, by adding more nodes in its faces and projecting the new nodes on a sphere[40] (Fig. 1). Our simulations typically relied on two or three such splitting iterations, yielding 162 and 642 nodes, respectively. The normals and curvatures on each vertex are found by fitting a paraboloid on the relevant vertex and its immediate neighbors.[27]

A. Mesh maintenance

The velocity distribution on the droplet's surface is non-uniform. Therefore, if we were to simply move the (initially uniformly distributed) mesh nodes with the surface velocity, the mesh would quickly degrade—some triangles would get stretched much more than others. To mitigate this, multiple mesh stabilization techniques are employed throughout the simulations. The methods utilized in this paper are explained below.

1. Passive stabilization

Since the dynamics of the droplet shape is determined by the normal velocity component only, the mesh may be stabilized by using proper tangential velocity components. In passive stabilization,[28]

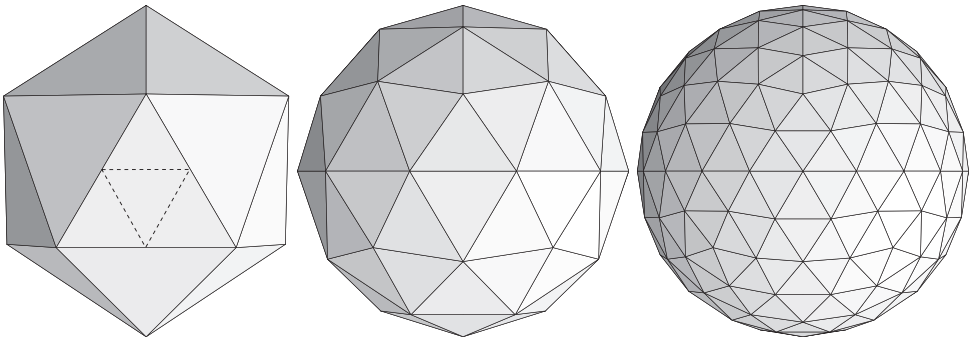

FIG. 1. Mesh creation by iteratively splitting an icosahedron (left) once (middle), yielding 42 nodes, and twice (right), yielding 162 nodes.

the tangential components can be adjusted in order to minimize a "kinetic energy" function

$$F = \sum_{\boldsymbol{x}_{ij}} \left[\frac{d}{dt} \left(\frac{|\boldsymbol{x}_{ij}|^2}{h_{ij}^2} + \frac{h_{ij}^2}{|\boldsymbol{x}_{ij}|^2} \right) \right]^2 + 0.4 \sum_{\Delta} \frac{1}{C_\Delta^2} \left(\frac{dC_\Delta}{dt} \right)^2, \quad (20)$$

where the first sum pertains to edges between nodes i and j and tries to keep edges at the optimal lengths of h_{ij} as determined by local curvatures,[28] while the second sum pertains to mesh surface triangles and tries to keep the triangles as regular as possible, using the "compactness" of a triangle $C_\Delta = S_\Delta/(a^2 + b^2 + c^2)$, where a, b, and c represent the lengths of its sides, as a guide.[28]

2. Active stabilization

The above algorithm slows the mesh degradation but does not stop it completely. In addition, active stabilization[28] between iterations is necessary whereby the nodes are translated along the surface of the droplet in order to minimize a "potential energy" function

$$E = \sum_{\boldsymbol{x}_{ij}} \left[\frac{1}{2} \left(\frac{|\boldsymbol{x}_{ij}|^2}{h_{ij}^2} + \frac{h_{ij}^2}{|\boldsymbol{x}_{ij}|^2} \right) \right]^{50} + \sum_{\Delta} \left(\frac{C_\Delta^{reg}}{C_\Delta} \right)^{100}, \quad (21)$$

where $C_\Delta^{reg} = \sqrt{3}/12$ is the compactness value of a regular triangle. This function E assumes large values when $\boldsymbol{x}_{ij}$ differs much from its optimal length of h_{ij}, and so, it avoids both unwarranted crowding and dispersion of vertices, as well disallowing triangles to deviate much from the optimal compactness of a regular triangle. In order to translate the node $\boldsymbol{x}^i$ along the droplet surface, we use the previously fitted paraboloid used in the normal vector calculations, with $\boldsymbol{x}^i$ lying at its tip. These paraboloids locally approximately coincide with the droplet surface. The node $\boldsymbol{x}^i$ is moved in space along the negative gradient of the potential energy function E. This procedure might make the node not coincide with the original droplet surface anymore, so it is projected onto a nearest paraboloid, thus bringing it back to the droplet surface. This approach effectively "slides" the node along the surface in order to minimize the potential energy function E.

The above energy functions E and F can have their gradients expressed in an explicit analytical form, allowing for efficient optimization. We use the conjugate gradient method to find the minimum of F. To minimize E, we use a modified gradient descent, where after each step we project the points back on the paraboloid that describes the local droplet surface.[28]

3. Edge flipping

Edges between vertices may be flipped. Consider a quadrilateral described by vertices $[\boldsymbol{x}^a, \boldsymbol{x}^b, \boldsymbol{x}^d, \boldsymbol{x}^c]$ with an additional edge, connecting the two diagonally opposite vertices $[\boldsymbol{x}^a, \boldsymbol{x}^d]$. This edge might be flipped to instead connect the vertices $[\boldsymbol{x}^b, \boldsymbol{x}^c]$, provided that

$$|\boldsymbol{x}^b - \boldsymbol{x}^c|^2 < |(\boldsymbol{x}^b - \boldsymbol{O}^b)(\boldsymbol{x}^c - \boldsymbol{x}^b)| + |(\boldsymbol{x}^c - \boldsymbol{O}^c)(\boldsymbol{x}^c - \boldsymbol{x}^b)|,$$

where $\boldsymbol{O}^k$ is the circumcenter of the triangle $[\boldsymbol{x}^a, \boldsymbol{x}^d, \boldsymbol{x}^k]$, where $k \in \{b, c\}$.[28,29] Such flips allow for increasingly regular triangles, and they have to be applied iteratively to all of the edges until no more flips are possible. An edge will not be flipped, if it would result in a node with less than five connected nodes. This is done to ensure that a general paraboloid can be fitted on every node and its neighbors. Edge flipping is applied at each simulation step. If an edge is flipped, *active* stabilization is applied again.

4. Node addition

We found that to achieve accurate results, a larger number of nodes are needed in regions of high curvature than can be sustained with the above-mentioned techniques; therefore, we employ a node addition routine. For every vertex, we compute the magnitude of curvature $H = \sqrt{k_1^2 + k_2^2}$, where k_1 and k_2 are the principal curvatures that we obtained from the fitted paraboloids. Then, for each triangle, we compute the mean curvature of its vertices $H_\Delta = \frac{1}{3}\sum_{i\in\Delta} H_i$ and the square root of its area $\sqrt{S_\Delta}$, signifying the length scale of the triangle. Each triangle with $H_\Delta\sqrt{S_\Delta} > \varepsilon$ is marked for splitting, where ε is an empirical cutoff criteria. Furthermore, if a triangle has two or more marked neighboring triangles, it also is marked.

To determine an optimal ε value, a droplet was stretched in a constant field with different ε values and the ratio of the droplet semiaxes evolution compared (Fig. 2). A threshold for cutoff of 0.2 was determined to be sufficient for a precision of 0.1%. Smaller values of ε quickly increase the number of nodes and, thus, significantly increase the computation time, which scales as roughly as $O(N^2)$, where N is the number of nodes.

The marked triangles will have new nodes added at the midpoint of each of their edges.[29] The added nodes are mutually connected in such a way that all nodes have at least five neighbors. Each of the new nodes will also be projected on the one of the original triangle's node's paraboloid to which the new node is the closest to. The neighborhood of triangles affected by this addition is also actively stabilized similarly to Ref. 29. The node addition procedure is illustrated in Fig. 3.

5. Time integration scheme

We found that space-discretization has a larger impact than time-discretization on convergence.

Therefore, a simple Euler method for time integration is used; however, it introduces some volume change in each iteration. We remedy this by rescaling the volume at every iteration. We use an adaptive time step Δt inspired by[41]

$$\Delta\tau = 7.4 \min\left\{ \left(\frac{\Delta x_{min}}{|k|_{max}} \right)_i \right\},$$
$$\Delta t = \min\left\{ \Delta\tau, 0.05\frac{2\pi}{\omega}, 0.07 \right\}, \quad (22)$$

where Δx_{min} is the shortest edge next to the node i, $|k|_{max}$ is the largest principal curvature by absolute value at node i, and ω is the dimensionless magnetic field rotation frequency.

6. Summary

The numerical algorithm can be briefly summarized as follows:

- For the given external magnetic field, solve the boundary integral equation for the magnetic potential ψ on the droplet surface (16).

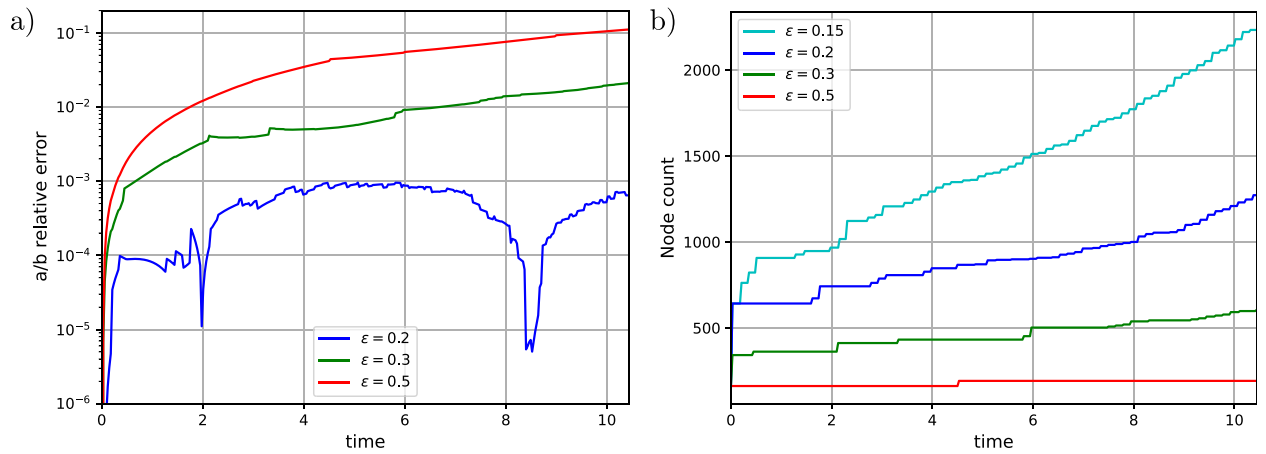

FIG. 2. An initially spherical droplet with $\lambda = 1$, $\mu = 22$ is being elongated in a constant magnetic field such that $Bm = 5.8$. The simulation time step is sufficiently small $\Delta t = 0.03$. (a) depicts the relative error of the droplet axis ratio with different cutoffs for node addition ε compared to $\varepsilon = 0.15$. The use of $\varepsilon = 0.2$ was chosen for further simulations unless stated otherwise, and it introduces an error of around 0.1%. (b) depicts the number of nodes as the simulation progresses for different values of ε.

- Calculate the tangential field component $\boldsymbol{H_t} = |(I - \boldsymbol{n} \otimes \boldsymbol{n})\, \nabla\psi|$. Express the normal field component $\boldsymbol{H_n}$ in a regularized form in terms of the tangential component (13).
- Find the normal magnetic surface forces $\boldsymbol{f_M}$ (6).
- Nodes describing the droplet surface are moved by the first-order explicit Euler method according to the velocities found by solution of Eq. (5) and adjusted by passive stabilization. Afterward, droplet volume is rescaled.
- Mesh maintenance via node addition and edge flipping are applied at every iteration of the simulation. Active stabilization is utilized every hundred iterations, unless any nodes have been added or any edges have been flipped, in which case active stabilization is used immediately.

In integral equation representation, the velocity and magnetic potential on each point in the surface are dependent on the contribution from all other points on the surface. Therefore, it follows that the complexity of the algorithm scales as $O(N^2)$, where N is the number of nodes.[28] As mentioned before, most of the time is spent in populating the matrices corresponding to the integral operator. This can, however, be accelerated using parallel computation.

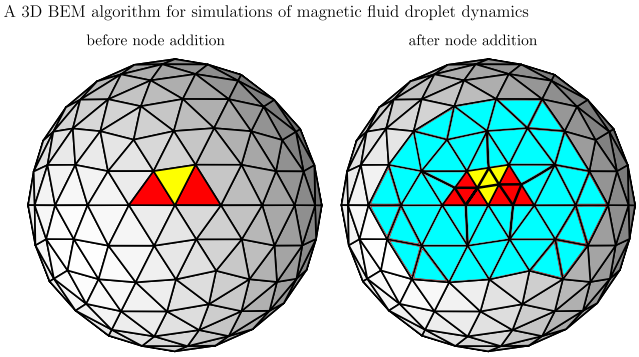

FIG. 3. Before node addition, the red triangles are marked for splitting. Since the yellow triangle has two neighbors that are marked for splitting, it also gets marked. After node addition, new triangles are created in such a way to ensure that there are at least five neighbors for each node. The new triangles and those (marked in blue) that are "two layers" around the triangles marked for splitting are actively stabilized to improve the resultant mesh.

IV. ALGORITHM VALIDATION

The algorithm has been validated with known theoretical relationships for droplet equilibrium configurations and dynamics when available.

A. Relaxation to a sphere

An elongated droplet approximated as an ellipsoid of rotation can be described by the Taylor deformation parameter

$$D = \frac{a-b}{a+b}, \tag{23}$$

where a and b are its major and minor semi-axes, respectively. In the absence of an external field, small elongations decay exponentially due to capillary forces $D \propto e^{-t/\tau}$, where the characteristic relaxation time τ, renormalized by the timescale of the system, reads[42]

$$\frac{\tau}{\eta^{(e)} R_0/\gamma} = \frac{(16+19\lambda)(3+2\lambda)}{40(1+\lambda)}. \tag{24}$$

The numerically determined relaxation times are presented in Fig. 4.

B. Equilibrium elongation in constant field

We can further compare its equilibrium configurations against relations given below. Figure 5 shows the comparison between the calculated equilibrium shapes of the droplets in a given magnetic field with the theoretical relation from Refs. 5 and 12,

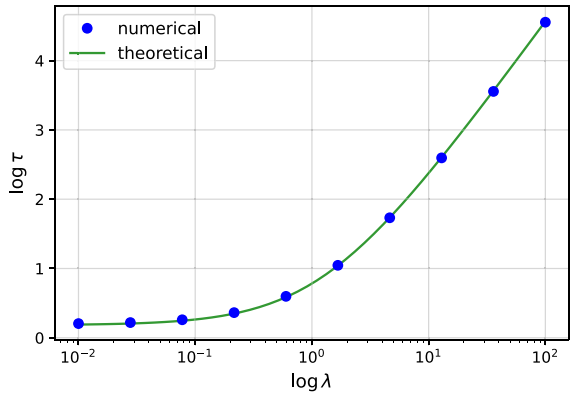

FIG. 4. Characteristic relaxation dimensionless time τ of an elongated droplet depending on the droplet/fluid viscosity ratio λ. The points are the numerical results that closely follow theoretical curve (24).

$$Bm = \left[\frac{4\pi}{\mu - 1} + N\right]^2 \frac{1}{2\pi} \frac{\left(\frac{3-2e^2}{e^2} - \frac{(3-4e^2)\arcsin e}{e^3(1-e^2)^{1/2}}\right)}{(1-e^2)^{2/3}\left(\frac{(3-e^2)}{e^5}\log\left(\frac{1+e}{1-e}\right) - \frac{6}{e^4}\right)}, \tag{25}$$

where $e = \sqrt{1 - b^2/a^2}$ represents the eccentricity of the ellipsoid with b, a being its short and long semi-axes, respectively, and N is the demagnetizing factor that for prolate ellipsoids reads

$$N = \frac{4\pi(1-e^2)}{2e^3}\left(\log\frac{1+e}{1-e} - 2e\right). \tag{26}$$

Equilibrium relation (25) is derived for an axisymmetric ellipsoidal droplet, an approximation that holds until the axial ratio of about 7.[6] This limit is also evidenced in Fig. 5 where the numerical result deviates at large droplet elongation, an effect explained by the droplet developing sharper tips than a fitted ellipsoid would have at the corresponding elongation and, thus, no longer yielding to the ellipsoidal approximation.

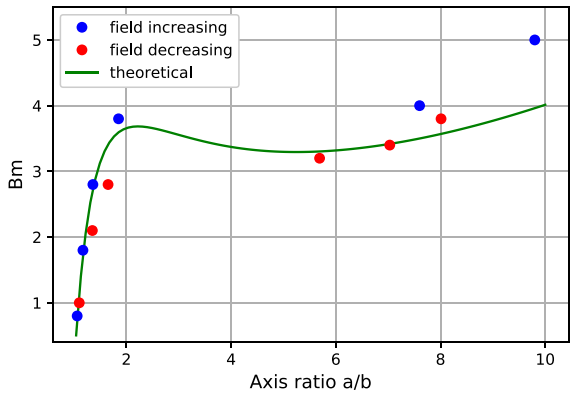

FIG. 5. Evolution of droplet through the hysteresis region. The blue (red) points and arrows indicate the calculated hysteresis trajectory with the increase (decrease) in the magnetic field once the droplet has equilibrated. The simulation used $\mu = 30$ and $\lambda = 7.6$.

As the simulation approaches equilibrium, the collocation points are moved by progressively smaller displacements. To calculate the $t \to \infty$ behavior of the elongated axis ratio, the equilibrated points shown in Fig. 5 are obtained by using the Shanks transformation.[43]

There is a qualitative change in the equilibrium curve (25) that occurs with the increase in permeability μ values. At $\mu \gtrsim 21$, the equilibrium curve becomes multivalued with respect to the magnetic field,[5] indicating an instability onset (Fig. 5). If in this particular case with $\mu = 30$, Bm is increased past the critical value, $Bm_c \approx 3.68$, the elongation of the droplet no longer lies on the equilibrium curve, thus rendering it unstable. To reach a stable configuration, the droplet has to elongate until the equilibrium curve is reached on the right region of Fig. 5. Once the droplet has reached this new stable configuration, the field can be lowered below the critical value; however, the droplet will not "jump" back (contract) to its previously stable configuration, but rather slowly trace the equilibrium curve. This phenomenon is called hysteresis, whereby the system reverts to a state other than its original, when external perturbations have returned to their initial values.

With the decrease in fields, the droplet would trace the curve until a second critical field value of around $Bm \approx 3.32$ (for $\mu = 30$) is reached. With even lower fields, the droplet would once again suddenly jump back (contract). Figure 5 shows the hysteresis path calculated by the algorithm. In these simulations, node addition was disabled since accurate description of such highly elongated droplets would require prohibitively many points. However, all other mesh maintenance techniques were still employed. Therefore, the results should be interpreted only qualitatively. An example of intermediate droplet shapes during the stretching phase can be observed in Fig. 8, where the droplet undergoes this jump as well.

C. Elongation of quasi-stable droplets

1. Elongation bottleneck

The closer the field is over the critical value, the longer the droplet will spend in this quasi-stable state, before "jumping" over to a truly stable configuration, indicating a time bottleneck region. The dynamics of this jump instability are governed by a hyperbolic equation shown by Ref. 14 for small t

$$\frac{a}{b} - \left(\frac{a}{b}\right)_c = S\,\tau \tan\frac{t}{\tau}, \tag{27}$$

where a/b is the semi-axial length ratio; here, τ is the characteristic time spent in the bottleneck region before the jump, t represents time, S is a numerical constant, and the subscript c indicates critical value, i.e., the one at the extremum of the equilibrium curve (25).

Examples of multiple droplet trajectories at different fields $h = H/H_c - 1$ are shown in Fig. 6, with the corresponding tangential fits (27) of τ and S overlayed. The trajectories were obtained by putting an ellipsoidal droplet ($\mu = 30$, $\lambda = 7.6$) elongated to the corresponding critical (pre-hysteresis jump) axis ratio of $a/b = 2.21$ and letting it evolve in various field strengths. It can be observed that the initial slow dynamics, indicating that the bottleneck region is followed by a rather quick stretching—the jump—afterward finally saturating into a new equilibrium position.

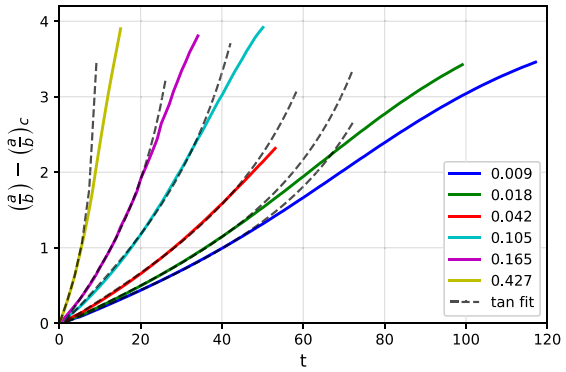

FIG. 6. Elongations of the droplet while "jumping over" the hysteresis region at various external field h values, with an overlaid tangential fits, according to (27). The initially accelerated dynamics saturate as the droplet reaches its new equilibrium. Simulated using $\mu = 30$, $\lambda = 7.6$.

Figure 7 shows the numerically determined bottleneck behavior of the droplet close to the critical field parameter Bm_c before jumping over the unstable region to a stable configuration. The time spent in the bottleneck is expected to follow $\tau \sim \frac{1}{\sqrt{h}}$, where $h = \frac{H}{H_c} - 1 = \sqrt{\frac{Bm}{Bm_c}} - 1$, or $\log \tau \sim -0.5 \log h$ in logarithmic terms,[14] which as shown in Fig. 7 is in good agreement with the value of $k = -0.534$ determined from numerical simulation.

2. Virial theorem approach

Analysis of this dynamics allows one to probe the applicability of another theoretical magnetic fluid droplet description, which is based on the Rayleigh dissipation function[44,45] and the virial theorem.[1,12] In the bottleneck region, the sum of its surface and magnetic energies has stationary point of inflection with respect to its eccentricity $\partial_e E = \partial^2_{ee} E = 0$.[5] This allows for an approximation of bottleneck dynamics around the critical point in terms of unspecified constants:[14]

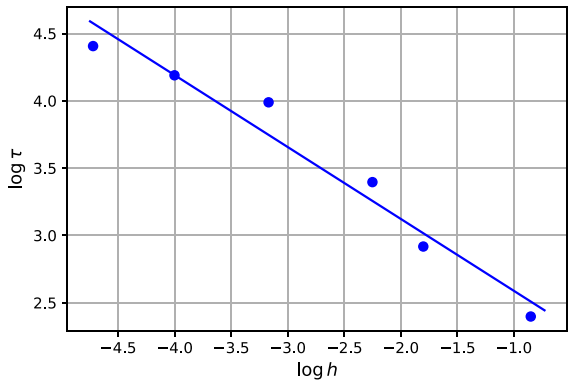

FIG. 7. Characteristic time τ spent in the bottleneck region before a hysteresis jump with different magnetic fields that stretch the droplet. $h = \frac{H}{H_c} - 1$. The points are obtained from numerical simulations, and the line is the linear fit with a slope of $k = -0.534$, closely following the theoretical slope of -0.5.[14]

$$D\dot{e} = Ah + B(e - e_c)^2, \tag{28}$$

with the constants taken at $e = e_c$ and $H = H_c$:

$$D = -\eta R_0^3 f(e_c), \quad A = H_c \frac{\partial^2 E}{\partial H \partial e}, \quad B = \frac{1}{2}\frac{\partial^3 E}{\partial e^3}, \tag{29}$$

where η is the droplet viscosity and $f(e)$ is an unknown function of the droplet shape, to be determined from an interplay of the Rayleigh dissipation function and the virial theorem. Furthermore, taking into account boundary conditions leads to the explicit expressions for the constants, as shown in Appendix D:

$$D = \frac{8e_c}{9(1-e_c^2)^{1/2}}, \quad A = \frac{8\pi}{3} Bm_c \frac{6e_c + (e_c^2 - 3)\log\left[\frac{1+e_c}{1-e_c}\right]}{2e_c^4},$$
$$B = -\frac{1}{2}\frac{\partial^3 E}{\partial e^3}\frac{(1-e_c^2)^3}{e_c^2}.$$

Fitting (27) to numerical data of the bottleneck region dynamics gives the value of the constant $S = A/(2D)(H^2/H_c^2 - 1)$,[14] afterwards allowing to extract the $A/2D$ ratio from the S vs H^2 linear fit. Furthermore, fitting $\tau = \tau_0/\sqrt{h}$[14] to the characteristic times spent in the bottleneck region τ (Fig. 7) gives the estimate for the capillary time $\tau_0 = \sqrt{AB}/D$.

A comparison of determined calculated constant values is shown in Table I.

V. SIMULATIONS

A. Constant field

A spherical magnetic droplet subjected to a constant homogeneous magnetic field elongates at a certain rate until it reaches an equilibrium point where the surface tension balances the magnetic forces and possibly even develops sharp conical tips similar to what has been predicted[23] and observed[5] before, as shown by simulation results in Fig. 8. The simulation shown in Fig. 8 was manually stopped at $t = 80.96$ before it had reached the equilibrium value due to slow iteration steps. Each time step ($\Delta t = 0.006$ and decreasing with more nodes added) was taking up around 5 min with 2466 nodes.

Figure 9 shows qualitatively distinct behavior for different values of magnetic permeability μ. The range of μ is chosen so that it contains the critical value of $\mu \simeq 21$ at which the hysteresis phenomenon starts manifesting itself.[5] At larger μ values during the stretching of the droplet, it may develop conical tips, an effect not observed at lower μ values.[23]

Such conical tip development has been captured previously in axi-symmetric simulations.[24]

It is possible to capture the rate of droplet elongation using this algorithm. Figure 10 shows experimentally the elongation of a magnetic droplet with a stepwise increasing magnetic field.

TABLE I. Comparison of determined constant values with various approaches.

	Bacri84	Virial th.	Numerical
$A/2D$	0.73	1.18	0.98
$\sqrt{AB}/D$	0.9	0.6	1.0

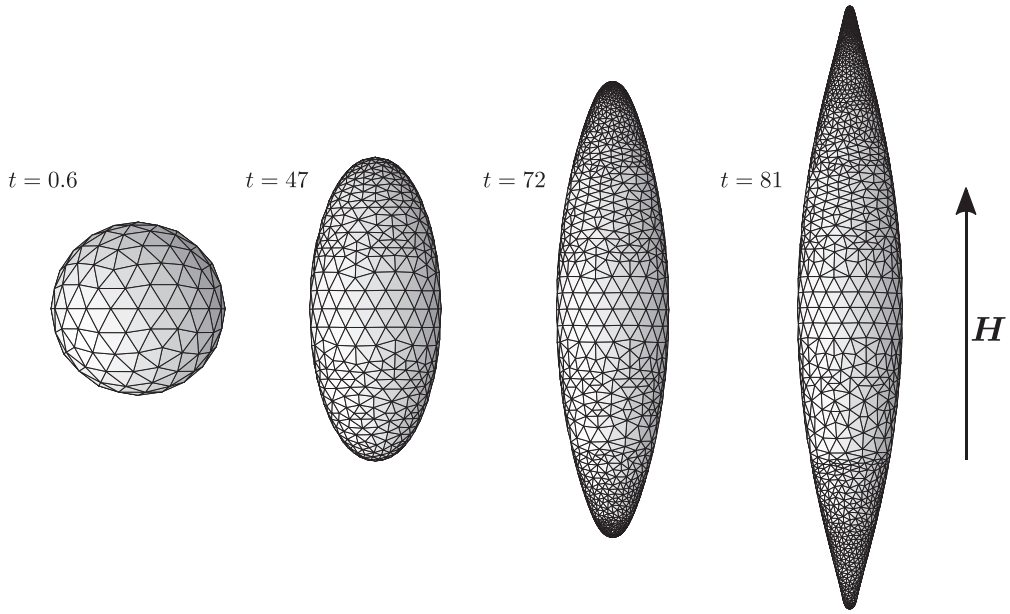

FIG. 8. Droplet stretching in a constant field with $Bm = 5$, $\mu = 30$, $\lambda = 10$. Conical tip development can be observed as well as node addition in regions of the high surface curvature. Simulation was stopped at $t = 80.96$ before reaching the equilibrium value due to prohibitively many points near the tips of the droplets.

The characteristics of the droplet were determined by an elongation–relaxation measurement of the droplet as described in Ref. 35 and are stated in Fig. 10. By varying the droplet parameters within the margins of error, we were able to calculate rates of elongation significantly faster and slower than the ones observed experimentally. Therefore, by finding the elongation rate that best fits the observation, it should be possible to notably increase the precision in the measurements of droplet parameters. This is something not easily done for microscopic droplets.

It is, however, worth mentioning that the calculations are significantly time consuming with a full simulation of a medium deformation droplet ($N \approx 1000$) taking up around a week in real world time with a modern desktop computer. There are three parameters that should be honed in on (the viscosity ratio λ, surface tension coefficient γ, and the relative magnetic permeability μ), which makes using this method for determining them a bit unwieldy at present. It could perhaps be mitigated by observing only small deformations of the droplet where the simulations could be run with a relatively small number (≈650) of collocation points.

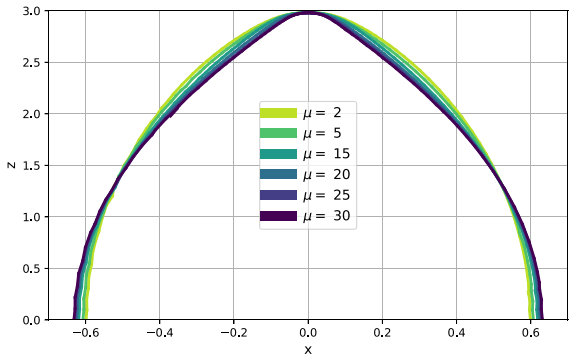

FIG. 9. Outlines of droplets that are being elongated at various μ values in a constant magnetic field, obtained by projecting the full 3D simulation in a plane. All droplets are being elongated in a field that corresponds to an equilibrium axis ratio of $a/b = 13$, the graph shows a snapshot when their tips reached $z = 3$. It is observed that at larger μ values, the droplets develop sharper tips even when the equilibrium shape has not yet been reached. The axes have been rescaled to emphasize differences between the outlines.

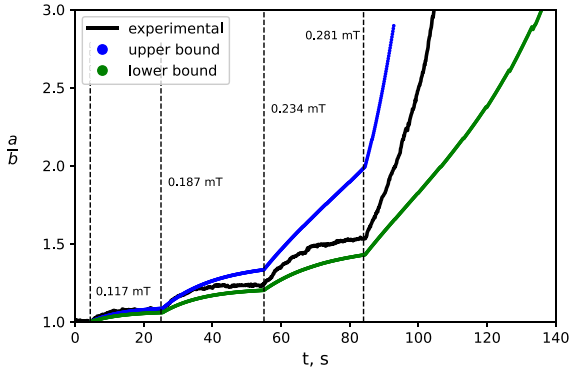

FIG. 10. Semi-axis ratio time evolution of a magnetic droplet. Black curve—experiment with $\mu = 34 \pm 1.5$, $\gamma = (8.2 \pm 0.4) \times 10^{-7}\,\mathrm{J/m^2}$, $\lambda = 10.1 \pm 2.5$) in an external field. The blue and green curves are obtained numerically with ($\mu = 34$, $\gamma = 7.7 \times 10^{-7}\,\mathrm{J/m^2}$, $\lambda = 7.6$) and ($\mu = 34$, $\gamma = 8.2 \times 10^{-7}\,\mathrm{J/m^2}$, $\lambda = 7.6$), respectively. The magnetic field at first is 0 and is increased at the dotted lines.

B. Rotating field

1. Phase plot of different field strengths and frequencies

It has been experimentally observed that magnetic droplets form various qualitatively different shapes in a rotating magnetic field depending on the field frequency and the field strength (Fig. 4 in Ref. 46). To explore it numerically, we simulated initially spherical droplets that were subjected to various magnetic field strengths and rotation frequencies (characterized by Bm and ω, respectively) that we show in a phase diagram (Fig. 11). The simulation parameters were $\lambda = 100$ and $\mu = 10$.

We fitted a tri-axial ellipsoid to the points that describe the droplet's surface to show how the semi-axes evolve over time. It was found that such a fit well described the droplets when the elongation was not too large. For the droplets inside the red outline in Fig. 11, the fit did not accurately capture the shape of the tips, that started to form more of an "S" shape as the viscous forces drag them behind (Fig. 12). For low ω and Bm, the droplets can be described as a tri-axial ellipsoid. The shape become more oblate as ω increases at $\omega = 1$; the shape is already nearly identical to the case when $\omega = \infty$, which is completely axisymmetric.

Similarly to the experimental results,[46] we also obtained that for low enough ω and high enough Bm, the droplets elongate. However, experimentally it was also observed that the field rotation suppresses the elongation and droplets remained spherical. As can be seen by our simulations, that is not the case. The droplets take up a quasi-oblate shapes, which observed from the field rotation direction would appear nearly indistinguishable from a spherical droplet.

A small deformation theory based on a phenomenological anisotropy tensor formalism was recently developed to describe the motion of magnetic droplets in a rotating field valid up to $O(Bm)$.[47] There it is shown that the droplet can be described by an ellipsoid with semi-axes $a \geq b \geq c$ and an angle β between the droplet's largest axis and the magnetic field, such that $\beta < 0$ if the droplet is trailing the field. The droplet's shape evolution is governed by

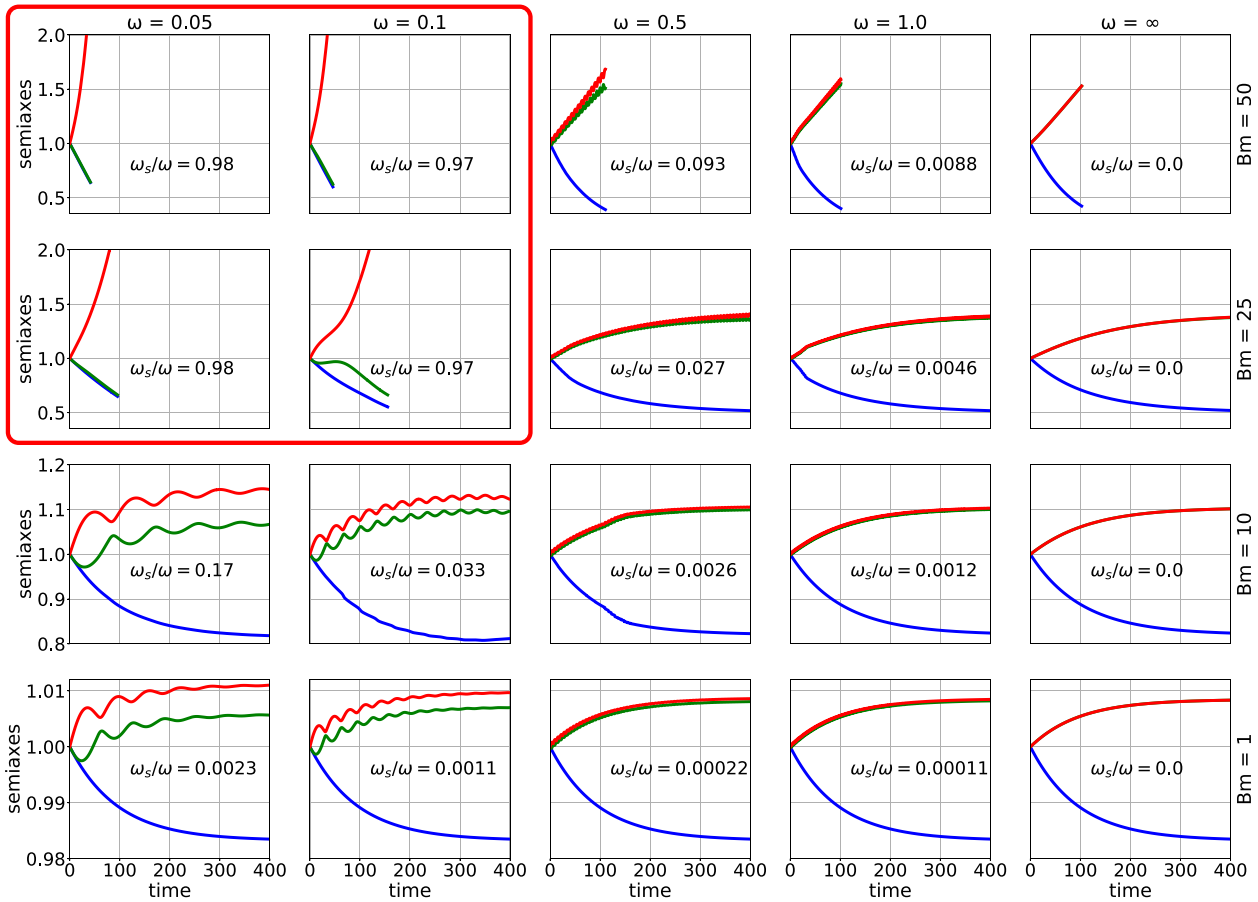

FIG. 11. Phase diagram of droplet semi-axes evolution in dimensionless time t in a rotating magnetic field of different dimensionless frequencies ω and magnetic Bond numbers Bm. The length of the longest semi-axis is shown in red, middle semi-axis in green, and the shortest in blue color. The region encircled by the red line shows the region of the phase space where the droplets are elongated; in the rest of the phase space, they are flattened. ω_s/ω is the ratio of the average surface angular velocity over the magnetic field angular velocity on the last simulation step ($\omega_s = \langle |\boldsymbol{r}_p \times \boldsymbol{v}|/r_p^2 \rangle$, $\boldsymbol{r}_p$ is the radius vector projection in the rotation plane). $\omega_s/\omega \approx 1$ indicates that the droplet rotates similar to a rigid body, whereas $\omega_s/\omega \ll 1$ indicates that the droplet seems to rotate following the field, but this apparent rotation is mostly caused by a surface deformation. The droplet parameters are $\lambda = 100$, $\mu = 10$.

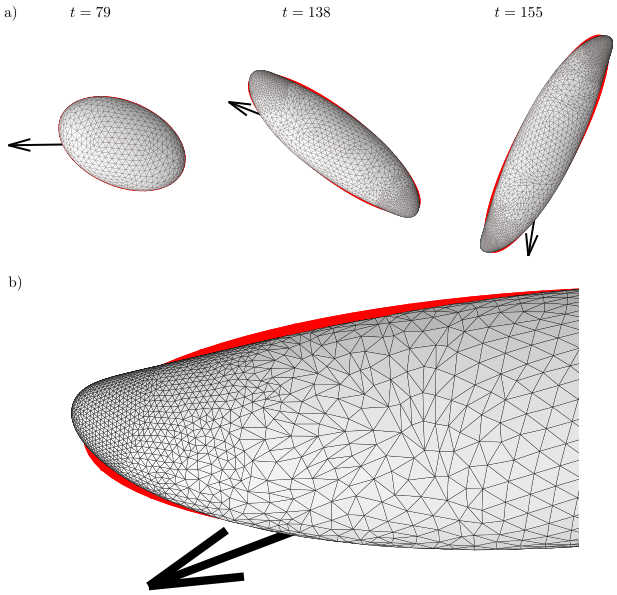

FIG. 12. (a) shows the evolution of a magnetic droplet in a counterclockwise rotating magnetic field. The simulation parameters are such that the droplet elongates instead of remaining flattened: $Bm = 25$, $\mu = 30$, $\lambda = 100$, $\omega = 0.1$. The mesh is overlaid over a best-fit ellipsoid colored in red. The black arrows indicate the momentary magnetic field direction. (b) shows a zoom of part of the droplet at $t = 155$ to illustrate the discrepancies between the droplet shape and the best-fit ellipsoid. Notably the tips start deforming in an "S" shape due to the viscous drag.

$$\begin{cases} \dfrac{d\epsilon_1}{dt} = -\dfrac{1}{\tau}\left(\epsilon_1 - \delta\cos(2\beta)\right), \\ \dfrac{d\epsilon_2}{dt} = -\dfrac{1}{\tau}\left(\epsilon_2 - \delta\sin^2(\beta)\right), \\ \dfrac{d\beta}{dt} = -\omega - \dfrac{\delta\cos(\beta)\sin(\beta)}{\tau\epsilon_1}, \end{cases} \tag{30}$$

where $\epsilon_1 = (a-b)/b$, $\epsilon_2 = (b-c)/b$ together with the incompressibility condition $abc = 1$ fully determine the semi-axes, τ is the dimensionless small deformation relaxation time (24), and ω is the dimensionless magnetic field rotation angular frequency and

$$\delta = \frac{9Bm}{32\pi}\frac{(\mu-1)^2}{(\mu+2)^2}. \tag{31}$$

For small Bm, the BEM simulations follow closely to the shape predicted by (30) (Fig. 13). The simulations were also used to determine the limits of the small deformation theory.[47]

How do the droplets change their orientation in the rotating field? They can rotate or the change in orientation can arise due to surface deformations. To determine which of these effects is dominant, we compare the angular velocity of the magnetic field ω with the average surface angular velocity

$$\omega_s = \left\langle \frac{|\boldsymbol{r_p} \times \boldsymbol{v}|}{r_p^2} \right\rangle, \tag{32}$$

where the averaging is done over all the nodes and $\boldsymbol{r_p}$ is the radius vector to a given node projected to the rotation plane.

In the region, where ω is small and Bm large (denoted by the red outline in Fig. 11), the droplets elongate and rotate in the direction of the field more or less like a rigid body ($\omega_s/\omega \approx 1$), albeit still deforming. When the Bm is small or ω large, the droplets take up a flattened shape, which still has one axis larger than the other. The flattened drops also seem to rotate in the direction of the field, but this apparent rotation is caused by surface deformations, which can be seen by the fact that the surface of the droplet almost does not rotate ($\omega_s/\omega \ll 1$).

In the phase space outside the region where droplets become elongated, their axes undergo oscillations with roughly twice the magnetic field frequency as they settle into equilibrium values, these oscillations get smaller in magnitude as ω increases. These results agree with the $O(Bm)$ small deformation theory,[47] where it was shown that close to the equilibrium shape, the lengths of the droplet axes oscillate with 2ω and the droplet surface angular velocity scales as $O(Bm^2)$.

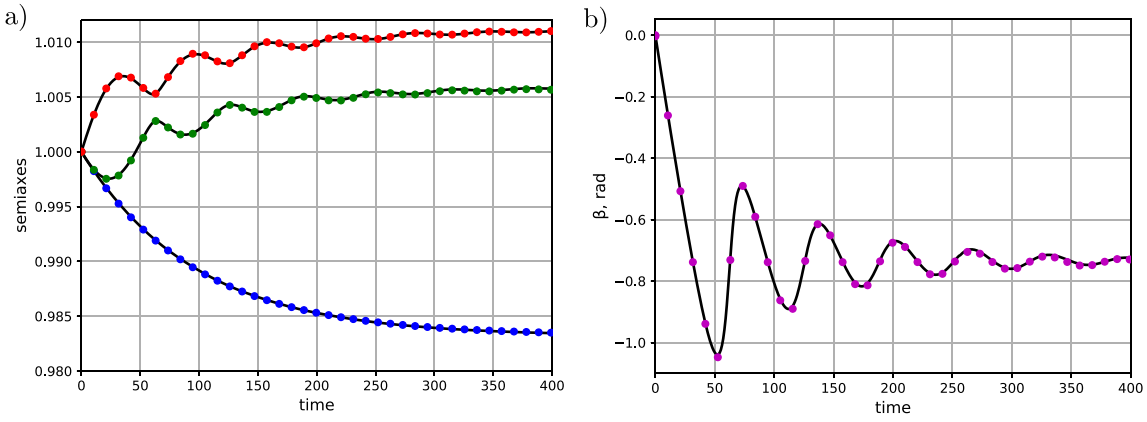

FIG. 13. The evolution of an initially spherical droplet's shape in a rotating magnetic field. The points are the simulation results (every 100th time step is shown for clarity), and the black lines are from Eq. (30). The simulation parameters are $\lambda = 100$, $\mu = 10$, $Bm = 1$, and $\omega = 0.05$. (a) shows the evolution of the droplet semi-axes, and (b) shows the angle β between the droplet's largest axis and the magnetic field. Negative β means that the droplet is trailing the field.

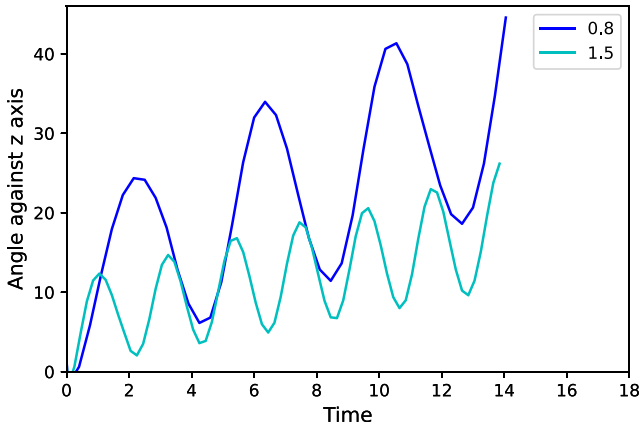

FIG. 14. Example of observed back-and-forth motion of an initially elongated droplet in moderately fast rotating fields of different frequencies ω. The lines indicate the angle between longest axis of the droplet and the stationary z axis. Simulations used $\mu = 30$, $\lambda = 1$.

2. Back-and-forth motion

Another approach investigated in a rotating field was a droplet, initially extended in a constant field and stretched to an axis ratio of about 7, was put in a rotating field at various frequencies. Highly elongated droplets tend to contract at the same time as undergoing the back-and-forth motion. At low frequencies, the droplet just follows the external field. At higher frequencies, a back-and-forth motion was observed as shown in Fig. 14, similarly, as is the case with a solid elongated paramagnetic particle,[48] magnetotactic bacteria,[49] and self-propelling magnetic particles with a permanent magnetic moment.[50] In these simulations, node addition was disabled since accurate description of such highly elongated droplets would require prohibitively many points, other mesh maintenance techniques were still employed. Therefore, the results should be interpreted only qualitatively.

C. Field threshold for starfish stability

The algorithm allows to investigate the onset of the starfish instability shown in Fig. 15, known to occur at strong enough rotating and fast enough magnetic fields, whereby the oblate droplet develops

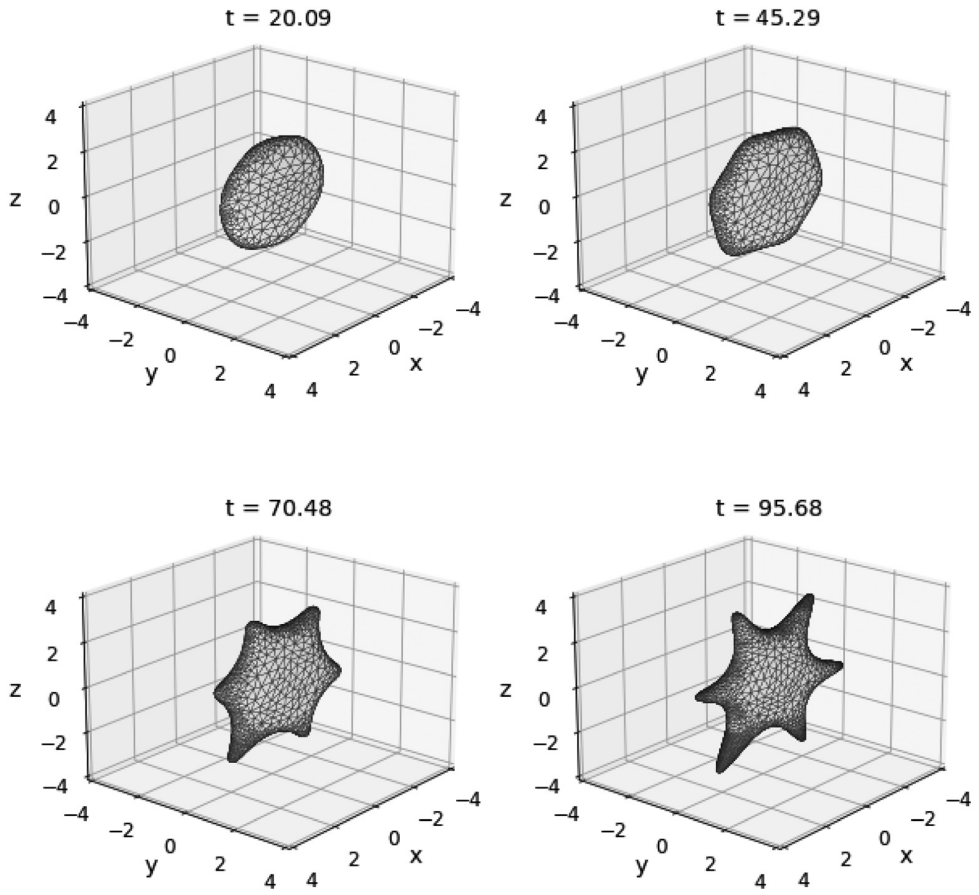

FIG. 15. Example of the starfish instability using $Bm = 35$, $\mu = 10$, $\omega = 10$, $\lambda = 7.6$ and the node addition cutoff criteria of 0.4.

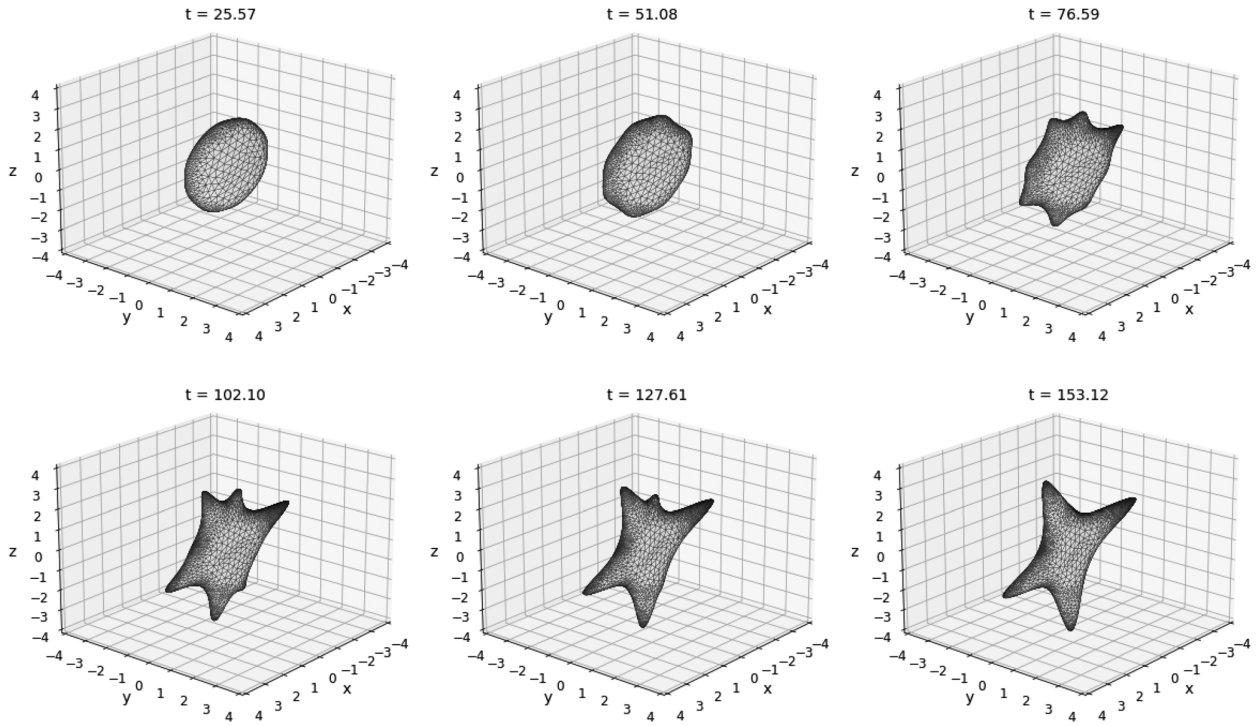

FIG. 16. Example of various starfish mode competition using $Bm = 30$, $\mu = 10$, $\omega = 10$, $\lambda = 7.6$ and the node addition cutoff criteria of 0.4. At first, six tips seem to be forming, but at a later time, only four remain.

finger-like structures on its perimeter.[7] We have observed competition between these modes (configurations of different number of "fingers"), as shown in Fig. 16 where the initially manifested mode of $n = 6$ is subsequently overtaken by the mode $n = 4$. In both of these cases, the droplet developed these fingers spontaneously from some asymmetries in the droplet mesh.

To investigate carefully the evolution and competition of different modes, we start with a axially symmetric oblate ellipsoid, obtained from a minimal energy configuration in an infinitely fast rotating field.[7,8] Then, a small initial sinusoidal perturbation of a specific mode n (representing the number of starfish fingers) is added along its perimeter in the plane of the rotating field $r(\theta) = \varepsilon \cos(\omega_n \theta)$ with $\varepsilon = 0.01 R_0$. The perturbed droplet is then allowed to evolve in an period-averaged high frequency field (the governing equations for the averaged field are described in Ref. 35) of varying strengths.

One goal aim of such an analysis would be to determine the critical magnetic field value at which the oblate–prolate transition occurs, shown in Fig. 17, as indicated by the onset of the $n = 2$ mode. Finally, analysis of Fourier amplitudes of the droplet's perimeter yields the dynamics of the mode amplitude as shown in Fig. 18, assuming exponential growth of nth mode near equilibrium $A_n(t) = C_n e^{\beta_n t}$ with β_n being the logarithmic increment to be determined.

It is observed that the β_n's tend to increase with the increase in magnetic field strengths, shown in Fig. 19, allowing to determine the critical field of the oblate–prolate droplet transition as evidenced by β_2 becoming positive. The critical field determined this way coincides nicely with the field predicted by numerically minimizing the energy of an presumably ellipsoidal droplet[8,35] as shown in Fig. 17. This energy minimization procedure and experimental observations[7] also anticipate the droplet becoming oblate again at large enough magnetic fields $Bm \gtrsim 70$. This reentrant transition is qualitatively observed in the short perturbed simulations with β_2 becoming negative at larger field strengths $Bm \gtrsim 50$ as shown in Fig. 20. The discrepancy of the predicted field of the prolate–oblate transition may be explained by

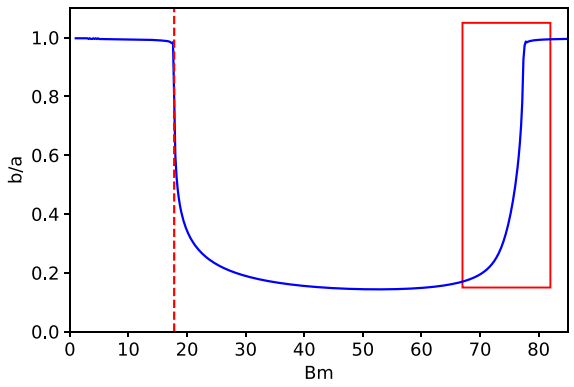

FIG. 17. The vertical line on the left indicates the critical field determined by analysis of the logarithmic increment β_2, it coincides very well with the value determined via droplet energy minimization. The region on the right represents the droplet becoming oblate again.

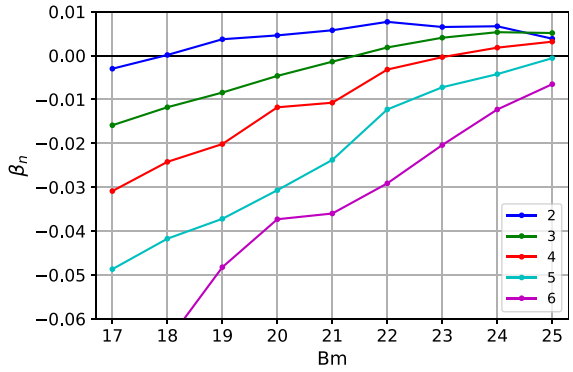

FIG. 18. Rates of growth β_n of various finger modes at different magnetic fields *Bm*. Competition of modes can be observed as the logarithmic increment β approach one another at larger magnetic fields.

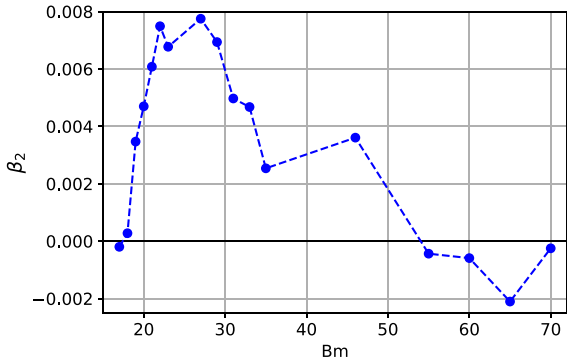

FIG. 20. The logarithmic increment of the starfish mode $n = 2$ becomes positive in a certain field strength region, indicating a transition to a prolate shape, which can be reversed at large fields, when the droplet becomes oblate again—this reentrant transition was predicted and observed in Ref. 7.

the fact that we started from an oblate shape and observed how the perturbations would grow or decay. However, to accurately capture the prolate–oblate transition, we would have to start from the prolate shape and observe its change.

VI. CONCLUSIONS AND DISCUSSION

The elaboration of the numerical algorithm for 3D dynamics of magnetic droplet shapes allows to validate different relations describing their behavior and may be used for comparison with experimental data, for example, as seen in Fig. 10, thus providing information about the physical properties of the concentrated phase of magnetic colloids. These colloids may possess very interesting properties due to their highly magnetic nature—such as field dependent surface tension or dependence of rheological properties on the magnetic field.

The developed algorithm has been compared with some theoretical solutions where available—equilibrium curves for droplet deformation in constant magnetic fields for various relative magnetic permeability μ values, the exponential decay of small elongations under surface tension, the dynamical behavior around hysteresis bottleneck instability regions, as well as droplet dynamics in various rotating field configurations and the critical fields for oblate–prolate transition. These comparisons allow to test the limits of various theoretical approximations widely used in description of magnetic fluid droplets, most notably the assumption of the ellipsoidal shape.[6,14,51]

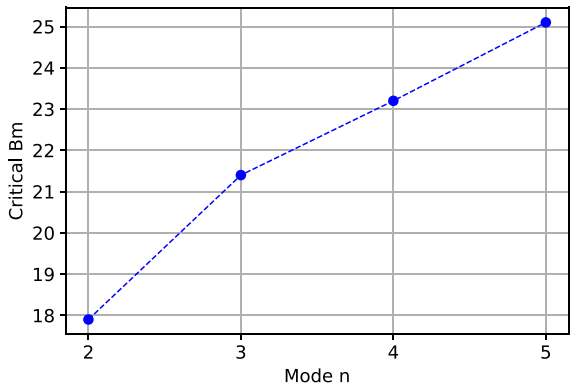

FIG. 19. The critical field above which a mode can start growing increases with mode number *n*. This does not mean, however, that the particular mode will be observed as others might be growing faster.

The agreement of numerical results and theoretical considerations also extends the limits of applicability of the simple magnetic fluid model description of these droplets, which admittedly are a new kind of soft magnetic matter with *a priori* nontrivial mathematical representation.

It has also been shown to be applicable in prediction of full 3D droplet dynamics with arbitrary droplet–fluid viscosity ratios in uniform fields, both static and rotating up to moderately large droplet deformations. This is an important achievement, as experimentally magnetic fluid droplets are often not axisymmetric and can reach viscosity ratios of $\lambda \approx 100$. Our algorithm also allows for probing droplet dynamics at rotating magnetic fields of rotation periods that are comparable in magnitude to the droplet relaxation time (24), where the fast-rotating field averaging approximation does not hold, which has not been previously possible.

The algorithm can capture characteristic behavior of droplets in rotating magnetic fields, namely, following the external field at low frequencies and exhibiting a back-and-forth motion at moderately fast fields, similarly to a magnetic solid rods, as well as the droplet undergoing the oblate–prolate–oblate transition at rotating fields of increasing strength.

At present, the algorithm is limited in its ability to simulate large deformations of the droplet. It also is unable to simulate a symmetrical appearance of the starfish instability modes without an artificial perturbation of the droplet's shape. To reduce the simulation times, the option of node removal in regions of small surface curvature could be implemented, as has been demonstrated previously.[29] The current implementation also relies on assumptions of uniform surface tension and linear magnetization of the droplet. Moreover, the present algorithm cannot handle topological changes of droplets like coalescence or breakup, as well as multiple drops interacting. It is, however, possible to extend the BEM algorithm to these cases.[28]

Important contribution of the present work is the numerical confirmation of the main aspects of the magnetic droplets behavior in static and rotating fields that opens the possibility of study of droplet dynamics in highly non-equilibrium situations not accessible at present by theoretical description. Among the problems to be studied by the developed tools, we should mention droplet dynamics in the

intermediate range of frequencies, droplet breakup, and ensembles of interacting magnetic droplets.[36]

ACKNOWLEDGMENTS

A.L. acknowledges the financial support of the European Union's Horizon 2020 research and innovation program under Grant Agreement MAMI No. 766007.

A.P.S. is thankful to SIA "Mikrotīkls" and the Embassy of France in Latvia for supporting cotutelle studies.

A.P.S. acknowledges the financial support of "Strengthening of the capacity of doctoral studies at the University of Latvia within the framework of the new doctoral model," Identification No. 8.2.2.0/20/I/006.

A.C. and A.P.S. acknowledge the financial support of grant of Scientific Council of Latvia lzp-2020/1-0149.

AUTHOR DECLARATIONS

Conflict of Interest

The authors have no conflicts to disclose.

DATA AVAILABILITY

The data that support the findings of this study are available from the corresponding author upon reasonable request.

APPENDIX A: WIELANDT'S DEFLATION

After straightforward algebraic operations with the regularized integrals in Sec. II D, we get that the equation for velocity reads

$$\begin{aligned} v_k(\boldsymbol{y}) = \frac{1}{8\pi}\int_S &(r_i n_i(\boldsymbol{x}) n_k(\boldsymbol{y}) + r_i n_i(\boldsymbol{y}) n_k(\boldsymbol{x}) + (1 - n_i(\boldsymbol{x}) n_i(\boldsymbol{y})) r_k \\ &- \frac{3 r_k (n_i(\boldsymbol{x}) + n_i(\boldsymbol{y})) r_i r_j n_j(\boldsymbol{x})}{|\boldsymbol{r}|^2}\Big) \frac{dS_x}{|\boldsymbol{r}|^3} \\ &+ \frac{1}{8\pi}\int_S f_M(\boldsymbol{x}) n_i(\boldsymbol{x}) G_{ik}(\boldsymbol{x},\boldsymbol{y}) dS_x \\ &+ \frac{1-\lambda}{8\pi}\int_S [v_i(\boldsymbol{x}) - v_i(\boldsymbol{y})] T_{ijk}(\boldsymbol{x},\boldsymbol{y}) n_j(\boldsymbol{x}) dS_x + v_k^{\infty}(\boldsymbol{y}). \end{aligned} \tag{A1}$$

To perform Wielandt's deflation, instead of solving for , we introduce an auxiliary field $\boldsymbol{w}$ similarly as Ref. 21, which is obtained from the integral equation that does not have the unwanted eigensolutions,

$$\begin{aligned} w_k(\boldsymbol{y}) = \frac{1}{8\pi}\int_S &(r_i n_i(\boldsymbol{x}) n_k(\boldsymbol{y}) + r_i n_i(\boldsymbol{y}) n_k(\boldsymbol{x}) + (1 - n_i(\boldsymbol{x}) n_i(\boldsymbol{y})) r_k \\ &- \frac{3 r_k (n_i(\boldsymbol{x}) + n_i(\boldsymbol{y})) r_i r_j n_j(\boldsymbol{x})}{|\boldsymbol{r}|^2}\Big) \frac{dS_x}{|\boldsymbol{r}|^3} \\ &+ \frac{1}{8\pi}\int_S f_M(\boldsymbol{x}) n_i(\boldsymbol{x}) G_{ik}(\boldsymbol{x},\boldsymbol{y}) dS_x \\ &+ \frac{1-\lambda}{2}\Big\{\frac{1}{4\pi}\int_S [w_i(\boldsymbol{x}) - w_i(\boldsymbol{y})] T_{ijk}(\boldsymbol{x},\boldsymbol{y}) n_j(\boldsymbol{x}) dS_x \\ &+ w_k'(\boldsymbol{y}) - \frac{n_k(\boldsymbol{y})}{S}\int_S w_i(\boldsymbol{x}) n_i(\boldsymbol{x}) dS_x\Big\} + v_k^{\infty}(\boldsymbol{y}), \end{aligned} \tag{A2}$$

where S is the surface area of the droplet and $\boldsymbol{w}'$ is the projection of $\boldsymbol{w}$ on the motion of a rigid body obtained as[27]

$$\boldsymbol{w}'(\boldsymbol{y}) = \boldsymbol{V} + \boldsymbol{\Omega} \times (\boldsymbol{y} - \boldsymbol{y}_c), \tag{A3}$$

where $\boldsymbol{y}_c$ is the center of mass of the droplet and $\boldsymbol{V}$ and $\boldsymbol{\Omega}$ are its translational and rotational velocities,

$$\boldsymbol{y}_c = \frac{1}{S}\int_S \boldsymbol{x} dS_x, \tag{A4}$$

$$\boldsymbol{V} = \frac{1}{S}\int_S \boldsymbol{w}(\boldsymbol{x}) dS_x, \tag{A5}$$

$$\boldsymbol{\Omega} = M^{-1} \cdot \int_S (\tilde{\boldsymbol{x}} \times \boldsymbol{w}(\boldsymbol{x})) dS_x, \tag{A6}$$

$$M_{ij} = \int_S \left(\tilde{x}_k \tilde{x}_k \delta_{ij} - \tilde{x}_i \tilde{x}_j\right) dS_x, \tag{A7}$$

where $\tilde{\boldsymbol{x}} = \boldsymbol{x} - \boldsymbol{y}_c$.

Finally the velocity is recovered by

$$\boldsymbol{v}(\boldsymbol{y}) = \boldsymbol{w}(\boldsymbol{y}) - \frac{\kappa}{1+\kappa}\boldsymbol{w}'(\boldsymbol{y}) = \boldsymbol{w}(\boldsymbol{y}) - \frac{1-\lambda}{2}\boldsymbol{w}'(\boldsymbol{y}). \tag{A8}$$

APPENDIX B: NORMAL FIELD CALCULATION WITHOUT THE TANGENTIAL COMPONENTS

Adjusting the approach seen in Ref. 34, we find an integral equation for the normal differences on the droplet surface

$$\begin{aligned} &[\![H_n(\boldsymbol{y})]\!]\left(\frac{\mu}{\mu - 1} - L(\boldsymbol{y})\right) \\ &\quad = H_{0n}(\boldsymbol{y}) - \int_S ([\![H_n(\boldsymbol{x})]\!] - [\![H_n(\boldsymbol{y})]\!]) \boldsymbol{n}(\boldsymbol{y}) \cdot \nabla_y \frac{1}{4\pi r} dS_x, \end{aligned} \tag{B1}$$

where we remember that $\boldsymbol{r} = \boldsymbol{y} - \boldsymbol{x}$ and where $[\![H_n(\boldsymbol{y})]\!] = H_n^{(e)}(\boldsymbol{y}) - H_n^{(i)}(\boldsymbol{y})$, and we have

$$H_n^{(e)} = \frac{[\![H_n]\!]}{\mu - 1}\mu \quad H_n^{(i)} = \frac{[\![H_n]\!]}{\mu - 1}. \tag{B2}$$

The function $L(\boldsymbol{y})$ is determined uniquely by the droplet shape

$$L(\boldsymbol{y}) = \frac{\boldsymbol{n}(\boldsymbol{y})}{4\pi} \cdot \int_S \left\{\left[\boldsymbol{n}(\boldsymbol{x}) \cdot \nabla\left(\frac{1}{r}\right)\right][\boldsymbol{n}(\boldsymbol{y}) - \boldsymbol{n}(\boldsymbol{x})] + \frac{\nabla \cdot \boldsymbol{n}(\boldsymbol{x})}{r}\boldsymbol{n}(\boldsymbol{x})\right\} dS_x. \tag{B3}$$

APPENDIX C: MAGNETIC FIELD TANGENTIAL COMPONENT

We start with an expression from Ref. 34 where we replace the electric field $\boldsymbol{E}$ with its magnetic counterpart $\boldsymbol{H}$

$$\boldsymbol{H}(\boldsymbol{y}) = \boldsymbol{H_0}(\boldsymbol{y}) - \int_S [\![H_n(\boldsymbol{x})]\!] \nabla_y \frac{1}{4\pi r} \mathrm{d}S_x - \frac{1}{2}[\![H_n(\boldsymbol{x})]\!]\boldsymbol{n}(\boldsymbol{y}). \tag{C1}$$

To get the tangential component, we take a cross product with $\boldsymbol{n}(\boldsymbol{y})$:

$$\boldsymbol{n}(\boldsymbol{y}) \times \boldsymbol{H_t}(\boldsymbol{y}) = \boldsymbol{n}(\boldsymbol{y}) \times \boldsymbol{H_0}(\boldsymbol{y}) + \frac{1}{4\pi}\int_S [\![H_n(\boldsymbol{x})]\!](\boldsymbol{n}(\boldsymbol{y}) \times \boldsymbol{r})\frac{\mathrm{d}S_x}{r^3}, \tag{C2}$$

where we remember that $\boldsymbol{r} = \boldsymbol{y} - \boldsymbol{x}$, also we note that only the tangential component of the field contributes to the cross product.

The integral, however, is strongly singular: as $\boldsymbol{x} \to \boldsymbol{y}$, the integrand scales as $O(1/r^2)$.

Regularizing the equation by multiplying $[\![H_n(\boldsymbol{y})]\!]$ with the identity

$$\int_S \frac{\boldsymbol{n}(\boldsymbol{x}) \times \boldsymbol{r}}{4\pi r^3} \mathrm{d}S_x = \int_V \boldsymbol{\nabla} \times \left(\frac{\vec{r}}{4\pi r^3}\right) \mathrm{d}V = \int_V \boldsymbol{\nabla} \times \left(\boldsymbol{\nabla} \frac{1}{4\pi r}\right) \mathrm{d}V = 0 \tag{C3}$$

and subtracting it from (C2), we obtain

$$\boldsymbol{n}(\boldsymbol{y}) \times \boldsymbol{H}_t(\boldsymbol{y}) = \boldsymbol{n}(\boldsymbol{y}) \times \boldsymbol{H_0}(\boldsymbol{y}) + \frac{1}{4\pi} \times \int_S \frac{\mathrm{d}S_x}{r^3} \left([\![H_n(\boldsymbol{x})]\!] \boldsymbol{n}(\boldsymbol{y}) - [\![H_n(\boldsymbol{y})]\!] \boldsymbol{n}(\boldsymbol{x}) \right] \times \boldsymbol{r} \big). \tag{C4}$$

This integrand scales as $O(1/r)$ as $\boldsymbol{x} \to \boldsymbol{y}$ and can now be calculated using, for example, local polar coordinates centered at $\boldsymbol{y}$ for the singular elements.

The norm of the left hand side of (C4) simplifies to $|\boldsymbol{n}(\boldsymbol{y})||\boldsymbol{H_t}(\boldsymbol{y})| \sin(\pi/2) = H_t(\boldsymbol{y})$, as the normal is unit length, and it makes a right angle with the tangential component of the magnetic field. Therefore, we can calculate the magnitude of the tangential magnetic field. This approach avoids the more numerically unstable method of numerical differentiation of the magnetic potential ψ on the droplet surface.

APPENDIX D: THE VIRIAL THEOREM APPROACH

The droplet dynamics around this "hysteresis jump" region can be considered on the basis of the Rayleigh dissipation function R when the energy of the droplet reads $dE/dt = -2R$ and R is expressed as a quadratic function of the generalized velocity of the system—in this case, de/dt or $d(a/b)/dt$:

$$R = \frac{D\dot{e}^2}{2}. \tag{D1}$$

Combining the above relations in an Euler–Lagrange equation gives

$$\frac{\partial E}{\partial e} = -D\dot{e}. \tag{D2}$$

Near the threshold of the instability $\partial_e E = \partial^2_{ee} E = 0$, we have

$$\frac{\partial E}{\partial e} \simeq \frac{1}{2}\frac{\partial^3 E}{\partial e^3}(e - e_c)^2 + H_c \frac{\partial^2 E}{\partial e \partial H} \frac{H - H_c}{H_c}, \tag{D3}$$

or in terms of the constants A, B, D

$$D\dot{e} = Ah + B(e - e_c)^2. \tag{D4}$$

Since the viscosity of the magnetic droplet is much larger than the viscosity of surrounding liquid, it can be neglected. Then, the condition of the force balance on the surface of the droplet reads

$$-p + \sigma^v_{nn} = -\gamma\left(\frac{1}{R_1} + \frac{1}{R_2}\right) + \frac{\mu_0}{2} M_n^2, \tag{D5}$$

where σ^v is the viscous stress tensor and M is the magnetization, and the equation of motion of the magnetic fluid assuming its ellipsoidal shape reads

$$-\partial_i p + \partial_m \sigma^v_{im} = 0. \tag{D6}$$

After multiplying (D6) by x_k and integrating over the volume of the droplet and using boundary condition (D5) gives the virial coefficients

$$V_{ik} = \delta_{ik} \int p dV - \int \gamma x_k n_i \boldsymbol{\nabla} \cdot \vec{n}\, dS + \int x_k n_k \frac{\mu_0}{2} M_n^2 dS - \int \sigma^v_{ik} dV = 0. \tag{D7}$$

Using $\int x_k n_i \boldsymbol{\nabla} \cdot \vec{n}\, dS = -\int (\delta_{ik} - n_i n_k)\, dS$ among other relations,[12] it can show that $V_{33} - \frac{1}{2}(V_{11} + V_{22}) = 0$ may be expressed as

$$\begin{aligned} &-\int \left[\sigma^v_{33} - \frac{1}{2}(\sigma^v_{11} + \sigma^v_{22})\right] dV \\ &+2\pi\gamma R_0^2 \left\{ \frac{\mu_0}{2} Bm \left[\frac{(1-e^2)}{2} \left(\frac{(3-e^2)}{e^5} \log\left(\frac{1+e}{1-e}\right) - \frac{6}{e^4} \right) \right] \right. \\ &\left. + \frac{\frac{(3-4e^2)\arcsin e}{e^3} - \frac{(3-2e^2)(1-e^2)^{1/2}}{e^2}}{2(1-e^2)^{1/6}} \right\} = 0, \end{aligned} \tag{D8}$$

with Bm here being $\frac{M^2 R_0}{\gamma}$ rather than the usual $\frac{H^2 R}{\gamma}$.

Remembering that droplet energy is expressed as

$$E = -\frac{1}{2} \frac{\chi H^2}{1 + \chi N/4\pi} \frac{R_0^3}{3} + \frac{2\pi\gamma R_0^2}{(1-e^2)^{1/6}} \left[\frac{\arcsin e}{e} + (1-e^2)^{1/2} \right], \tag{D9}$$

where χ is the magnetic susceptibility and N is the demagnetization coefficient, and a little algebra, we can identify the second term in (D8) to be equal to

$$-\frac{\partial E}{\partial e} \frac{3(1-e^2)}{2e}. \tag{D10}$$

Moreover, in terms of Lagrangian displacement $\xi_3 = L_{33} x_3$, the first term in (D8) can be expressed as

$$-3\eta \dot{L}_{33} \frac{4\pi}{3} R_0^3. \tag{D11}$$

Finally, taking into account the relation[37]

$$\dot{L}_{33} = \frac{2e\dot{e}}{3(1-e^2)}, \tag{D12}$$

we obtain

$$4\pi\eta R_0^3 \dot{e} + \frac{\partial E}{\partial e} \left(\frac{3(1-e^2)}{2e} \right)^2 = 0. \tag{D13}$$

Expressing this equation and the droplet energy in terms of an experimentally more convenient parameter—the axis ratio $a/b = 1/\sqrt{1-e^2}$ (droplet energy further denoted by $\tilde{E}$ and axis ratio by e) allows one to identify the capillary relaxation time $\tau_c = \eta R_0/\gamma$ in the dynamical equation

$$\frac{d}{dt}\left(\frac{a}{b}\right) = -\frac{1}{\tau_c}\frac{9(1-e^2)^{1/2}}{8e}\frac{\partial \tilde{E}}{\partial e}. \tag{D14}$$

Evaluation of the expansion of $\frac{\partial \tilde{E}}{\partial e}$ at either e_c or H_c allows to obtain expressions for the constants A or B accordingly. The constant D can be easily identified after integration of (D14) and reproducing (27) for small t:

$$\left(\frac{a}{b}\right) - \left(\frac{a}{b}\right)_c = -\frac{A}{2D}\frac{t}{\tau_c}\left(\frac{H^2}{H_c^2} - 1\right). \tag{D15}$$

The constants obtained in this manner yield (Sec. IV C 2)

$$A = \frac{8\pi}{3} Bm_c \frac{6e_c + (e_c^2 - 3)\log\left[\frac{1+e_c}{1-e_c}\right]}{2e_c^4}, \quad B = -\frac{1}{2}\frac{\partial^3 \tilde{E}}{\partial e^3}\frac{(1-e_c^2)^3}{e_c^2},$$
$$D = \frac{8e_c}{9(1-e_c^2)^{1/2}}.$$

REFERENCES

[1]S. Chandrasekhar, *Ellipsoidal Figures of Equilibrium* (Yale University Press, Dover, 1969).
[2]G. Taylor, "Disintegration of water drops in an electric field," Proc. R. Soc. London, Ser. A **280**, 383–397 (1964).
[3]R. Rosensweig, *Ferrohydrodynamics, Dover Books on Physics* (Dover Publications, 1985).
[4]V. Drozdova, T. Skrobotova, and V. Chekanov, "Experimental study of the hydrostatics characterizing the interphase boundary in a ferrofluid," Magnetohydrodynamics **15**, 12–14 (1979).
[5]J. Bacri and D. Salin, "Instability of ferrofluid magnetic drops under magnetic field," J. Phys. Lett. **43**, 649–654 (1982).
[6]V. G. Bashtovoi, S. G. Pogirnitskaya, and A. G. Reks, "Determination of the shape of a free drop of magnetic fluid in a uniform magnetic field," Magnetohydrodynamics **23**, 49–54 (1987).
[7]J.-C. Bacri, A. O. Cebers, and R. Perzynski, "Behavior of a magnetic fluid microdrop in a rotating magnetic field," Phys. Rev. Lett. **72**, 2705–2708 (1994).
[8]K. I. Morozov and A. V. Lebedev, "Bifurcations of the shape of a magnetic fluid droplet in a rotating magnetic field," J. Exp. Theor. Phys. **91**, 1029–1032 (2000).
[9]A. Cebers and M. Mayorov, "Structures of interface a bubble and magnetic fluid in a field," Magnetohydrodynamics **16**, 231–235 (1980).
[10]L. H. P. Cunha, I. R. Siqueira, F. R. Cunha, and T. F. Oliveira, "Effects of external magnetic fields on the rheology and magnetization of dilute emulsions of ferrofluid droplets in shear flows," Phys. Fluids **32**, 073306 (2020).
[11]J.-C. Bacri and D. Salin, "Bistability of ferrofluid magnetic drops under magnetic field," J. Magn. Magn. Mater. **39**, 48–50 (1983).
[12]A. Cebers, "Virial method of investigation of statics and dynamics of drops of magnetizable liquids," Magnetohydrodynamics **21**, 19–27 (1985).
[13]S. Afkhami, A. J. Tyler, Y. Renardy, M. Renardy, T. G. St. Pierre, R. C. Woodward, and J. S. Riffle, "Deformation of a hydrophobic ferrofluid droplet suspended in a viscous medium under uniform magnetic fields," J. Fluid Mech. **663**, 358–384 (2010).
[14]J.-C. Bacri and D. Salin, "Dynamics of the shape transition of a magnetic ferrofluid drop," J. Phys. Lett. **44**, 415–420 (1983).
[15]J. V. I. Timonen, M. Latikka, L. Leibler, R. H. A. Ras, and O. Ikkala, "Switchable static and dynamic self-assembly of magnetic droplets on superhydrophobic surfaces," Science **341**, 253–257 (2013).
[16]F. Serwane, A. Mongera, P. Rowghanian, D. A. Kealhofer, A. A. Lucio, Z. M. Hockenbery, and O. Campàs, "*In vivo* quantification of spatially varying mechanical properties in developing tissues," Nat. Methods **14**, 181–186 (2017).
[17]U. Banerjee, C. Mandal, S. K. Jain, and A. K. Sen, "Cross-stream migration and coalescence of droplets in a microchannel co-flow using magnetophoresis," Phys. Fluids **31**, 112003 (2019).
[18]R. Zhao, X. Dou, D. Zhang, and J. Huang, "Numerical study of the magnetohydrodynamic flow instability and its effect on energy conversion in the annular linear induction pump," Phys. Fluids **33**, 067125 (2021).
[19]S. Zhang, J. Zhou, and C. Shao, "Numerical investigation on yielding phenomena of magnetorheological fluid flowing through microchannel governed by transverse magnetic field," Phys. Fluids **31**, 022005 (2019).
[20]C. Pozrikidis, *A Practical Guide to Boundary Element Methods With the Software Library BEMLIB* (Chapman & Hall/CRC, 2002).
[21]C. Pozrikidis, *Boundary Integral and Singularity Methods for Linearized Viscous Flow* (Cambridge University Press, Cambridge, 1992).
[22]J. D. Sherwood, "Breakup of fluid droplets in electric and magnetic fields," J. Fluid Mech. **188**, 133–146 (1988).
[23]H. A. Stone, J. R. Lister, and M. P. Brenner, "Drops with conical ends in electric and magnetic fields," Proc. R. Soc. London, Ser. A **455**, 329–347 (1999).
[24]O. Lavrova, G. Matthies, T. Mitkova, V. Polevikov, and L. Tobiska, "Numerical treatment of free surface problems in ferrohydrodynamics," J. Phys.: Condens. Matter **18**, S2657–S2669 (2006).
[25]K. Misra, "Magnetic (electric) drop deformation in uniform external fields: Volume averaged methods and formation of static and dynamic conical tips," Phys. Fluids **32**, 107104 (2020).
[26]I. Drikis, J.-C. Bacri, and A. Cebers, "Labyrinthine pattern formation in disordered system of the magnetic fluid drops: Numerical simulation," Magnetohydrodynamics **35**, 157–169 (1999).
[27]A. Z. Zinchenko, M. A. Rother, and R. H. Davis, "A novel boundary-integral algorithm for viscous interaction of deformable drops," Phys. Fluids **9**, 1493–1511 (1997).
[28]A. Z. Zinchenko and R. H. Davis, "Emulsion flow through a packed bed with multiple drop breakup," J. Fluid Mech. **725**, 611–663 (2013).
[29]V. Cristini, J. Bławzdziewicz, and M. Loewenberg, "An adaptive mesh algorithm for evolving surfaces: Simulations of drop breakup and coalescence," J. Comput. Phys. **168**, 445–463 (2001).
[30]W. C. Jesus, A. M. Roma, and H. D. Ceniceros, "Deformation of a sheared magnetic droplet in a viscous fluid," Commun. Comput. Phys. **24**, 332–355 (2018).
[31]C. S. Peskin, "Flow patterns around heart valves: A numerical method," J. Comput. Phys. **10**, 252–271 (1972).
[32]X. Li, Z.-Q. Dong, P. Yu, X.-D. Niu, L.-P. Wang, D.-C. Li, and H. Yamaguchi, "Numerical investigation of magnetic multiphase flows by the fractional-step-based multiphase lattice Boltzmann method," Phys. Fluids **32**, 083309 (2020).
[33]S. Afkhami and Y. Renardy, "Ferrofluids and magnetically guided superparamagnetic particles in flows: A review of simulations and modeling," J. Eng. Math. **107**, 231–251 (2017).
[34]D. Das and D. Saintillan, "Electrohydrodynamics of viscous drops in strong electric fields: Numerical simulations," J. Fluid Mech. **829**, 127–152 (2017).
[35]J. Erdmanis, G. Kitenbergs, R. Perzynski, and A. Cēbers, "Magnetic microdroplet in rotating field: Numerical simulation and comparison with experiment," J. Fluid Mech. **821**, 266–295 (2017).
[36]A. Stikuts, R. Perzynski, and A. Cēbers, "Spontaneous order in ensembles of rotating magnetic droplets," J. Magn. Magn. Mater. **500**, 166304 (2020).
[37]E. Blūms, A. O. Cebers, and M. M. Maĭorov, *Magnetic Fluids* (Walter de Gruyter, Berlin/New York, 1997).
[38]A. Z. Zinchenko, M. A. Rother, and R. H. Davis, "Cusping, capture, and breakup of interacting drops by a curvatureless boundary-integral algorithm," J. Fluid Mech. **391**, 249–292 (1999).
[39]S. Kim and S. J. Karrila, *Microhydrodynamics: Principles and Selected Applications*, Butterworth-Heinemann Series in Chemical Engineering (Butterworth-Heinemann, Boston, 1991).
[40]I. R. Siqueira, R. B. Rebouças, T. F. Oliveira, and F. R. Cunha, "A new mesh relaxation approach and automatic time-step control method for boundary integral simulations of a viscous drop," Int. J. Numer. Methods Fluids **84**, 221–238 (2017).
[41]A. Z. Zinchenko and R. H. Davis, "Algorithm for direct numerical simulation of emulsion flow through a granular material," J. Comput. Phys. **227**, 7841–7888 (2008).

[42]Y. Dikansky, A. Cebers, and V. P. Shatsky, "Magnetic emulsion properties in electric and magnetic fields," Magnetohydrodynamics **26**, 25–30 (1990).
[43]J. M. Rallison, "A numerical study of the deformation and burst of a viscous drop in general shear flows," J. Fluid Mech. **109**, 465–482 (1981).
[44]J. W. Strutt, "Some general theorems relating to vibrations," Proc. London Math. Soc. **s1–s4**, 357–368 (1871).
[45]L. D. Landau and E. M. Lifshitz, *Mechanics, Third Edition: Volume 1 (Course of Theoretical Physics)*, 3rd ed. (Butterworth-Heinemann, 1976).
[46]E. Janiaud, F. Elias, J.-C. Bacri, V. Cabuil, and R. Perzynski, "Spinning ferrofluid microscopic droplets," Magnetohydrodynamics **36**, 300–378 (2000).
[47]A. P. Stikuts, R. Perzynski, and A. Cēbers, "Small deformation theory for a magnetic droplet in a rotating field," arXiv:2112.07000 (2021).
[48]J. C. imurs, A. Brasovs, and K. Ērglis, "Stability analysis of a paramagnetic spheroid in a precessing field," J. Magn. Magn. Mater. **491**, 165630 (2019).
[49]K. Ērglis, Q. Wen, V. Ose, A. Zeltins, A. Sharipo, P. A. Janmey, and A. Cēbers, "Dynamics of magnetotactic bacteria in a rotating magnetic field," Biophys. J. **93**, 1402–1412 (2007).
[50]A. Cēbers and M. Ozols, "Dynamics of an active magnetic particle in a rotating magnetic field," Phys. Rev. E **73**, 021505 (2006).
[51]A. Cēbers, "Dynamics of an elongated magnetic droplet in a rotating field," Phys. Rev. E **66**, 061402 (2002).

C Extended summaries in French and Latvian

Extended summaries of the thesis are provided hereafter in French and Latvian.

Résumé en français

1 Introduction

Les fluides magnétiques sont des colloïdes stables constitués d'une dispersion de nanoparticules magnétiques solides dans un fluide porteur. La petite taille des nanoparticules ($d \approx 10\ nm$) garantit que chaque particule possède un seul domaine magnétique. Le fluide magnétique, également appelé ferrofluide, présente des propriétés superparamagnétiques. Le fluide est fortement aimanté lorsque les moments magnétiques des nanoparticules s'alignent dans un champ magnétique externe. Cependant, lorsque le champ est supprimé, les fluctuations thermiques désorientent les moments magnétiques des nanoparticules et l'aimantation du ferrofluide revient à zéro [1].

Il est possible de créer des gouttes magnétiques en émulsionnant le ferrofluide dans un fluide non miscible ou, ce qui nous interesse ici, en induisant une séparation de phase dans un ferrofluide [2]. Cette dernière méthode crée des gouttes avec une perméabilité magnétique exceptionnellement élevée ($\mu/\mu_0 \approx 40$) et un faible coefficient de tension superficielle ($\gamma \approx 10^{-6}\ N/m$), ce qui permet d'observer des phénomènes intéressants dès de faibles champs magnétiques. Les gouttes magnétiques se déforment facilement sous champ magnétique. Elles s'allongent dans la direction d'un champ magnétique appliqué jusqu'à ce que les forces magnétiques soient équilibrées par les forces de tension de surface (figure 1.1).

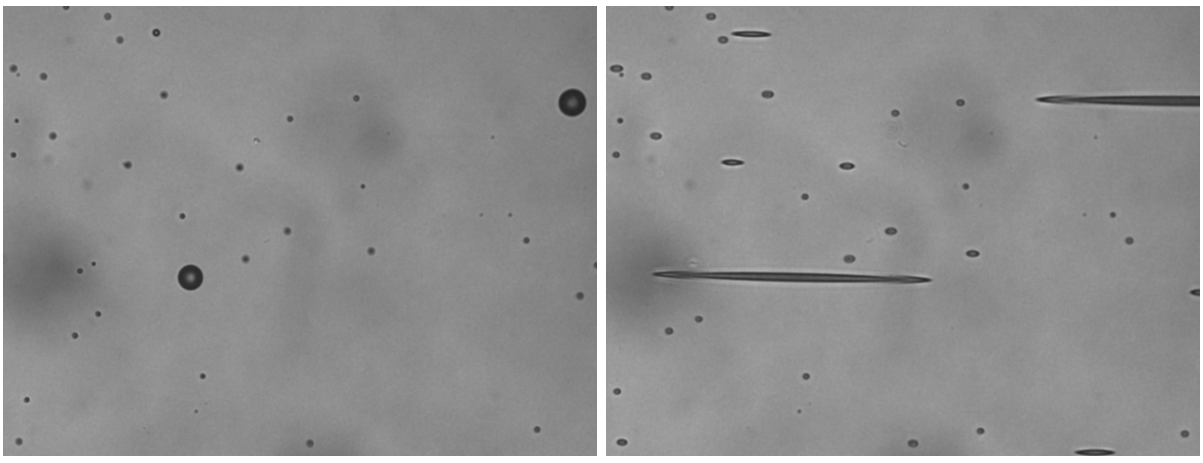

FIGURE 1.1 – Gouttes créées par une séparation de phases. La phase concentrée forme des gouttes magnétiques vues sur la photo comme des disques plus sombres de différents diamètres entourés d'une phase diluée (à gauche). Les gouttes s'allongent dans la direction du champ appliqué (à droite). Le champ de vision est de 132 $\mu m \times 100\ \mu m$.

Le comportement de la goutte magnétique dans un champ constant est assez bien

compris. L'allongement à l'équilibre peut être calculé analytiquement en supposant une forme sphéroïdale [3, 4, 5]. L'approximation sphéroïdale peut être utilisée pour calculer la dynamique de l'allongement des gouttes [6, 7]. Pour une aimantation linéaire, l'élongation à l'équilibre est décrite par l'équation [3, 4]

$$\frac{\mu_0 H_\infty^2 R_0}{2\gamma} = \left(\frac{1}{\frac{\mu}{\mu_0} - 1} + N_d \right)^2 \frac{\left(3 - 2e^2 - \frac{(3-4e^2)\arcsin e}{e(1-e^2)^{1/2}} \right)}{(1-e^2)^{2/3} \left(-\frac{6}{e^2} + \frac{3-e^2}{e^3} \ln \frac{1+e}{1-e} \right)}, \tag{1.1}$$

où μ_0 est la perméabilité magnétique du vide, H_∞ est l'intensité du champ magnétique appliqué, R_0 est le rayon de la goutte non déformée, γ est le coefficient de tension superficielle, μ est la perméabilité magnétique de la goutte, e est l'excentricité de la goutte et

$$N_d = \frac{1-e^2}{2e^3} \left(-2e + \ln \frac{1+e}{1-e} \right), \tag{1.2}$$

est le facteur de démagnétisation. L'équation (1.1) peut être utilisée pour déterminer les paramètres de la goutte tels que sa perméabilité magnétique et son coefficient de tension superficielle.

Dans un champ tournant, le mouvement des gouttes magnétiques devient plus complexe. Si la fréquence de rotation est lente, la goutte s'allonge et tourne lentement en suivant le champ. Une scission des gouttes peut se produire en raison de la friction visqueuse [8]. Lorsque la fréquence de rotation du champ est élevée, la goutte peut subir une série d'instabilités de forme. Tout d'abord, lorsque le champ est faible, la goutte prend une forme sphéroïdale oblate - aplatie dans le plan du champ tournant. Ensuite, lorsque l'intensité du champ dépasse une valeur seuil, la goutte subit une rupture de symétrie spontanée et s'allonge dans le plan du champ tournant. Enfin, en augmentant encore l'intensité du champ, au-delà d'un autre seuil critique, la goutte reprend une forme quasi-oblate, qui est fortement aplatie dans le plan du champ tournant, et une couronne de pics apparaît sur son périmètre : [9]. Cette transition de forme oblate-prolate-oblate a été décrite théoriquement en assimilant la goutte à un sphéroïde [9]. Cette description a ensuite été généralisée au cas d'un ellipsoïde à trois axes [10]. Récemment, les formes d'équilibre dans un champ en rotation rapide ont été obtenues numériquement par la méthode des éléments de frontière (BEM) [11]. Les auteurs de la simulation dans [11] ont supposé que les viscosités de la goutte et du milieu environnant étaient égales, ce qui simplifie considérablement le calcul, mais ne permet pas de modéliser la dynamique des gouttes. Actuellement, la dynamique des gouttes magnétiques dans les champs tournants

reste largement inexplorée, même si en fonction de l'intensité et de la fréquence du champ tournant, des formes intéressantes sont attendues [12].

Ceci motive l'objectif de ce travail : **Explorer la dynamique des gouttes magnétiques dans un champ magnétique tournant en fonction du temps.** Les tâches suivantes étant à effectuer pour atteindre l'objectif :

1. En utilisant le modèle du fluide magnétique, développer une description analytique de la dynamique des gouttes individuelles dans des cas simples, tels que les champs faibles et les petites déformations, en tenant compte des différentes viscosités à l'intérieur et à l'extérieur de la goutte.
2. En utilisant le modèle du fluide magnétique, développer un logiciel de simulation pour calculer la dynamique des gouttes dans des situations où les descriptions analytiques ne fonctionnent plus.
3. A l'aide du logiciel de simulation, caractériser le mouvement des gouttes magnétiques dans les champs tournants.
4. Effectuez des mesures expérimentales sur des gouttes magnétiques microscopiques obtenues par séparation de phases et évaluez dans quelle mesure le modèle de fluide magnétique décrit bien leur dynamique.
5. Observer expérimentalement la dynamique collective d'ensembles de gouttes.
6. Développer des modèles qui décrivent la dynamique collective des ensembles de gouttes.

Ce résumé est divisé en plusieurs sections. La section 2 présente le modèle du fluide magnétique tel qu'il est utilisé dans la description théorique de la goutte. La section 3 montre la solution analytique du modèle dans la limite des petites déformations à champ faible. Elle montre également une comparaison avec l'expérience utilisant les gouttes magnétiques obtenues par séparation de phase. La section 4 décrit la simulation basée sur la méthode des éléments de frontière, qui a été utilisée pour calculer la dynamique des gouttes magnétiques avec des déformations importantes. La section 5 traite de l'observation expérimentale d'ensembles de gouttes dans un champ tournant et de leur modélisation à l'aide d'approximations simples. Enfin, 6 est une section de conclusion qui résume les principaux résultats de ce travail.

2 Formulation du modèle

Les gouttes magnétiques issues d'une séparation de phase constituent un matériau unique, dont les propriétés ne sont pas encore suffisamment comprises. À l'intérieur des gouttes, la concentration de nanoparticules magnétiques est très importante (leur fraction volumique est d'environ $\phi_{drop} \approx 30\%$ [13]). Cela pourrait signifier que des amas de nanoparticules pourraient se former à l'intérieur des gouttes, ce qui pourrait influencer leurs propriétés magnétiques et rhéologiques. De plus, les gouttes sont en équilibre thermodynamique en ce qui concerne les nanoparticules magnétiques qui sortent et entrent du corps de la goutte. Ce mouvement des nanoparticules se produit par le biais de la surface, ce qui peut modifier sa taille de quelques ordres de grandeur dans les expériences. En résumé, le système est compliqué, cependant, nous cherchons à trouver un modèle relativement simple qui rende compte du comportement observé des gouttes dans un champ tournant. Nous examinerons le modèle d'un fluide magnétique simple [1], qui a fonctionné dans le passé pour calculer les formes d'équilibre des gouttes dans un champ magnétique à rotation rapide [11].

Nous considérons une goutte de fluide magnétique en suspension dans un fluide porteur infini non magnétique (figure 2.1). La goutte magnétique (domaine intérieur, dont les propriétés seront désignées par l'exposant (i)) possède la perméabilité magnétique μ et la viscosité $\eta^{(i)}$. Le fluide environnant (domaine extérieur, dont les propriétés seront désignées par l'exposant (e)) a une perméabilité magnétique égale à la perméabilité magnétique du vide μ_0 et une viscosité $\eta^{(i)}$. Une tension superficielle caractérisée par le coefficient de tension superficielle γ existe entre les deux domaines. Un champ magnétique tournant $\boldsymbol{H}_\infty$ est appliqué. La vitesse angulaire du champ est $\boldsymbol{\omega}$. On considère une aimantation linéaire $\boldsymbol{M} = \chi \boldsymbol{H}$, où $\chi = \mu/\mu_0 - 1$ est la susceptibilité magnétique. L'induction du champ magnétique est alors $\boldsymbol{B} = \mu_0(\boldsymbol{H} + \boldsymbol{M}) = \mu \boldsymbol{H}$.

L'écoulement est régi par les équations de Stokes [14] avec un terme de force magnétique [15] et la condition d'incompressibilité

$$-\boldsymbol{\nabla} p + \eta \Delta \boldsymbol{v} + \boldsymbol{f} = \boldsymbol{0}, \quad \boldsymbol{\nabla} \cdot \boldsymbol{v} = 0, \tag{2.1}$$

où p est la pression et $\boldsymbol{v}$ est la vitesse du fluide, $f_i = \partial_j T_{ij} = \mu_0 M_j \partial_j H_i$ est la force magnétique du corps, et $T_{ij} = -\mu_0 H^2 \delta_{ij}/2 + H_i B_j$ est le tenseur des contraintes de Maxwell. Les conditions aux limites de l'écoulement sont les suivantes. La vitesse à la

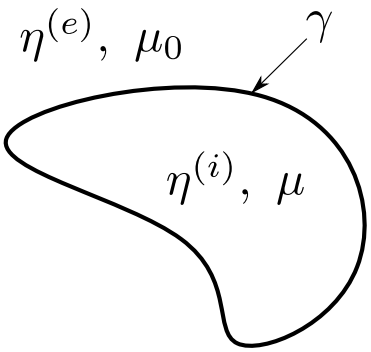

FIGURE 2.1 – Croquis de la goutte magnétique de viscosité $\eta^{(i)}$ et de perméabilité magnétique μ en suspension dans un fluide infini de viscosité $\eta^{(e)}$ et de perméabilité magnétique μ_0. La tension superficielle agit sur la goutte avec le coefficient de tension superficielle γ.

surface de la goutte est continue

$$\boldsymbol{v}^{(i)} - \boldsymbol{v}^{(e)} = \boldsymbol{0}. \tag{2.2}$$

La somme de toutes les forces sur la surface de la goutte est nulle dans la direction normale

$$\boldsymbol{n} \cdot (\boldsymbol{\sigma}^{(e)} - \boldsymbol{\sigma}^{(i)}) \cdot \boldsymbol{n} + \frac{\mu_0}{2} {M_n^{(i)}}^2 - \gamma(k_1 + k_2) = 0, \tag{2.3}$$

et également dans la direction tangentielle

$$\boldsymbol{t} \cdot (\boldsymbol{\sigma}^{(e)} - \boldsymbol{\sigma}^{(i)}) \cdot \boldsymbol{n} = 0, \tag{2.4}$$

où $\boldsymbol{n}$ est le vecteur normal extérieur de la goutte, $\boldsymbol{t}$ est un vecteur tangentiel, $M_n^{(i)}$ est la composante normale de l'aimantation à l'intérieur de la goutte, $(k_1 + k_2)$ est la somme des courbures principales, et $\sigma_{ij} = -p\delta_{ij} + \eta(\partial_j v_i + \partial_i v_j)$ est le tenseur des contraintes hydrodynamiques. Loin de la goutte, nous imposons que la pression et la vitesse prennent les valeurs de l'écoulement global imposé p_∞ et $\boldsymbol{v}_\infty$ (généralement fixé à zéro)

$$p^{(e)}|_{r\to\infty} = p_\infty, \quad \boldsymbol{v}^{(e)}|_{r\to\infty} = \boldsymbol{v}_\infty. \tag{2.5}$$

Les forces magnétiques sont trouvées en résolvant d'abord le champ magnétique à l'aide des équations de la magnétostatique : [16]

$$\boldsymbol{\nabla} \times \boldsymbol{H} = \boldsymbol{0}, \quad \boldsymbol{\nabla} \cdot \boldsymbol{B} = 0. \tag{2.6}$$

Elles sont satisfaites, si le potentiel magnétique $\boldsymbol{H} = \boldsymbol{\nabla}\psi$ satisfait l'équation de Laplace

$$\Delta\psi = 0. \tag{2.7}$$

Les conditions aux limites à la surface des gouttes sont les suivantes

$$\mu_0 \boldsymbol{n} \cdot \boldsymbol{\nabla}\psi^{(e)} - \mu \boldsymbol{n} \cdot \boldsymbol{\nabla}\psi^{(i)} = 0 \tag{2.8}$$

et

$$\psi^{(e)} - \psi^{(i)} = 0. \tag{2.9}$$

Loin de la goutte, nous imposons que le champ soit égal au champ appliqué $\boldsymbol{H}_\infty$.

$$\boldsymbol{\nabla}\psi^{(e)}|_{r\to\infty} = \boldsymbol{H}_\infty. \tag{2.10}$$

Trois paramètres sans dimension apparaissent dans la solution du problème.

- $\lambda = \frac{\eta^{(i)}}{\eta^{(e)}}$, le rapport de viscosité,
- $\mu_r = \frac{\mu}{\mu_0}$, la perméabilité magnétique relative,
- $Bm = 4\pi\mu_0 \frac{R_0 H_\infty^2}{\gamma}$, le nombre de Bond magnétique. Il est proportionnel à une force magnétique caractéristique sur une force caractéristique due à la tension de surface. R_0 est le rayon d'une goutte non déformée.

3 Dynamique des petites déformations

Les solutions analytiques pour la dynamique des gouttes magnétiques ne sont possibles que dans les cas les plus simples. L'un de ces cas est la limite où la goutte est proche de la sphère. La dynamique des petites déformations des gouttes dans un champ stationnaire homogène (électrique ou magnétique) a été étudiée analytiquement. Il y a été montré qu'une goutte se rapproche exponentiellement d'une forme d'équilibre ellipsoïdale [17]. La dynamique des gouttes visqueuses non magnétiques dans des écoulements externes a également été largement explorée théoriquement dans la limite des petites déformations [18]. Une approche courante pour calculer le mouvement des gouttes ellipsoïdales dans les écoulements externes est celle de modèles phénoménologiques de l'évolution temporelle d'un tenseur qui décrit la forme de la goutte [19]. La nature phénoménologique de ces modèles nous permet de les modifier pour inclure différents phénomènes supplémentaires

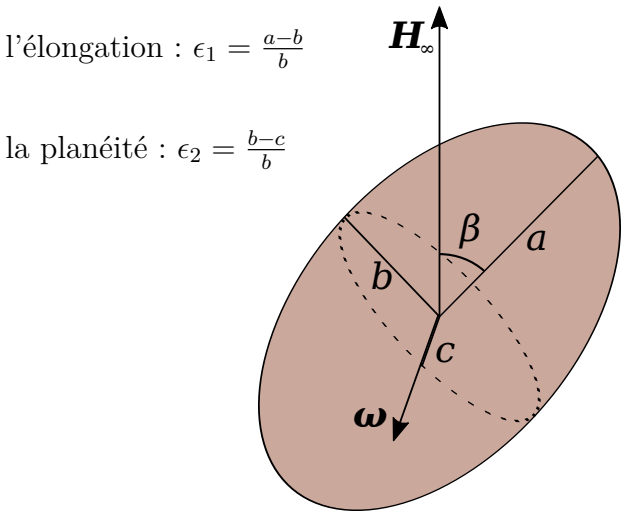

FIGURE 3.1 – Les paramètres décrivant la forme de la goutte dans un champ magnétique tournant. Le paramètre β est négatif lorsque le grand axe de la goutte suit le champ magnétique tournant $\boldsymbol{H}_\infty$. Le champ tourne dans la direction $\boldsymbol{\omega}$.

tels que, par exemple, les interactions magnétiques. Cependant, les modèles phénoménologiques doivent être testés en les comparant à une théorie plus fondamentale, à des simulations ou à des expériences.

Dans la limite où les forces magnétiques sont beaucoup plus faibles que les forces capillaires ($Bm \ll 1$), la goutte peut être décrite comme un ellipsoïde avec les semi-axes $a \geq b \geq c$. Alternativement, deux paramètres de déformation non négatifs peuvent être utilisés pour décrire la forme de la goutte, l'élongation

$$\epsilon_1 = \frac{a-b}{b} \tag{3.1}$$

et la planéité

$$\epsilon_2 = \frac{b-c}{b}, \tag{3.2}$$

qui, avec la condition d'incompressibilité $abc = R_0^3$, peuvent être utilisées pour retrouver les demi-axes. Lorsque le mouvement se fait dans le plan du champ magnétique tournant, l'axe le plus court c est aligné avec la direction de la vitesse angulaire du champ magnétique et l'orientation de la goutte est déterminée par un seul angle β que son axe le plus long fait avec le champ magnétique (Figure 3.1). L'angle β est choisi pour être positif lorsque le plus grand axe de la goutte est en avant du champ et négatif lorsqu'il est en arrière du champ.

La résolution d'une équation phénoménologique [20, 21] conduit à un système d'équa-

tions pour les paramètres de déformation

$$\begin{cases} \dfrac{d\epsilon_1}{dt} = -\dfrac{1}{\tau}\left(\epsilon_1 - \delta\cos(2\beta)\right) \\ \dfrac{d\epsilon_2}{dt} = -\dfrac{1}{\tau}\left(\epsilon_2 - \delta\sin^2(\beta)\right) \\ \dfrac{d\beta}{dt} = -\omega - \dfrac{\delta\cos(\beta)\sin(\beta)}{\tau\epsilon_1} \end{cases}, \tag{3.3}$$

où τ et δ sont des constantes phénoménologiques. En résolvant le problème hydrodynamique complet formulé dans la section 2 asymptotiquement pour de petits Bm, et de petits ϵ_1 et ϵ_2, nous obtenons le même système d'équations (3.3) validant ainsi l'équation phénoménologique. Nous obtenons que les constantes phénoménologiques sont

$$\delta = \frac{9Bm}{32\pi}\frac{(\mu_r - 1)^2}{(\mu_r + 2)^2}, \tag{3.4}$$

et

$$\tau = \frac{R_0\eta^{(e)}}{\gamma}\frac{(3 + 2\lambda)(16 + 19\lambda)}{40(1 + \lambda)}. \tag{3.5}$$

En analysant le système d'équations (3.3), nous voyons que les points fixes pour le système (3.3) sont

$$\begin{cases} \epsilon_1^* = \dfrac{\delta}{\sqrt{1 + 4\tau^2\omega^2}} \\ \epsilon_2^* = \dfrac{\delta}{2}\left(1 - \dfrac{1}{\sqrt{1 + 4\tau^2\omega^2}}\right) \\ \beta^* = -\dfrac{1}{2}\arctan(2\tau\omega) + n\pi \end{cases}, \tag{3.6}$$

où n est un entier. Ce sont des foyers stables pour tous les paramètres du problème. Jusqu'à une certaine échelle, le comportement des gouttes dans la limite des petites déformations est régi par un seul paramètre $\tau\omega$. Le paramètre $\tau\omega$ est proportionnel au nombre capillaire, qui est le rapport des forces visqueuses aux forces de tension superficielle [22]. Dans le régime des petites déformations, les gouttes sont en pseudo-rotation suivant le champ magnétique - leur axe le plus long suit le champ, imitant une rotation, cependant, les champs de vitesse ne sont pas en rotation (figure 3.2).

Selon les équations (3.3), lorsqu'une goutte est dans un champ non rotatif, elle relaxe jusqu'à l'allongement d'équilibre ϵ_1^* de manière exponentielle

$$(\epsilon_1 - \epsilon_1^*) \propto e^{-t/\tau_{rel}}. \tag{3.7}$$

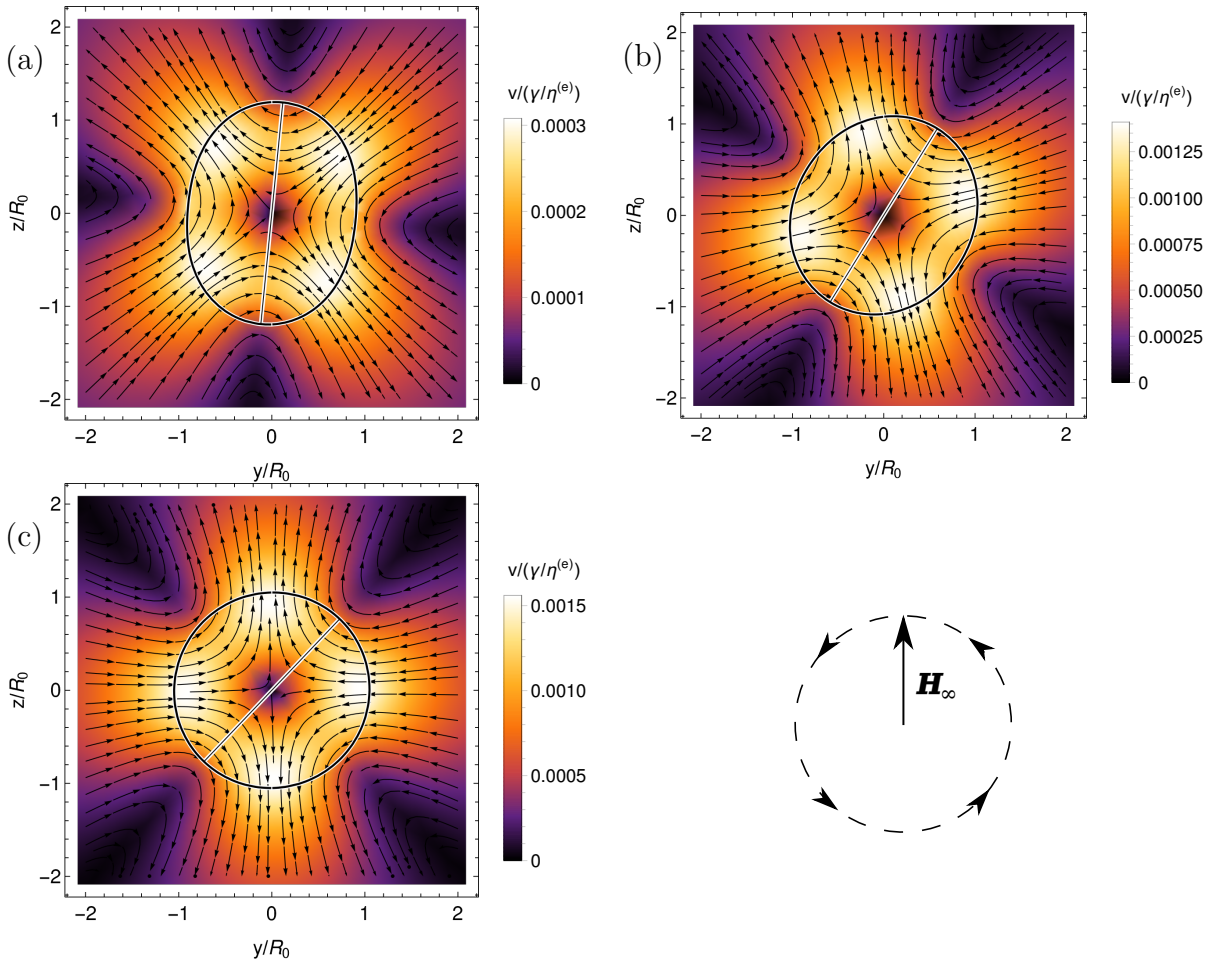

FIGURE 3.2 – Illustration du champ de vitesse autour de gouttes ayant atteint leur forme d'équilibre dans un champ magnétique tournant de différentes fréquences, qui sont (a) $\tau\omega = 0.1$, (b) $\tau\omega = 1$ et (c) $\tau\omega = 10$. Le champ est tel que $\delta = 0.3$. La section transversale à $x = 0$ est représentée. Les formes des gouttes et leur axe le plus long sont soulignés, et l'amplitude de la vitesse, mise à l'échelle par $\gamma/\eta^{(e)}$, est représentée en couleur. Le tracé est réalisé dans le cadre de référence du laboratoire, où le champ magnétique tourne dans le sens inverse des aiguilles d'une montre et pointe momentanément le long de l'axe z. Le champ de vitesse est tel que la goutte se déforme de manière à ce que son axe le plus long suive le champ.

Et dans un champ tournant, lorsqu'il atteint l'équilibre, il est en retard sur le champ d'un angle $\beta^* = -\frac{1}{2}\arctan(2\tau_{rot}\omega)$. Théoriquement, τ_{rot} et τ_{rel} devraient être identiques. Or, on a observé expérimentalement que les deux valeurs s'écartent significativement (table 1).

	$\tau_{rel},\ s$	$\tau_{rot},\ s$
Goutte 1	7.7 ± 0.2	0.11 ± 0.03
Goutte 2 en présence de champ	6.65 ± 0.02	
Goutte 2 en champ nul	4.02 ± 0.02	
Goutte 3	16.4 (théorique)	0.16

TABLE 1 – Le temps de décroissance caractéristique des petites déformations τ_{rel} tel que mesuré par l'expérience de relaxation en utilisant la formule (3.7), et τ_{rot} tel que mesuré à partir de la forme d'équilibre des gouttes dans un champ tournant en utilisant les formules (3.6).

Ainsi, pour pouvoir reproduire les observations expérimentales, il manque quelque chose dans la description théorique de la goutte, qui ici ne prend en compte que la force normale de surface due au tenseur des contraintes de Maxwell. Nous pourrions proposer par exemple une organisation interne des nanoparticules dans la goutte de fluide magnétique concentré, qui ne répondrait pas à la même échelle de temps à une rotation et à une relaxation.

Quoi qu'il en soit, afin de déterminer les limites d'applicabilité de cette théorie dynamique des petites déformations, nous effectuons des calculs par éléments de frontière dans la partie suivante, dans un cadre plus large, ce qui pourrait nous fournir de nouveaux résultats dynamiques plus généraux.

4 Calculs par éléments de frontière

Une méthode numérique souvent utilisée pour calculer la dynamique des gouttes est la méthode des éléments de frontière (BEM) [23, 24]. Elle a été récemment utilisée pour calculer les valeurs d'équilibre des gouttes magnétiques dans un champ en rotation infiniment rapide [11]. Nous cherchons ici à développer un algorithme BEM pour calculer la dynamique des gouttes magnétiques dans le régime où l'approximation des petites déformations (discutée dans la section 3) ne tient plus. L'algorithme fonctionne pour toute vitesse angulaire de champ en prenant en compte la différence de viscosité entre la goutte et le milieu extérieur.

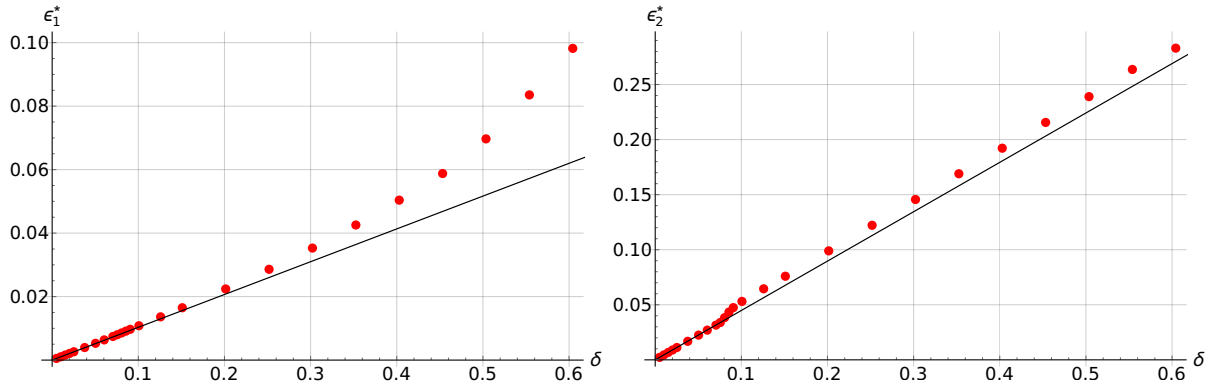

FIGURE 4.1 – Allongement à l'équilibre ϵ_1 et planéité ϵ_2 en fonction de l'intensité du champ magnétique tournant, mesurée par le paramètre δ. La fréquence du champ est telle que $\tau\omega = 4.8$. Les lignes sont les valeurs analytiques d'équilibre (3.6) et les points rouges sont issus des simulations BEM.

Les équations formulées dans la section 2 sont reformulées sous forme d'équations intégrales, où les intégrales sont sur la surface de la goutte. Cela nous permet de résoudre numériquement le problème dans tout le domaine infini en maillant simplement la surface de la goutte. Nous calculons la vitesse à la surface de la goutte et la déplaçons en conséquence à chaque pas de temps. D'importantes procédures de maintien du maillage sont nécessaires pour garantir l'exactitude des calculs.

Nous avons d'abord utilisé la simulation pour déterminer les limites d'applicabilité de la théorie des petites déformations (figure 4.1). Nous voyons que pour avoir moins de 10% d'erreur, la théorie des petites déformations doit être utilisée pour des champs magnétiques suffisamment faibles pour que $\delta \lesssim 0.3$.

Le développement de l'algorithme BEM nous permet d'explorer la dynamique des gouttes magnétiques dans un champ tournant en fonction de la fréquence et de l'intensité du champ (figure 4.2). Nous voyons qu'en général les gouttes développent une forme triaxiale, dont les axes oscillent. En fonction de Bm et de $\tau\omega$, les gouttes peuvent être plus aplaties ou plus allongées. Lorsque Bm est petit et que la goutte est quasi aplatie, l'angle β entre le champ s'approche d'une valeur stationnaire (proche de $-\pi/4$ lorsque $\tau\omega$ est grand). Cependant, lorsque Bm est grand et que $\tau\omega$ est également grand, il ne se stabilise pas (β oscille). Dans ce régime, la forme initiale quasi-oblate semble être instable, et les gouttes commencent à développer une forme allongée : la bifurcation oblate-prolate se produit comme prévu pour le champ tournant infiniment rapide [11, 10].

Les gouttes peuvent changer d'orientation soit par une déformation de la surface, soit par rotation solide. Ce phénomène est caractérisé par le rapport ω_s/ω, où ω est la fréquence de rotation du champ magnétique et ω_s est la vitesse angulaire de la surface

définie comme suit

$$\omega_s = \left\langle \frac{|\boldsymbol{x}_p \times \boldsymbol{v}|}{x_p^2} \right\rangle, \tag{4.1}$$

où $\boldsymbol{x}_p$ est le rayon vecteur d'un sommet donné projeté sur le plan de rotation du champ magnétique (le centre de masse étant à l'origine), $\boldsymbol{v}$ est la vitesse dudit sommet. La moyenne est prise sur l'ensemble des points du maillage. Les valeurs proches de 1 indiquent que les gouttes tournent comme un corps rigide, et les valeurs proches de 0 signifient que l'orientation change à cause des déformations de la surface. Ce rapport a été calculé pour la dernière étape de simulation et est représenté dans le diagramme de phase (figure 4.2). Nous voyons que les formes allongées présentent une dynamique de corps rigide, tandis que les formes aplaties se déplacent en raison des déformations de surface.

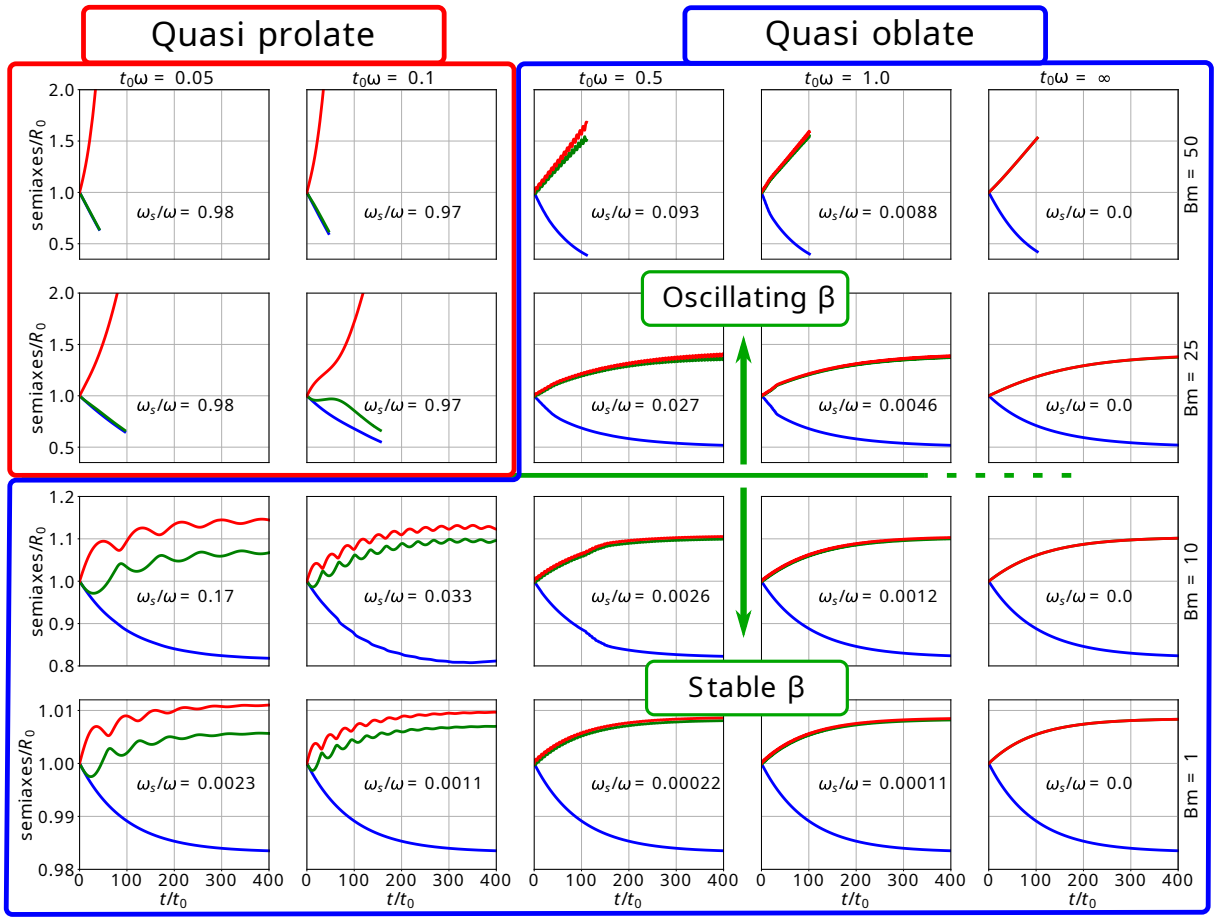

FIGURE 4.2 – Diagramme de phase montrant l'évolution des demi-axes des gouttes en fonction de ω et Bm. Les paramètres de simulation sont $\mu_r = 10$, $\lambda = 100$. L'échelle de temps est $t_0 = R_0\eta^{(e)}/\gamma$. Le rapport ω_s/ω caractérise dans quelle mesure les gouttes tournent comme un corps rigide lors du dernier pas de simulation. Les valeurs proches de 1 signifient que le mouvement est proche de la rotation en tant que corps rigide. Les valeurs proches de 0 signifient que la goutte change d'orientation en raison des déformations de la surface. La valeur de ω_s est calculée à l'aide de l'équation (4.1). β est l'angle entre le plus grand axe de la goutte et le champ magnétique.

Les gouttes sont presque ellipsoïdales lorsqu'elles sont quasi aplaties. Cependant,

lorsque la goutte s'allonge fortement et tourne en suivant le champ, la friction visqueuse peut faire plier ses extrémités en créant une forme en "S" (figure 4.3). Une telle courbure a été observée expérimentalement dans une plus large mesure dans [8, 12].

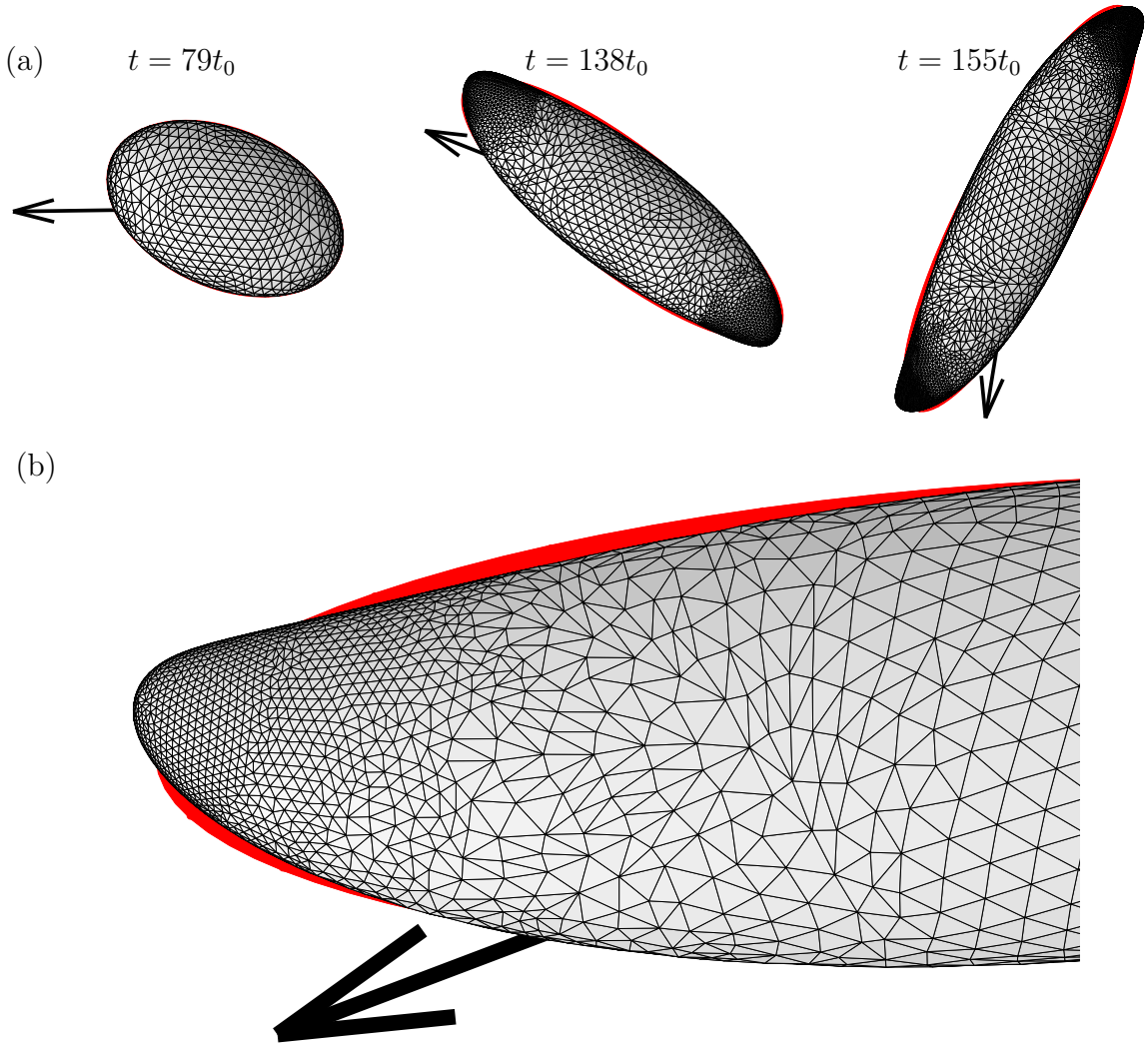

FIGURE 4.3 – Le maillage d'une goutte avec $\lambda = 100$, $\mu_r = 10$, $Bm = 25$, $t_0\omega = 0.1$ dans un champ magnétique tournant dans le sens inverse des aiguilles d'une montre. L'échelle de temps est $t_0 = R_0\eta^{(e)}/\gamma$. Le maillage est dessiné sur un ellipsoïde rouge pour illustrer la similarité des formes des gouttes avec un ellipsoïde. La flèche noire indique la direction du champ magnétique momentané. (a) montre un instantané à différents moments de la simulation. (b) montre un zoom sur une partie du maillage à $t = 155t_0$.

Il est donc possible de modéliser numériquement la dynamique de la forme des gouttes individuelles par des calculs par éléments de frontière, en tenant compte du contraste de viscosité entre l'intérieur et l'extérieur des gouttes, jusqu'à des déformations moyennes des gouttes. Dans ce but, une méthode adaptée d'ajustement du maillage près des extrémités est obligatoire. Une vision précise de cette dynamique est alors obtenue, conduisant à un diagramme de phase en fonction de la fréquence du champ et du nombre de Bond magné-

tique. Il montre une évolution des gouttes quasi-prolates (en rotation de corps rigide) vers des formes quasi-oblates (se déformant sous l'effet des déformations de surface). Pour de faibles déformations, les résultats du modèle analytique de la section 3 sont retrouvés.

Ceci marque la fin de la présente étude dynamique du comportement individuel des gouttes sous champ tournant. Analysons maintenant le comportement collectif d'un ensemble de petites gouttes allongées sous champ tournant.

5 Dynamique collective des gouttes magnétiques

Un phénomène intéressant qui a retenu l'attention des chercheurs ces dernières années est l'auto-assemblage de colloïdes sous l'effet du champ [25]. Il a été démontré que dans un champ tournant, des particules magnétiques solides peuvent s'auto-organiser en cristaux rotatifs bidimensionnels [26, 27, 28]. Un autre travail a considéré l'auto-assemblage dans un champ en précession de gouttes contenant des chaînes magnétiques à la surface d'un liquide [29]. Dans cette section, nous présentons un nouveau type de cristaux rotatifs bidimensionnels, où les gouttes magnétiques s'auto-organisent dans un champ tournant.

Lorsqu'un champ magnétique tournant ($f = 15\ Hz$, $\mu_0 H_\infty = 6\ mT$) est appliqué, si les gouttes sont au-dessus d'un volume critique $V_{crit} \approx \pi(3.5\ \mu m)^3/6$, la goutte prend une forme aplatie oblate. Cette goutte aplatie tourne et aspire des gouttes plus petites dans son voisinage immédiat. Si la goutte est plus petite que V_{crit}, elle s'allonge jusqu'à prendre la forme d'une aiguille et tourne avec la vitesse angulaire du champ magnétique sans coalescer avec ses voisines, sauf si des collisions aléatoires se produisent. Ce comportement est représenté sur la figure 5.1. Il est intéressant de noter qu'en ajustant la mise au point du microscope, nous avons déterminé que les gouttes allongées tournent dans le même plan focal à une distance de $h = (9 \pm 1)\mu m$ au-dessus du fond de la cellule optique contenant l'échantillon qui a une épaisseur totale d'environ 130 μm. Et les gouttes aplaties tournent quelques μm plus bas que les aiguilles.

Après un certain temps sous champ tournant (quelques minutes), les petites gouttes allongées s'organisent en structures régulières - des cristaux rotatifs bidimensionnels (voir figure 5.2 (a)). Les gouttes forment un réseau d'ordre triangulaire qui tourne lui-même comme un corps rigide dans la direction du champ magnétique, mais plus lentement que celui-ci. On observe une certaine dérive des gouttes dans la couche la plus externe. Les gouttes individuelles à l'intérieur du cristal tournent toujours avec la vitesse angulaire du champ. On a observé que 2 gouttes tournent de manière stable autour d'un centre de

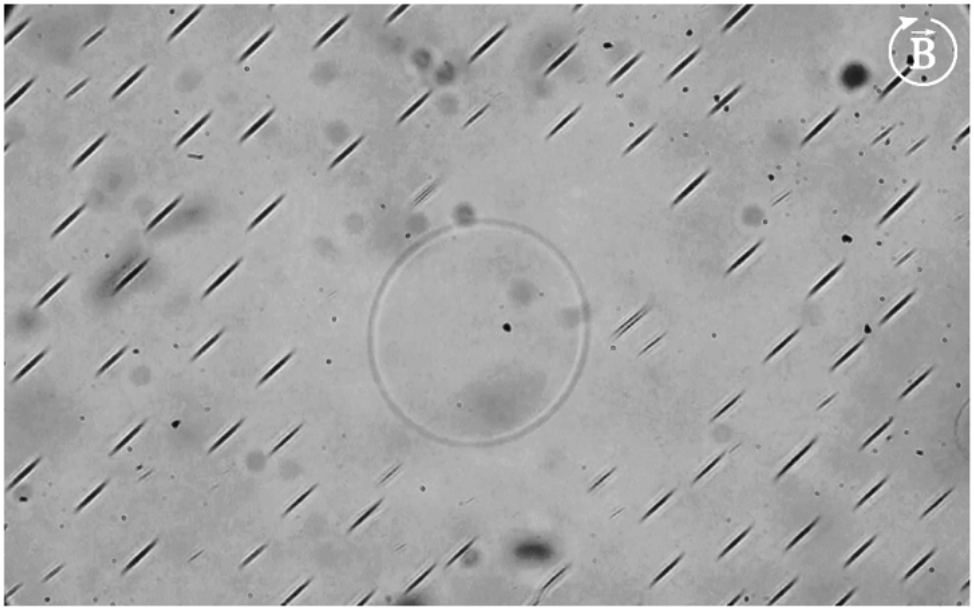

FIGURE 5.1 – Une vue des gouttes après l'activation d'un champ magnétique rotatif. Les petites gouttes prennent une forme allongée, tandis qu'une plus grande (légèrement hors champ) est ici quasi-oblate. Champ de vision = 400 $\mu m \times 250$ μm. Le champ magnétique ($f = 15$ Hz, $\mu_0 H_\infty = 6$ mT) tourne dans le plan d'observation. La figure est tirée de [30].

masse commun. 4 gouttes forment un quadrilatère dont les diagonales oscillent en longueur lorsque l'ensemble tourne (voir figure 5.2 (b)).

Si la densité des gouttes est importante, les gouttes forment des cristaux qui sont trop grands pour tourner de manière perceptible (voir figure 5.3.). Les gouttes forment une structure stationnaire très régulière même si le système n'est pas stationnaire et qu'il existe un flux entre les gouttes produit par leur rotation. On peut le constater en observant une goutte plus petite qui serpente entre les points du réseau. En utlisant la méthode de triangulation de Delaunay des centres des gouttes, il devient plus facile de visualiser la structure cristalline. Nous pouvons observer différents grains du cristal séparés par une frontière de dislocations.

Nous avons réussi à reproduire le mouvement des petits ensembles de gouttes en modélisant les gouttes comme des couples ponctuels au-dessus d'une paroi sans glissement. Par exemple, les oscillations diagonales de l'ensemble de quatre gouttes se manifestent dans les solutions de ce modèle (figure 5.4). Le modèle ne peut pas reproduire le mouvement de plus grands ensembles de gouttes (par exemple (a) dans la figure 5.2). Comme il n'y a rien qui impose la distance d'équilibre entre les gouttes, les grands ensembles de gouttes ne tournent pas comme des cristaux rigides, mais se désintègrent rapidement.

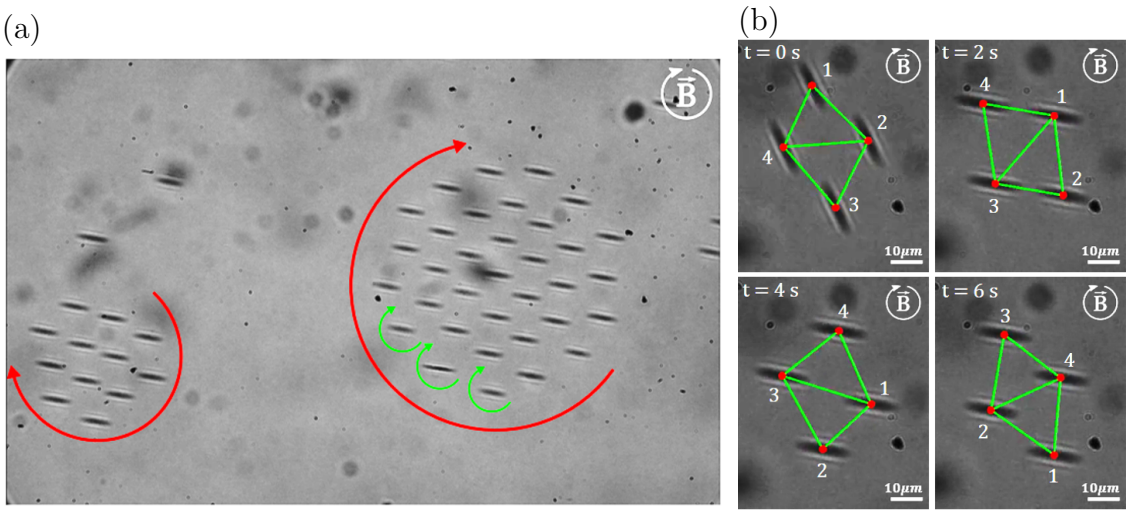

FIGURE 5.2 – Ensembles de gouttes magnétiques en rotation. Le champ magnétique ($f = 15\ Hz$, $\mu_0 H_\infty = 6\ mT$) tourne dans le plan d'observation. (a) Montre des cristaux de gouttes en forme d'aiguille en rotation. Champ de vision = 400 $\mu m \times 250\ \mu m$. (b) Montre comment quatre gouttes forment un quadrilatère rotatif dont la longueur des diagonales varie. Les gouttes sont étiquetées 1-4 et sont triangulées selon la méthode de Delaunay pour mieux illustrer leur mouvement. Les instantanés sont pris toutes les 2 secondes. La figure provient de [30].

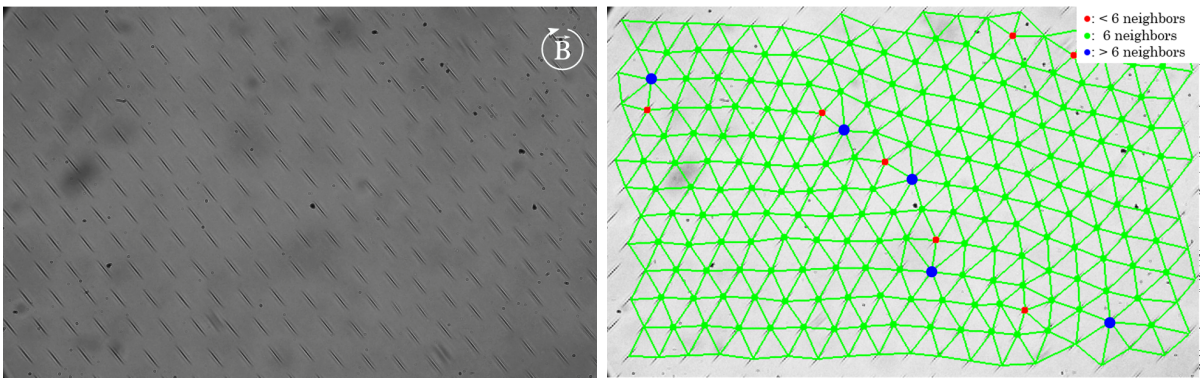

FIGURE 5.3 – Si les gouttes sont densément situées, elles s'organisent en un grand réseau triangulaire 2D. Chaque goutte tourne toujours dans la direction et à la fréquence du champ magnétique, mais le cristal entier est stationnaire. Sur le côté droit, les centres des gouttes sont triangulés selon la méthode de Delaunay pour illustrer la structure cristalline. Champ de vision = 400 $\mu m \times 250\ \mu m$. Champ magnétique ($f = 15\ Hz$, $\mu_0 H_\infty = 6\ mT$) et les gouttes sont en rotation dans le plan d'observation. La figure est tirée de [30].

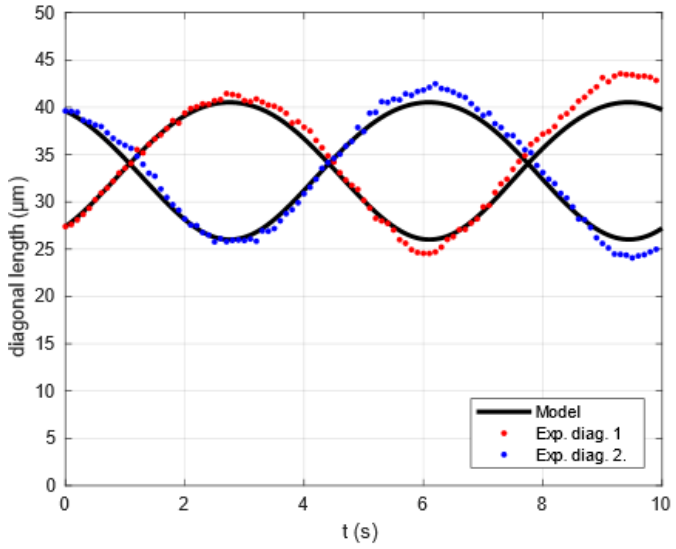

FIGURE 5.4 – Oscillations diagonales dans un ensemble de quatre gouttes. Les points bleus et rouges sont les valeurs expérimentales de (figure 5.2 (b)). Les lignes noires montrent la solution du modèle, où les paramètres d'entrée ont été ajustés dans les marges d'erreur pour produire un bon accord avec les oscillations expérimentales. La figure provient de [30].

6 Conclusions

Dans ce travail, nous avons étudié la dynamique de gouttes de fluide magnétique sous un champ tournant. Les gouttes flottent dans un milieu liquide externe, dont la viscosité est significativement plus petite que la viscosité des gouttes elles-mêmes. Nous avons d'abord étudié ces gouttes comme des objets déformants uniques et isolés, puis comme des ensembles auto-organisés d'objets à dynamique collective. Plusieurs approches complémentaires ont été utilisées pour décrire la dynamique des gouttes isolées. Pour le cas simple d'une goutte presque sphérique, nous avons produit des expressions analytiques faciles à analyser. Nous avons ensuite développé des simulations pour pouvoir calculer la dynamique de gouttes présentant des déformations plus importantes. Enfin, plusieurs gouttes magnétiques obtenues par séparation de phase ont été examinées expérimentalement pour voir dans quelle mesure le modèle du fluide magnétique utilisé dans les deux approches précédentes permet de décrire leur comportement dans un champ tournant. En ce qui concerne le comportement collectif de petites gouttes magnétiques dans un champ tournant, nous l'avons d'abord observé expérimentalement, puis un modèle simple a été proposé pour capturer leur dynamique.

Lorsque le champ magnétique, et donc la déformation d'une goutte individuelle, est faible, nous avons montré comment une équation phénoménologique pour le tenseur d'anisotropie qui décrit la forme de la goutte peut être utilisée pour calculer sa dynamique dans un champ en rotation ou en précession. En modélisant la goutte comme une région de fluide magnétique dans un liquide porteur non magnétique, nous pouvons utiliser la solution de Lamb pour les équations de Stokes en coordonnées sphériques pour calculer la dynamique des gouttes dans la limite des petites déformations. Nous avons montré que cette solution hydrodynamique coïncide avec la solution des équations phénoménologiques jusqu'au premier ordre en nombre de Bond magnétique Bm et amplitude de déformation ε. Dans cette limite, le mouvement de la goutte magnétique dans un champ tournant est régi par un seul paramètre adimensionnel $\tau\omega$ - le produit du temps de décroissance caractéristique des petites déformations et de la fréquence angulaire de rotation du champ. Le paramètre $\tau\omega$ détermine si la goutte sera plus allongée ou plus aplatie et si sa forme subira des oscillations lorsqu'elle atteindra l'équilibre. La goutte est en pseudo-rotation : elle semble suivre le champ magnétique tournant, mais ce mouvement est dû aux déformations de la surface et aucun couple n'est exercé par la goutte sur le fluide. Selon la théorie des petites déformations, la valeur du temps de décroissance des petites défor-

mations τ devrait être la même dans un champ tournant et dans un champ stationnaire ou nul. Expérimentalement, la valeur τ_{rel} décrivant l'approche exponentielle de la forme d'équilibre est supérieure de quelques ordres de grandeur à la valeur τ_{rot} obtenue à partir de la forme d'équilibre de la goutte dans un champ tournant. Par conséquent, le modèle de fluide magnétique qui ne prend en compte que la force normale de surface due au tenseur de contraintes de Maxwell doit être amélioré pour pouvoir décrire quantitativement le mouvement des gouttes magnétiques dans un champ tournant.

Nous avons pu modéliser une goutte sans la limitation des petites déformations de notre description analytique, en utilisant une simulation basée sur la méthode des éléments de frontière (BEM). Nous pouvons utiliser la simulation BEM pour calculer la dynamique tridimensionnelle d'une goutte dans des champs magnétiques et d'écoulement externes jusqu'à des déformations modérées de la goutte. Un maintien important du maillage est nécessaire pour simuler avec précision la dynamique des gouttes. Les simulations BEM ont montré que dans un champ magnétique tournant, les gouttes prennent une forme triaxiale qui peut légèrement dévier d'un ellipsoïde. Par exemple, les extrémités d'une goutte allongée se courbent en raison de la friction visqueuse, ce qui est observé expérimentalement. Nous constatons que pour un grand Bm et une petite fréquence de rotation du champ magnétique ω, les gouttes s'allongent et tournent comme des corps rigides suivant le champ magnétique tournant. Cependant, une grande fréquence de rotation du champ magnétique ω supprime l'élongation des gouttes, et leur forme est proche de celle d'un ellipsoïde oblate. Dans ce régime, les gouttes sont en pseudo-rotation : elles suivent le champ magnétique tournant en raison des déformations de surface. Les simulations permettent de retrouver d'autres observations importantes, par exemple, dans un champ en rotation rapide avec une intensité de champ supérieure à l'instabilité de la forme oblate-prolate [9, 11], une goutte initialement sphérique s'aplatit d'abord avant de s'allonger. Enfin, à l'aide des simulations BEM, il a été possible de déterminer les limites d'applicabilité de la théorie des petites déformations.

Pour les ensembles de gouttes, nous avons observé pour la première fois des structures hors équilibre, ordonnées et rotatives, de gouttes magnétiques dans un champ tournant. Pour certains paramètres de champ, les gouttes allongées en forme d'aiguille forment des cristaux rotatifs bidimensionnels d'ordre triangulaire. Les gouttes dans les cristaux tournent avec la fréquence du champ magnétique, mais les cristaux eux-mêmes tournent plus lentement. La fréquence de rotation du cristal diminue avec sa taille, et les très grands cristaux semblent être stationnaires dans l'expérience. Les ensembles de gouttes présentent

les caractéristiques typiques d'un cristal bidimensionnel, comme différents grains reliés par une frontière de dislocations. Dans le cristal, les gouttes s'organisent toutes dans un seul plan tournant à environ 9 μm au-dessus du fond de la cellule expérimentale. Le modèle qui traite les gouttes comme des couples ponctuels au-dessus d'une paroi sans glissement est capable de reproduire quantitativement le mouvement de petits ensembles de gouttes. Cependant, le modèle cesse d'être précis lorsque la taille des ensembles augmente. Puisque dans le modèle il n'y a pas de forces qui déterminent la distance d'équilibre entre les gouttes, de grands ensembles de gouttes ne peuvent pas former de cristaux rotatifs, ils se désintègrent.

En résumé, nous pouvons conclure ce qui suit. Le modèle du fluide magnétique est capable de décrire qualitativement le mouvement dans un champ tournant de gouttes individuelles de fluide magnétique, obtenues par séparation de phases. Les simulations BEM peuvent être utilisées pour étudier efficacement la dynamique des formes complexes adoptées par ces gouttes en présence d'un champ tournant. Dans certaines situations, une auto-organisation collective de gouttes de liquide magnétique peut se produire en présence d'un champ tournant. On observe alors des structures intriquées hors-équilibre, qui ne sont pas encore entièrement comprises.

Références

[1] R. E. Rosensweig, *Ferrohydrodynamics*. Mineola, New York : Dover Publications, fév. 2014.

[2] J.-C. Bacri, R. Perzynski, V. Cabuil et R. Massart, "Phase diagram of an ionic magnetic colloid : Experimental study of the effect of ionic strength," *Journal of Colloid and Interface Science*, t. 132, n° 1, p. 43-53, oct. 1989. doi : 10.1016/0021-9797(89)90214-2.

[3] J.-C. Bacri et D. Salin, "Instability of ferrofluid magnetic drops under magnetic field," *Journal de Physique Lettres*, t. 43, n° 17, p. 649-654, 1982. doi : 10.1051/jphyslet:019820043017064900.

[4] A. O. Tsebers, "Virial method of investigation of statics and dynamics of drops of magnetizable liquids," *Magnetohydrodynamics*, t. 21, p. 19-26, 1985.

[5] S. Afkhami et al., "Deformation of a hydrophobic ferrofluid droplet suspended in a viscous medium under uniform magnetic fields," *Journal of Fluid Mechanics*, t. 663, p. 358-384, nov. 2010. doi : 10.1017/S0022112010003551.

[6] J.-C. Bacri et D. Salin, "Dynamics of the shape transition of a magnetic ferrofluid drop," *Journal de Physique Lettres*, t. 44, n° 11, p. 415-420, 1983. doi : 10.1051/jphyslet:019830044011041500.

[7] A. Langins, A. P. Stikuts et A. Cēbers, "A three-dimensional boundary element method algorithm for simulations of magnetic fluid droplet dynamics," *Physics of Fluids*, t. 34, n° 6, p. 062 105, juin 2022. doi : 10.1063/5.0092532.

[8] O. Sandre, J. Browaeys, R. Perzynski, J.-C. Bacri, V. Cabuil et R. E. Rosensweig, "Assembly of microscopic highly magnetic droplets : Magnetic alignment versus viscous drag," *Physical Review E*, t. 59, n° 2, p. 1736-1746, fév. 1999. doi : 10.1103/PhysRevE.59.1736.

[9] J.-C. Bacri, A. O. Cebers et R. Perzynski, "Behavior of a magnetic fluid microdrop in a rotating magnetic field," *Physical Review Letters*, t. 72, n° 17, p. 2705-2708, avr. 1994. doi : 10.1103/PhysRevLett.72.2705.

[10] K. I. Morozov et A. V. Lebedev, "Bifurcations of the shape of a magnetic fluid droplet in a rotating magnetic field," *Journal of Experimental and Theoretical Physics*, t. 91, n° 5, p. 1029-1032, nov. 2000. doi : 10.1134/1.1334993.

[11] J. Erdmanis, G. Kitenbergs, R. Perzynski et A. Cēbers, "Magnetic microdroplet in rotating field : numerical simulation and comparison with experiment," *Journal of Fluid Mechanics*, t. 821, p. 266-295, juin 2017. doi : 10.1017/jfm.2017.238.

[12] E. Janiaud, F. Elias, J.-C. Bacri, V. Cabuil et R. Perzynski, "Spinning ferrofluid microscopic droplets," *Magnetohydrodynamics*, t. 36, n° 4, p. 365-378, 2000.

[13] R. Massart, E. Dubois, V. Cabuil et E. Hasmonay, "Preparation and properties of monodisperse magnetic fluids," *Journal of Magnetism and Magnetic Materials*, t. 149, n° 1-2, p. 1-5, août 1995. doi : 10.1016/0304-8853(95)00316-9.

[14] G. K. Batchelor, *An introduction to fluid dynamics*, 1. Cambridge mathematical ed., 14. print, sér. Cambridge mathematical library. Cambridge : Cambridge Univ. Press, 2010, OCLC : 838184093.

[15] E. Blūms, A. Cēbers et M. M. Maiorov, *Magnetic fluids*. Berlin ; New York : Walter de Gruyter, 1997.

[16] J. A. Stratton, *Electromagnetic Theory*. New York et London : Mcgraw Hill Book Company, 1941.

[17] A. Esmaeeli et P. Sharifi, "Transient electrohydrodynamics of a liquid drop," *Physical Review E*, t. 84, n° 3, p. 036 308, sept. 2011. doi : 10.1103/PhysRevE.84.036308.

[18] J. M. Rallison, "The Deformation of Small Viscous Drops and Bubbles in Shear Flows," *Annual Review of Fluid Mechanics*, t. 16, n° 1, p. 45-66, jan. 1984. doi : 10.1146/annurev.fl.16.010184.000401.

[19] M. Minale, "Models for the deformation of a single ellipsoidal drop : a review," *Rheologica Acta*, t. 49, n° 8, p. 789-806, août 2010. doi : 10.1007/s00397-010-0442-0.

[20] Y. I. Dikanskii, A. O. Tsebers et V. P. Shatskii, "Magnetic emulsion properties in electric and magnetic fields. 1. Statics.," *Magnetohydrodynamics*, t. 26, p. 25-30, 1990.

[21] A. P. Stikuts, R. Perzynski et A. Cēbers, "Small deformation theory for a magnetic droplet in a rotating field," *Physics of Fluids*, t. 34, n° 5, p. 052 010, mai 2022. doi : 10.1063/5.0091453.

[22] H. A. Stone, "Dynamics of Drop Deformation and Breakup in Viscous Fluids," *Annual Review of Fluid Mechanics*, t. 26, n° 1, p. 65-102, jan. 1994. doi : 10.1146/annurev.fl.26.010194.000433.

[23] C. Pozrikidis, *Boundary Integral and Singularity Methods for Linearized Viscous Flow*. Cambridge : Cambridge University Press, 1992. doi : 10.1017/CBO9780511624124.

[24] A. Z. Zinchenko et R. H. Davis, "Motion of Deformable Drops Through Porous Media," *Annual Review of Fluid Mechanics*, t. 49, n° 1, p. 71-90, jan. 2017. doi : 10.1146/annurev-fluid-010816-060331.

[25] L. H. P. Cunha, I. R. Siqueira, T. F. Oliveira et H. D. Ceniceros, "Field-induced control of ferrofluid emulsion rheology and droplet break-up in shear flows," *Physics of Fluids*, t. 30, n° 12, p. 122 110, déc. 2018. doi : 10.1063/1.5055943.

[26] B. A. Grzybowski, H. A. Stone et G. M. Whitesides, "Dynamic self-assembly of magnetized, millimetre-sized objects rotating at a liquid–air interface," *Nature*, t. 405, n° 6790, p. 1033-1036, juin 2000. DOI : 10.1038/35016528.

[27] B. A. Grzybowski, X. Jiang, H. A. Stone et G. M. Whitesides, "Dynamic, self-assembled aggregates of magnetized, millimeter-sized objects rotating at the liquid-air interface : Macroscopic, two-dimensional classical artificial atoms and molecules," *Physical Review E*, t. 64, n° 1, p. 011 603, juin 2001. DOI : 10.1103/PhysRevE.64.011603.

[28] J. Yan, S. C. Bae et S. Granick, "Rotating Crystals of Magnetic Janus Colloids," *Soft Matter*, p. 9, 2014.

[29] Q. Wang, L. Yang, B. Wang, E. Yu, J. Yu et L. Zhang, "Collective Behavior of Reconfigurable Magnetic Droplets via Dynamic Self-Assembly," *ACS Applied Materials & Interfaces*, t. 11, n° 1, p. 1630-1637, jan. 2019. DOI : 10.1021/acsami.8b17402.

[30] A. Stikuts, R. Perzynski et A. Cēbers, "Spontaneous order in ensembles of rotating magnetic droplets," *Journal of Magnetism and Magnetic Materials*, t. 500, p. 166 304, avr. 2020. DOI : 10.1016/j.jmmm.2019.166304.

Kopsavilkums latviešu valodā

1 Ievads

Magnētiskie šķidrumi ir stabili koloīdi, ko veido cietu magnētisku nanodaļiņu dispersija nesējšķidrumā. Nelielais nanodaļiņu izmērs ($d \approx 10\ nm$) nodrošina, ka katrai daļiņai ir viens magnētiskais domēns. Magnētiskajam šķidrumam piemīt superparamagnētiskas īpašības. Tas stipri magnetizējas, kad nanodaļiņu magnētiskie momenti nostājās vienā virzienā ar uzlikto ārējo magnētisko lauku. Taču, kad lauks tiek noņemts, termiskās svārstības izjauc nanodaļiņu magnētisko momentu orientāciju, un magnētiskā šķidruma magnetizācija atgriežas nulles līmenī [1].

Magnētiskos pilienus ir iespējams izveidot, emulģējot magnētisko šķidrumu citā šķidrumā, kas ar to nesajaucas. Magnētiskos pilienus ir iespējams iegūt arī, izraisot fāžu atdalīšanos magnētiskajā šķidrumā [2]. Otrā metode rada pilienus ar neparasti augstu magnētisko caurlaidību ($\mu/\mu_0 \approx 40$) un mazu virsmas spraiguma koeficientu ($\gamma \approx 10^{-6} N/m$), kas ļauj novērot interesantas parādības jau pie vāja magnētiskā lauka. Magnētiskos pilienus var ietekmēt ar magnētisko lauku. Tie pagarinās pieliktā magnētiskā lauka virzienā, līdz magnētiskos spēkus līdzsvaro virsmas spraiguma spēki (attēls 1.1).

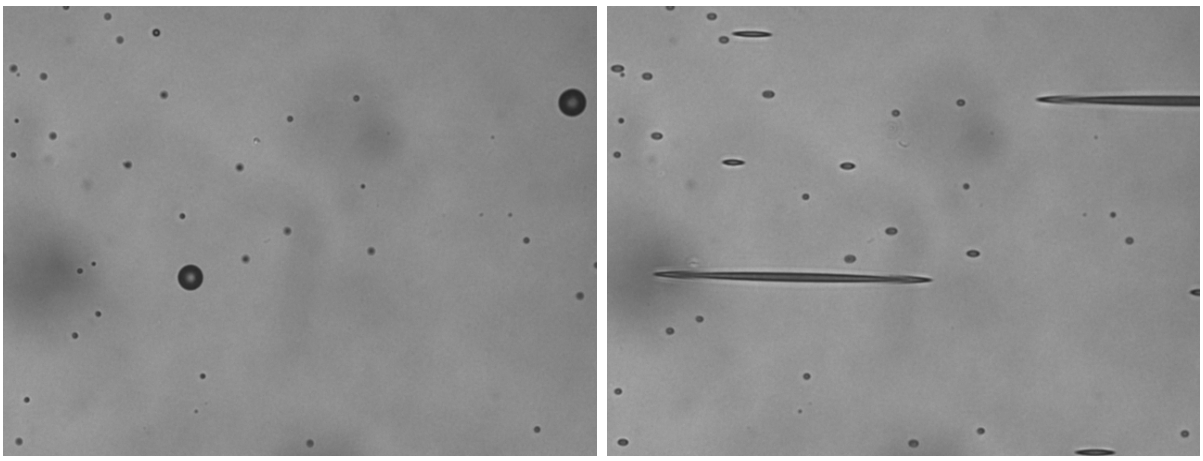

Att. 1.1: Fāžu atdalīšanas rezultātā radušies pilieni. Koncentrētā fāze veido magnētiskus pilienus, kas redzami kā tumšāki dažāda diametra apļi, kurus ieskauj atšķaidītā fāze (pa kreisi). Pilieni izstiepjas pieliktā lauka virzienā (pa labi). Redzes lauks ir $132\mu m \times 100\mu m$.

Magnētiskā piliena uzvedība konstantā nekustīgā laukā ir diezgan labi izpētīta. Līdzsvara izstiepumu var aprēķināt analītiski, pieņemot, ka piliens ieņem sferoidālu formu [3, 4, 5]. Sferoidālo tuvinājumu var izmantot, lai aprēķinātu pilienu izstiepšanās dinamiku [6, 7]. Lineāras magnetizācijas gadījumā līdzsvara izstiepumu apraksta vienādojums [3,

4].

$$\frac{\mu_0 H_\infty^2 R_0}{2\gamma} = \left(\frac{1}{\frac{\mu}{\mu_0} - 1} + N_d\right)^2 \frac{\left(3 - 2e^2 - \frac{(3-4e^2)\arcsin e}{e(1-e^2)^{1/2}}\right)}{(1-e^2)^{2/3}\left(-\frac{6}{e^2} + \frac{3-e^2}{e^3}\ln\frac{1+e}{1-e}\right)}, \tag{1.1}$$

kur μ_0 ir vakuuma magnētiskā caurlaidība, H_∞ ir pieliktā magnētiskā lauka intensitāte, R_0 ir nedeformēta piliena rādiuss, γ ir virsmas spraiguma koeficients, μ ir piliena magnētiskā caurlaidība, e ir piliena ekscentricitāte un

$$N_d = \frac{1-e^2}{2e^3}\left(-2e + \ln\frac{1+e}{1-e}\right), \tag{1.2}$$

ir demagnetizācijas koeficients. Vienādojumu (1.1) var izmantot, lai noteiktu piliena fizikālos parametrus, piemēram, tā magnētisko caurlaidību un virsmas spraiguma koeficientu.

Rotējošā laukā magnētisko pilienu uzvedība kļūst sarežģītāka. Ja rotācijas frekvence ir lēna, pilieni izstiepjas un lēni rotē, sekojot laukam. Viskozās berzes dēļ pilieni var saplīst [8]. Ja lauka rotācijas frekvence ir liela, pilienam var rasties virkne formas nestabilitāšu. Vispirms, kad lauks ir vājš, piliens ieņem saplacināta sferoīda formu - saplacināta rotējošā lauka plaknē. Tad, palielinot lauka stiprumu virs kādas kritiskās vērtības, pilienam notiek spontāna simetrijas laušana un tas izstiepjas rotējošā lauka plaknē. Visbeidzot, palielinot lauka intensitāti vēl vairāk, virs citas kritiskās vērtības, piliens atkal iegūst rotējošā lauka plaknē stipri saplacināta sferoīda formu, un ap tā perimetru parādās pirkstu vainags [9]. Aproksimējot pilienu kā sferoīdu, šī saplacinātās-iztieptās-saplacinātās formas pāreja tika aprakstīta teorētiski [9]. Vēlāk apraksts tika vispārināts trīsasu elipsoīda gadījumam [10]. Nesen līdzsvara formas bezgalīgi ātri rotējošā laukā tika iegūtas skaitliski ar robeželementu metodi [11]. Skaitliskās simulacijas darba autori [11] pieņēma, ka piliena un apkārtējās vides viskozitātes ir vienādas, kas ievērojami vienkāršo aprēķinus, bet neļauj aprēķināt piliena dinamiku. Pašlaik magnētisko pilienu dinamika rotējošos laukos joprojām ir lielā mērā neizpētīta, taču eksperimentāli ir novērots, ka atkarībā no rotējošā lauka stipruma un frekvences ir sagaidāmas interesantas nestacionāras piliena formas [12].

Tas motivē izvirzīt šādu darba mērķi: **Izpētīt magnētisko pilienu no laika atkarīgo dinamiku rotējošā magnētiskajā laukā.** Mērķis tiek sasniegts, veicot šādus uzdevumus:

1. Izmantojot magnētiskā šķidruma modeli, izstrādāt atsevišķa piliena dinamikas analītisku aprakstu vienkāršos gadījumos, piemēram, vājā laukā un mazu deformāciju gadījumā, ņemot vērā atšķirīgu viskozitāti piliena iekšpusē un ārpusē.

2. Izmantojot magnētiskā šķidruma modeli, izstrādāt simulācijas programmatūru, lai aprēķinātu piliena dinamiku situācijās, kad analītiskais apraksts vairs nav spēkā.

3. Izmantojot simulācijas programmatūru, raksturot magnētisko pilienu uzvedību rotējošā laukā.

4. Veikt eksperimentālus mērījumus mikroskopiskiem magnētiskiem pilieniem, kas iegūti, sadalot fāzēs magnētisko šķidrumu, un novērtēt, cik labi magnētiskā šķidruma modelis apraksta to dinamiku.

5. Eksperimentāli novērot pilienu ansambļu dinamiku.

6. Izstrādāt modeļus, kas apraksta pilienu ansambļu dinamiku.

Šis kopsavilkums ir sadalīts vairākās nodaļās. Nodaļā 2 ir aprakstīts magnētiskā šķidruma modelis, kas tiek izmantots pilienu teorētiskajā aprakstā. Nodaļā 3 parādīts modeļa analītiskais risinājums mazu deformāciju un vāja lauka robežā. Tajā pašā nodaļā ir arī parādīts salīdzinājums ar eksperimentu. Nodaļā 4 aprakstīta simulācija (balstīta uz robeželementu metodi), kas tika izmantota, lai aprēķinātu magnētisko pilienu dinamiku lielāku deformāciju gadījumā. Nodaļā 5 aplūkots eksperimentāls pilienu ansambļu novērojums rotējošā laukā un to modelēšana, izmantojot vienkāršus tuvinājumus. Visbeidzot nodaļā 6 ir apkopoti šī darba galvenie rezultāti un veikti secinājumi.

2 Modeļa formulēšana

Fāžatdalītie magnētiskie pilieni ir samērā unikāls materiāls, kura īpašības nav pietiekami izprastas. Magnētisko nanodaļiņu koncentrācija pilienu iekšpusē ir ļoti liela (to tilpuma daļa ir aptuveni $\phi_{drop} \approx 30\%$ [13]). Tas varētu nozīmēt, ka pilienu iekšienē iespējams veidojas nanodaļiņu ķēdītes un aglomerāti, kas var ietekmēt to magnētiskās un reoloģiskās īpašības. Turklāt fāžatdalītie pilieni atrodas termodinamiskajā līdzsvarā - magnētiskās nanodaļiņas nepārtraukti ieiet un pamet piliena tilpumu. Šī nanodaļiņu kustība notiek caur piliena virsmas laukumu, kas eksperimentos var mainīties izmērā par vairākām lieluma kārtām. Apkopojot redzams, ka fāžatdalīto magnētisko pilienu pilnīgs apraksts ir sarežģīts, tomēr mēs cenšamies atrast relatīvi vienkāršu modeli, kas reproducē novēroto pilienu uzvedību rotējošā laukā. Mēs aplūkosim vienkāršu magnētiskā šķidruma modeli [1], kas iepriekš labi darbojās, lai aprēķinātu pilienu līdzsvara formas bezgalīgi ātri rotējošā magnētiskajā laukā [11].

Mēs aplūkojam magnētiska šķidruma pilienu, kas suspendēts bezgalīgā nemagnētiskā nesējšķidrumā (attēls 2.1). Magnētiskajam pilienam (iekšējais apgabals, kura īpašības apzīmēsim ar indeksu (i)) ir magnētiskā caurlaidība μ un viskozitāte $\eta^{(i)}$. Apkārtējam šķidrumam (ārējais apgabals, kura īpašības apzīmē ar indeksu (e)) magnētiskā caurlaidība ir vienāda ar vakuuma magnētisko caurlaidību μ_0, un viskozitāte ir $\eta^{(e)}$. Starp abiem apgabaliem pastāv virsmas spraigums, ko raksturo virsmas spraiguma koeficients γ. Tiek pielikts ārējs rotējošs magnētiskais lauks $\boldsymbol{H}_\infty$. Lauka leņķiskais ātrums ir $\boldsymbol{\omega}$. Mēs pieņemam lineāru magnetizāciju $\boldsymbol{M} = \chi \boldsymbol{H}$, kur $\chi = \mu/\mu_0 - 1$ ir magnētiskā uzņēmība. Magnētiskā lauka indukcija tādā gadījumā ir $\boldsymbol{B} = \mu_0(\boldsymbol{H} + \boldsymbol{M}) = \mu \boldsymbol{H}$.

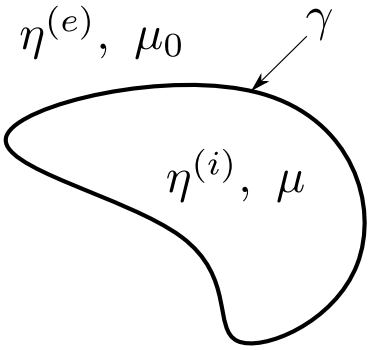

Att. 2.1: Zīmējums ar magnētisko pilienu, kura viskozitāte ir $\eta^{(i)}$ un magnētiskā caurlaidība ir μ. Tas ir suspendēts bezgalīgā nesējšķidrumā ar viskozitāti $\eta^{(e)}$ un magnētisko caurlaidību μ_0. Uz pilienu iedarbojas virsmas spraigums ar virsmas spraiguma koeficientu γ.

Plūsmu nosaka Stoksa vienādojums [14] kopā ar magnētiskā spēka locekli [15] un nesaspiežamības nosacījumu

$$-\boldsymbol{\nabla} p + \eta \Delta \boldsymbol{v} + \boldsymbol{f} = \boldsymbol{0}, \quad \boldsymbol{\nabla} \cdot \boldsymbol{v} = 0, \tag{2.1}$$

kur p ir spiediens un $\boldsymbol{v}$ ir šķidruma ātrums, $f_i = \partial_j T_{ij} = \mu_0 M_j \partial_j H_i$ ir magnētiskais spēks uz tilpuma vienību un $T_{ij} = -\mu_0 H^2 \delta_{ij}/2 + H_i B_j$ ir Maksvela sprieguma tenzors. Plūsmas robežnosacījumi ir šādi. Ātrums uz piliena virsmas ir nepārtraukts

$$\boldsymbol{v}^{(i)} - \boldsymbol{v}^{(e)} = \boldsymbol{0}. \tag{2.2}$$

Visu spēku summa uz piliena virsmas normāles virzienā ir vienāda ar nulli.

$$\boldsymbol{n} \cdot (\boldsymbol{\sigma}^{(e)} - \boldsymbol{\sigma}^{(i)}) \cdot \boldsymbol{n} + \frac{\mu_0}{2} {M_n^{(i)}}^2 - \gamma(k_1 + k_2) = 0, \tag{2.3}$$

un arī tangenciālā virzienā tā ir nulle

$$\boldsymbol{t} \cdot (\boldsymbol{\sigma}^{(e)} - \boldsymbol{\sigma}^{(i)}) \cdot \boldsymbol{n} = 0, \tag{2.4}$$

kur $\boldsymbol{n}$ ir piliena ārējais normāles vektors, $\boldsymbol{t}$ ir tangenciāls vektors, $M_n^{(i)}$ ir normālā magnetizācijas komponente piliena iekšpusē, $(k_1 + k_2)$ ir galveno liekumu summa un $\sigma_{ij} = -p\delta_{ij} + \eta(\partial_j v_i + \partial_i v_j)$ ir hidrodinamiskais sprieguma tenzors. Tālu no piliena mēs pieprasām, lai spiediens un ātrums pieņemtu uzliktās fona plūsmas vērtības p_∞ un $\boldsymbol{v}_\infty$ (parasti iestatītas uz nulli)

$$p^{(e)}|_{r\to\infty} = p_\infty, \quad \boldsymbol{v}^{(e)}|_{r\to\infty} = \boldsymbol{v}_\infty. \tag{2.5}$$

Magnētiskos spēkus aprēķina, vispirms atrodot magnētisko lauku, izmantojot magnetostatikas vienādojumus [16]

$$\boldsymbol{\nabla} \times \boldsymbol{H} = \boldsymbol{0}, \quad \boldsymbol{\nabla} \cdot \boldsymbol{B} = 0. \tag{2.6}$$

Tie ir apmierināti, ja magnētiskais potenciāls $\boldsymbol{H} = \boldsymbol{\nabla}\psi$ apmierina Laplasa vienādojumu

$$\Delta\psi = 0. \tag{2.7}$$

Robežnosacījumi uz piliena virsmas ir

$$\mu_0 \boldsymbol{n} \cdot \boldsymbol{\nabla}\psi^{(e)} - \mu \boldsymbol{n} \cdot \boldsymbol{\nabla}\psi^{(i)} = 0 \tag{2.8}$$

un

$$\psi^{(e)} - \psi^{(i)} = 0. \tag{2.9}$$

Tālu no piliena mēs pieprasām, lai lauks būtu vienāds ar uzlikto lauku $\boldsymbol{H}_\infty$

$$\boldsymbol{\nabla}\psi^{(e)}|_{r\to\infty} = \boldsymbol{H}_\infty. \tag{2.10}$$

Problēmas atrisinājumā parādās trīs bezdimensionāli parametri

- $\lambda = \frac{\eta^{(i)}}{\eta^{(e)}}$, viskozitāšu attiecība,
- $\mu_r = \frac{\mu}{\mu_0}$, relatīvā magnētiskā caurlaidība,
- $Bm = 4\pi\mu_0 \frac{R_0 H_\infty^2}{\gamma}$, magnētiskais Bonda skaitlis. Tas ir proporcionāls attiecībai starp

raksturīgu magnētisko un virsmas spraiguma spēku. R_0 ir sfēriska piliena rādiuss.

3 Mazo deformāciju dinamika

Magnētisko pilienu dinamikas analītiski atrisinājumi ir iespējami tikai visvienkāršākajos gadījumos. Viens no šādiem gadījumiem ir tuvinājums, kad piliens ir teju sfērisks. Analītiski ir pētīta pilienu mazo deformāciju dinamika homogēnā stacionārā laukā (elektriskā vai magnētiskā), kur tika parādīts, ka piliens eksponenciāli tuvojas elipsoidālai līdzsvara formai [17]. Plaši teorētiski pētīta ir arī nemagnētisku viskozu pilienu dinamika ārējās plūsmās mazu deformāciju tuvinājumā [18]. Lai aprēķinātu elipsoidālu pilienu uzvedību ārējās plūsmās, bieži mēdz izmantot fenomenoloģiskus modeļus, kas apraksta piliena anizotropijas tenzora attīstību laikā [19]. Šādu modeļu fenomenoloģiskais raksturs ļauj tos modificēt, lai iekļautu dažādas papildu parādības, piemēram, magnētisko mijiedarbību. Tomēr fenomenoloģiskie modeļi ir jāpārbauda, salīdzinot tos ar fundamentālāku teoriju, simulācijām vai eksperimentiem.

Ja magnētiskie spēki ir daudz vājāki par kapilārajiem spēkiem ($Bm \ll 1$), pilienu var aprakstīt kā elipsoīdu ar pusasīm $a \geq b \geq c$. Alternatīvi var izmantot divus nenegatīvus deformācijas parametrus, lai aprakstītu piliena formu: izstiepumu

$$\epsilon_1 = \frac{a-b}{b} \tag{3.1}$$

un plakanumu

$$\epsilon_2 = \frac{b-c}{b}, \tag{3.2}$$

ko kopā ar nesaspiežamības nosacījumu $abc = R_0^3$ var izmantot, lai atgūtu pusasu vērtības. Ja kustība notiek rotējošā magnētiskā lauka plaknē, īsākā ass c ir vērsta magnētiskā lauka leņķiskā ātruma virzienā, un piliena orientāciju nosaka viens leņķis β, ko tā garākā ass veido ar magnētisko lauku (attēls 3.1). β ir izvēlēts pozitīvs, ja piliena lielākā ass ir lauka priekšgalā, un negatīvs, ja tā ir lauka aizmugurē.

Atrisinot fenomenoloģisku vienādojumu [20, 21], tiek iegūta vienādojumu sistēma pi-

izstiepums: $\epsilon_1 = \frac{a-b}{b}$

plakanums: $\epsilon_2 = \frac{b-c}{b}$

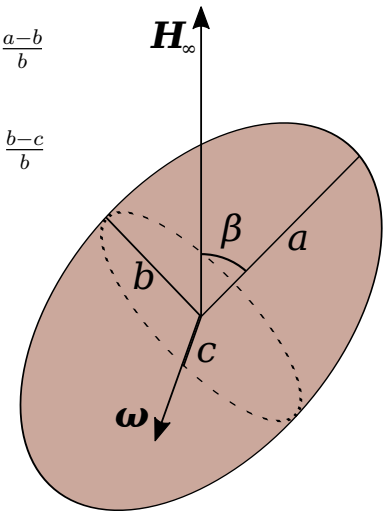

Att. 3.1: Parametri, kas raksturo piliena formu rotējošā magnētiskajā laukā. β ir negatīvs, ja piliena lielākā ass atpaliek no rotējošā magnētiskā lauka $\boldsymbol{H}_\infty$. Lauks rotē $\boldsymbol{\omega}$ virzienā.

liena deformācijas parametriem

$$\begin{cases} \dfrac{d\epsilon_1}{dt} = -\dfrac{1}{\tau}\left(\epsilon_1 - \delta\cos(2\beta)\right) \\ \dfrac{d\epsilon_2}{dt} = -\dfrac{1}{\tau}\left(\epsilon_2 - \delta\sin^2(\beta)\right) \\ \dfrac{d\beta}{dt} = -\omega - \dfrac{\delta\cos(\beta)\sin(\beta)}{\tau\epsilon_1} \end{cases}, \tag{3.3}$$

kur τ un δ ir fenomenoloģiskas konstantes. Asimptotiski atrisinot pilno hidrodinamisko problēmu, kas formulēta sadaļā 2, maziem Bm un maziem ϵ_1 un ϵ_2, mēs iegūstam to pašu vienādojumu sistēmu (3.3), tādējādi apstiprinot fenomenoloģisko vienādojumu. Turklāt mēs iegūstam, ka fenomenoloģiskās konstantes ir

$$\delta = \frac{9Bm}{32\pi}\frac{(\mu_r - 1)^2}{(\mu_r + 2)^2}, \tag{3.4}$$

un

$$\tau = \frac{R_0\eta^{(e)}}{\gamma}\frac{(3+2\lambda)(16+19\lambda)}{40(1+\lambda)}. \tag{3.5}$$

Apskatot vienādojumu sistēmu (3.3), mēs redzam, ka tās stacionārie punkti ir

$$\begin{cases} \epsilon_1^* = \dfrac{\delta}{\sqrt{1+4\tau^2\omega^2}} \\ \epsilon_2^* = \dfrac{\delta}{2}\left(1 - \dfrac{1}{\sqrt{1+4\tau^2\omega^2}}\right) \\ \beta^* = -\dfrac{1}{2}\arctan(2\tau\omega) + n\pi \end{cases}, \tag{3.6}$$

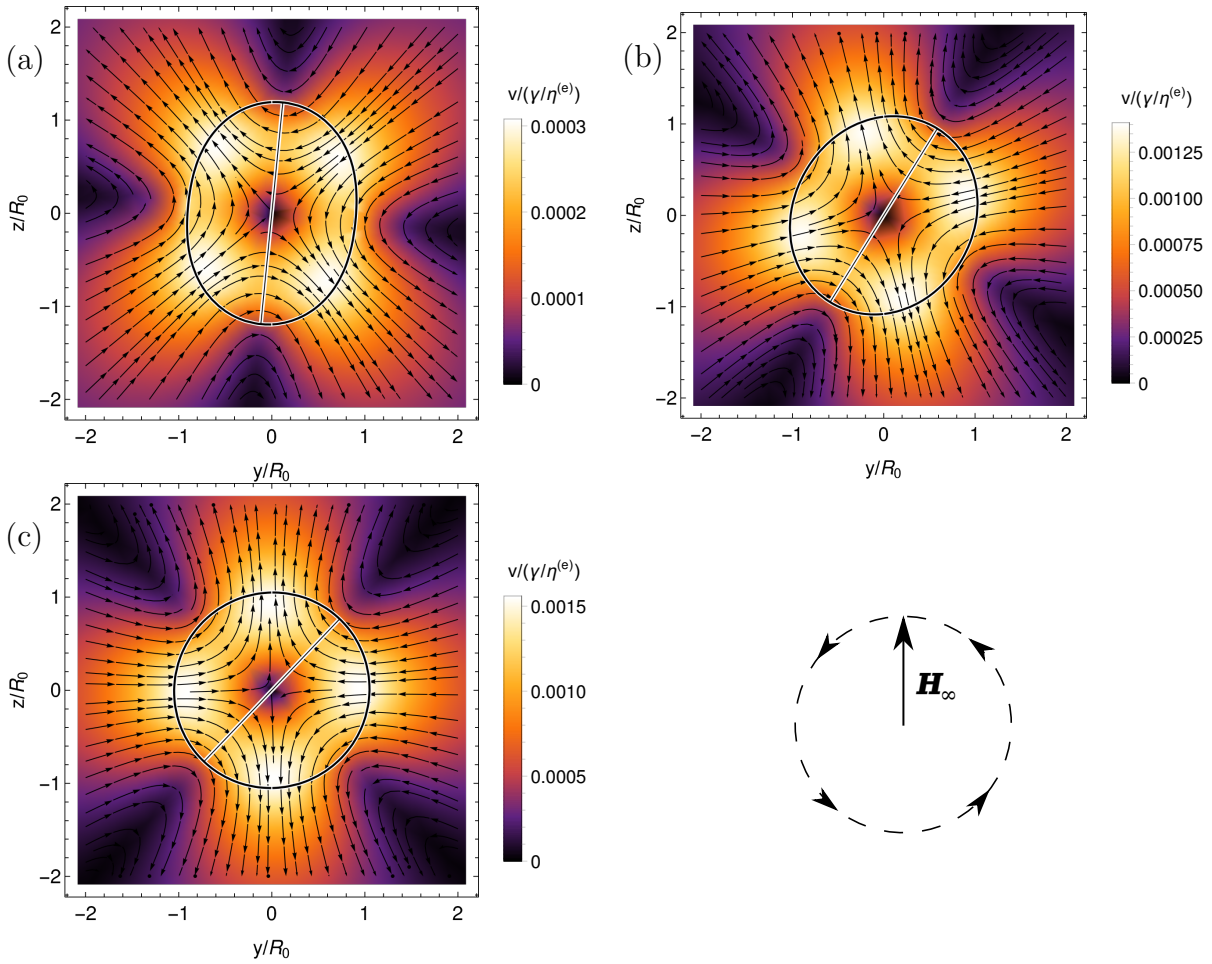

Att. 3.2: Ātruma lauka plūsmas līnijas ap pilieniem, kas ir sasnieguši līdzsvara formu rotējošā magnētiskajā laukā ar dažādām frekvencēm (a) $\tau\omega = 0,1$, (b) $\tau\omega = 1$ un (c) $\tau\omega = 10$. Lauks ir tāds, ka $\delta = 0,3$. Parādīts šķērsgriezums pie $x = 0$. Ir iezīmētas pilienu formas, to garākās asis un ar krāsām attēlots ātruma lielums, kas mērogots ar $\gamma/\eta^{(e)}$. Attēls ir uzzīmēts laboratorijas atskaites sistēmā, kur magnētiskais lauks griežas pretēji pulksteņrādītāja virzienam un momentāni ir vērsts z ass virzienā. Ātruma lauks ir tāds, ka piliens deformējas tā, lai tā garākā ass sekotu laukam.

kur n ir vesels skaitlis. Tie ir stabili fokusi visiem problēmas parametriem. Līdz mērogošanai piliena uzvedību mazu deformāciju tuvinājumā nosaka viens vienīgs parametrs $\tau\omega$. Parametrs $\tau\omega$ ir proporcionāls kapilārajam skaitlim, kas ir viskozo spēku attiecība pret virsmas spraiguma spēkiem [22]. Mazo deformāciju režīmā pilieni pseidorotē - to garākā ass seko laukam, imitējot rotāciju, tomēr plūsmas ātruma lauks nav rotējošs (attēls 3.2).

Saskaņā ar vienādojumiem (3.3), kad piliens atrodas nerotējošā laukā, tas eksponenciāli relaksējas līdz līdzsvara izstiepumam ϵ_1^*.

$$(\epsilon_1 - \epsilon_1^*) \propto e^{-t/\tau_{rel}}. \tag{3.7}$$

Savukārt rotējošā laukā, sasniedzot līdzsvaru, tas atpaliek no lauka par leņķi $\beta^* =$

$-\frac{1}{2}\arctan(2\tau_{rot}\omega)$. Teorētiski τ_{rot} un τ_{rel} vajadzētu būt vienādiem. Tomēr eksperimentāli tika novērots, ka abas vērtības ievērojami atšķiras (tabula 1).

	$\tau_{rel},\ s$	$\tau_{rot},\ s$
Piliens 1	7.7 ± 0.2	0.11 ± 0.03
Piliens 2 ieslēgts lauks	6.65 ± 0.02	
Piliens 2 izslēgts lauks	4.02 ± 0.02	
Piliens 3	16.4 (teorētiski)	0.16

Tabula 1: Raksturīgais mazu perturbāciju relaksācijas laiks τ_{rel}, kas izmērīts relaksācijas eksperimentā, izmantojot formulu (3.7), un τ_{rot}, kas izmērīts no piliena līdzsvara formas rotējošā laukā, izmantojot formulas (3.6).

Redzams, ka, lai varētu reproducēt eksperimentālos novērojumus, kaut kas iztrūkst piliena teorētiskajā aprakstā, kurā ņemts vērā tikai spēks, ko rada Maksvela sprieguma tenzors. Mēs varētu hipotezēt, piemēram, kādu iekšēju nanodaļiņu organizāciju magnētiskā šķidruma pilienā, kas rotācijā un relaksācijā reaģētu ar dažādām laika skalām.

Lai noteiktu šīs dinamiskās mazo deformāciju teorijas pielietojamības robežas, nākamajā bodaļā mēs veiksim robeželementu aprēķinus. Tie ļaus arī veikt vispārīgākus secinājumus par pilienu dinamiku rotējošā laukā.

4 Robeželementu aprēķini

Bieži izmantota skaitliskā metode pilienu dinamikas aprēķināšanai ir robeželementu metode (BEM) [23, 24]. Nesen tā tika izmantota, lai aprēķinātu magnētisko pilienu līdzsvara vērtības bezgalīgi ātri rotējošā laukā [11]. Šeit mēs cenšamies izstrādāt BEM algoritmu, lai aprēķinātu magnētisko pilienu dinamiku režīmā, kurā mazo deformāciju aproksimācija (aplūkota sadaļā 3) vairs nav spēkā. Algoritms darbojas jebkādam lauka leņķiskajam ātrumam, paņemot vērā viskozitātes izmaiņu starp pilienu un ārējo vidi.

Nodaļā 2 formulētie vienādojumi ir pārveidoti integrālvienādojumu formā, kur integrālis ir pa piliena virsmu. Tas ļauj skaitliski atrisināt problēmu visā bezgalīgajā apgabalā, diskretizējot tikai piliena virsmu. Mēs aprēķinām ātrumu uz piliena virsmas un attiecīgi pārvietojam režģa punktus katrā laika solī. Lai nodrošinātu aprēķinu precizitāti, ir nepieciešamas procedūras, kas uztur režģi labā kvalitātē.

Vispirms mēs izmantojām simulācijas, lai noteiktu mazo deformāciju teorijas pielietojamības robežas (attēls 4.1). Mēs redzam, ka, lai kļūdas būtu mazākas par 10%, mazo

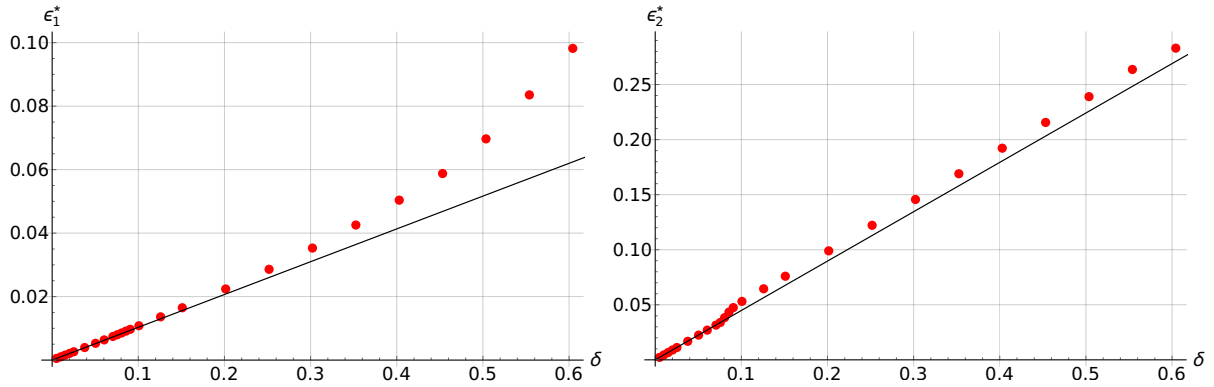

Att. 4.1: Līdzsvara izstiepums ϵ_1 un plakanums ϵ_2 kā funkcija no rotējošā magnētiskā lauka intensitātes, ko raksturo ar parametru δ. Lauka frekvence ir tāda, ka $\tau\omega = 4.8$. Līnijas ir analītiskās līdzsvara vērtības (3.6), bet sarkanie punkti ir no BEM simulācijām.

deformāciju teorija jāizmanto pietiekami vājiem magnētiskajiem laukiem - tādiem, lai $\delta \lesssim 0.3$.

BEM algoritma izstrāde ļauj izpētīt magnētisko pilienu dinamiku rotējošā laukā atkarībā no lauka frekvences un stipruma (attēls 4.2). Mēs redzam, ka vispārīgā gadījumā pilieni iegūst trīsasu formu, kuras asu garumi svārstās. Atkarībā no Bm un $\tau\omega$ pilieni var būt vairāk izstiepti vai vairāk saplacināti. Ja Bm ir mazs un piliens ir saplacināts, leņķis β starp lauku un piliena garāko asi norimst uz stacionāru vērtību (tuvu $-\pi/4$, ja $\tau\omega$ ir liels). Tomēr, ja Bm ir liels un $\tau\omega$ arī ir liels, β nenorimst, bet gan turpina svārstīties. Šajā režīmā sākotnējā saplacinātā forma ir nestabila, un pilieni sāk veidot izstieptu formu: notiek saplacinātās-izstieptās formas bifurkācija, kā tas ir prognozēts bezgalīgi ātri rotējošam laukam [11, 10].

Pilieni var mainīt savu orientāciju, deformējot virsmu, rotējot kā cietam ķermenim, vai arī veicot abas šīs kustības reizē. Orientācijas maiņas veidu raksturo attiecība ω_s/ω, kur ω ir magnētiskā lauka rotācijas frekvence un ω_s ir virsmas leņķiskais ātrums, ko nosaka kā

$$\omega_s = \left\langle \frac{|\boldsymbol{x}_p \times \boldsymbol{v}|}{x_p^2} \right\rangle, \tag{4.1}$$

kur $\boldsymbol{x}_p$ ir konkrētā režģa punkta rādiusvektors, kas projicēts uz magnētiskā lauka rotācijas plakni, $\boldsymbol{v}$ ir šī režģa punkta ātrums. Tiek vidējots pa visiem režģa punktiem. Attiecības ω_s/ω vērtības, kas tuvas 1, norāda, ka pilieni rotē kā ciets ķermenis, bet vērtības, kas tuvas 0, nozīmē, ka orientācija mainās virsmas deformāciju dēļ. Šī attiecība tika aprēķināta pēdējam simulācijas solim un tika parādīta fāžu diagrammā (attēls 4.2). Mēs redzam, ka izstieptus pilienus raksturo cieta ķermeņa dinamika, bet saplacinātie pilieni pārorientējas virsmas deformāciju dēļ.

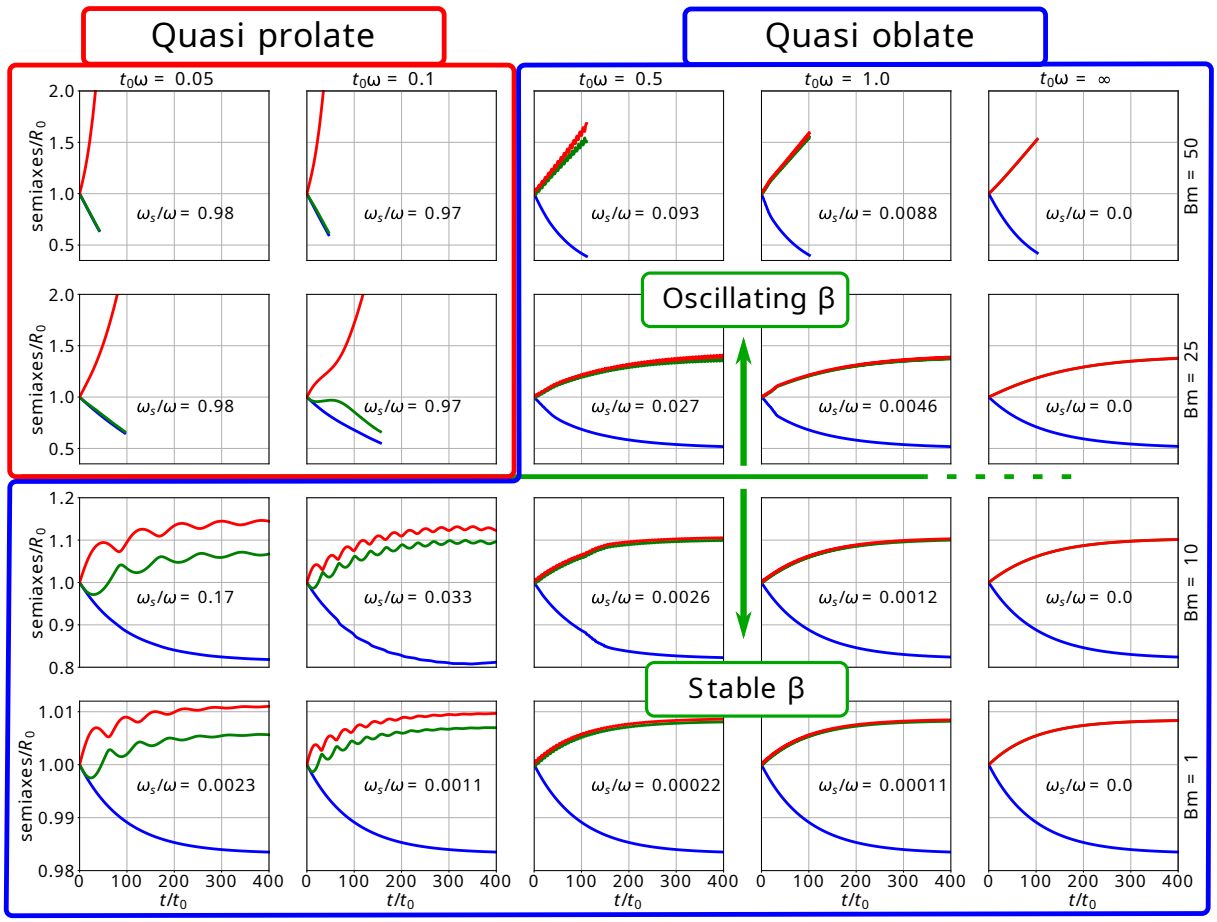

Att. 4.2: Fāžu diagramma, kurā parādīta pilienu pusasu izmaiņa laikā atkarībā no ω un Bm. Simulāciju parametri ir $\mu_r = 10$, $\lambda = 100$. Laika skala ir $t_0 = R_0\eta^{(e)}/\gamma$. Attiecība ω_s/ω raksturo, cik lielā mērā pēdējā simulācijas solī pilieni rotē kā ciets ķermenis. Vērtības, kas tuvākas 1, nozīmē, ka kustība ir tuva rotācijai kā cietam ķermenim. Vērtības, kas tuvas 0, nozīmē, ka piliens maina orientāciju virsmas deformāciju dēļ. ω_s aprēķina, izmantojot vienādojumu (4.1). β ir leņķis starp piliena garāko asi un magnētisko lauku.

Kad pilieni ir saplacināti, to forma labi aprakstās ar elipsoīdu. Tomēr, kad piliens stipri izstiepjas un rotē, sekojot laukam, viskozā berze var izraisīt tā galu noliekšanos, veidojot ”S” formu (attēls 4.3). Šāda izliekšanās ir tikusi novērota eksperimentāli [8, 12].

Šādi ir iespējams skaitliski modelēt atsevišķu pilienu formas dinamiku līdz vidēji lielām piliena deformācijām, izmantojot robeželementu aprēķinus, ņemot vērā viskozitātes kontrastu starp pilienu iekšpusi un ārpusi. Lai precīzi aprēķinātu pilienu dinamiku, ir nepieciešams pievienot režģa punktus pilienu galos, kas var kļūt samērā spici. Rezultātā tiek iegūta fāžu diagramma kā pilieni deformējas atkarībā no lauka frekvences un magnētiskā Bonda skaitļa. Tā parāda evolūciju no izstieptiem pilieniem (cieta ķermeņa rotācijā) uz saplacinātām formām (kas kustas virsmas deformāciju dēļ). Nelielu deformāciju tuvinājumā tika replicēti rezultāti no analītiskā risinājuma sadaļas 3.

Šādi noslēdzas individuāla piliena dinamikas izpēte rotējošā magnētiskajā laukā. Ta-

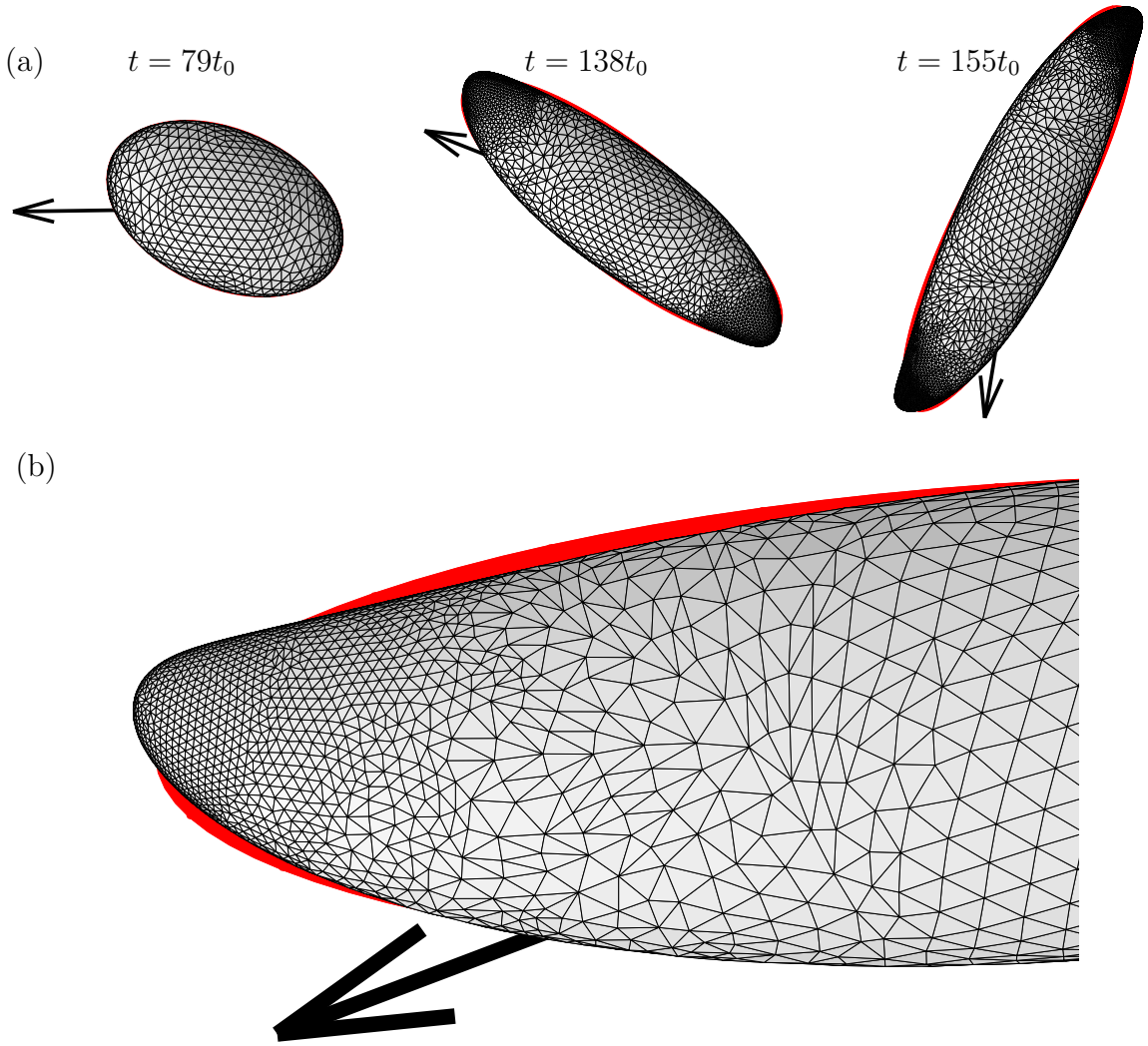

Att. 4.3: Piliens ar parametriem $\lambda = 100$, $\mu_r = 10$, $Bm = 25$, $t_0\omega = 0.1$ magnētiskajā laukā, kas griežas pretēji pulksteņrādītāja virzienam. Laika skala ir $t_0 = R_0\eta^{(e)}/\gamma$. Lai ilustrētu, cik tuvas elipsoīdam ir pilienu formas, režģis tika uzzīmēts virs sarkana elipsoīda, kas tika piedzīts pilienu režģa punktiem. Ar melno bultiņu ir norādīts momentānais magnētiskā lauka virziens. (a) attēlots režģis dažādos simulācijas laikos. (b) parādīta palielināts režģis pie $t = 155t_0$.

gad pievērsīsimies mazu izstieptu pilienu ansambļa dinamikas izpētei rotējošā laukā.

5 Magnētisku pilienu kolektīvā dinamika

Interesants fenomens, kas pēdējos gados ir piesaistījis zinātnieku uzmanību, ir lauka izraisīta koloīdu pašsakārtošanās [25]. Ir nodemonstrēts, ka rotējošā laukā cietās magnētiskās daļiņas var pašsakārtoties divdimensiju rotējošos kristālos [26, 27, 28]. Citā darbā tika aplūkota magnētiskas ķēdītes saturošu pilienu pašsakārtošanās uz šķidruma virsmas precesējošā laukā [29]. Šajā nodaļā mēs iepazīstinām ar jauna veida divdimensiju rotējošiem kristāliem, kur magnētiskie pilieni pašsakārtojas rotējošā laukā.

Ja uzliek rotējošu magnētisko lauku ($f = 15Hz$, $\mu_0 H_\infty = 6mT$) un ja pilieni ir virs kritiskā tilpuma $V_{crit} \approx \pi(3.5\mu m)^3/6$, piliens iegūst saplacinātu formu. Šis saplacinātais piliens rotē un iesūc mazākus pilienus no savas apkārtnes. Ja piliens ir mazāks par V_{crit}, tas ieņem adatai līdzīgu formu un griežas ar magnētiskā lauka leņķisko ātrumu, nesaplūstot ar citiem pilieniem, izņemot gadījumus, kad dažkārt notiek nejaušas sadursmes. Šāda uzvedība ir attēlota attēlā 5.1. Pielāgojot mikroskopa fokusu, mēs noskaidrojām, ka iegarenie pilieni rotē vienā fokusa plaknē attālumā $h = (9 \pm 1)\mu m$ virs mikroskopa šūnas apakšdaļas (pašas mikroskopa šūnas biezums ir aptuveni 130 μm). Savukārt saplacinātie pilieni rotē pāris μm zemāk.

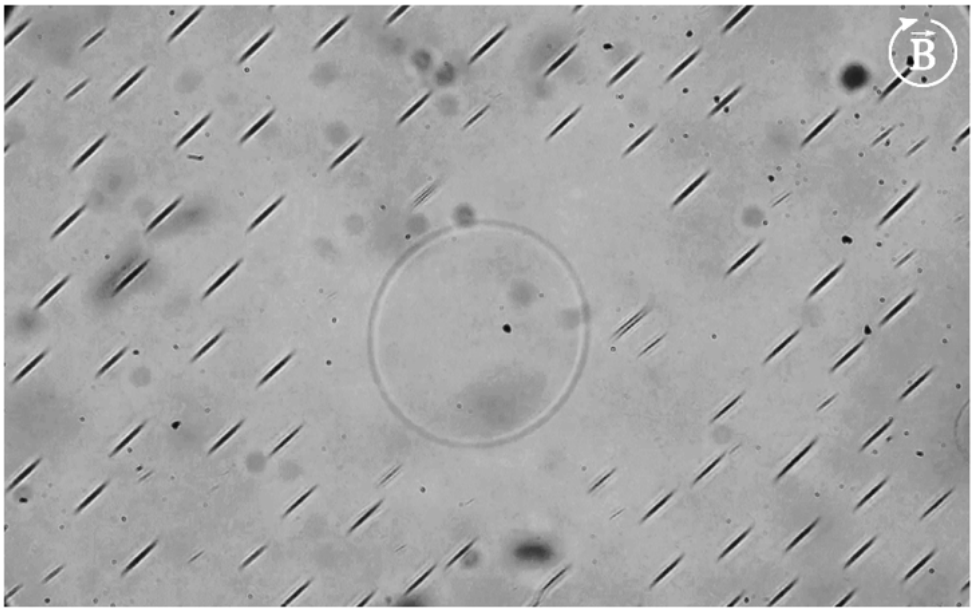

Att. 5.1: Skats uz pilieniem pēc rotējošā magnētiskā lauka ieslēgšanas. Maziem pilieniem veidojas iegarena forma, bet lielāks piliens (nedaudz ārpus fokusa) ir saplacināts. Redzeslauks = $400\mu m \times 250\mu m$. Magnētiskais lauks ($f = 15Hz$, $\mu_0 H_\infty = 6mT$) rotē attēla plaknē. Attēls ir no [30].

Pēc kāda laika zem rotējošā lauka (dažas minūtes) mazie iegarenie pilieni sakārtojas regulārās struktūrās - divdimensiju rotējošos kristālos (sk. attēlu 5.2 (a)). Pilieni veido trīsstūrveida režģi, kas pats rotē kā ciets ķermenis magnētiskā lauka virzienā, tomēr lēnāk

par to. Atsevišķi pilieni kristāla iekšienē joprojām rotē ar lauka leņķisko ātrumu. Ārējā slānī novērojams zināms pilienu dreifs. Tika novērots, ka 2 pilieni rotē stabili ap kopīgu masas centru. 4 pilieni veido četrstūri, kura diagonāles svārstās, ansamblim rotējot (sk. attēlu 5.2 (b)).

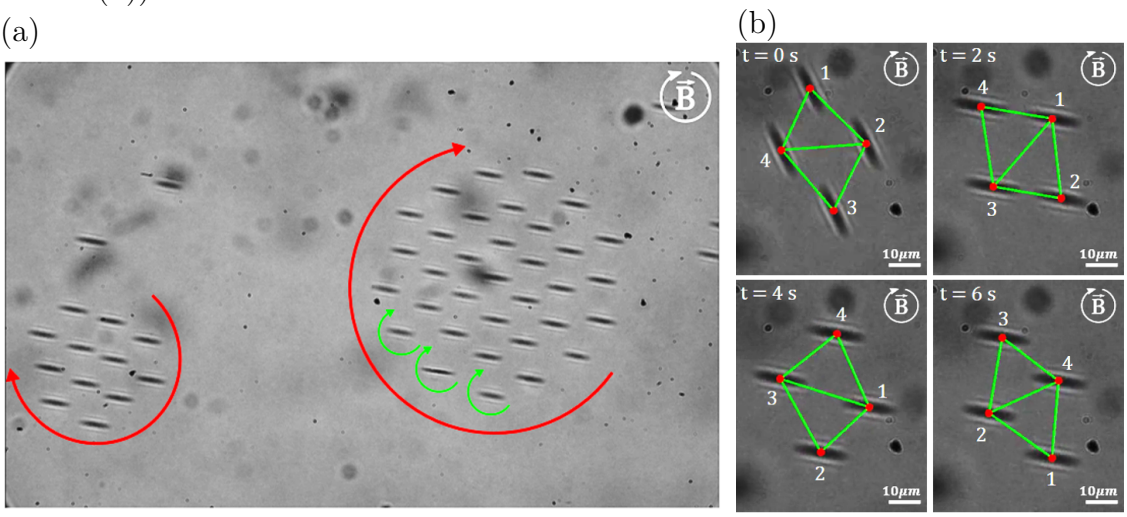

Att. 5.2: Rotējošu magnētisku pilienu ansambļi. Magnētiskais lauks ($f = 15Hz$, $\mu_0 H_\infty = 6mT$) rotē attēla plaknē. (a) Redzami rotējoši kristāli, ko veido izstiepti magnētiskie pilieni. Redzeslauks = $400\mu m \times 250\mu m$. (b) Parādīts, kā četri pilieni veido rotējošu četrstūri ar svārstīgām diagonālēm. Lai labāk ilustrētu pilienu kustību, tie ir apzīmēti ar 1-4, un tie ir Delonē triangluēti. Kadri tiek attēloti ar 2 sekunžu intervālu. Attēls ir no [30].

Ja pilienu blīvums ir liels, pilieni veido kristālus, kas ir pārāk lieli, lai manāmi rotētu (sk. attēlu 5.3.). Pilieni veido ļoti regulāru stacionāru struktūru, tomēr pati sistēma nav stacionāra un starp pilieniem ir plūsma, ko rada to rotācija. To var redzēt, novērojot mazāku pilienu līkumošanu starp režģa punktiem. Delonē triangulējot pilienu centrus, kļūst vieglāk vizualizēt kristālisko struktūru. Var novērot dažādus kristāla graudus, kurus atdala dislokāciju robeža.

Mums izdevās reproducēt mazu pilienu ansambļu kustību, modelējot pilienus kā punktveida spēka momentus virs cietas virsmas. Piemēram, četru pilienu ansambļa diagonāļu svārstības parādās šī modeļa atrisinājumā (attēls 5.4). Tomēr šis modelis nespēj reproducēt lielāku pilienu ansambļu kustību (piemēram, (a) attēlā 5.2). Tā kā modelī nekas nenodrošina līdzsvara attālumu starp pilieniem, lieli pilienu ansambļi nekustas kā rotējoši kristāli, bet gan strauji izšķīst.

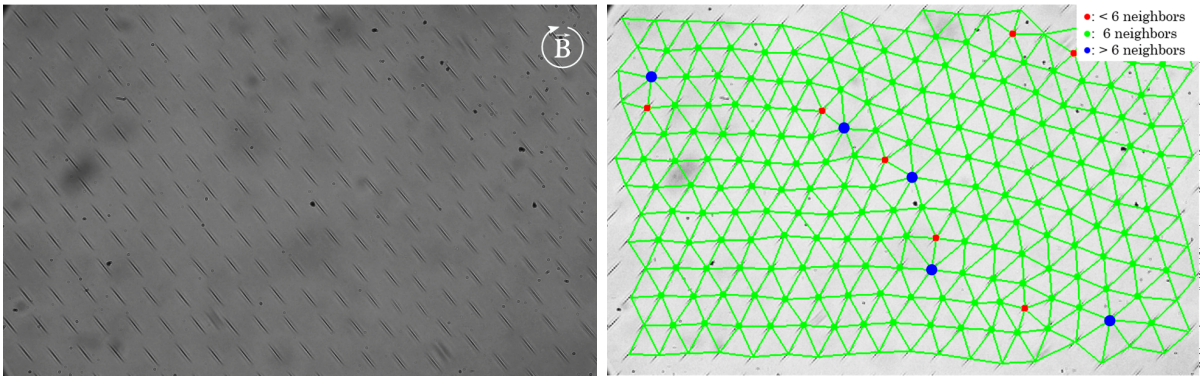

Att. 5.3: Ja pilieni ir blīvi izvietoti, tie sakārtojas lielā 2D trīsstūrveida režģī. Katrs piliens joprojām griežas magnētiskā lauka virzienā un ar tā frekvenci, bet viss kristāls ir nekustīgs. Lai ilustrētu kristālisko struktūru, labajā pusē pilienu centri ir Delonē triangulēti. Redzeslauks = $400\mu m \times 250\mu m$. Magnētiskais lauks ($f = 15Hz$, $\mu_0 H_\infty = 6mT$) rotē attēla plaknē. Attēls ir no [30].

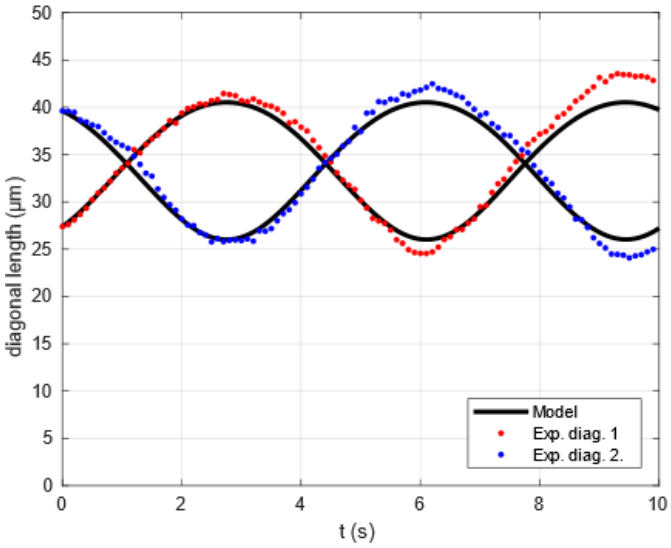

Att. 5.4: Diagonāļu svārstības četru pilienu ansamblī. Zilie un sarkanie punkti ir eksperimentālās vērtības (attēls 5.2 (b)). Melnās līnijas ir modeļa atrisinājums, kur ieejas parametri tika izvēlēti kļūdas robežās tā, lai iegūtu labu atbilstību ar eksperimentālajām svārstībām. Attēls ir no [30].

6 Secinājumi

Šajā darbā tika pētīta magnētiskā šķidruma pilienu dinamika rotējošā laukā. Pilieni atradās ārējā šķidrā vidē, kuras viskozitāte ir ievērojami mazāka par pašu pilienu viskozitāti. Vispirms mēs pētījām šos pilienus kā atsevišķus un izolētus deformējošus objektus, pēc tam apskatījām to pašsakārtotus ansambļus ar kolektīvo dinamiku. Lai aprakstītu izolēto pilienu dinamiku, tika izmantotas vairākas savstarpēji komplementāras pieejas. Gandrīz sfēriska piliena gadījumā mēs izvedām analītiskus vienādojumus, kurus ir viegli analizēt. Pēc tam mēs izstrādājām simulācijas, lai varētu aprēķināt pilienu dinamiku ar lielākām deformācijām. Visbeidzot, mēs veicām eksperimentus ar fāžatdalītiem magnētiskajiem pilieniem, lai redzētu, cik lielā mērā iepriekšējās divās pieejās izmantotais magnētiskā šķidruma modelis var aprakstīt to uzvedību rotējošā laukā. Attiecībā uz magnētisko pilienu kolektīvo uzvedību rotējošā laukā mēs vispirms to novērojām eksperimentāli, un pēc tam tika ierosināts vienkāršs modelis, lai atspoguļotu to dinamiku.

Ja magnētiskais lauks un līdz ar to arī atsevišķa piliena deformācija ir maza, mēs parādījām, kā anizotropijas tenzora fenomenoloģisko vienādojumu, kas apraksta piliena formu, var izmantot, lai aprēķinātu tā dinamiku rotējošā vai precesējošā magnētiskajā laukā. Modelējot pilienu kā magnētiska šķidruma apgabalu nemagnētiskā nesējšķidrumā, mēs varam izmantot Lemba risinājumu Stoksa vienādojumam sfēriskajās koordinātās, lai aprēķinātu pilienu dinamiku mazu deformāciju tuvinājumā. Mēs parādījām, ka šis hidrodinamiskais atrisinājums sakrīt ar fenomenoloģisko atrisinājumu līdz pirmajai kārtai magnētiskajā Bonda skaitlī Bm un deformācijas amplitūdā ε. Šajā tuvinājumā magnētiskā piliena kustību rotējošā laukā kvalitatīvi nosaka viens bezdimensionāls parametrs $\tau\omega$ - raksturīgā mazas perturbācijas dilšanas laika un lauka rotācijas leņķiskās frekvences reizinājums. $\tau\omega$ nosaka, vai piliens būs vairāk izstiepts vai vairāk saplacināts un vai tā forma svārstīsies, pirms tā ieņem līdzsvaru. Piliens pseidorotē: piliens seko rotējošajam magnētiskajam laukam, bet šo kustību izraisa virsmas deformācijas, un piliens nerada spēka momentu uz apkārtējo šķidrumu. Saskaņā ar mazo deformāciju teoriju mazas perturbācijas dilšanas laika τ vērtībai vajadzētu būt vienādai gan rotējošā laukā, gan stacionārā vai nulles laukā. Eksperimentāli iegūtā vērtība τ_{rel}, kas raksturo eksponenciālu tuvošanos līdzsvara formai, ir par pāris lieluma kārtām lielāka nekā τ_{rot}, ko iegūst no piliena līdzsvara formas rotējošā laukā. Tāpēc magnētiskā šķidruma modelis, kurā ņem vērā Maksvela sprieguma tenzoru, ir jāuzlabo, lai varētu kvantitatīvi aprakstīt magnētisko pilienu kustību rotējošā laukā.

Mēs varējām modelēt piliena dinamiku bez mazu deformāciju ierobežojuma, izmantojot simulāciju, kas balstīta uz robeželementu metodi (BEM). Mēs varam izmantot BEM simulāciju, lai aprēķinātu piliena trīsdimensiju dinamiku ārējos magnētiskajos un plūsmas laukos līdz pat vidēji lielām piliena deformācijām. Lai precīzi simulētu pilienu dinamiku, ir nepieciešama ievērojama režģa apkope simulācijas laikā. Ar BEM simulācijām tika parādīts, ka rotējošā magnētiskajā laukā pilieni iegūst trīsasu formu, kas var nedaudz novirzīties no elipsoīdālas. Piemēram, iegarena piliena gali kļūst izliektāki viskozās berzes dēļ, kas ir novērots arī eksperimentāli. Mēs redzam, ka pie liela Bm un mazas magnētiskā lauka rotācijas frekvences ω pilieni izstiepjas un rotē līdzīgi cietiem ķermeņiem, kas seko magnētiskajam laukam. Tomēr liela magnētiskā lauka rotācijas frekvence ω izjauc pilienu izstiepšanos, un to forma kļūst saplacināta. Šajā režīmā pilieni pseidorotē: tie seko rotējošajam magnētiskajam laukam virsmas deformāciju dēļ. Ar simulācijām tiek replicēti arī citi svarīgi novērojumi, piemēram, ātri rotējošā laukā ar lauka intensitāti virs saplacinātās-izstieptās formas nestabilitātes [9, 11], sākotnēji sfērisks piliens vispirms saplacinās, bet pēc tam izstiepjas. Visbeidzot, izmantojot BEM simulācijas, bija iespējams noteikt mazo deformāciju teorijas pielietojamības robežas.

Mēs pirmo reizi novērojām rotējošas sakārtotas magnētisko pilienu struktūras rotējošā laukā - pie noteiktiem lauka parametriem izstiepti adatveida pilieni veido divdimensiju rotējošus trīsstūrveida kristālus. Kristālos esošie pilieni rotē ar magnētiskā lauka frekvenci, tomēr paši kristāli rotē lēnāk. Kristāla rotācijas frekvence samazinās līdz ar tā lielumu, un ļoti lieli kristāli eksperimentā šķita nekustīgi. Pilienu ansambļiem piemīt divdimensiju kristālam raksturīgas iezīmes, piemēram, dažādi graudi savienoti ar dislokāciju robežu. Visi kristāla pilieni organizējas vienā plaknē, kas rotē aptuveni 9 μm virs mikroskopa šūnas apakšas. Modelis, kurā pilieni tiek uzskatīti par punktveida spēka momentiem virs cietas sienas, spēj kvantitatīvi atveidot mazu pilienu ansambļu kustību. Tomēr modelis vairs nav precīzs, kad ansambļu lielums palielinās. Tā kā modelī nav spēku, kas nosaka līdzsvara attālumu starp pilieniem, lieli pilienu ansambļi neveido rotējošus kristālus, bet gan sadalās.

Kopsavilkumā varam izdarīt šādus secinājumus. Magnētiskā šķidruma modelis spēj kvalitatīvi aprakstīt atsevišķa magnētiskā šķidruma piliena (iegūtu ar fāžatdalīšanu) kustību rotējošā laukā. BEM simulācijas var izmantot, lai efektīvi pētītu šādu magnētiskā šķidruma piliena formas dinamiku. Rotējoši magnētiskā šķidruma pilieni kopā var radīt sakārtotas dinamiskas struktūras, kuras vēl nav pilnībā izprastas.

Literatūras saraksts

[1] R. E. Rosensweig, *Ferrohydrodynamics*. Mineola, New York: Dover Publications, 2014. g. febr.

[2] J.-C. Bacri, R. Perzynski, V. Cabuil un R. Massart, "Phase diagram of an ionic magnetic colloid: Experimental study of the effect of ionic strength", *Journal of Colloid and Interface Science*, izdev. 132, nr. 1, 43.—53. lpp., 1989. g. okt. DOI: 10.1016/0021-9797(89)90214-2.

[3] J.-C. Bacri un D. Salin, "Instability of ferrofluid magnetic drops under magnetic field", *Journal de Physique Lettres*, izdev. 43, nr. 17, 649.—654. lpp., 1982. DOI: 10.1051/jphyslet:019820043017064900.

[4] A. O. Tsebers, "Virial method of investigation of statics and dynamics of drops of magnetizable liquids", *Magnetohydrodynamics*, izdev. 21, 19.—26. lpp., 1985.

[5] S. Afkhami u. c., "Deformation of a hydrophobic ferrofluid droplet suspended in a viscous medium under uniform magnetic fields", *Journal of Fluid Mechanics*, izdev. 663, 358.—384. lpp., 2010. g. nov. DOI: 10.1017/S0022112010003551.

[6] J.-C. Bacri un D. Salin, "Dynamics of the shape transition of a magnetic ferrofluid drop", *Journal de Physique Lettres*, izdev. 44, nr. 11, 415.—420. lpp., 1983. DOI: 10.1051/jphyslet:019830044011041500.

[7] A. Langins, A. P. Stikuts un A. Cēbers, "A three-dimensional boundary element method algorithm for simulations of magnetic fluid droplet dynamics", *Physics of Fluids*, izdev. 34, nr. 6, 62105. lpp., 2022. g. jūn. DOI: 10.1063/5.0092532.

[8] O. Sandre, J. Browaeys, R. Perzynski, J.-C. Bacri, V. Cabuil un R. E. Rosensweig, "Assembly of microscopic highly magnetic droplets: Magnetic alignment versus viscous drag", *Physical Review E*, izdev. 59, nr. 2, 1736.—1746. lpp., 1999. g. febr. DOI: 10.1103/PhysRevE.59.1736.

[9] J.-C. Bacri, A. O. Cebers un R. Perzynski, "Behavior of a magnetic fluid microdrop in a rotating magnetic field", *Physical Review Letters*, izdev. 72, nr. 17, 2705.—2708. lpp., 1994. g. apr. DOI: 10.1103/PhysRevLett.72.2705.

[10] K. I. Morozov un A. V. Lebedev, "Bifurcations of the shape of a magnetic fluid droplet in a rotating magnetic field", *Journal of Experimental and Theoretical Physics*, izdev. 91, nr. 5, 1029.—1032. lpp., 2000. g. nov. DOI: 10.1134/1.1334993.

[11] J. Erdmanis, G. Kitenbergs, R. Perzynski un A. Cēbers, "Magnetic micro-droplet in rotating field: numerical simulation and comparison with experiment", *Journal of Fluid Mechanics*, izdev. 821, 266.—295. lpp., 2017. g. jūn. DOI: 10.1017/jfm.2017.238.

[12] E. Janiaud, F. Elias, J.-C. Bacri, V. Cabuil un R. Perzynski, "Spinning ferrofluid microscopic droplets", *Magnetohydrodynamics*, izdev. 36, nr. 4, 365.—378. lpp., 2000.

[13] R. Massart, E. Dubois, V. Cabuil un E. Hasmonay, "Preparation and properties of monodisperse magnetic fluids", *Journal of Magnetism and Magnetic Materials*, izdev. 149, nr. 1-2, 1.—5. lpp., 1995. g. aug. DOI: 10.1016/0304-8853(95)00316-9.

[14] G. K. Batchelor, *An introduction to fluid dynamics*, 1. Cambridge mathematical ed., 14. print, sērija Cambridge mathematical library. Cambridge: Cambridge Univ. Press, 2010, OCLC: 838184093.

[15] E. Blūms, A. Cēbers un M. M. Maiorov, *Magnetic fluids*. Berlin ; New York: Walter de Gruyter, 1997.

[16] J. A. Stratton, *Electromagnetic Theory*. New York un London: Mcgraw Hill Book Company, 1941.

[17] A. Esmaeeli un P. Sharifi, "Transient electrohydrodynamics of a liquid drop", *Physical Review E*, izdev. 84, nr. 3, 36308. lpp., 2011. g. sept. DOI: 10.1103/PhysRevE.84.036308.

[18] J. M. Rallison, "The Deformation of Small Viscous Drops and Bubbles in Shear Flows", *Annual Review of Fluid Mechanics*, izdev. 16, nr. 1, 45.—66. lpp., 1984. g. janv. DOI: 10.1146/annurev.fl.16.010184.000401.

[19] M. Minale, "Models for the deformation of a single ellipsoidal drop: a review", *Rheologica Acta*, izdev. 49, nr. 8, 789.—806. lpp., 2010. g. aug. DOI: 10.1007/s00397-010-0442-0.

[20] Y. I. Dikanskii, A. O. Tsebers un V. P. Shatskii, "Magnetic emulsion properties in electric and magnetic fields. 1. Statics.", *Magnetohydrodynamics*, izdev. 26, 25.—30. lpp., 1990.

[21] A. P. Stikuts, R. Perzynski un A. Cēbers, "Small deformation theory for a magnetic droplet in a rotating field", *Physics of Fluids*, izdev. 34, nr. 5, 52010. lpp., 2022. g. maijs. DOI: 10.1063/5.0091453.

[22] H. A. Stone, "Dynamics of Drop Deformation and Breakup in Viscous Fluids", *Annual Review of Fluid Mechanics*, izdev. 26, nr. 1, 65.—102. lpp., 1994. g. janv. DOI: 10.1146/annurev.fl.26.010194.000433.

[23] C. Pozrikidis, *Boundary Integral and Singularity Methods for Linearized Viscous Flow*. Cambridge: Cambridge University Press, 1992. DOI: 10.1017/CBO9780511624124.

[24] A. Z. Zinchenko un R. H. Davis, "Motion of Deformable Drops Through Porous Media", *Annual Review of Fluid Mechanics*, izdev. 49, nr. 1, 71.—90. lpp., 2017. g. janv. DOI: 10.1146/annurev-fluid-010816-060331.

[25] L. H. P. Cunha, I. R. Siqueira, T. F. Oliveira un H. D. Ceniceros, "Field-induced control of ferrofluid emulsion rheology and droplet break-up in shear flows", *Physics of Fluids*, izdev. 30, nr. 12, 122110. lpp., 2018. g. dec. DOI: 10.1063/1.5055943.

[26] B. A. Grzybowski, H. A. Stone un G. M. Whitesides, "Dynamic self-assembly of magnetized, millimetre-sized objects rotating at a liquid–air interface", *Nature*, izdev. 405, nr. 6790, 1033.—1036. lpp., 2000. g. jūn. DOI: 10.1038/35016528.

[27] B. A. Grzybowski, X. Jiang, H. A. Stone un G. M. Whitesides, "Dynamic, self-assembled aggregates of magnetized, millimeter-sized objects rotating at the liquid-air interface: Macroscopic, two-dimensional classical artificial atoms and molecules", *Physical Review E*, izdev. 64, nr. 1, 11603. lpp., 2001. g. jūn. DOI: 10.1103/PhysRevE.64.011603.

[28] J. Yan, S. C. Bae un S. Granick, "Rotating Crystals of Magnetic Janus Colloids", *Soft Matter*, 9. lpp., 2014.

[29] Q. Wang, L. Yang, B. Wang, E. Yu, J. Yu un L. Zhang, "Collective Behavior of Reconfigurable Magnetic Droplets via Dynamic Self-Assembly", *ACS Applied Materials & Interfaces*, izdev. 11, nr. 1, 1630.—1637. lpp., 2019. g. janv. DOI: 10.1021/acsami.8b17402.

[30] A. Stikuts, R. Perzynski un A. Cēbers, "Spontaneous order in ensembles of rotating magnetic droplets", *Journal of Magnetism and Magnetic Materials*, izdev. 500, 166304. lpp., 2020. g. apr. DOI: 10.1016/j.jmmm.2019.166304.

References

[1] *Historical and international aspects of the SI*. [Online]. Available: https://physics.nist.gov/cuu/Units/international.html.

[2] J. D. Jackson, *Classical Electrodynamics*. John Wiley & Sons, 1998.

[3] R. B. Goldfarb, "The Permeability of Vacuum and the Revised International System of Units," *IEEE Magnetics Letters*, vol. 8, pp. 1–3, 2017. DOI: 10.1109/LMAG.2017.2777782.

[4] E. Tiesinga, P. Mohr, D. B. Newell, and B. Taylor, "2018 CODATA recommended values of the fundamental constants of physics and chemistry," Jun. 2019, Last Modified: 2021-04-06T08:04-04:00.

[5] Papell Solomon Stephen, "Low viscosity magnetic fluid obtained by the colloidal suspension of magnetic particles," US3215572A, Nov. 1965.

[6] J.-C. Bacri, R. Perzynski, and D. Salin, "Magnetic liquids," *Endeavour*, vol. 12, no. 2, pp. 76–83, Jan. 1988. DOI: 10.1016/0160-9327(88)90085-3.

[7] R. Rosensweig, "Ferrofluids: Introduction," in *Reference Module in Materials Science and Materials Engineering*, Elsevier, 2016, B9780128035818024772. DOI: 10.1016/B978-0-12-803581-8.02477-2. [Online]. Available: https://linkinghub.elsevier.com/retrieve/pii/B9780128035818024772.

[8] G. Bossis, S. Lacis, A. Meunier, and O. Volkova, "Magnetorheological fluids," *Journal of Magnetism and Magnetic Materials*, vol. 252, pp. 224–228, Nov. 2002. DOI: 10.1016/S0304-8853(02)00680-7.

[9] J. de Vicente, D. J. Klingenberg, and R. Hidalgo-Alvarez, "Magnetorheological fluids: A review," *Soft Matter*, vol. 7, no. 8, p. 3701, 2011. DOI: 10.1039/c0sm01221a.

[10] S. Odenbach, Ed., *Colloidal Magnetic Fluids: Basics, Development and Application of Ferrofluids*, ser. Lecture Notes in Physics. Berlin, Heidelberg: Springer Berlin Heidelberg, 2009, vol. 763. DOI: 10.1007/978-3-540-85387-9.

[11] I. Torres-Díaz and C. Rinaldi, "Recent progress in ferrofluids research: Novel applications of magnetically controllable and tunable fluids," *Soft Matter*, vol. 10, no. 43, pp. 8584–8602, Sep. 2014. DOI: 10.1039/C4SM01308E.

[12] X. Zhang, L. Sun, Y. Yu, and Y. Zhao, "Flexible Ferrofluids: Design and Applications," *Advanced Materials*, vol. 31, no. 51, p. 1 903 497, Dec. 2019. DOI: 10.1002/adma.201903497.

[13] S. Kodama, "Dynamic ferrofluid sculpture: Organic shape-changing art forms," *Communications of the ACM*, vol. 51, no. 6, pp. 79–81, Jun. 2008. DOI: 10.1145/1349026.1349042.

[14] J. L. Neuringer and R. E. Rosensweig, "Ferrohydrodynamics," *Physics of Fluids*, vol. 7, no. 12, p. 1927, 1964. DOI: 10.1063/1.1711103.

[15] R. E. Rosensweig, *Ferrohydrodynamics*. Mineola, New York: Dover Publications, Feb. 2014.

[16] E. Blūms, A. Cēbers, and M. M. Maiorov, *Magnetic fluids*. Berlin ; New York: Walter de Gruyter, 1997.

[17] J.-C. Bacri, R. Perzynski, D. Salin, V. Cabuil, and R. Massart, "Magnetic colloidal properties of ionic ferrofluids," *Journal of Magnetism and Magnetic Materials*, vol. 62, no. 1, pp. 36–46, Nov. 1986. DOI: 10.1016/0304-8853(86)90731-6.

[18] R. Massart, "Preparation of aqueous magnetic liquids in alkaline and acidic media," *IEEE Transactions on Magnetics*, vol. 17, no. 2, pp. 1247–1248, Mar. 1981. DOI: 10.1109/TMAG.1981.1061188.

[19] J. C. Riedl, M. A. Akhavan Kazemi, F. Cousin, E. Dubois, S. Fantini, S. Loïs, R. Perzynski, and V. Peyre, "Colloidal dispersions of oxide nanoparticles in ionic liquids: Elucidating the key parameters," *Nanoscale Advances*, vol. 2, no. 4, pp. 1560–1572, 2020. DOI: 10.1039/C9NA00564A.

[20] A. O. Tsebers, "Thermodynamic stability of magnetofluids," *Magnetohydrodynamics*, vol. 18, no. 2, pp. 137–142, 1982.

[21] K. Sano and M. Doi, "Theory of Agglomeration of Ferromagnetic Particles in Magnetic Fluids," *Journal of the Physical Society of Japan*, vol. 52, no. 8, pp. 2810–2815, Aug. 1983. DOI: 10.1143/JPSJ.52.2810.

[22] J.-C. Bacri, R. Perzynski, V. Cabuil, and R. Massart, "Phase diagram of an ionic magnetic colloid: Experimental study of the effect of ionic strength," *Journal of Colloid and Interface Science*, vol. 132, no. 1, pp. 43–53, Oct. 1989. DOI: 10.1016/0021-9797(89)90214-2.

[23] R. Massart, E. Dubois, V. Cabuil, and E. Hasmonay, "Preparation and properties of monodisperse magnetic fluids," *Journal of Magnetism and Magnetic Materials*, vol. 149, no. 1-2, pp. 1–5, Aug. 1995. DOI: 10.1016/0304-8853(95)00316-9.

[24] J.-C. Bacri and D. Salin, "Instability of ferrofluid magnetic drops under magnetic field," *Journal de Physique Lettres*, vol. 43, no. 17, pp. 649–654, 1982. DOI: 10.1051/jphyslet:019820043017064900.

[25] L. M. Pop and S. Odenbach, "Investigation of the microscopic reason for the magnetoviscous effect in ferrofluids studied by small angle neutron scattering," *Journal of Physics: Condensed Matter*, vol. 18, no. 38, S2785–S2802, Sep. 2006. DOI: 10.1088/0953-8984/18/38/S17.

[26] P. G. Saffman and G. I. Taylor, "The penetration of a fluid into a porous medium or Hele-Shaw cell containing a more viscous liquid," *Proceedings of the Royal Society of London. Series A. Mathematical and Physical Sciences*, vol. 245, no. 1242, pp. 312–329, Jun. 1958. DOI: 10.1098/rspa.1958.0085.

[27] J. Eggers, "Nonlinear dynamics and breakup of free-surface flows," *Reviews of Modern Physics*, vol. 69, no. 3, pp. 865–930, Jul. 1997. DOI: 10.1103/RevModPhys.69.865.

[28] M. D. Cowley and R. E. Rosensweig, "The interfacial stability of a ferromagnetic fluid," *Journal of Fluid Mechanics*, vol. 30, no. 4, pp. 671–688, Dec. 1967. DOI: 10.1017/S0022112067001697.

[29] A. Gailītis, "Formation of the hexagonal pattern on the surface of a ferromagnetic fluid in an applied magnetic field," *Journal of Fluid Mechanics*, vol. 82, no. 3, pp. 401–413, Sep. 1977. DOI: 10.1017/S0022112077000731.

[30] J.-C. Bacri and D. Salin, "First-order transition in the instability of a magnetic fluid interface," *Journal de Physique Lettres*, vol. 45, no. 11, pp. 559–564, 1984. DOI: 10.1051/jphyslet:019840045011055900.

[31] R. E. Zelazo and J. R. Melcher, "Dynamics and stability of ferrofluids: Surface interactions," *Journal of Fluid Mechanics*, vol. 39, no. 1, pp. 1–24, Oct. 1969. DOI: 10.1017/S0022112069002011.

[32] A. Völkel, A. Kögel, and R. Richter, "Measuring the Kelvin-Helmholtz instability, stabilized by a tangential magnetic field," *Journal of Magnetism and Magnetic Materials*, vol. 505, p. 166 693, Jul. 2020. DOI: 10.1016/j.jmmm.2020.166693.

[33] A. Kögel, A. Völkel, and R. Richter, "Calming the waves, not the storm: Measuring the Kelvin–Helmholtz instability in a tangential magnetic field," *Journal of Fluid Mechanics*, vol. 903, A47, Nov. 2020. DOI: 10.1017/jfm.2020.642.

[34] L. Romankiw, M. Slusarczuk, and D. Thompson, "Liquid magnetic bubbles," *IEEE Transactions on Magnetics*, vol. 11, no. 1, pp. 25–28, Jan. 1975. DOI: 10.1109/TMAG.1975.1058543.

[35] N. Wilke, J. Bugase, L.-M. Treffenstädt, and T. M. Fischer, "Wrinkled labyrinths in critical demixing ferrofluid," *Soft Matter*, vol. 13, no. 40, pp. 7307–7311, 2017. DOI: 10.1039/C7SM01475A.

[36] A. O. Tsebers and M. M. Maiorov, "Magnetostatic instabilities in plane layers of magnetizable liquids," *Magnetohydrodynamics*, vol. 16, no. 1, pp. 21–28, 1980.

[37] M. M. Maiorov and A. O. Tsebers, "Magnetic microconvection on the diffusion front of ferroparticles," *Magnetohydrodynamics*, vol. 19, no. 4, pp. 376–380, 1983.

[38] K. Ērglis, A. Tatulcenkov, G. Kitenbergs, O. Petrichenko, F. G. Ergin, B. B. Watz, and A. Cēbers, "Magnetic field driven micro-convection in the Hele-Shaw cell," *Journal of Fluid Mechanics*, vol. 714, pp. 612–633, Jan. 2013. DOI: 10.1017/jfm.2012.512.

[39] G. Kitenbergs, A. Tatuļčenkovs, L. Puķina, and A. Cēbers, "Gravity effects on mixing with magnetic micro-convection in microfluidics," *The European Physical Journal E*, vol. 41, no. 11, p. 138, Nov. 2018. DOI: 10.1140/epje/i2018-11749-9.

[40] M. I. Shliomis, "Effective viscosity of magnetic suspensions," *Soviet Physics JETP*, vol. 34, no. 6, pp. 1291–1294, Dec. 1972.

[41] J. P. McTague, "Magnetoviscosity of Magnetic Colloids," *The Journal of Chemical Physics*, vol. 51, no. 1, pp. 133–136, Jul. 1969. DOI: 10.1063/1.1671697.

[42] E. Al-Hetlani and M. O. Amin, "Continuous magnetic droplets and microfluidics: Generation, manipulation, synthesis and detection," *Microchimica Acta*, vol. 186, no. 2, p. 55, Feb. 2019. DOI: 10.1007/s00604-018-3118-6.

[43] X. Fan, M. Sun, L. Sun, and H. Xie, "Ferrofluid Droplets as Liquid Microrobots with Multiple Deformabilities," *Advanced Functional Materials*, vol. 30, no. 24, p. 2 000 138, Jun. 2020. DOI: 10.1002/adfm.202000138.

[44] X. Fan, X. Dong, A. C. Karacakol, H. Xie, and M. Sitti, "Reconfigurable multifunctional ferrofluid droplet robots," *Proceedings of the National Academy of Sciences*, vol. 117, no. 45, pp. 27 916–27 926, Nov. 2020. DOI: 10.1073/pnas.2016388117.

[45] K. Doubrovinski, M. Swan, O. Polyakov, and E. F. Wieschaus, "Measurement of cortical elasticity in *Drosophila melanogaster* embryos using ferrofluids," *Proceedings of the National Academy of Sciences*, vol. 114, no. 5, pp. 1051–1056, Jan. 2017. DOI: 10.1073/pnas.1616659114.

[46] F. Serwane, A. Mongera, P. Rowghanian, D. A. Kealhofer, A. A. Lucio, Z. M. Hockenbery, and O. Campàs, "In vivo quantification of spatially varying mechanical properties in developing tissues," *Nature Methods*, vol. 14, no. 2, pp. 181–186, Feb. 2017. DOI: 10.1038/nmeth.4101.

[47] C. T. R. Wilson and G. I. Taylor, "The bursting of soap-bubbles in a uniform electric field," *Mathematical Proceedings of the Cambridge Philosophical Society*, vol. 22, no. 5, pp. 728–730, Jul. 1925. DOI: 10.1017/S0305004100009609.

[48] G. Taylor, "Disintegration of water drops in an electric field," *Proceedings of the Royal Society of London. Series A. Mathematical and Physical Sciences*, vol. 280, no. 1382, pp. 383–397, Jul. 1964. DOI: 10.1098/rspa.1964.0151.

[49] J. R. Melcher and G. I. Taylor, "Electrohydrodynamics: A Review of the Role of Interfacial Shear Stresses," *Annual Review of Fluid Mechanics*, vol. 1, no. 1, pp. 111–146, Jan. 1969. DOI: 10.1146/annurev.fl.01.010169.000551.

[50] S. Krause and P. Chandratreya, "Electrorotation of Deformable Fluid Droplets," *Journal of Colloid and Interface Science*, vol. 206, no. 1, pp. 10–18, Oct. 1998. DOI: 10.1006/jcis.1998.5716.

[51] D. Das and D. Saintillan, "Electrohydrodynamics of viscous drops in strong electric fields: Numerical simulations," *Journal of Fluid Mechanics*, vol. 829, pp. 127–152, Oct. 2017. DOI: 10.1017/jfm.2017.560.

[52] I. E. Tarapov, "Hydrodynamics of magnetizable and polarizable media," *Fluid Dynamics*, vol. 9, no. 5, pp. 806–810, 1976. DOI: 10.1007/BF01017431.

[53] V. I. Arkhipenko, Y. D. Barkov, and V. G. Bashtovoi, "Shape of a drop of magnetized fluid in a homogeneous magnetic field," *Magnetohydrodynamics*, vol. 14, p. 373, 1978.

[54] C. Rigoni, J. Fresnais, D. Talbot, R. Massart, R. Perzynski, J.-C. Bacri, and A. Abou-Hassan, "Magnetic Field-Driven Deformation, Attraction, and Coalescence of Nonmagnetic Aqueous Droplets in an Oil-Based Ferrofluid," *Langmuir*, vol. 36, no. 18, pp. 5048–5057, May 2020. DOI: 10.1021/acs.langmuir.0c00060.

[55] V. G. Bashtovoi, S. G. Pogirnitskaya, and A. G. Reks, "Determination of the shape of a free drop of magnetic fluid in a uniform magnetic field," *Magnetohydrodynamics*, vol. 23:3, pp. 248–251, 1988.

[56] H. A. Stone, J. R. Lister, and M. P. Brenner, "Drops with conical ends in electric and magnetic fields," *Proceedings of the Royal Society of London. Series A: Mathematical, Physical and Engineering Sciences*, vol. 455, no. 1981, pp. 329–347, Jan. 1999. DOI: 10.1098/rspa.1999.0316.

[57] P. Rowghanian, C. D. Meinhart, and O. Campàs, "Dynamics of ferrofluid drop deformations under spatially uniform magnetic fields," *Journal of Fluid Mechanics*, vol. 802, pp. 245–262, Sep. 2016. DOI: 10.1017/jfm.2016.447.

[58] A. O. Tsebers, "Virial method of investigation of statics and dynamics of drops of magnetizable liquids," *Magnetohydrodynamics*, vol. 21, pp. 19–26, 1985.

[59] A. Langins, A. P. Stikuts, and A. Cēbers, "A three-dimensional boundary element method algorithm for simulations of magnetic fluid droplet dynamics," *Physics of Fluids*, vol. 34, no. 6, p. 062 105, Jun. 2022. DOI: 10.1063/5.0092532.

[60] S. Afkhami, A. J. Tyler, Y. Renardy, M. Renardy, T. G. St. Pierre, R. C. Woodward, and J. S. Riffle, "Deformation of a hydrophobic ferrofluid droplet suspended in a viscous medium under uniform magnetic fields," *Journal of Fluid Mechanics*, vol. 663, pp. 358–384, Nov. 2010. DOI: 10.1017/S0022112010003551.

[61] K. Misra, "Magnetic (electric) drop deformation in uniform external fields: Volume averaged methods and formation of static and dynamic conical tips," *Physics of Fluids*, vol. 32, no. 10, p. 107 104, Oct. 2020. DOI: 10.1063/5.0023594.

[62] J. Erdmanis, G. Kitenbergs, R. Perzynski, and A. Cēbers, "Magnetic micro-droplet in rotating field: Numerical simulation and comparison with experiment," *Journal of Fluid Mechanics*, vol. 821, pp. 266–295, Jun. 2017. DOI: 10.1017/jfm.2017.238.

[63] J.-C. Bacri and D. Salin, "Dynamics of the shape transition of a magnetic ferrofluid drop," *Journal de Physique Lettres*, vol. 44, no. 11, pp. 415–420, 1983. DOI: 10.1051/jphyslet:019830044011041500.

[64] Y. I. Dikanskii, A. O. Tsebers, and V. P. Shatskii, "Magnetic emulsion properties in electric and magnetic fields. 1. Statics.," *Magnetohydrodynamics*, vol. 26, pp. 25–30, 1990.

[65] A. Esmaeeli and P. Sharifi, "Transient electrohydrodynamics of a liquid drop," *Physical Review E*, vol. 84, no. 3, p. 036 308, Sep. 2011. DOI: 10.1103/PhysRevE.84.036308.

[66] S. Lācis, "Behaviour of a magnetic fluid drop in a time dependent magnetic field: Theory and simulation," PhD, Université Paris VII, Feb. 1996.

[67] O. Sandre, J. Browaeys, R. Perzynski, J.-C. Bacri, V. Cabuil, and R. E. Rosensweig, "Assembly of microscopic highly magnetic droplets: Magnetic alignment versus viscous drag," *Physical Review E*, vol. 59, no. 2, pp. 1736–1746, Feb. 1999. DOI: 10.1103/PhysRevE.59.1736.

[68] J.-C. Bacri, A. O. Cebers, and R. Perzynski, "Behavior of a magnetic fluid microdrop in a rotating magnetic field," *Physical Review Letters*, vol. 72, no. 17, pp. 2705–2708, Apr. 1994. DOI: 10.1103/PhysRevLett.72.2705.

[69] G. Kitenbergs, "Hydrodynamic instabilities in microfluidic magnetic fluid flows," PhD, UNIVERSITÉ PIERRE ET MARIE CURIE, Jul. 2015.

[70] K. I. Morozov and A. V. Lebedev, "Bifurcations of the shape of a magnetic fluid droplet in a rotating magnetic field," *Journal of Experimental and Theoretical Physics*, vol. 91, no. 5, pp. 1029–1032, Nov. 2000. DOI: 10.1134/1.1334993.

[71] E. Janiaud, F. Elias, J.-C. Bacri, V. Cabuil, and R. Perzynski, "Spinning ferrofluid microscopic droplets," *Magnetohydrodynamics*, vol. 36, no. 4, pp. 365–378, 2000.

[72] A. Cēbers, "Dynamics of an elongated magnetic droplet in a rotating field," *Physical Review E*, vol. 66, no. 6, p. 061 402, Dec. 2002. DOI: 10.1103/PhysRevE.66.061402.

[73] A. Cebers and G. Bossis, "Internal motion due to the spinning particles in the magnetic liquid droplets in an alternating magnetic field," *Magnetohydrodynamics*, vol. 34, no. 4, pp. 311–323, 1998.

[74] S. Afkhami and Y. Renardy, "Ferrofluids and magnetically guided superparamagnetic particles in flows: A review of simulations and modeling," *Journal of Engineering Mathematics*, vol. 107, no. 1, pp. 231–251, Dec. 2017. DOI: 10.1007/s10665-017-9931-9.

[75] O. Lavrova, G. Matthies, T. Mitkova, V. Polevikov, and L. Tobiska, "Numerical treatment of free surface problems in ferrohydrodynamics," *Journal of Physics: Condensed Matter*, vol. 18, no. 38, S2657–S2669, Sep. 2006. DOI: 10.1088/0953-8984/18/38/S09.

[76] S. Lācis and A. Cēbers, "Magnetic fluid free surface instabilities in high frequency rotating magnetic fields," *Brazilian Journal of Physics*, vol. 25, no. 2, pp. 101–111, 1995.

[77] C. Pozrikidis, *Boundary Integral and Singularity Methods for Linearized Viscous Flow*. Cambridge: Cambridge University Press, 1992. DOI: 10.1017/CBO9780511624124.

[78] C. Pozrikidis, *A practical guide to boundary element methods with the software library BEMLIB*. Boca Raton, Fla.: Chapman & Hall/CRC, 2002, OCLC: 845494352.

[79] A. Z. Zinchenko and R. H. Davis, "Emulsion flow through a packed bed with multiple drop breakup," *Journal of Fluid Mechanics*, vol. 725, pp. 611–663, Jun. 2013. DOI: 10.1017/jfm.2013.197.

[80] A. Z. Zinchenko and R. H. Davis, "Motion of Deformable Drops Through Porous Media," *Annual Review of Fluid Mechanics*, vol. 49, no. 1, pp. 71–90, Jan. 2017. DOI: 10.1146/annurev-fluid-010816-060331.

[81] R. Navarro, A. Z. Zinchenko, and R. H. Davis, "Boundary-integral study of a freely suspended drop in a T-shaped microchannel," *International Journal of Multiphase Flow*, vol. 130, p. 103 379, Sep. 2020. DOI: 10.1016/j.ijmultiphaseflow.2020.103379.

[82] V. Liljeström, C. Chen, P. Dommersnes, J. O. Fossum, and A. H. Gröschel, "Active structuring of colloids through field-driven self-assembly," *Current Opinion in Colloid & Interface Science*, vol. 40, pp. 25–41, Apr. 2019. DOI: 10.1016/j.cocis.2018.10.008.

[83] B. A. Grzybowski, H. A. Stone, and G. M. Whitesides, "Dynamic self-assembly of magnetized, millimetre-sized objects rotating at a liquid–air interface," *Nature*, vol. 405, no. 6790, pp. 1033–1036, Jun. 2000. DOI: 10.1038/35016528.

[84] P. Tierno, R. Muruganathan, and T. M. Fischer, "Viscoelasticity of Dynamically Self-Assembled Paramagnetic Colloidal Clusters," *Physical Review Letters*, vol. 98, no. 2, p. 028 301, Jan. 2007. DOI: 10.1103/PhysRevLett.98.028301.

[85] J. Yan, S. C. Bae, and S. Granick, "Rotating Crystals of Magnetic Janus Colloids," *Soft Matter*, p. 9, 2014.

[86] F. J. Maier and T. M. Fischer, "Transport on Active Paramagnetic Colloidal Networks," *The Journal of Physical Chemistry B*, vol. 120, no. 38, pp. 10 162–10 165, Sep. 2016. DOI: 10.1021/acs.jpcb.6b07775.

[87] O. Petrichenko, G. Kitenbergs, M. Brics, E. Dubois, R. Perzynski, and A. Cēbers, "Swarming of micron-sized hematite cubes in a rotating magnetic field – Experiments," *Journal of Magnetism and Magnetic Materials*, vol. 500, p. 166 404, Apr. 2020. DOI: 10.1016/j.jmmm.2020.166404.

[88] A. P. Petroff, X.-L. Wu, and A. Libchaber, "Fast-Moving Bacteria Self-Organize into Active Two-Dimensional Crystals of Rotating Cells," *Physical Review Letters*, vol. 114, no. 15, p. 158 102, Apr. 2015. DOI: 10.1103/PhysRevLett.114.158102.

[89] *Motion of magnetotactic bacteria swarms in an external field*, Number: arXiv:1707.02827 arXiv:1707.02827 [cond-mat], Jul. 2017. [Online]. Available: http://arxiv.org/abs/1707.02827.

[90] J. V. I. Timonen, M. Latikka, L. Leibler, R. H. A. Ras, and O. Ikkala, "Switchable Static and Dynamic Self-Assembly of Magnetic Droplets on Superhydrophobic Surfaces," *Science*, vol. 341, no. 6143, pp. 253–257, Jul. 2013. DOI: 10.1126/science.1233775.

[91] Q. Wang, L. Yang, B. Wang, E. Yu, J. Yu, and L. Zhang, "Collective Behavior of Reconfigurable Magnetic Droplets via Dynamic Self-Assembly," *ACS Applied Materials & Interfaces*, vol. 11, no. 1, pp. 1630–1637, Jan. 2019. DOI: 10.1021/acsami.8b17402.

[92] C.-Y. Chen, H.-C. Hsueh, S.-Y. Wang, and Y.-H. Li, "Self-assembly and novel planetary motion of ferrofluid drops in a rotational magnetic field," *Microfluidics and Nanofluidics*, vol. 18, no. 5-6, pp. 795–806, May 2015. DOI: 10.1007/s10404-014-1472-1.

[93] M. Qiu, S. Afkhami, C.-Y. Chen, and J. J. Feng, "Interaction of a pair of ferrofluid drops in a rotating magnetic field," *Journal of Fluid Mechanics*, vol. 846, pp. 121–142, Jul. 2018. DOI: 10.1017/jfm.2018.261.

[94] J. A. Stratton, *Electromagnetic Theory*. New York and London: Mcgraw Hill Book Company, 1941.

[95] G. K. Batchelor, *An introduction to fluid dynamics*, 1. Cambridge mathematical ed., 14. print, ser. Cambridge mathematical library. Cambridge: Cambridge Univ. Press, 2010, OCLC: 838184093.

[96] A. Stikuts, R. Perzynski, and A. Cēbers, "Spontaneous order in ensembles of rotating magnetic droplets," *Journal of Magnetism and Magnetic Materials*, vol. 500, p. 166 304, Apr. 2020. DOI: 10.1016/j.jmmm.2019.166304.

[97] L. H. P. Cunha, I. R. Siqueira, F. R. Cunha, and T. F. Oliveira, "Effects of external magnetic fields on the rheology and magnetization of dilute emulsions of ferrofluid droplets in shear flows," *Physics of Fluids*, vol. 32, no. 7, p. 073 306, Jul. 2020. DOI: 10.1063/5.0009983.

[98] F. Cousin, E. Dubois, and V. Cabuil, "Tuning the interactions of a magnetic colloidal suspension," *Physical Review E*, vol. 68, no. 2, p. 021 405, Aug. 2003. DOI: 10.1103/PhysRevE.68.021405.

[99] E. C. Stoner, "XCVII. The demagnetizing factors for ellipsoids," *The London, Edinburgh, and Dublin Philosophical Magazine and Journal of Science*, vol. 36, no. 263, pp. 803–821, Dec. 1945. DOI: 10.1080/14786444508521510.

[100] D. Zwillinger, *Standard mathematical tables and formulae*, 31st ed. Boca Raton London New York [etc.]: Chapman & Hall/CRC, 2003.

[101] J. M. Rallison, "The Deformation of Small Viscous Drops and Bubbles in Shear Flows," *Annual Review of Fluid Mechanics*, vol. 16, no. 1, pp. 45–66, Jan. 1984. DOI: 10.1146/annurev.fl.16.010184.000401.

[102] M. Minale, "Models for the deformation of a single ellipsoidal drop: A review," *Rheologica Acta*, vol. 49, no. 8, pp. 789–806, Aug. 2010. DOI: 10.1007/s00397-010-0442-0.

[103] P. M. Vlahovska, "On the rheology of a dilute emulsion in a uniform electric field," *Journal of Fluid Mechanics*, vol. 670, pp. 481–503, Mar. 2011. DOI: 10.1017/S0022112010005379.

[104] D. Das and D. Saintillan, "A nonlinear small-deformation theory for transient droplet electrohydrodynamics," *Journal of Fluid Mechanics*, vol. 810, pp. 225–253, Jan. 2017, arXiv: 1605.04036. DOI: 10.1017/jfm.2016.704.

[105] M. Doi and T. Ohta, "Dynamics and rheology of complex interfaces. I," *The Journal of Chemical Physics*, vol. 95, no. 2, pp. 1242–1248, Jul. 1991. DOI: 10.1063/1.461156.

[106] A. S. Almusallam, R. G. Larson, and M. J. Solomon, "A constitutive model for the prediction of ellipsoidal droplet shapes and stresses in immiscible blends," *Journal of Rheology*, vol. 44, no. 5, pp. 1055–1083, Sep. 2000. DOI: 10.1122/1.1287288.

[107] P. Maffettone and M. Minale, "Equation of change for ellipsoidal drops in viscous flow," *Journal of Non-Newtonian Fluid Mechanics*, vol. 78, no. 2-3, pp. 227–241, Aug. 1998. DOI: 10.1016/S0377-0257(98)00065-2.

[108] E. Boonen, P. Van Puyvelde, and P. Moldenaers, "Droplet dynamics in mixed flow conditions: Effect of shear/elongation balance and viscosity ratio," *Journal of Rheology*, vol. 54, no. 6, pp. 1285–1306, Nov. 2010. DOI: 10.1122/1.3490661.

[109] A. P. Stikuts, R. Perzynski, and A. Cēbers, "Small deformation theory for a magnetic droplet in a rotating field," *Physics of Fluids*, vol. 34, no. 5, p. 052 010, May 2022. DOI: 10.1063/5.0091453.

[110] R. G. Cox, "The deformation of a drop in a general time-dependent fluid flow," *Journal of Fluid Mechanics*, vol. 37, no. 3, pp. 601–623, Jul. 1969. DOI: 10.1017/S0022112069000759.

[111] P. M. Vlahovska, J. Bławzdziewicz, and M. Loewenberg, "Small-deformation theory for a surfactant-covered drop in linear flows," *Journal of Fluid Mechanics*, vol. 624, pp. 293–337, Apr. 2009. DOI: 10.1017/S0022112008005417.

[112] D. Das and D. Saintillan, "A three-dimensional small-deformation theory for electrohydrodynamics of dielectric drops," *Journal of Fluid Mechanics*, vol. 914, A22, May 2021. DOI: 10.1017/jfm.2020.924.

[113] G. B. Arfken and H.-J. Weber, *Mathematical methods for physicists*, 6th ed. Boston: Elsevier, 2005.

[114] L. D. Landau, E. M. Lifšic, L. P. Pitaevskij, and L. D. Landau, *Electrodynamics of continuous media*, 2. ed., rev. and enl, ser. Course of theoretical physics by L. D. Landau and E. M. Lifshitz ; Vol. 8. Amsterdam [u.a]: Elsevier, Butterworth-Heinemann, 2008, OCLC: 837370199.

[115] H. Lamb, *Hydrodynamics*, 6th ed. Cambridge Univ. Press, 1975.

[116] S. Kim and S. J. Karrila, *Microhydrodynamics: principles and selected applications*, ser. Butterworth-Heinemann series in chemical engineering. Boston: Butterworth-Heinemann, 1991.

[117] H. A. Stone, "Dynamics of Drop Deformation and Breakup in Viscous Fluids," *Annual Review of Fluid Mechanics*, vol. 26, no. 1, pp. 65–102, Jan. 1994. DOI: 10.1146/annurev.fl.26.010194.000433.

[118] O. Ghazian, K. Adamiak, G. Peter Castle, and Y. Higashiyama, "Oscillation, pseudo-rotation and coalescence of sessile droplets in a rotating electric field," *Colloids and Surfaces A: Physicochemical and Engineering Aspects*, vol. 441, pp. 346–353, Jan. 2014. DOI: 10.1016/j.colsurfa.2013.09.017.

[119] A. P. Stikuts, A. Langins, and J. Erdmanis, *MDrops*. [Online]. Available: https://github.com/neonjoo/MDrops.

[120] M. Guiggiani, "The evaluation of cauchy principal value integrals in the boundary element method—a review," *Mathematical and Computer Modelling*, vol. 15, no. 3-5, pp. 175–184, 1991. DOI: 10.1016/0895-7177(91)90063-D.

[121] E. E. Keaveny and M. J. Shelley, "Applying a second-kind boundary integral equation for surface tractions in Stokes flow," *Journal of Computational Physics*, vol. 230, no. 5, pp. 2141–2159, Mar. 2011. DOI: 10.1016/j.jcp.2010.12.010.

[122] C. Pozrikidis and J. H. Ferziger, "*Introduction to Theoretical and Computational Fluid Dynamics*," *Physics Today*, vol. 50, no. 9, pp. 72–74, Sep. 1997. DOI: 10.1063/1.881920.

[123] A. Z. Zinchenko, M. A. Rother, and R. H. Davis, "A novel boundary-integral algorithm for viscous interaction of deformable drops," *Physics of Fluids*, vol. 9, no. 6, pp. 1493–1511, Jun. 1997. DOI: 10.1063/1.869275.

[124] A. Chamolly and E. Lauga, "Stokes flow due to point torques and sources in a spherical geometry," *Physical Review Fluids*, vol. 5, no. 7, p. 074 202, Jul. 2020. DOI: 10.1103/PhysRevFluids.5.074202.

[125] A. Z. Zinchenko, M. A. Rother, and R. H. Davis, "Cusping, capture, and breakup of interacting drops by a curvatureless boundary-integral algorithm," *Journal of Fluid Mechanics*, vol. 391, pp. 249–292, Jul. 1999. DOI: 10.1017/S0022112099005285.

[126] S. Jin, R. R. Lewis, and D. West, "A comparison of algorithms for vertex normal computation," *The Visual Computer*, vol. 21, no. 1-2, pp. 71–82, Feb. 2005. DOI: 10.1007/s00371-004-0271-1.

[127] K. E. Atkinson, *An introduction to numerical analysis*, 2nd ed. New York: Wiley, 1989.

[128] J. M. Rallison, "A numerical study of the deformation and burst of a viscous drop in general shear flows," *Journal of Fluid Mechanics*, vol. 109, no. -1, p. 465, Aug. 1981. DOI: 10.1017/S002211208100116X.

[129] J. Bezanson, A. Edelman, S. Karpinski, and V. B. Shah, "Julia: A Fresh Approach to Numerical Computing," *SIAM Review*, vol. 59, no. 1, pp. 65–98, Jan. 2017. DOI: 10.1137/141000671.

[130] A. Z. Zinchenko and R. H. Davis, "Algorithm for direct numerical simulation of emulsion flow through a granular material," *Journal of Computational Physics*, vol. 227, no. 16, pp. 7841–7888, Aug. 2008. DOI: 10.1016/j.jcp.2008.05.004.

[131] M. Loewenberg and E. J. Hinch, "Numerical simulation of a concentrated emulsion in shear flow," *Journal of Fluid Mechanics*, vol. 321, pp. 395–419, Aug. 1996. DOI: 10.1017/S002211209600777X.

[132] A. P. Stikuts, "Trīsdimensionāla robežintegrālvienādojumu algoritma izveide un tā testēšana piliena formas dinamikai kapilāro un viskozo spēku iedarbībā," Master's thesis, University of Latvia, 2018.

[133] P. K. Mogensen and A. N. Riseth, "Optim: A mathematical optimization package for Julia," p. 3, 2018.

[134] V. Cristini, J. Bławzdziewicz, and M. Loewenberg, "An Adaptive Mesh Algorithm for Evolving Surfaces: Simulations of Drop Breakup and Coalescence," *Journal of Computational Physics*, vol. 168, no. 2, pp. 445–463, Apr. 2001. DOI: 10.1006/jcph.2001.6713.

[135] G. I. Taylor, "The formation of emulsions in definable fields of flow," *Proc. R. Soc. Lond. A*, vol. 146, no. 858, pp. 501–523, Oct. 1934.

[136] L. Petzold, "Automatic Selection of Methods for Solving Stiff and Nonstiff Systems of Ordinary Differential Equations," *SIAM Journal on Scientific and Statistical Computing*, vol. 4, no. 1, pp. 136–148, Mar. 1983. DOI: 10.1137/0904010.

[137] B. Frka-Petesic, K. Erglis, J. Berret, A. Cebers, V. Dupuis, J. Fresnais, O. Sandre, and R. Perzynski, "Dynamics of paramagnetic nanostructured rods under rotating field," *Journal of Magnetism and Magnetic Materials*, vol. 323, no. 10, pp. 1309–1313, May 2011. DOI: 10.1016/j.jmmm.2010.11.036.

[138] J. Cīmurs, A. Brasovs, and K. Ērglis, "Stability analysis of a paramagnetic spheroid in a precessing field," *Journal of Magnetism and Magnetic Materials*, vol. 491, p. 165 630, Dec. 2019. DOI: 10.1016/j.jmmm.2019.165630.

[139] T. Brochu and R. Bridson, "Robust Topological Operations for Dynamic Explicit Surfaces," *SIAM Journal on Scientific Computing*, vol. 31, no. 4, pp. 2472–2493, Jan. 2009. DOI: 10.1137/080737617.

[140] L. H. P. Cunha, I. R. Siqueira, T. F. Oliveira, and H. D. Ceniceros, "Field-induced control of ferrofluid emulsion rheology and droplet break-up in shear flows," *Physics of Fluids*, vol. 30, no. 12, p. 122 110, Dec. 2018. DOI: 10.1063/1.5055943.

[141] B. A. Grzybowski, X. Jiang, H. A. Stone, and G. M. Whitesides, "Dynamic, self-assembled aggregates of magnetized, millimeter-sized objects rotating at the liquid-air interface: Macroscopic, two-dimensional classical artificial atoms and molecules," *Physical Review E*, vol. 64, no. 1, p. 011 603, Jun. 2001. DOI: 10.1103/PhysRevE.64.011603.

[142] J. W. Anthony, Ed., *Handbook of mineralogy*. Tucson, Ariz: Mineral Data Pub, 1990.

[143] M. Raboisson-Michel, J. Queiros Campos, S. Schaub, A. Zubarev, G. Verger-Dubois, and P. Kuzhir, "Kinetics of field-induced phase separation of a magnetic colloid under rotating magnetic fields," *The Journal of Chemical Physics*, vol. 153, no. 15, p. 154 902, Oct. 2020. DOI: 10.1063/5.0023706.

[144] Q. Liu and A. Prosperetti, "Wall effects on a rotating sphere," *Journal of Fluid Mechanics*, vol. 657, pp. 1–21, Aug. 2010. DOI: 10.1017/S002211201000128X.

[145] J. R. Blake and A. T. Chwang, "Fundamental singularities of viscous flow: Part I: The image systems in the vicinity of a stationary no-slip boundary," *Journal of Engineering Mathematics*, vol. 8, no. 1, pp. 23–29, Jan. 1974. DOI: 10.1007/BF02353701.

[146] S.-M. Yang and L. G. Leal, "Particle motion in Stokes flow near a plane fluid-fluid interface. Part 1. Slender body in a quiescent fluid," *Journal of Fluid Mechanics*, vol. 136, no. -1, p. 393, Nov. 1983. DOI: 10.1017/S0022112083002207.

[147] W. Bickley, "The secondary flow due to a sphere rotating in a viscous fluid," *The London, Edinburgh, and Dublin Philosophical Magazine and Journal of Science*, vol. 25, no. 170, pp. 746–752, May 1938. DOI: 10.1080/14786443808562058. (visited on 08/02/2022).

[148] *Wolfram Research (2007), Chemical Data, Wolfram Language function.* [Online]. Available: https://reference.wolfram.com/language/ref/ChemicalData.html.

[149] J. Belk, *Does the Divergence Theorem Work on a Surface?* Oct. 2012. [Online]. Available: https://math.stackexchange.com/questions/130081/does-the-divergence-theorem-work-on-a-surface.

[150] C. E. Weatherburn, *Differential geometry of three dimensions.* Cambridge At the University Press, 1955.

Résumé

En raison de la combinaison de leur réactivité aux champs magnétiques externes et de leur déformabilité, les gouttes de fluide magnétique constituent un matériau intéressant qui a trouvé de nombreuses applications en microfluidique. Ce travail explore la dynamique de ces gouttes dans un champ magnétique tournant. Les gouttes sont examinées à l'aide de plusieurs approches - théoriques, expérimentales et de simulations. Lorsque le champ magnétique tournant est faible et que la déformation de la goutte est petite, le mouvement de la goutte est calculé analytiquement. On constate que l'évolution de la forme de la goutte est régie par un système de trois équations différentielles non linéaires. Dans la limite des petites déformations, le mouvement de la goutte est qualitativement régi par un paramètre proportionnel au nombre capillaire - le rapport entre la traînée visqueuse et la force de tension superficielle. L'observation expérimentale de gouttes magnétiques obtenues par la séparation en deux phases liquides d'un ferrofluide suit qualitativement la solution analytique, cependant, il y a une divergence quantitative significative. Une simulation basée sur la méthode des éléments finis de frontière est développée pour calculer la dynamique des gouttes jusqu'à des déformations moyennes. On constate qu'un bon maintien du maillage est nécessaire pour produire des résultats de simulation précis. Un diagramme de phase est produit, qui montre la dynamique des gouttes en fonction de l'intensité et de la fréquence du champ tournant. Enfin, la dynamique collective des gouttes est examinée expérimentalement. Pour une certaine intensité et fréquence du champ magnétique, les gouttes forment des ensembles rotatifs d'ordre triangulaire - des cristaux rotatifs bidimensionnels. La dynamique de petits ensembles est reproduite en traitant les gouttes comme des couples ponctuels.

Mots clés : Goutte, Ferrofluide, Méthodes des éléments finis de frontière, Champ tournant

Abstract

Due to a combination of responsiveness to external magnetic fields and their deformability, magnetic fluid droplets make an interesting material that has found many applications in microfluidics. This work explores the dynamics of such droplets in a rotating magnetic field. The droplets are examined using multiple approaches – theoretically, experimentally and using simulations. When the rotating magnetic field is weak and the droplet's deformation is small, the droplet's motion is calculated analytically. It is found that the droplet's shape evolution is governed by a system of three nonlinear differential equations. In the small deformation limit, the motion of the droplet is qualitatively governed by a parameter proportional to the capillary number – the ratio of viscous drag to surface tension forces. The experimental observation of magnetic droplets obtained by the separation of a ferrofluid in two liquid phases, qualitatively follows the analytic solution, however, there is a significant quantitative discrepancy. A simulation based on the boundary element methods is developed to calculate the dynamics of the droplets up to medium deformations. It is found that good mesh maintenance is required to produce accurate simulation results. A phase diagram is produced, which shows the droplet dynamics depending on the rotating field strength and frequency. Finally, the collective dynamics of the droplets is examined experimentally. For a certain magnetic field strength and frequency, the droplets form rotating ensembles with a triangular order – two dimensional rotating crystals. The dynamics of small ensembles is reproduced by treating the droplets as point torques.

Key words: Droplet, Ferrofluid, Boundary element methods, Rotating field